Vibration-based Electromagnetic Energy Harvesters for MEMS Applications

by

Syed Farid Ullah Khan

B.Sc., Mechanical Engineering, NWFP University of Engineering and Technology, Peshawar, Pakistan, 1997
M.Sc., Mechanical Engineering Design, NWFP University of Engineering and Technology, Peshawar, Pakistan, 2005

A THESIS SUBMITTED IN PARTIAL FULFILMENT OF
THE REQUIRMENTS FOR THE DEGREE OF

DOCTOR OF PHILOSOPHY

in

THE FACULTY OF GRADUATE STUDIES

(Mechanical Engineering)

THE UNIVERSITY OF BRITISH COLUMBIA
(Vancouver)

April 2011

Abstract

This thesis investigates vibration-based electromagnetic energy harvesters (EMEHs) for application in low power autonomous sensors. It makes contributions pertaining to the development of a low cost fabrication technology, analytical modeling, simulations and characterization of EMEHs under harmonic and random vibrations.

A novel, low cost, one mask fabrication technology devised in this thesis is used to develop a copper foil-type linear EMEH, and a polydimethylsiloxane (PDMS) membrane type nonlinear EMEH. The voltage and power generated by these harvesters are comparable to existing EMEHs which use more involved fabrication processes. In the membrane type EMEH the inclusion of a more flexible PDMS membrane design reduces the harvester resonant frequency and makes it suitable for extracting energy from low level vibration environments. For acceleration levels greater than 0.1 g, this harvester exhibits a nonlinear behaviour. At higher levels of narrow band random excitations, the device therefore exhibits broadening of the load voltage spectrum in comparison to the response under relatively low levels of narrow band random excitations.

Analytical models for linear EMEHs with non-uniform magnetic field for harmonic vibrations are developed. A simple analytical model based on Faraday's law and uniform gradient of the normal component of the magnetic flux density is developed for EMEHs where the entire coil experiences approximately the same gradient of the normal component of the magnetic flux density. However, for EMEHs where the entire coil is not exposed to the same magnetic flux gradient a more robust model, based on the off-center analytical solution of the magnetic flux density is devised. The simulation results of the developed models are in good agreement with the experimental observations.

Analytical models for linear and nonlinear EMEHs under random vibrations are derived. The models are parameterized such that they are applicable to all architectures of EMEHs and can be utilized for designing and performance estimation of EMEHs. Nonlinear harvesters with spring nonlinearity and with combined spring and damping nonlinearity are modeled using the statistical linearization method. The developed models are useful in investigating the effects of the mechanical nonlinearity on the performance and bandwidth of the harvesters under random vibrations.

Preface

This thesis is based on four manuscripts, resulting from collaboration between three researchers.

A version of Chapter 2 appeared in: **Farid Khan, Farrokh Sassani and Boris Stoeber 2010 " Vibration-based electromagnetic energy harvester",** ***Proc. ASME IMECE2010*** and in: **Farid Khan, Farrokh Sassani and Boris Stoeber 2010 "Copper foil-type vibration-based electromagnetic energy harvester",** ***Journal of Micromechanics and Microengineering, vol. 20.*** The author's contributions in these papers were developing a low cost, one mask fabrication technology for the components of MEMS scale electromagnetic energy harvesters, developing an analytical model for linear electromagnetic energy harvesters with non-uniform magnetic field configuration, analytical simulation, Finite Element Analysis, experimental evaluation, and writing of the manuscripts. Dr. Farrokh Sassani and Dr. Boris Stoeber assisted with their suggestions in the analytical model, extraction of electrical damping co-efficient from the equivalent electrical circuit of the electromagnetic energy harvester and helped with phrasing and editing the manuscripts.

A version of Chapter 3 has been submitted for publication: **Farid Khan, Farrokh Sassani and Boris Stoeber "Modeling of linear electromagnetic energy harvesters with non-uniform magnetic field for sinusoidal vibrations".** The author's contributions in this paper were developing analytical models for linear electromagnetic energy harvesters with non-uniform magnetic field configuration and planar coils, extending the previously developed model to a more accurate and precise one for larger coils than magnets and for larger gaps between magnet and the coils. Analytical simulations of the developed models and validation with experimental results, optimization of the developed linear prototype with the devised model and writing of the manuscript were the other contributions of the author. Dr. Farrokh Sassani and Dr. Boris Stoeber suggested the extension of our previously developed model for a more robust analytical model, helped in phrasing and editing of the manuscript.

A version of Chapter 4 appeared in: **Farid Khan, Farrokh Sassani and Boris Stoeber 2010 "Vibration-based PDMS membrane type electromagnetic power generator for low vibration environments",** ***Proc. CSME FORUM 2010*** and the expanded full version has been submitted for publication: **Farid Khan, Farrokh Sassani and Boris Stoeber "Nonlinear**

behaviour of membrane type electromagnetic energy harvester under harmonic and random vibrations". The author's contributions in this paper were the fabrication of the electromagnetic energy harvester for low level sinusoidal and random vibration, magnetostatic analysis in COMSOL multiphysics®, design and preparation of the experimental setup for sinusoidal and random excitation, development of a program in LabVIEW Signal Express (Sound and Vibration assistance) for random vibration generation, spectral analysis of the random signals from the harvester and accelerometer and preparation of the manuscripts. Dr. Farrokh Sassani and Dr. Boris Stoeber suggested the idea of characterization of the device under random excitation, helped in data acquisition and processing under random vibration and editing the manuscripts.

A version of Chapter 5 has been submitted for publication: **Farid Khan, Farrokh Sassani and Boris Stoeber "Modeling and simulation of linear and nonlinear MEMS scale electromagnetic energy harvester for random vibration environment".** The author's contributions in this paper were developing analytical models for linear and nonlinear electromagnetic energy harvesters for broadband and narrow band vibration, developing of the MATLAB® code for the analytical simulation, Dr. Farrokh Sassani and Dr. Boris Stoeber proposed the idea of extending the modeling of linear and nonlinear electromagnetic energy harvesters for random excitation and helped editing the manuscript.

Table of Contents

List of Tables

List of Figures

List of Abbrevations

CVD	Chemical vapour deposition
DAQ	Data acquisition
DRIE	Deep reactive ion etching
EMEH	Electromagnetic energy harvester
EMPG	Electromagnetic power generator
ESEH	Electrostatic energy harvester
KOH	Potassium hydroxide
LIGA	Lithographie Galvanoformung Abformung
LPCVD	Low pressure chemical vapour deposition
MEMS	Microelectromechanical system
MPG	Micro power generator
PCB	Printed circuit board
PDMS	Polydimethylsiloxane
PECVD	Plasma enhanced chemical vapour deposition
PEEH	Piezoelectric energy harvester
PI	Polyimide
PMMA	Polymethylmethacrylate
POM	Product of merit
PSD	Power spectral density
PZT	Lead zirconate titanate
RIE	Reactive ion etching
SD	Spectral density
SPICE	Simulation program with integrated circuit emphasis
TPMS	Tire-pressure monitoring system
ULP	Ultra low power
ULV	Ultra low voltage

List of Symbols

A	Base acceleration of vibration
B_r	Remanent flux density
B_x	x-component of the magnetic flux density
B_y	y-component of the magnetic flux density
B_z	Normal component of the magnetic flux density
b	Spacing between the adjacent turns
b_c	Critical damping coefficient
b_e	Electrical damping coefficient
b_m	Mechanical damping coefficient
b_T	Total damping coefficient
D	Length of the magnet
$D(\dot{z})$	Nonlinear damping function
$d(\dot{z})$	Damping force
F_e	Force acting on the magnet due to the current flowing through the coil
f_m	Magnetic force per unit charge
f_1	Fundamental frequency
G	Transformation factor
$H(i\omega)$	Complex frequency response
k	Spring stiffness
L_i	One side length of a turn
L_1	Length of the side of the first turn
m	Inertial mass
N	Number of turns of the coil
NA	Area sum of the individual turns
$N(z)$	Nonlinear spring stiffness function
P_L	Amplitude of the power delivered to the load
P_{L_1}	Amplitude of the power delivered to the load at resonance
Q_e	Electrical quality factor of the harvester
Q_m	Mechanical quality factor of the harvester

Q_T	Total quality factor of the harvester
R	Radius of cylindrical magnet
R_C	Coil resistance
R_L	Load resistance
R_i	Inner radius of the circular spiral planar coil
$R_{L,opt}$	Optimum load resistance
r_m	Input impedance at the transformer element
S	Sum of the areas of the individual coil turns
S_i	Areas of the individual coil turn
S_0	Spectral density of acceleration for Gaussian white noise process
$s(z)$	Spring force
$S_A(\omega)$	Spectral density of the base acceleration
$S_U(\omega)$	Spectral density of the relative velocity
$S_{P_L}(\omega)$	Spectral density of power delivered into the load
$S_{V_L}(\omega)$	Spectral density of the load voltage
T	Combined thickness of the two magnets
t	Thickness of the planar coil
U	Amplitude of the relative velocity of the mass
V_G	Induced open-circuit voltage in a single coil
V_L	Amplitude of the voltage
V_{L_1}	Maximum voltage at resonance
$\overline{V_L^2}$	Mean square value of the load voltage
Y	Base amplitude of vibration
Z	Amplitude of the relative displacement of the mass
Z_{max}	Amplitude of the relative displacement at resonance
$z(t)$	Relative displacement
$\dot{z}(t)$	Relative velocity
$\ddot{z}(t)$	Relative acceleration
α	Scaling factor of nonlinear damping
$\Delta\omega$	Bandwidth of harvester
ζ_e	Electrical damping ratio

ζ_m	Mechanical damping ratio
ζ_T	Total damping ratio
ζ_{eq_T}	Equivalent total damping ratio of the equivalent linear EMEH
η	Scaling factor of nonlinear spring
μ_{eq}	Equivalent damping term of the equivalent linear EMEH
ρ_c	Resistivity of the coil material
σ_z	Standard deviation of the relative displacement $z(t)$
$\sigma_{\dot{z}}$	Standard deviation of the relative velocity $\dot{z}(t)$
σ_z^2	Variance of the relative velocity of the nonlinear EMEH
$\sigma_{\dot{z}}^2$	Variance of the relative velocity of the nonlinear EMEH
$\sigma_{z_{Lin}}$	Standard deviation of the relative displacement for linear case, $\eta = 0$
$\sigma_{\dot{z}_L}^2$	Variance of the relative velocity of the linear EMEH
$\sigma_{z_L}^2$	Variance of the relative displacement of the linear EMEH
ϕ	Angle traced by the circular spiral coil turn/s
$\phi_{\max}$	Maximum angle traced by the circular spiral coil turn/s
ω	Frequency of excitation
ω_{eq}	Equivalent frequency of the equivalent linear EMEH
ω_n	Natural frequency of the harvester

Acknowledgements

I would like to thank my supervisors, Dr. Farrokh Sassani and Dr. Boris Stoeber, for their valuable insight, constructive feedback, guidance and support during the course of my research. I also owe thanks to my supervisory committee members Dr. Edmond Cretu and Dr. Srikantha Phani for providing critical and constructive feedback during supervisory committee meetings. My thanks also go to Instrumentation Laboratory, MEMS Laboratory, Dynamics and applied mechanics Laboratory at UBC for providing access to the experimental facilities.

My special thanks to my parents and family without whose unconditional love and support this work would not have been accomplished.

Finally, I would like to acknowledge the institutions, The University of British Columbia, Higher Education Commission of Pakistan, and NWFP University of Engineering and Technology for their generous financial support through fellowships and grants during my studies.

To my parents

1 Introduction

1.1 Motivation

There are a number of challenges in generating power from vibration-based electromagnetic energy harvesters (EMEHs) these include: reducing fabrication costs, developing analytical models for harmonic and random vibrations, exploiting low levels of vibration, and characterizing device performance.

In the development of EMEHs, the fabrication of micro-coils, accurate mounting of the high flux density permanent magnets, and the spring that supports the magnets or coil are crucial tasks. Multi-mask microfabrication processes are typically used to produce planar coils and planar springs for EMEHs adding complexity towards fabrication and contributing to high fabrication cost of such devices. Most of the previously reported approaches use silicon-based multi-mask processes or complex fabrication methods to develop planar coils and planar springs. Applications to low cost wireless sensors require a simple and cost effective fabrication process with a small number of masks and fabrication steps, using low cost materials and eliminating costly process steps. Moreover the high young's modulus of silicon (185 GPa) results in a high device frequency, whereas its low material damping characteristics lead to a narrow bandwidth of the device, which contribute to poor device performance at off-resonant frequency excitation. Incorporating materials like copper, that have a relatively low young's modulus (118 GPa) and high material damping would result in a lower device frequency and a relatively broad bandwidth response.

The development of a novel, low cost fabrication technique that uses one mask and fewer processing steps to produce the planar copper coils and planar copper springs for vibration-based EMEHs is one motivation of this research. Planar copper coils and planar spring to support the motion of the permanent magnets have been fabricated from commercially available copper foils. Two identical coils are used, one on either side of the magnets in order to enhance the power generation for the same footprint of the EMEH.

Beside fabrication and characterization of EMEHs under harmonic vibration, the analytical models for the electromechanical transduction have proved to be very useful tools for the performance estimation and designing of these devices. The analytical modeling is

challenging, since it depends on the EMEH architecture (wound coil or planar coil), magnetic field configuration between the magnet and a coil (uniform magnetic field or non-uniform magnetic field), response characteristic (linear or nonlinear) and even on the nature of excitation (harmonic or random).

Linear harvesters with non-uniform field configuration under harmonic excitation, require better models that precisely estimate the performance of the harvester, even though, the planar coil is larger than the size of the magnet and the gap between the coil and the magnet is relatively large.

Most of the developed linear and nonlinear resonant energy harvesters have been tested and characterized under harmonic excitation, however, real environmental vibrations do not lead to single frequency excitation but rather the vibrational energy content is distributed over a narrow or broad band of frequencies and random in nature. The harvester performance can be quite different if instead of harmonic vibrations it is subjected to random vibrations. Similarly, the analytical models developed for harmonic vibrations are not suitable to estimate the performance under narrow band or broadband random vibrations. The developed EMEHs not only need to be characterized for random vibrations but also need analytical models to predict their performance and to optimize design parameters for the power generation over broader bandwidth of random vibrations. The mechanical nonlinearity in EMEHs must also be investigated and its effect on the device power generation and bandwidth must be determined when the harvester is subjected to random vibrations.

1.2 Background

Energy harvesting for autonomous and self powered microelectromechanical system (MEMS) sensors for industrial, healthcare and personal applications has been a major challenge. In the ambient, several energy sources are available to harvest energy for the power requirement of autonomous sensor nodes. An autonomous sensor node is a wireless sensor integrated with an energy harvester. Architecture of an autonomous sensor is shown in Figure 1.1, it consists of an energy harvester, rectifier, power distribution circuit, sensor, signal processing circuit and RF transmitter. The super capacitor is there to store the excessive energy for the instance when the power generation capability of the energy harvester decreases due to the unavailability of sufficient ambient energy.

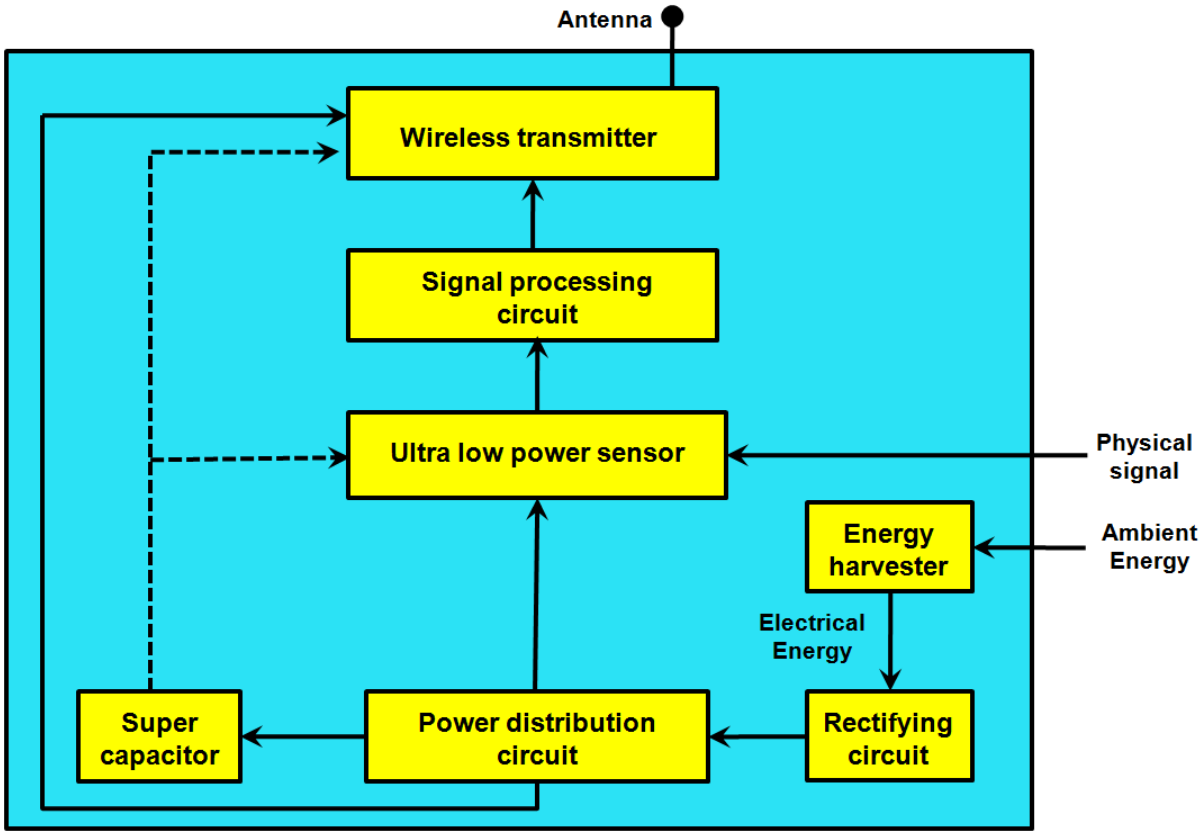

Figure 1.1: Architecture of an autonomous sensor node.

Significant work has been reported in the literature, regarding energy harvesters capable of generating electrical energy from acoustical waves [1-8], thermal gradients [9-17], RF radiations [18-22], solar radiations [23-27] and direct air flow [28-30]. However, generating power from the motion and mechanical vibration has gained increased interest in the last few years. The vibrational energy in the environment of sensors and other devices can be utilized to convert them into self-contained and maintenance-free units. The vibration of industrial machines, such as, compressors, turbines and electrical motors can be used to develop autonomous sensors for the condition and health monitoring of these machines. Smart tires in the automobile and in the aviation industry will soon be a reality, with autonomous tire-pressure monitoring systems (TPMS) [31-35], completely powered from the vibration present in cars and aircrafts. Intelligent cutting tools with vibration-powered embedded sensor nodes for precision machining will be attainable. Autonomous temperature and pressure sensors in the air conditioning ducts can be operated by generating power from air flow induced vibrations. The condition and health monitoring of aircraft wings can be done with sensors powered by the

vibrations of the wings. Even the low levels of vibration in household and office appliances can be used to harvest energy for the sensors in these appliances.

Vibration-based energy harvesters are inertial micro-generators that consist of a proof/inertial mass supported by a suspension spring. The mass oscillates relative to the device frame when subjected to vibration from the source. The oscillation of the mass is affected by the mechanical damping (air, material, and support damping) and by the electrical damping produced due to electromechanical transduction. There are typically three types of vibration-based energy harvesters, piezoelectric [36-39], electrostatic [40-43] and electromagnetic [44-46].

1.2.1 Piezoelectric energy harvesters

A piezoelectric energy harvester (PEEH) consists of piezoelectric material [47], which when subjected to mechanical deformation or strain, results in an electrical potential difference across the material. This property of piezoelectricity attributes to the spontaneous polarization within certain crystals (gallium orthophosphate and lagasite), polycrystalline ceramics (barium titanate, lead titanate and lead zirconate titanate) and piezoelectric polymer (polyvinlidene fluoride). The piezoelectric materials consist of polar domains, which are oriented randomly under unloaded condition. However, when the piezoelectric material is subjected to the mechanical strain, the dipole domains orient themselves and create a charge separation across the material, resulting in the voltage.

The cantilever beam is the most common architecture in piezoelectric energy harvesters according to the literature [48]. Thin layers of piezoelectric material, normally, lead zirconate titanate (PZT) are deposited on a micro-fabricated cantilever beam, and a proof mass at the tip of the beam is used to tune the frequency of the harvester. Interdigitated electrodes made up of thin layer of gold are used for electrical current regulation during the operation. Energy harvesters with only one layer of PZT on the cantilever beam are known as unimorph piezoelectric harvesters [49, 50], whereas cantilever beams with two layers of PZT (on either side of the beam) is referred to as the bimorph piezoelectric harvesters [51-53]. Piezoelectric energy harvesters with an array of PZT coated cantilever beams [54] have also been developed and reported for harvesting energy over a broader band of input frequencies.

The main advantage of PEEHs, is their ability to generat high voltage levels (>1 V) and hence ordinary rectifying circuits can be used for AC to DC conversion. However, due to the

high output impedance of these devices, normally in MΩ range, low levels of output current are available. The resonant frequency of these devices is also high and requires a proof mass to lower and tune the harvester frequency to typical environmental excitation frequencies. Moreover, the mechanical properties of the piezoelectric materials restrict the operation only to low levels of vibration amplitudes. The integration of the fabrication of these devices with standard MEMS fabrication processes is also a challenging task.

1.2.2 Electrostatic energy harvesters

An electrostatic energy harvester (ESEH) is essentially a variable gap capacitor and as such it is also known as the capacitive micro power generator. In its simplest form, it consists of two parallel conductive plates, which are separated by a dielectric, normally air. The principle of operation is based on the change of capacitance between the parallel plates. When the plates move relative to each other due to vibrations, the capacitance between the conductors changes which in turn causes an increase in the energy stored in the harvester. There are two modes of operation for ESEHs, charge constrained mode and the voltage constrained mode. In the charge constrained mode of operation, charge on the capacitor is held constant and when the capacitance reduces, due to the increase in the gap between the plates or decrease of the overlap area, the voltage between the plates increases. In the voltage constrained mode, the voltage between the plates remains constant, therefore the charge on the plates increases when either the gap between the plates is reduced or the plates overlap area is increased. In the former mode of operation, one voltage sources would be required for the initial charging of the ESEH, whereas for the latter mode of operation two voltage sources would be needed, one for initial charging and the second one for keeping the voltage constant during operation. The comparison between the two modes of operation is well addressed in [55].

Three architectures are commonly employed for micromachined ESEHs [56]. In out-of-plane gap varying type ESEH [56, 57], the capacitance changes due to the change of the gap between the two parallel plates. The bottom, fixed plate is either the substrate or a conductive layer deposited on the substrate, however, the top plate is suspended by beams. In-plane overlap type [56, 58] and in-plane gap varying type [56, 59] ESEHs have interdigitated fingers, which act as several parallel plates. In the former, the capacitance changes due to the change of overlap area between the interdigitated fingers, however, in the latter, the changing gap between the interdigitated fingers contributes to the capacitance change.

The primary advantage of ESEHs, is the ease with which these harvesters can be integrated with the standard MEMS fabrication technology. Monolithic fabrication of these devices is possible, moreover, the multi-user MEMS processes (MUMPs), such as, poly MUMPs, metal MUMPs or silicon-on-insulator (SOI) can easily be utilized. Also ESEHs are capable of generating high voltage levels (>1 V) and hence ordinary rectifying circuits can be used for AC to DC conversion. However, similar to PEEHs, they exhibit high output impedances which result in low levels of output current. The need for a voltage source for the initial charging and the requirement of a switching circuit for their operation are the major concerns that restrict the practical use of ESEHs. Another disadvantage is the presence of the pull-in phenomenon that can lead to stiction or a short circuit in ESEHs. The resonant frequency of these harvesters is also relatively high.

1.2.3 Electromagnetic energy harvesters

An electromagnetic energy harvester (EMEH) generates power due to the relative motion between a coil and a permanent magnet. Typically, the coil is either a wound coil or a planar coil. The principle of operation of EMEHs is based on Faraday's law of electromagnetism. When the EMEH is subjected to vibration, the relative motion between the coil and the magnet induces voltage across the ends of the coil. In its simplest form, an EMEH consists of a magnet, a coil, a mechanical spring, and a frame. The spring supports either the magnet or the coil and allows the relative motion in the device. During oscillations both mechanical damping and electrical damping are present. The mechanical damping comprises of air damping, material damping and support damping, whereas, the electrical damping arises when current flows in the coil.

There are a number of criteria to classify EMEHs, for example, the configuration of the magnetic field in the harvester or the architecture of the harvester. On the basis of such configurations there are EMEHs with uniform [60] and EMEHs with non-uniform magnetic field configurations [61]. Two magnets are used to produce approximately a uniform magnetic field for the coil to oscillate within, as shown in Figure 1.2(a). The coil experiences a non-uniform magnetic field if it oscillates in the field of a single magnet, as shown in Figure 1.2(b).

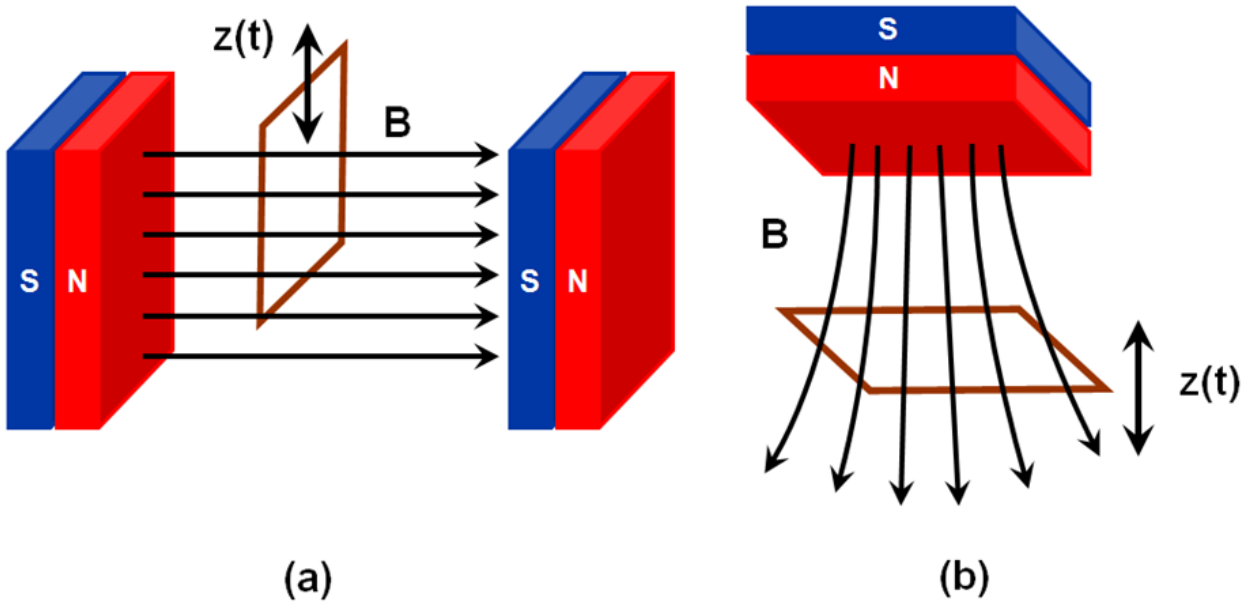

Figure 1.2: Magnetic field configuration in EMEH: (a) Uniform magnetic field configuration, (b) non-uniform magnetic field configuration.

In comparison to PEEHs and ESEHs, EMEHs generate low voltages, normally in the mV range, however, due to their lower output impedance relatively higher output current levels are available. Unlike the other two types of harvesters, several architectures for EMEHs are possible, and have been reported in literature. For example, moving magnet type [62], moving coil type [63], wound coil type [64], planar coil type [65], cantilever beam type [66], planar spring type [67], metallic spring type [68] and the polymeric membrane type [69]. The resonant frequency of the EMEHs is also low and with the proper selection of the magnet (mass) and the spring design these harvesters can easily be tune to low, medium and high g environments. The planar coil and the planar spring for the EMEHs can be produced with standard MEMS fabrication processes, such as SU8 molding and MEMS electroplating or even standard PCB technology can be utilized to produce the parts of the EMEHs.

1.3 Research objectives and contributions

The work documented in this thesis addressed the following objectives:

1. Developing a novel, low cost, one-mask fabrication technology for the components of EMEHs.

2. Developing an analytical model for linear EMEHs with non-uniform magnetic field configuration for sinusoidal vibrations.
3. Developing an analytical model for linear EMEHs for random vibrations.
4. Developing an analytical model for nonlinear EMEHs for random vibrations.

The following contributions have been made in the course of achieving these objectives:

- A non-silicon-based fabrication technique has been developed for the components of microelectromechanical systems, in which a commercially available copper foil is used to devise a foil-SU8 and a foil-PDMS fabrication technology.
    - The developed technology is versatile enough to fabricate the bonded as well as suspended structures.
    - The developed technology is not limited only to the fabrication of EMEH but can readily be extended to produce any of the following at low cost:
        - Variable gap capacitors/ electrostatic micro power generator
        - Pressure sensor
        - Actuator
        - Micro pump
        - Flow sensor
        - RF energy harvester
        - Acoustic energy harvester, etc.
- Analytical models for linear EMEHs with non-uniform magnetic field configuration and planar coil have been developed for harmonic excitations and have been validated by experimental observations.
    - An Analytical model for EMEHs with a square block magnet and a square spiral planar coil has been developed and validated through experimental assessment. The model is based on Faraday's law and a uniform gradient of the normal component of the magnetic flux density over the coil and utilizes the analytical solution of the normal component of the magnetic flux density along the line perpendicular to the center of the magnet. The model is suitable for EMEHs in which all the turns of the coil are experiencing approximately the same normal component of the magnetic flux density.

- The optimum load condition for linear EMEHs under sinusoidal vibration has been determined.
- An analytical model for EMEHs with a cylindrical magnet and a circular spiral planar coil has been developed for device output estimations.
- Analytical models based on the analytical solution of off-centre magnetic flux density have been developed for better estimation of output in EMEHs, where the normal component of the magnetic flux density is not uniform over all the turns of the coil.

- An analytical model for linear EMEHs under broadband and narrow band random vibrations has been developed.
  - The relationship between the mean output power and the EMEH design parameters (mechanical quality factor and transformation factor) has been established. The product of merit for better performance has been found and its significance has been theoretically analyzed.
  - The optimum load condition for linear EMEHs under random vibration has been determined.
- An analytical model for nonlinear EMEHs under broadband random vibrations has been developed.
  - It has been established analytically that for EMEHs with nonlinear stiffness and linear damping, the nonlinear spring hardening is responsible for the shift of the central (resonant) frequency of the load voltage spectral density.
  - For EMEHs with both nonlinear stiffness and damping a relationship of stiffness and damping on the central (resonant) frequency of the load voltage spectral density has been established. It has been found that the shift of the central frequency toward higher frequencies is due to the nonlinear stiffness and the nonlinear damping, and it tends to decrease this frequency shift.
  - It was found analytically that under random excitations, bandwidth broadening can be obtained in the nonlinear regime in comparison to operation of the harvester in the linear regime.
- Developed a nonlinear PDMS membrane type EMEH for low levels of harmonic and narrow band vibrations.
  - A PDMS membrane was incorporated in the EMEH.

- An experimental setup was established to generate random vibrations and to analyze the random signals from the EMEH.
- It was found experimentally that under high levels of random excitation, the spring hardening of the membrane is responsible for the shift of the central frequency of the load voltage spectral density.
- It was found experimentally that under random excitations, the bandwidth broadening can be obtained in the nonlinear regime in comparison to operation of the harvester in the linear regime.

1.4 Chapter summary

The overall goal of the research conducted in this thesis is to develop a low cost, one mask technique to fabricate the components for the EMEHs, experimentally evaluate the performance of the fabricated devices under sinusoidal as well as random vibrations, and to develop and validate analytical models for linear and nonlinear EMEHs under harmonic and random excitations. This thesis has been written in the manuscript-based format, as specified by the Faculty of Graduate Studies at the University of British Columbia. In the manuscript-based thesis, each chapter represents an individual work that has been published, submitted or prepared for submission to a peer reviewed journal. Each chapter is self-contained in the sense that it comprises an introduction to the work presented, the methodology, results and the discussion. The thesis also provides overall conclusions in the last chapter. The references summarized in the bibliography and the appendices associated with the chapters are presented at the end of the thesis.

In Chapter 2, modeling, simulation, fabrication, and characterization of a linear vibration-based electromagnetic energy harvester are presented. A novel, low cost, one-mask technique is developed to fabricate the planar coils and the planar spring for the EMEH. This fabrication technique can provide an alternative for processes such as Lithographie Galvanoformung Abformung (LIGA) or SU-8 molding and MEMS electroplating. Commercially available copper foils are used for the planar coils and the planar spring to fabricate a non silicon-based, low cost EMEH. A novel architecture for the EMEH is proposed in which planar coils on either side of the magnets are used to enhance the power generation for the same footprint of the device. An analytical model for the EMEH with square block magnets and square spiral planar coils is

developed. The model is based on Faraday's law and a uniform magnetic flux gradient of the normal component of the magnetic flux density over the coil; and it is suitable for EMEHs in which all the turns of the coil are experiencing approximately the same normal component of the magnetic flux density. The simulations based on the analytical model are also presented, which are in good agreement with the experimental results.

Chapter 3 describes the analytical modeling and simulation for the electromechanical transduction of linear EMEHs with non-uniform magnetic field configuration, under harmonic vibrations. Models are developed for linear EMEHs with planar coils using Faraday's law of electromagnetic induction and the Lorentz force law. For better prediction of the performance of the EMEH with larger coils than the size of magnet and/or larger gaps between the magnet and a coil, the analytical solution of the off-center magnetic flux density for a square magnet is used. Simulation results of the developed models show good agreement with the experimental results. Further simulations of the previously developed EMEH show an improvement of the load voltage and the power when optimizing the magnet-coil distance. Moreover maximizing the number of coil turns for the optimized gap, the simulation yields a load voltage raise to almost twice the experimental values and an increase of the load power to almost three times the experimental result.

In Chapter 4, the fabrication and characterization of a nonlinear vibration-based polydimethylsiloxane (PDMS) membrane type electromagnetic energy harvester (EMEH) is presented. Instead of a planar spring, a PDMS membrane is used to support the magnets in order to allow large amplitudes for the vibration of the magnet at low levels of base excitation. Slotted polycarbonate plastic spacers are introduced in the device enclosure to permit flow of the air between coil substrate and the membrane, which results in reduced air damping and enhanced power generation. To understand how the number of turns or the overall area of the coil is affected by the magnetic flux density distribution, a 2-D magnetostatic analysis is performed in COMSOL multiphysics®. For maximum voltage generation, the same simulation model is used to find an appropriate gap between the magnets and the coil. The harvester is characterized under sinusoidal as well as narrow band random excitations. Under low levels of sinusoidal excitation, it exhibits a linear response. However, at high acceleration levels the behaviour of the EMEH is nonlinear, exhibiting sharp jump and hysteresis phenomena during frequency sweeps. The nonlinear behaviour of the EMEH is exploited to harvest energy under narrow band random

excitations. With increasing levels of narrow band random excitations, the device exhibits a broadening of the load voltage spectrum in comparison to the response under low levels of random excitations. The results show that the nonlinear behaviour of the PDMS membrane can be utilized to enhance bandwidth of the harvester under narrow band random excitations and provides a simple alternative for other bandwidth broadening methods such as beam prestress, resonance tuning, or stopper impacts.

Chapter 5 presents the analytical modeling and simulation of linear and nonlinear electromagnetic energy harvesters (EMEHs) for random vibrations. For linear harvesters, an analytical relationship of the harvester output with the design parameters is established and simulation results for mean power, mean square load voltage and output spectral densities are presented. The significance of increasing both the transformation factor and the mechanical quality factor for the energy harvesting is analyzed. Moreover, the optimum load condition for better performance of the harvester is investigated. The method of statistical linearization is used to model nonlinear EMEH with a duffing spring and linear plus cubic damping. The simulation of the nonlinear model for low levels as well as relatively high levels of broadband stationary Gaussian random vibrations is performed. The effects of the nonlinear spring stiffness and the nonlinear damping on the maximum load voltage, the central frequency, and the bandwidth of the load voltage spectral density are investigated and presented.

2 Copper foil-type vibration-based electromagnetic energy harvester[1]

2.1 Introduction

Wireless sensor nodes have a wide range of application from condition monitoring of machines, such as electric motors and compressors to tire pressure monitoring systems (TPMS) in automobiles. One of the most challenging problems for wireless sensor nodes is providing the required power [70, 71]. Batteries have a limited life and their use in wireless sensor nodes may restrict the application of such devices in embedded and harsh environments. Harvesting energy from the ambient will have a significant impact on the field of wireless sensors. Converting ambient mechanical vibration into electrical energy for wireless sensor nodes with vibration-based micro power generators (MPGs) is suitable for applications such as non-destructive health monitoring of structures and machines. In industrial machines, such as electric motors, generators, compressors, reciprocating engines or turbines, vibration levels for a frequency range of 0 to 5000 Hz vary from 0.5 to 15 g peak acceleration [72]. Whereas the vibration levels for some production machines, such as lathes and drilling presses, and for household appliances typically range from 30 to 200 Hz and vary from 0.01 to 1.1 g peak acceleration [73]. The general aim of research in the area of energy harvesting is to develop devices suitable for harvesting energy from these commonly available vibration sources to power wireless sensors and transmitters. The power provided by vibration-based energy harvesters tends to be low, however, with the rapid advancement in ultra low power (ULP) MEMS sensors and microelectronics the power need is on a decline to a few µW. The power requirements of commercially available ULP sensors depend on the type (pressure, temperature or acceleration) and model of the sensor. For their operation, ULP acceleration sensors need more power (at least 21.6 µW for a supply current of 10 µA) in comparison to pressure sensors (at least 1.8 µW for a supply current of 1 µA) and temperature sensors (at least 1.89 µW for a supply current of 0.9 µA). The overall power consumption of ULP sensors ranges from 1.8 to 324 µW for supply current range of 1 to 180 µA [74].

[1] A version of this chapter has been published. Farid Khan, Farrokh Sassani and Boris Stoeber 2010 "Copper foil-type vibration-based electromagnetic energy harvester", Journal of Micromechanics and Microengineering 20 125006

Due to such ultra low power needs, energy harvesting has the potential for integration into these sensors to provide unlimited maintenance-free operation. The power need of wireless sensors is typically a few mW [71], which is relatively high and a major portion of the power is required for RF transmission. The current MEMS-scale energy harvesting techniques are not developed far enough to completely eliminate the battery from the wireless sensor nodes, however, upon subjecting the device output voltage to an ultra low voltage (ULV) and ULP rectifier, and the resulting DC voltage to an ULV DC-DC step-up converter, these harvesters can be integrated to supplement the power provided by the battery and increase its life span.

Several vibration-based power generators, based on piezoelectric [75], electrostatic [76] and electromagnetic [77] transduction, have been demonstrated. Out of these, electromagnetic power generators (EMPGs) have the advantages of low output impedance and high output current [78]. Vibration-based electromagnetic energy harvesters typically consist of a permanent magnet, a coil, and a suspension spring. Electrical energy is generated when the coil experiences a change in magnetic flux as a result of a relative motion between the magnet and the coil, and an emf is generated across its ends according to Faraday's law of electromagnetic induction. There are two well known architectures used for EMPGs to achieve this energy transduction. In one architecture of EMPG the magnet is mounted on a suspension spring and the coil is stationary, whereas in the other the magnet is fixed and the coil rides on a suspension spring. However, the former is preferred since the magnet acts as the inertial mass and this has the advantage of lowering the resonant frequency and enhancing the device's power generation [79]. For both EMPG architectures, different methods to fabricate the coils and the suspension springs have been reported in the literature.

2.1.1 Moving magnet EMPGs

This type of EMPG mostly consists of a bulk permanent magnet bonded to a microfabricated planar spring, and a coil, which is either a microfabricated planar coil or a wound coil. Wang *et al.* [80] have reported a moving magnet type EMPG, comprised of a NdFeB magnet, a two-layer planar copper coil on a glass substrate, and a planar copper spring fabricated on a double-side thermally oxidized silicon wafer. The planar spring is fabricated by selective etching of SiO_2 with buffered hydrofluoric acid (BHF), sputtering of Cr/Cu as seed layer, molding and electroplating of copper, and backside wet etching of silicon and SiO_2. Each layer of the coil is

produced by molding and electroplating of copper. A 150 nm Cr/Cu seed layer is sputtered for this purpose. A cured, ground and polished polyimide layer is used as an insulation between the two copper coils. A 2 mm x 2 mm x 1 mm NdFeB magnet is attached to the platform of the planar spring, which is then bonded onto the substrate containing the copper coils to form an MPG. The reported maximum 60 mV peak-to-peak open circuit voltage had been generated at 121.3 Hz for 1.5 g base acceleration. A silicon EMPG for wearable micro devices reported in [81] consists of a planar spring and a magnet which moves within a central recess of the substrate carrying the coil. The nickel iron (Ni-Fe) spring is fabricated on a silicon wafer with the following process steps: application of nitride by low pressure chemical vapour deposition (LPCVD), backside patterning of nitride, and etching of silicon with potassium hydroxide (KOH) to obtain a supporting 30 µm silicon membrane, deposition of a Ti/Cu seed layer on the frontside, molding and electroplating of a 20 µm thick Ni-Fe layer, and finally removing of the backside silicon membrane and nitride by reactive ion etching (RIE) to release the suspension spring. The planar copper coil is fabricated on the second silicon wafer using backside patterning of the nitride layer, silicon etching with KOH to achieve the supporting silicon membrane, sputtering and patterning of an aluminum layer on the front side, plasma enhanced chemical vapour deposition (PECVD) of oxide as an insulation layer, sputter deposition of Ti/Cu as a seed layer, followed by molding and electroplating of 100 µm thick copper. As a last step, a backside silicon and nitride etch by RIE produces the central recess for the movement of the magnet. After mounting the NdFeB magnet on the centre plate of the spring wafer, it is adhesive bonded to the coil wafer to form a 6 mm x 6 mm x 1 mm EMPG. The EMPG generated 1.4 µW when excited at 100 Hz and 50 µm base amplitude. Pan *et al.* [82] reported the development of a two-wafer EMPG, in which a sputtered iron-platinum (FePt) magnet on a spiral planar spring is used instead of a bulk magnet. In their device the silicon spiral spring is fabricated by bulk micromachining with a double-sided polished silicon wafer. The fabrication involves selective deep reactive ion etching (DRIE) to define the spiral, deposition of a SiO_2/Si_3Ni_4 layer, backside selective etching of silicon by KOH to form a spiral spring and then sputtering of the magnetic FePt film. A planar copper coil is made with a 4-mask process that needs a buffer layer coating, copper seed layer sputtering, molding and electroplating of routing copper, insulator polyimide (PI) layer coating and mold electroplating of copper. The two wafers are then joined by a low temperature bonding process to form a

0.45 cm^3 device. The authors reported a 40 mV voltage amplitude and 100 µW power generation at the excitation frequency of 60 Hz. A membrane type EMPG, containing a 127 µm thick kapton membrane to support NdFeB magnets, that moves in a recess provided within a silicon wafer, and within a printed circuit board (PCB) frame has been reported by Serre *et al.* [83]. The recess is produced by bulk micro-machining. A 52-turn, 15 µm thick electroplated planar copper coil, fabricated on a recessed silicon wafer is bonded to the recessed PCB wafer. The kapton membrane is glued to the backside of the PCB wafer to form the complete device. The response of their fabricated device is nonlinear. Under resonant condition at 5.1 µm base amplitude it produced a maximum power of 50 µW at matched load and a maximum voltage of 180 mV at a resistance load of 100 kΩ.

A combined electromagnetic and piezoelectric generator for harvesting energy from a computer keyboard is reported in [84]. The electromagnetic element of the device consists of a NdFeB magnet, a rubber cushion spring and a micro-machined bi-layer planar aluminum coil. 5 masks are used to fabricate the bi-layer aluminum planar coil on a thin lead zirconate titanate (PZT) plate. The fabrication comprises of 0.5 µm thick parylene deposition and patterning with RIE to open the contact pads for the PZT electrode, sputter deposition of 0.6 µm thick aluminum and patterning for the first spiral coil, deposition and patterning of 0.5 µm parylene as insulation layer, sputtering and patterning of 0.6 µm thick aluminum for the second spiral coil, and lastly deposition of 0.5 µm parylene as passivation layer. For electromagnetic conversion the authors reported a maximum of 1.15 µW with a 35 Ω load for a typing speed of 40 words per minute. The development of a wound copper coil harvester with NdFeB magnets and a tungsten proof mass on the tip of a laser etched beryllium copper (BeCu) cantilever beam is reported in [85]. The detailed fabrication of the 2800-turn stationary coil and 50 µm thick BeCu beam is not reported. The 150 mm^3 generator produced a power of 58 µW at 52 Hz and 0.6 m/s^2 acceleration, and successfully powered an RF accelerometer. A AA battery size power generator for wireless applications, which is composed of a hand wound coil and a spiral planar spring to support the magnet is reported in [86]. The spiral spring is fabricated by laser micromachining as well as by SU-8 molding and electroplating. A magnet is attached to the central platform of the spring and an inner housing, having a recess for the movement of the magnet, is bonded on either side of the spring. A wire is wound on the inner housing to form a coil for the power generator. It has been shown that when two such power generators are integrated with a power

management circuit (rectifiers and a capacitor) and packaged into a AA battery size container, it produced 1.6 V DC when subjected to vibration and charged for less than 1 minute.

2.1.2 Moving coil EMPGs

In a moving coil EMPG the coil moves relative to a fixed permanent magnet with the help of a suspension spring to generate the electrical power. A proof mass has to be used to tune the resonant frequency and enhance the power generation. Sari *et al.* [87] developed a moving coil type EMPG for wideband environmental vibrations that consists of an array of coil embedded cantilever beams and a fixed magnet. The EMPG is fabricated with a 5-mask process. The fabrication steps involved are thermal growth of 1 µm thick SiO_2, deposition and patterning of 1 µm thick parylene with RIE, sputtering and patterning of Ti/Au as coil material, deposition and patterning of 1 µm thick parylene as isolation layer, metal deposition for electrical routing, deposition of 13 µm thick parylene to define cantilevers, backside silicon etching by DRIE, and finally the sacrificial oxide etching by BHF results in the release of the beams. With an array of 35 beams and excitation at 1 µm base amplitude the reported device produced 10 mV voltage and 0.4 µW power over a bandwidth of 800 Hz (4.2-5 kHz). Kulkarni *et al.* [88] developed an EMPG consisting of four fixed NdFeB magnets and a planar copper coil fabricated on a silicon paddle. The fabrication of the planar coil and the silicon paddle comprised of chemical vapour deposition (CVD) of 0.5 µm thick oxide, sputtering and patterning of a 2 µm thick copper layer for electrical routing, deposition and patterning of 1.8 µm thick polyamide, molding and electroplating of the copper as coil, and DRIE with a patterned photoresist to form the silicon paddle, beam and frame. Two NdFeB magnets are assembled in a polymethylmethacrylate (PMMA) chip that is fabricated by conventional milling. The silicon chip and two such PMMA chips are then bonded together to produce a 0.1 cm^3 EMPG. At the resonant frequency of 9.84 kHz and for 9.8 m/s^2 acceleration the MPG has shown to generate a maximum power of 23 nW at a load of 52.7 Ω. An EMPG developed with standard silicon micromachining is reported in [89]. The EMPG consists of four fixed NdFeB magnets, a cantilevered paddle and a wound coil. The silicon paddle, frame and cantilever beam are fabricated by DRIE. A V groove in the cantilever beam (to channel the copper wire from the wound coil to the pads) is produced by selective etch of SiO_2/Si_3Ni_4 and KOH etch of the silicon, the aluminum pads are made by metallization and selective etching. Two magnets are positioned within the mechanically

machined recess in the capping PMMA chip. One of such PMMA chips is then bonded onto either side of the silicon chip to form a 100 mm^3 device. The device generated 122 nW of power for 0.4 g input acceleration at 9.5 kHz. An EMPG that consists of a hand wound coil attached to an etched stainless steel beam, which moves between two fixed NdFeB magnets is reported in [90]. The device has a natural frequency of 322 Hz and generated a maximum power of 37 µW at a base amplitude of 13 µm. Soliman *et al.* [91] report a wideband energy harvester consisting of four fixed magnets, a seismic mass and a wound coil supported by an aluminum cantilever beam. The 1 cm^2 wound coil has 22 turns and is made out of 160 µm thick copper wire. The details of the fabrication of the beam are not reported. A sliding stopper is used to restrict the motion of the beam to transform the harvester from a linear oscillator to a piecewise-linear oscillator. It has been shown that with this transformation a broad bandwidth is obtained in the vicinity of the natural frequency.

In EMPGs, the fabrication of micro-coils, accurate mounting of the high flux density permanent magnets, and the spring that supports the magnets or coil are challenging steps. Multi-mask microfabrication processes are typically used to produce planar coils and springs for EMPGs adding complexity to fabrication and contributing to high fabrication cost of such devices. Applications to low cost wireless sensors require a simple and cost effective fabrication process with a fewer number of masks and fabrication steps, using low cost materials and eliminating expensive process steps.

This chapter describes the fabrication of vibration-based EMPG in which the planar coil and the planar spring are fabricated by a novel, low cost, one mask process. The planar copper coils and the planar spring to support the motion of the permanent magnets have been fabricated from commercially available copper foils. Two identical coils are used, one on either side of the magnets in order to enhance the power generation for the same footprint of the EMPG. The detailed modeling and simulation for a device configuration in which a magnet is vibrating on top of a coil is performed and is found in good agreement with the experimental results. The equivalent electrical circuit model is used to extract the electrical damping ratio for load power computation.

2.2 Design and modeling

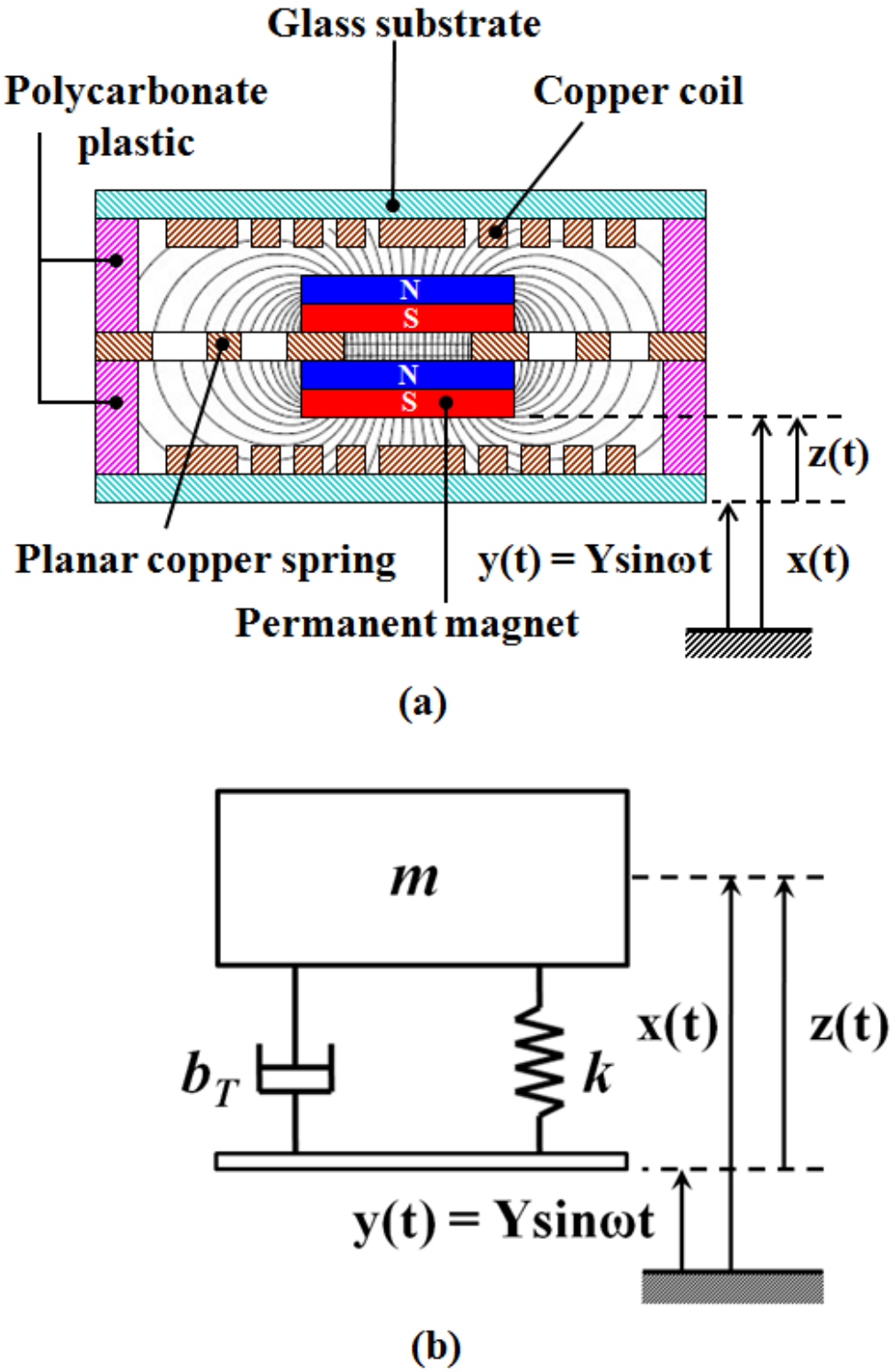

Figure 2.1: Schematic of the developed EMPG (a) cross-sectional view, (b) lumped parameter linear model for the EMPG.

The EMPG presented in this chapter consists of two NdFeB magnets (K & J Magnetics Inc. Jamison, PA, USA) mounted on a planar copper spring as shown in Figure 2.1. Planar copper micro-coils, fabricated on a glass substrate are placed on either side of the magnet assembly. The magnets and the micro-coils are held apart by 2 mm thick polycarbonate plastic spacers (Sheffield Plastics Inc. Sheffield, MA, USA). Figure 2.2 illustrates the exploded view of the device.

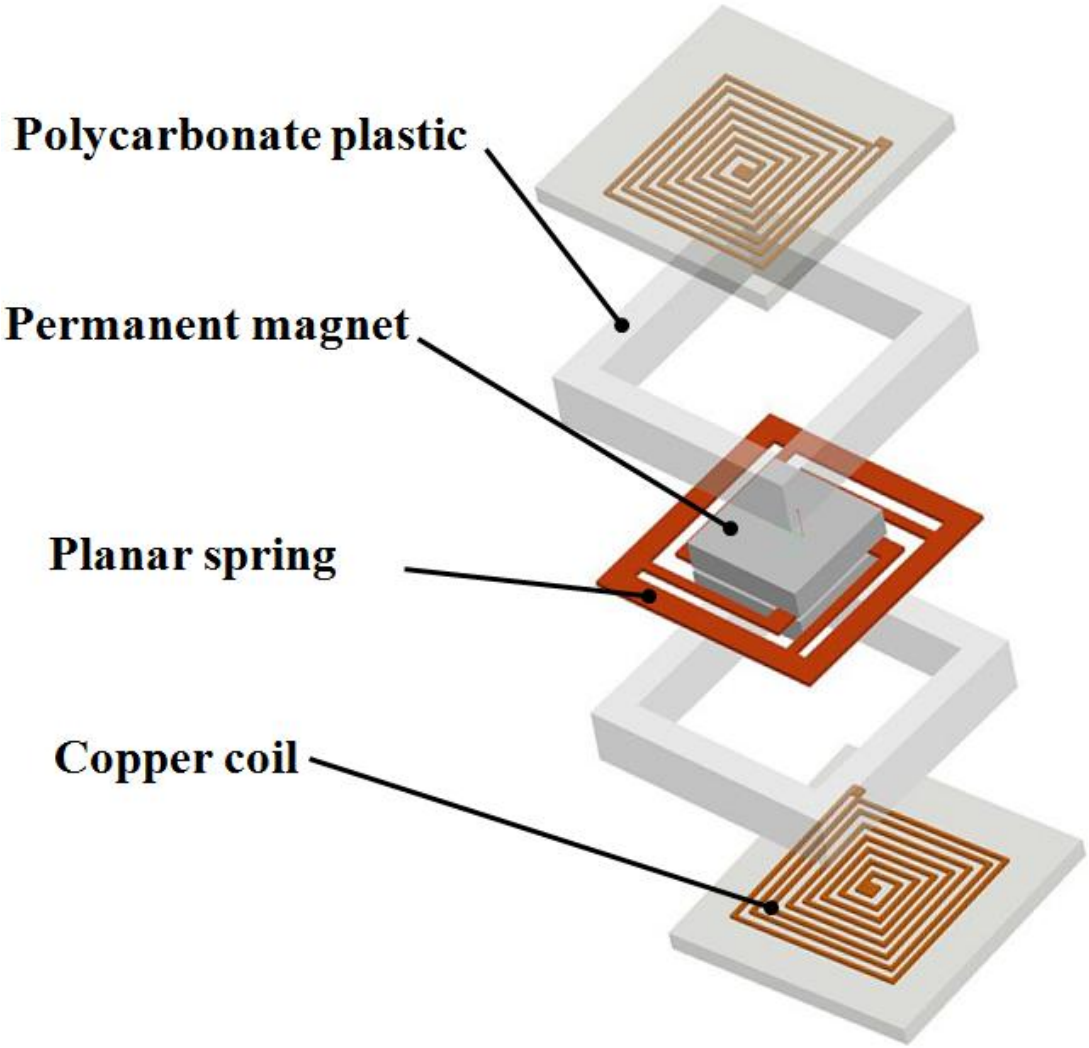

Figure 2.2: Exploded view of the EMPG.

By modeling the EMPG shown in Figure 2.1 as a spring-mass-damper system with base excitation, the amplitude of the relative displacement

$$Z = \frac{Y\omega^2}{\omega_n^2\sqrt{\left[1-\left(\omega/\omega_n\right)^2\right]^2+\left[2\zeta_T\left(\omega/\omega_n\right)\right]^2}} \qquad (2.1)$$

and the amplitude of the relative velocity

$$U = \frac{A\omega}{\omega_n^2\sqrt{\left[1-\left(\omega/\omega_n\right)^2\right]^2+\left[2\zeta_T\left(\omega/\omega_n\right)\right]^2}} \qquad (2.2)$$

between the magnets and housing of the device are determined in terms of the frequency of excitation ω, the natural frequency ω_n, the base amplitude of vibration Y, the base acceleration $A = \omega^2 Y$, and the total damping ratio ζ_T.

The natural frequency

$$\omega_n = \sqrt{\frac{k_{eq}}{m}} \qquad (2.3)$$

of the EMPG is expressed in terms of the device parameters, mass m of the magnets, and the equivalent stiffness k_{eq} of the planar spring. The planar spring in the harvester can be modeled as four fixed-guided beams in parallel with equivalent stiffness

$$k_{eq} = 4k = 4\left(\frac{12EI}{l_s^3}\right) = \frac{4Ew_s t_s^3}{l_s^3} \qquad (2.4)$$

depending on young's modulus E, width w_s, thickness t_s and length l_s of each beam.

The induced open-circuit voltage in a single coil of the device is approximated according to Faraday's law of electromagnetic induction [92, 93] as

$$V_G = -U\frac{\mathrm{d}B_z}{\mathrm{d}z}S, \qquad (2.5)$$

where B_z is the normal magnetic flux density and S is the sum of the areas S_i of the individual coil turns.

For a square spiral planar coil, Figure 2.3, with the length L_1 of the side of the first turn, line width w and spacing b between the adjacent turns, S can be approximated as

$$S = \sum_{i=1}^{n} S_i \approx \sum_{i=1}^{n} L_i^2 \qquad (2.6)$$

with

$$L_i = L_1 + 2(i-1)(w+b), \qquad (2.7)$$

where L_i is one side length of a turn.

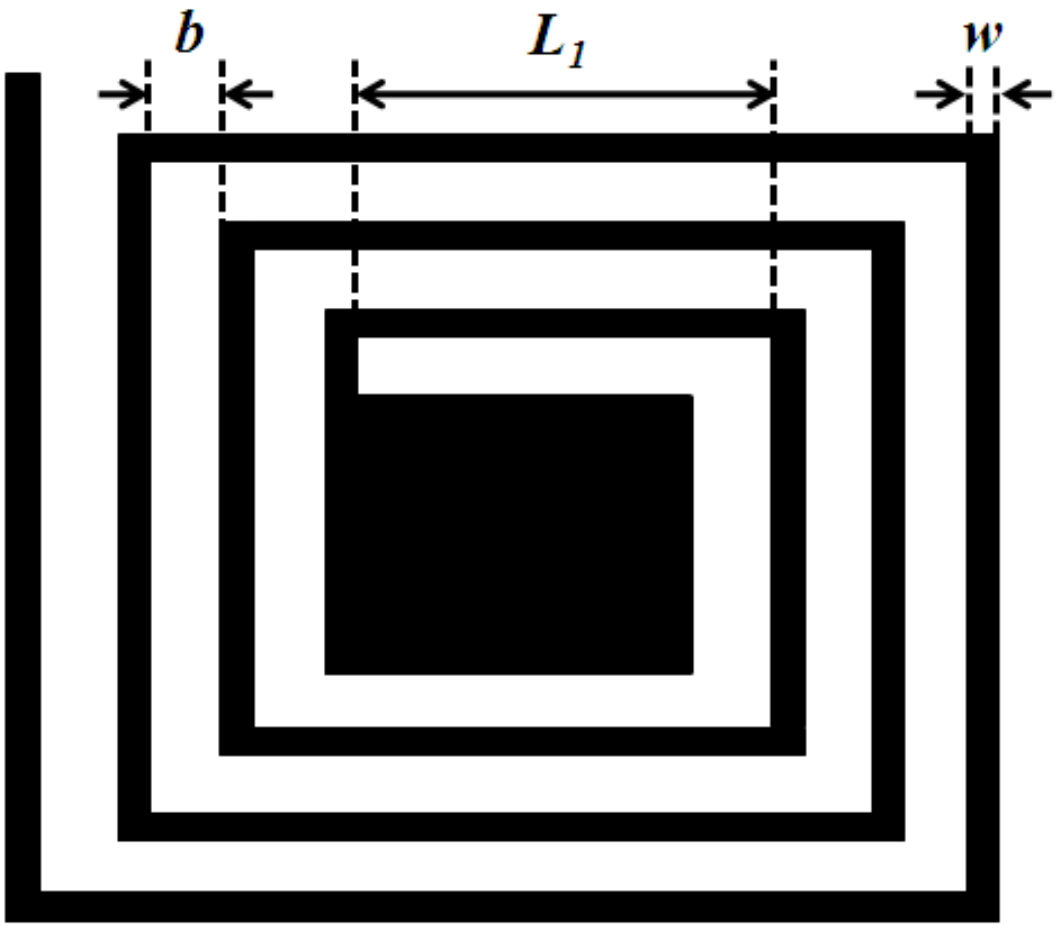

Figure 2.3 Square spiral planar coil.

The magnetic flux density for a rectangular block magnet [94] along a line normal to its centre

$$B_z = \frac{B_r}{\pi}\left\{\sin^{-1}\left[\frac{WD}{4\left[\left(W^2/4 + z^2\right)\left(D^2/4 + z^2\right)\right]^{1/2}}\right] - \sin^{-1}\left[\frac{WD}{4\left[\left(W^2/4 + (z+T)^2\right)\left(D^2/4 + (z+T)^2\right)\right]^{1/2}}\right]\right\} \qquad (2.8)$$

depends on the remanent flux density B_r, the width of magnet W, the length of the magnet D, the thickness or the combined thickness of the two magnets T in our case, and the distance from the magnets z.

For the analytical computations, $\frac{\mathrm{d}B_z}{\mathrm{d}z}$ is obtained by differentiating equation (2.8) with respect to z and then setting z equal to the gap between the magnet and a coil at rest.

The amplitude of the voltage

$$V_L = \left(\frac{R_L}{R_L + R_C}\right)\frac{A\omega}{\omega_n^2\sqrt{\left[1-\left(\omega/\omega_n\right)^2\right] + \left[2\zeta_T\left(\omega/\omega_n\right)\right]^2}}\frac{\mathrm{d}B_z}{\mathrm{d}z}S \qquad (2.9)$$

and the amplitude of the power

$$P_L = \frac{V_L^2}{2R_L} \qquad (2.10)$$

delivered to the load depend on the load resistance R_L and the coil resistance R_C.

The maximum voltage

$$V_{L,1} = \left(\frac{R_L}{R_L + R_C}\right)\frac{A}{2\omega_n\zeta_T}\frac{\mathrm{d}B_z}{\mathrm{d}z}S \qquad (2.11)$$

occurs at resonance.

The analytical model (equation 2.9) provides very good estimates for the EMPGs in which the planar coil is much smaller than the magnet and for small gaps between the coil and the magnet. However, it will slightly overestimate the EMPG performance if the outer edges of the coil face a smaller flux density than the maximum flux density given by equation (2.8).

The transformation factor G is an important parameter in inertial EMPGs. It describes the coupling between the mechanical and electrical energy domains and it therefore describes the energy conversion between the mechanical and the electrical domains. The open-circuit induced voltage across the coil

$$V_G = GU \qquad (2.12)$$

is therefore expressed by the transformation factor, and the force

$$F_e = GI \qquad (2.13)$$

acts on the magnet due to the current I flowing through the coil. Using equations (2.12) and (2.13), an inertial EMPG can be represented by the equivalent electrical circuit model shown in Figure 2.4. In the mechanical domain m, b_m and k represent the inertial mass, mechanical damping coefficient and spring stiffness, respectively. By ignoring the coil self inductance L_C that corresponds to a very small impedance at the frequencies of interest and combining the load and coil series resistances the input impedance at the transformer element, Figure 2.4(b), is expressed as

$$r_m = \frac{R_L + R_C}{G^2} \ . \qquad (2.14)$$

In the equivalent electrical circuit, Figure 2.4(c), the total damping coefficient of the EMPG $b_T = b_m + b_e$, includes the electrical damping coefficient

$$b_e = \frac{1}{r_m} = \frac{G^2}{R_L + R_C} \ . \qquad (2.15)$$

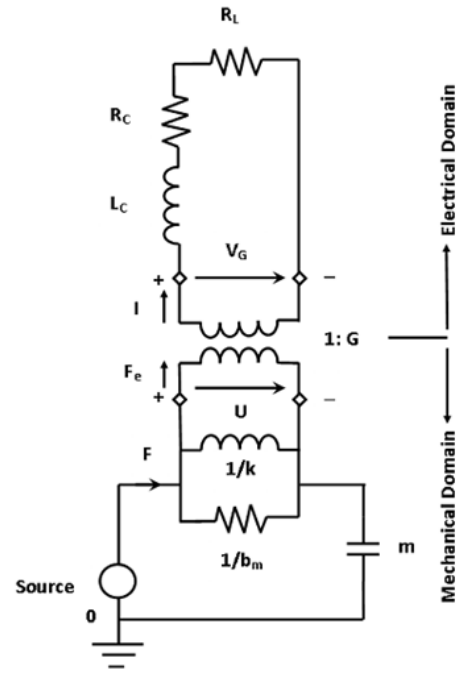

(a)

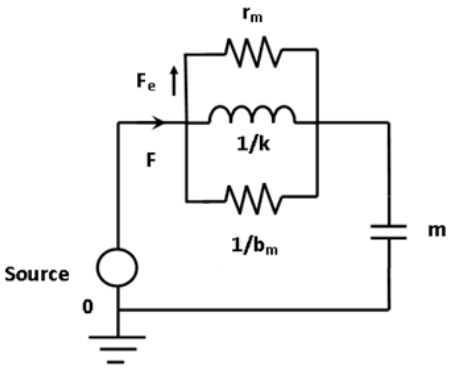

(b)

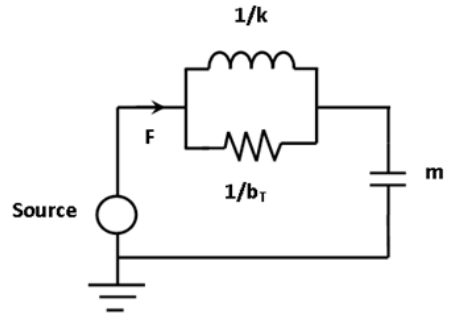

(c)

Figure 2.4: (a) Equivalent circuit model for an inertial EMPG, (b) equivalent circuit in the mechanical domain, (c) equivalent circuit with the combined damping coefficient.

The transformation factor

$$G = S\frac{\mathrm{d}B_z}{\mathrm{d}z} \qquad (2.16)$$

for our device configuration can be found from equations (2.5) and (2.12). The electrical damping coefficient b_e and critical damping coefficient b_c describe the electrical damping ratio ζ_e and using equations (2.15) and (2.16), the electrical damping ratio of the device can be expressed as

$$\zeta_e = \frac{1}{2m\omega_n(R_L + R_C)} S^2 \left(\frac{\mathrm{d}B_z}{\mathrm{d}z}\right)^2 . \qquad (2.17)$$

Equations (2.10), (2.11) and (2.17) yield the load power at resonance

$$P_{L,1} = \left(\frac{R_L}{R_L + R_C}\right)\frac{m\zeta_e}{4\omega_n}\left(\frac{A}{\zeta_m + \zeta_e}\right)^2 \qquad (2.18)$$

in terms of the electrical damping ratio ζ_e and the mechanical damping ratio ζ_m, where $\zeta_e+\zeta_m= \zeta_T$.

By eliminating the damping ratios ζ_e and ζ_m, equation (2.18) can be expressed in the form

$$P_{L,1} = \frac{G^2 S^2 m^2}{2}\frac{R_L}{\left[b_m(R_L + R_C) + G^2\right]^2}, \qquad (2.19)$$

which is more suitable to derive the optimum power condition for impedance matching. Optimizing equation (2.19) with respect to R_L yields the condition for optimum power transfer to the load as

$$R_{L,opt} = R_C + \frac{G^2}{b_m} . \qquad (2.20)$$

In EMPGs with large transformation factor G and small mechanical damping coefficient b_m the second term on the right hand side of equation (2.20) can be significant, however, for meso and micro scale EMPGs with planar coils, this term is negligible in comparison to the coil resistance R_C and can be ignored as will be shown for our device.

The induced open-circuit voltage in a single coil of the device, according to Faraday's law of electromagnetic induction, equation (2.5), depends on the relative velocity *U* between the magnets and the coil, the gradient of the normal component of the magnetic flux density $\frac{\mathrm{d}B_z}{\mathrm{d}z}$, and the number of turns of the coil *N* or area-sum of the individual turns *S*. To understand how the number of turns or the overall area of the coil is affected by the magnetic flux density distribution, a 2-D magnetostatic analysis is performed in COMSOL multiphysics®.

According to the manufacturer of the magnets the remanent magnetic flux density of the NdFeB magnets can range from 1-1.4 T. To model the magnets in COMSOL using the correct remanent flux density, the normal component of the magnetic flux density, along the axis passing through the center of the magnets is experimentally measured and compared with the COMSOL simulation results obtained for different remanent flux densities. Two NdFeB magnets of size 6 mm x 6 mm x 1.5 mm are stacked together and the normal component of the magnetic flux density is measured experimentally using a teslameter (Sypris Test & Measurement, Orlando, FL USA) and a measuring stage (Thorlabs, Newton, NJ USA). Figure 2.5 shows the experimental and the simulation results obtained along the line J, Figure 2.6. The simulation of the flux density along this line for 1.3 T remanent magnetic flux density agrees well with the experimental result and therefore 1.3 T remanent magnet flux density is used to model the magnets in COMSOL.

Figure 2.6 shows the magnetic flux density distribution along the magnets cross sectional plane. The simulation shows that the magnetic flux density is mostly concentrated in an area 8 mm x 8 mm, near the surface of the magnets. Away from the magnets the flux density decreases drastically.

Since the magnetic flux density gradient is high near the surface of the magnets, the gap between the coil and the magnets should be kept as small as possible, however, to accommodate the movement of the magnets the gap should be adjusted according to the amplitude of the displacement of the magnets at resonance. Figure 2.7 shows the distribution of the normal component of the magnetic flux density for gaps of 250, 500 and 750 μm (lines F, G, H respectively in Figure 2.6). The range of horizontal distance of 8 mm in Figure 2.7 corresponds to the width of the planar coil. The simulation result shows a fairly uniform distribution of the

flux density in the central portion of the coil, whereas near the edges of the coil the polarity of the flux density changes. By accounting for the displacement of the magnets, the requirement of approximately same polarity of the magnetic flux density over the coil and clearance for electrical wire that is to be bonded to the central pad of the planar coil, the initial gap between each magnet and coil is kept at 500 µm. The average normal component of the magnetic flux density, acting on the 8 mm x 8 mm planar coil for various gaps is obtained by averaging the values of the magnetic flux density in Figure 2.7, for each gap. The computed average normal component of the magnetic flux density at the gaps of 250, 500 and 750 µm is 0.203, 0.189, 0.175 T respectively, thus giving an approximate magnetic flux density gradient of 5.6×10^{-5} T/µm for a gap of 500 µm.

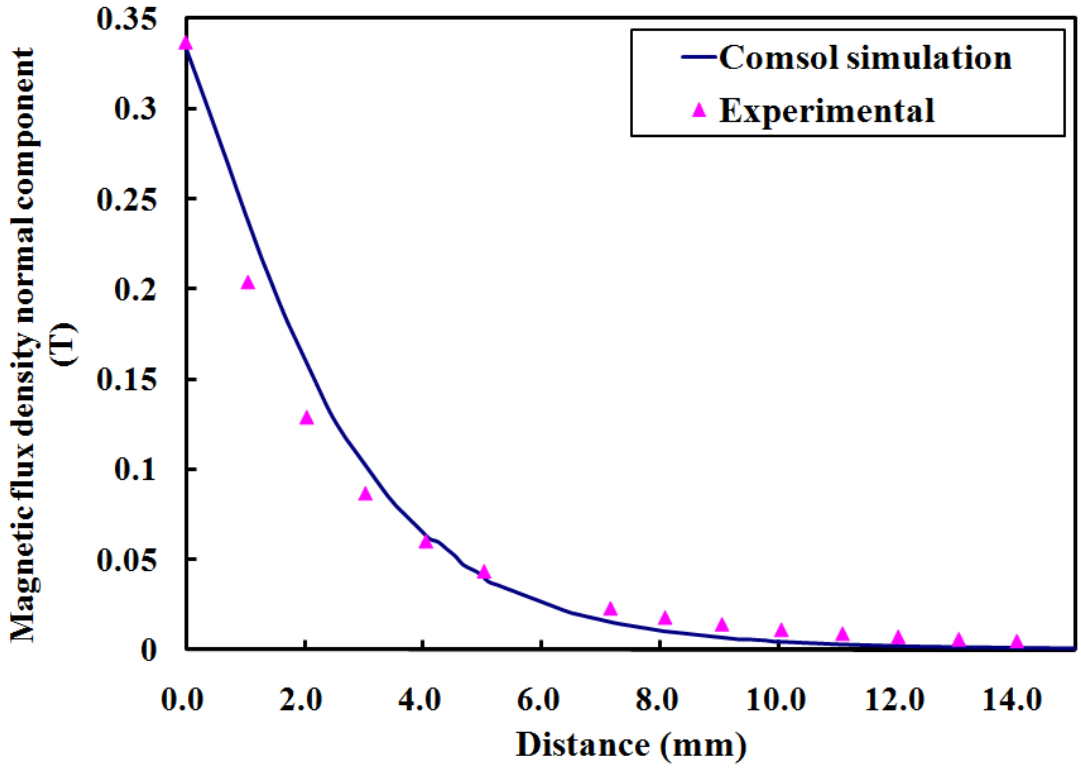

Figure 2.5: Magnetic flux density, normal component along the axis passing through the center of the magnets (line J in Figure 2.6).

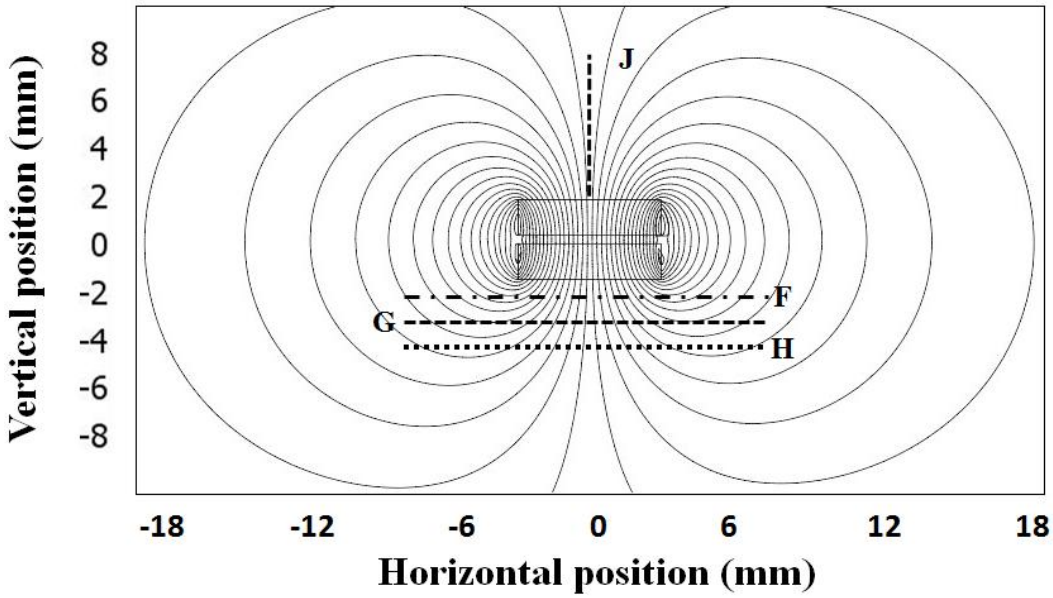

Figure 2.6**:** Simulated magnetic flux density distribution by COMSOL.

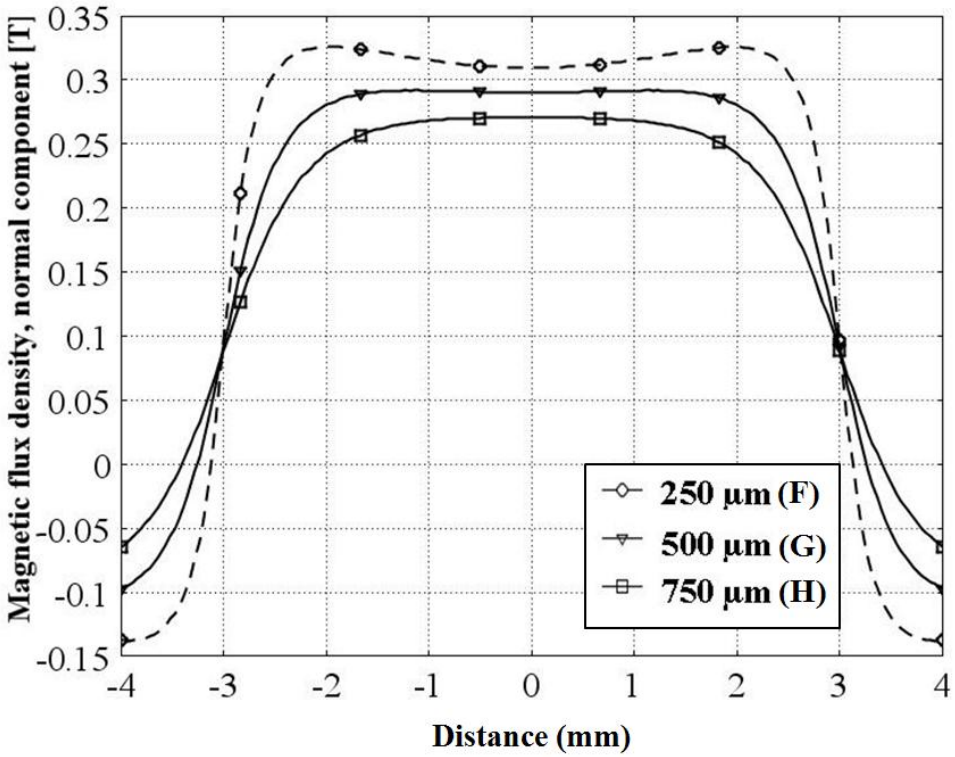

Figure 2.7**:** Normal component of the magnetic flux density for various gaps.

2.3 Fabrication of the prototype

The fabrication process of the planar copper coils is illustrated in Figure 2.8. A 20 µm-thick copper foil (Comet Metal Inc., Walton Hills, OH, USA) is bonded onto a glass substrate with polydimethylsiloxane (PDMS) (Dow Corning Corporation, Midland, MI, USA). PDMS (mixture

of 10 parts elastomer base and 1 part elastomer curing agent) is spun on the glass substrate at 500 rpm for 10 seconds followed by 1000 rpm for 30 seconds. Then the copper foil is pressed onto the uncured PDMS layer, using a weight of 196 N on top of the copper foil at room temperature to provide a uniform pressure for bonding, Figure 2.8(a). Cleanroom wipes are used between the dead weight and the substrate in order to prevent direct contact of the weight and the foil. After 1 hour the weight is removed and the sample is placed into an oven at 80^{o}C for 2 hours in order to cure the PDMS, which results in the bonding of the copper foil to the glass substrate. Photoresist SPR 220-7 (Rohm and Haas Company, Philadelphia, PA, USA) is then spun on, exposed with a mask aligner using a mask, and then developed, Figure 2.8(b). The copper foil is etched with a dilute solution of nitric acid (80 ml HNO_3 and 160 ml H_2O) at room temperature for 10 minutes, Figure 2.8(c). Finally, the photoresist is stripped off using acetone, Figure 2.8(d). Microscopic images of a fabricated micro-coil are shown in Figure 2.9.

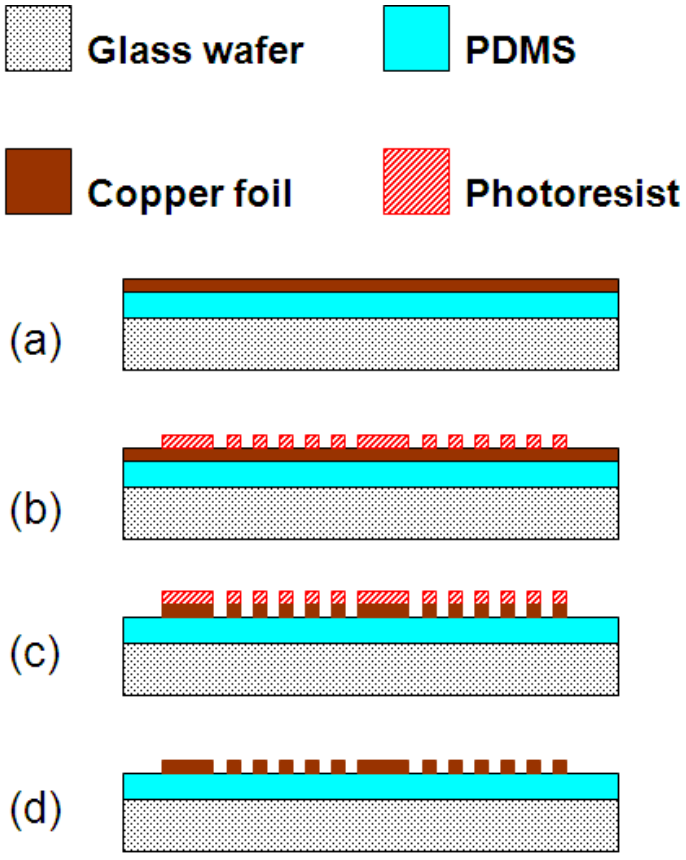

Figure 2.8: Fabrication steps of the copper micro-coil: (a) spin coat a PDMS layer on a glass wafer, and force bond a copper foil, (b) spin coat photoresist and perform photolithography, (c) copper etch using a dilute nitric acid solution, (d) strip off photoresist.

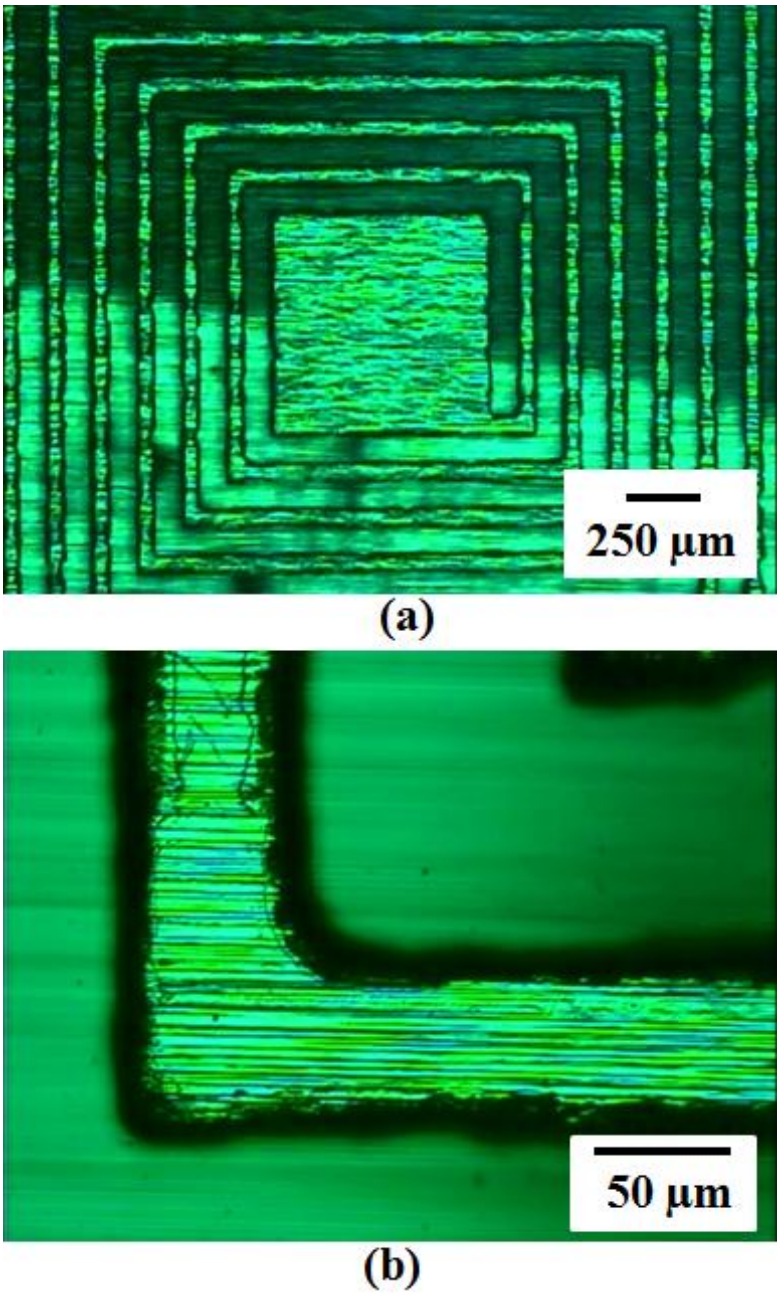

Figure 2.9: (a) Microscopic image of a copper micro-coil, (b) detailed view of a section of the coil.

The fabrication process of the planar copper spring used to support the permanent magnet is shown in Figure 2.10. The process starts with spinning a sacrificial layer of the negative photoresist SU-8 2075 (MicroChem Corp., Newton, MA, USA) onto a silicon wafer, followed by force bonding of a 350 µm thick copper foil (Storm Copper Components Co., Decatur, TN, USA) to the wafer, Figure 2.10(a). Again, the dead weight of 196 N is used for 1 hour, to provide a uniform pressure to bond the copper foil to the wafer. The weight is removed and the wafer is

then soft baked on a hot plate at 95^{o}C for 10 minutes. Photoresist SPR 220-7 is then spun on, exposed and developed, Figure 2.10(b). The selective etching of the copper foil is then performed using a 50% dilute solution of nitric acid (80 ml HNO_3 and 80 ml H_2O) at room temperature for 15 minutes, Figure 2.10(c). The fabricated structures are then separated from the wafer using SU-8 developer, Figure 2.10(d). Finally the separated structures are cleaned with acetone to remove the photoresist, Figure 2.10(e). Figure 2.11 shows the fabricated structures.

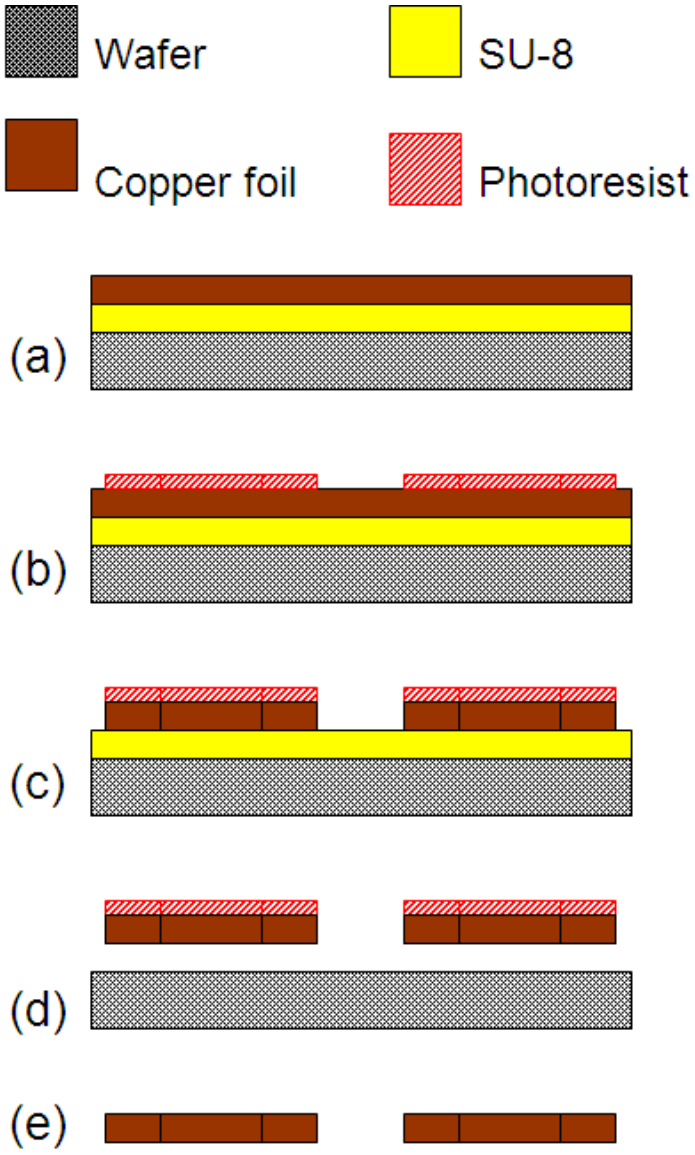

Figure 2.10: Fabrication steps of the planar spring: (a) spin cast photoresist SU-8 2075 and force bond a copper foil to the wafer, (b) spin coat photoresist SPR 220-7 followed by exposure and development, (c) copper etch in dilute nitric acid, (d) strip off SU-8 in developer solution, (e) strip off SPR 220-7 with acetone.

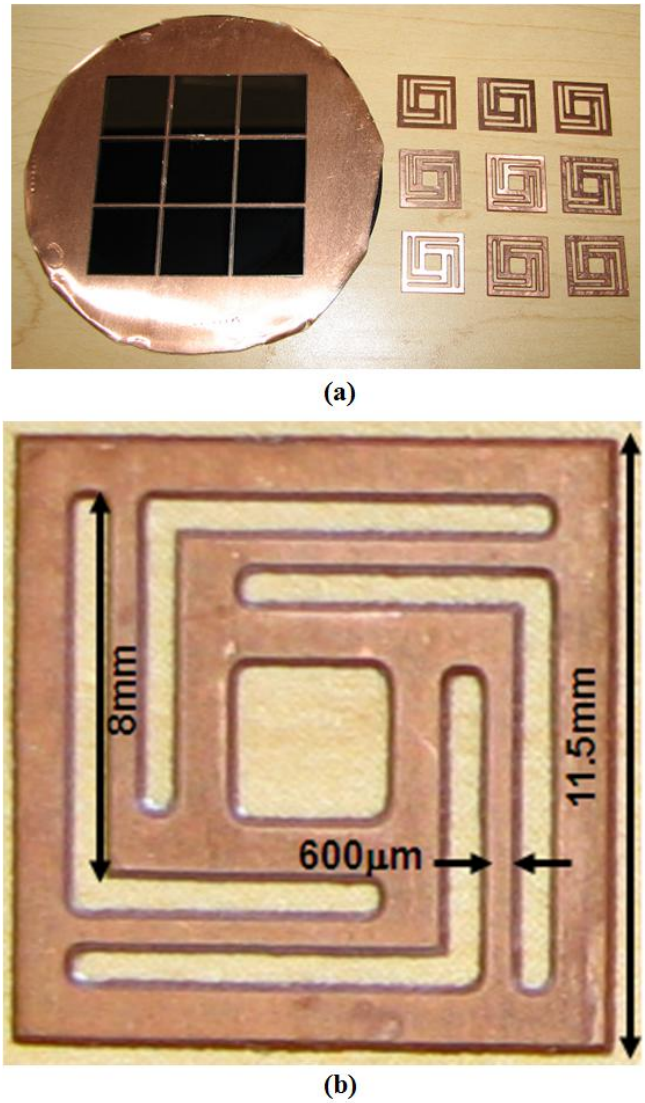

Figure 2.11: Photographs of batch fabricated planar springs: (a) processed copper foil on a silicon wafer with nine planar springs, (b) one of the planar springs.

The assembly of the EMPG is done under a stereo microscope (Olympus SZ61, Olympus Imaging America Inc., Center Valley, PA, USA). First, the two permanent magnets are mounted on the planar spring with the help of a specially designed jig, as shown in Figures 2.12(a) and 2.12(b). No adhesive is used to bond the magnets to the copper spring but rather, the force of attraction between the magnets is exploited to tightly sandwich the planar spring between the magnets, Figure 2.12(c). Two polycarbonate plastic spacers are then bonded on either side of the planar spring with epoxy, by doing so the sides of the planar spring are firmly sandwiched between the two spacers, Figure 2.12(d). Finally, the glass substrates, containing the micro-coils are bonded to the spacers, using the same adhesive, as shown in Figures 2.12(e) and 2.12(f). The dimensions and parameters of the assembled EMPG are listed in Table 2.1.

Table 2.1: Dimensions and parameters of the EMPG prototype.

Description	Value
Device size	12 mm X 12 mm X 7 mm
Magnet (NdFeB)	1.3 T
Magnet dimensions	6 mm X 6 mm X 1.5 mm
Mass of each magnet	0.465 g
Coil size	8 mm X 8 mm
Gap between magnet and coil	500 µm
No. of turns of coil	21
Resistance of coil	7.5 Ω
Spring beam length	8 mm
Spring beam thickness	350 µm
Spring beam width	600 µm

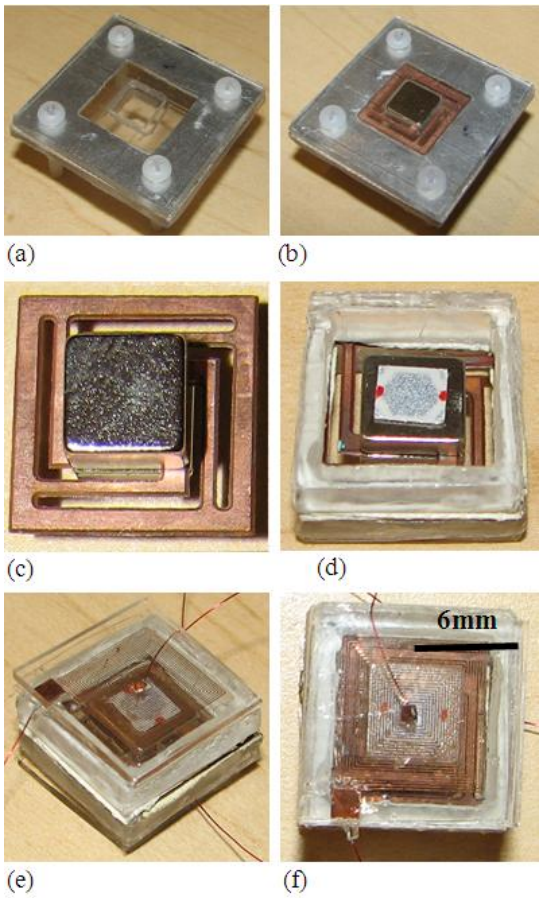

Figure 2.12: Photographic images of the prototype during various stages of assembly: (a) jig for mounting magnets onto planar spring, (b) magnets and planar spring in the jig, (c) magnets mounted onto the planar spring, (d) planar spring sandwiched between the plastic spacers, (e) glass substrates, containing the micro-coils bonded to the spacers, (f) top view of the assembled EMPG.

2.4 Modal analysis of the prototype

Modal analysis is performed in COMSOL multiphysics® in order to find the first few natural frequencies and the corresponding mode shapes of the prototype device. The results of the modal analysis are shown in Figure 2.13 and Table 2.2. The first mode, Figure 2.13(a), is the normal mode during which the magnets vibrate perpendicular to the plane of the spring. In the second mode, Figure 2.13(b) and third mode, Figure 2.13(c), the magnets appear to rotate about an axis parallel to the plane of the coil. The first mode is well within the intended frequency range for applications addressed in section 2.1.

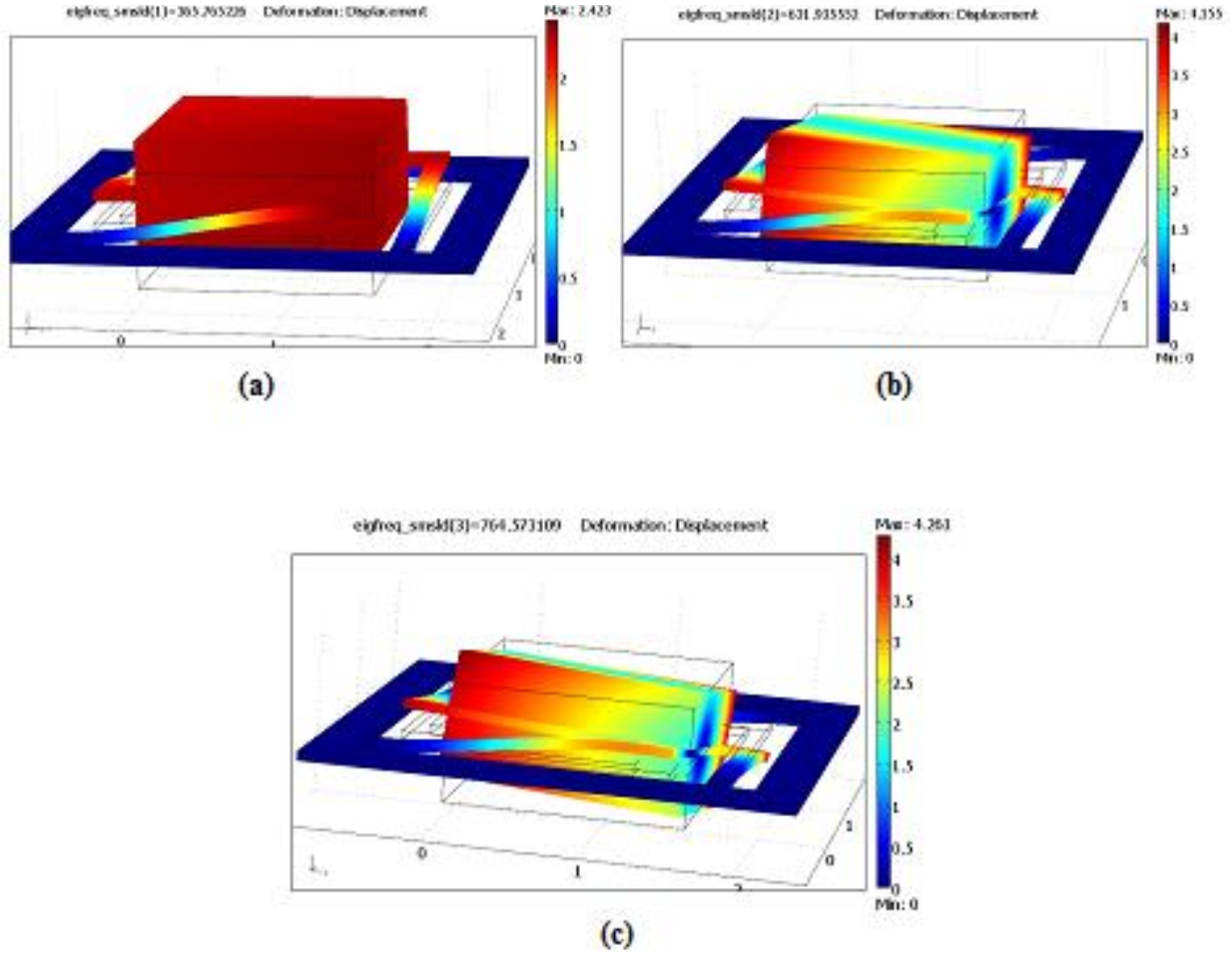

Figure 2.13**:** Modal analysis of the device: (a) first mode shape, (b) second mode shape, (c) third mode shape.

Table 2.2: Simulated natural frequencies of the prototype.

Mode	Natural frequency (Hz)
First Mode	375.8
Second Mode	631.9
Third Mode	764.6

2.5 Experimental setup and results

Figure 2.14 shows the schematic of the experimental setup used for the measurement of natural frequencies, vibration amplitude, and voltage output from the EMPG. The laser head and vibrometer (Polytech Inc., Northbrook, IL, USA) are used for the measurement of the vibration of the magnets and the device housing. The voltage output signal from the device and the signal from the vibrometer are simultaneously fed to the oscilloscope. The function generator and power amplifier control the frequency and vibration amplitude of the shaker (Model 4809, Bruel & Kjaer, Naerum, Denmark). A 7 cm thick Teflon spacer block is mounted onto the shaker table to safeguard the device from the ferromagnetic parts of the shaker. The EMPG and an accelerometer (MMA1200EG, Freescale Semiconductor, Austin, TX, USA) are bonded to the Teflon block by a double-sided adhesive tape.

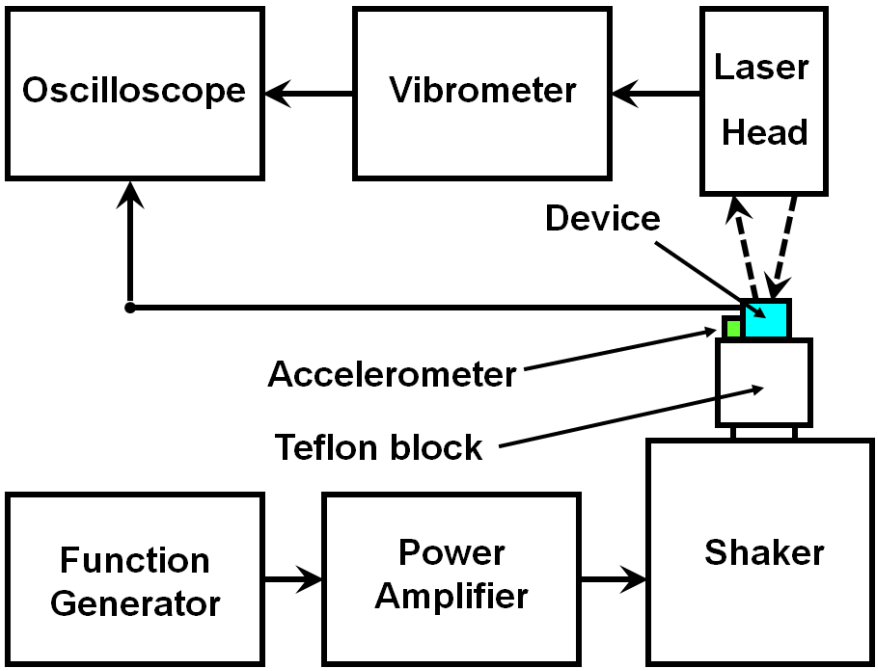

Figure 2.14: Schematic of the experimental setup.

Figure 2.15 shows the amplitude of the relative displacement between the magnets and a coil as a function of the excitation frequency. The experimental data is obtained without the top coil in place, instead a transparent glass piece is bonded to the top plastic spacer, such that the laser from the vibrometer could be focused on the top magnet. A 100 Ω load resistance is connected to the bottom coil and the EMPG is subjected to a frequency sweep from 200 to 800 Hz at A = 13.5 g base acceleration amplitude. The experimental results show the first three natural frequencies 371, 616 and 725 Hz, with the relative displacement between the magnets and the coils at these frequencies at 142.4, 52 and 38.6 μm, respectively. For simulation purposes the total damping ratio was calculated using the relationship

$$\zeta_T = \frac{Y}{2Z_{\max}} = \frac{A}{8\pi^2 f_1^2 Z_{\max}}, \qquad (2.21)$$

where $Z_{\max}$ is the relative displacement between the magnets and the coil at the fundamental frequency f_1. At the resonant frequency of f_1 = 371 Hz equation (2.21) yields a total damping ratio of ζ_T = 0.0857.

The relative displacement given by equation (2.1) is plotted in Figure 2.15 using the measured fundamental natural frequency of 371 Hz and the measured damping ratio ζ_T. The modal analysis described in section 2.4 confirms that the fundamental resonant frequency of 371 Hz corresponds to the mode during which the magnets vibrate normal to the plane of the spring, whereas the two higher resonant frequencies of 616 and 725 Hz correspond to the rotational modes where the magnets rotate about an axis parallel to the plane of the coil.

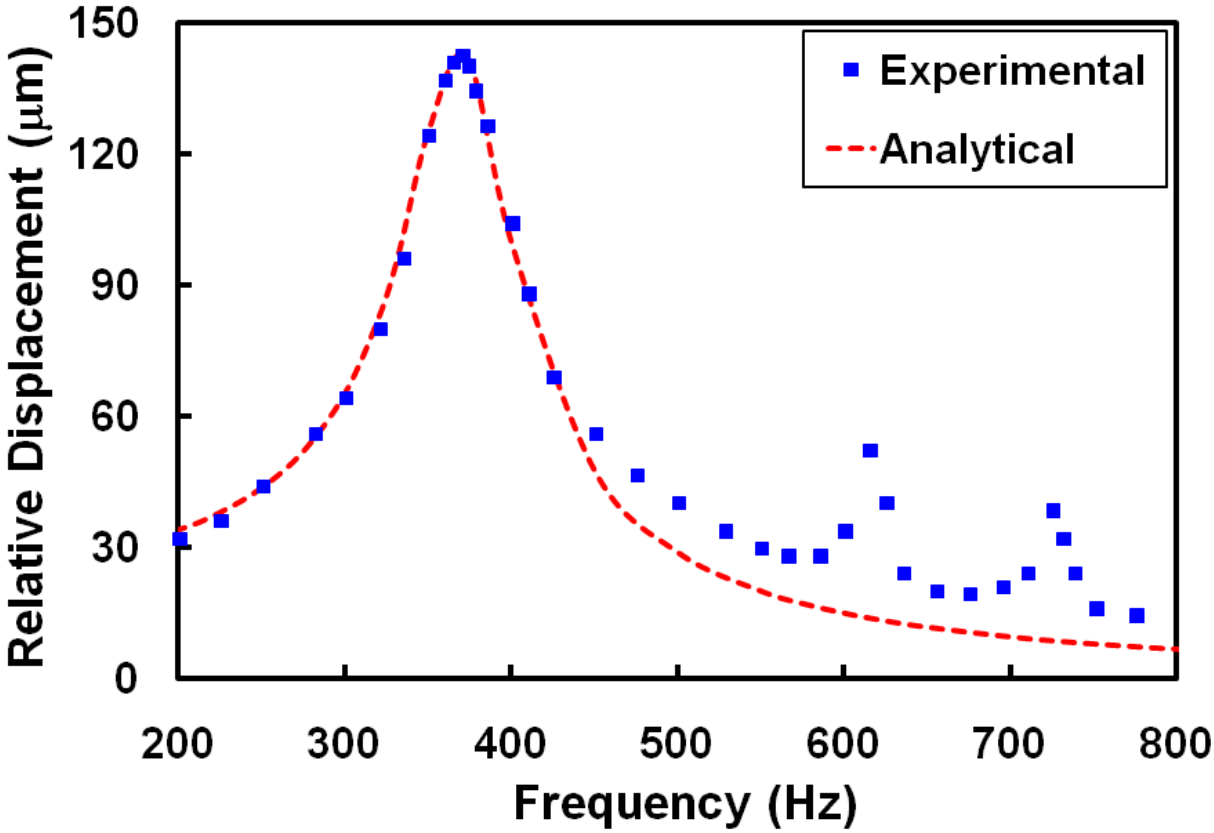

Figure 2.15: Relative displacement of the magnets versus input frequency at 13.5 g base acceleration amplitude.

The experimental resonance frequencies in Table 2.3, match well with the simulated results of the modal analysis. The slight difference between the experimental and simulated frequencies is likely due to the fabrication uncertainties and manual assembly of the prototype.

Table 2.3: Simulated and experimental frequencies.

Mode	**Experimental resonant frequency (Hz)**	**Simulated natural frequency (Hz)**
First Mode	371	375.8
Second Mode	616	631.9
Third Mode	725	764.6

Open circuit potentials (OCP) of 31.9 and 28.2 mV are produced by the two coils, when the EMPG is excited at the first resonance frequency of 371 Hz at 13.5 g. The difference in the output signals of the coils is postulated to be due to fabrication uncertainties. A 100 Ω resistance is connected to each coil and voltage signals across the resistances are algebraically summed in the oscilloscope to obtain the combined load voltage generated by the EMPG.

Figure 2.16 shows the load voltage amplitude measured experimentally and computed based on the model equation (2.9) using d*B*/d*z* = 124.8 T/m. When the EMPG is subjected to a frequency sweep from 200 to 800 Hz at 13.5 g acceleration amplitude, a maximum voltage of 46.3 mV is generated at the load at the fundamental frequency of 371 Hz. The voltage delivered at the second and third modes are 16.8 mV and 17.9 mV, respectively.

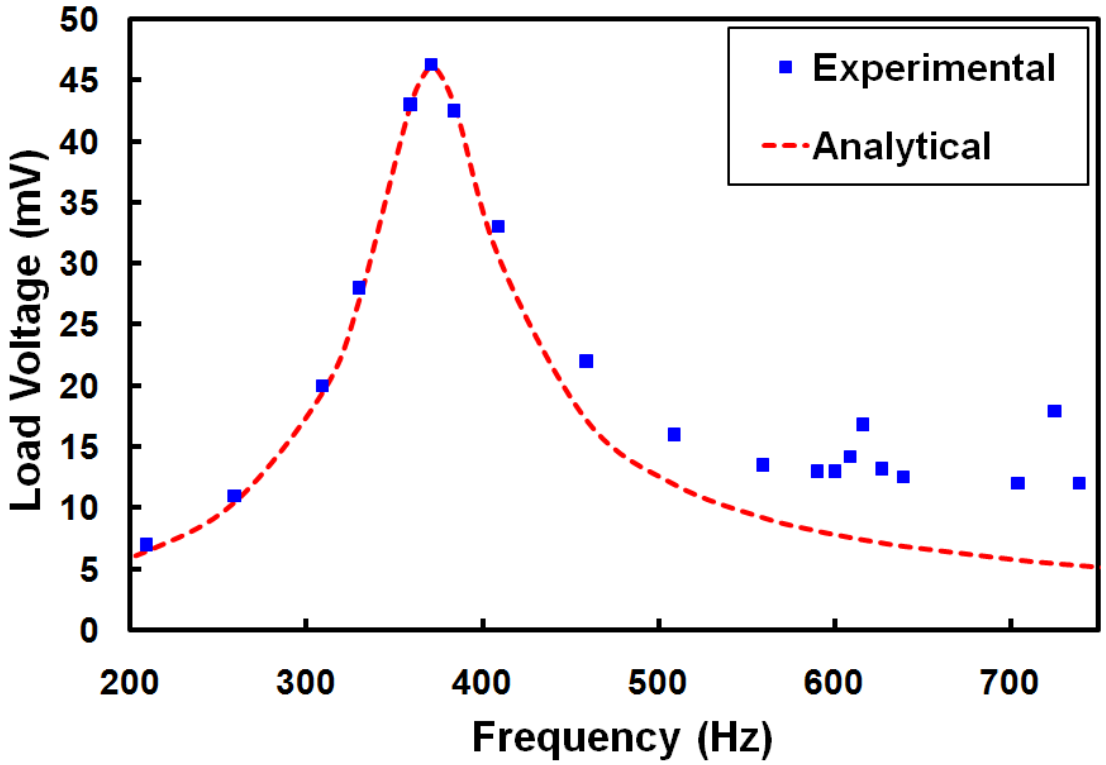

Figure 2.16: Load voltage for a 100 Ω load versus frequency at 13.5 g base excitation.

The power delivered to the 100 Ω load resistance as a function of frequency is plotted in Figure 2.17. The measured voltage across the 100 Ω load resistance is used to compute the power delivered to the load resistance whereas the analytical values are obtained from equation (2.10). The experimental data indicates that both coils are capable of producing a combined power of 10.7, 1.4 and 1.6 μW at 371, 616 and 725 Hz, respectively. Good agreement was found between the analytical and the experimental results for displacement, voltage, and power around the fundamental frequency. However, at relatively higher frequencies (beyond 390 Hz) a deviation between the curves appear, which is due to the presence of higher resonant modes and indicates that the device is no longer following the assumed single degree of freedom analytical model.

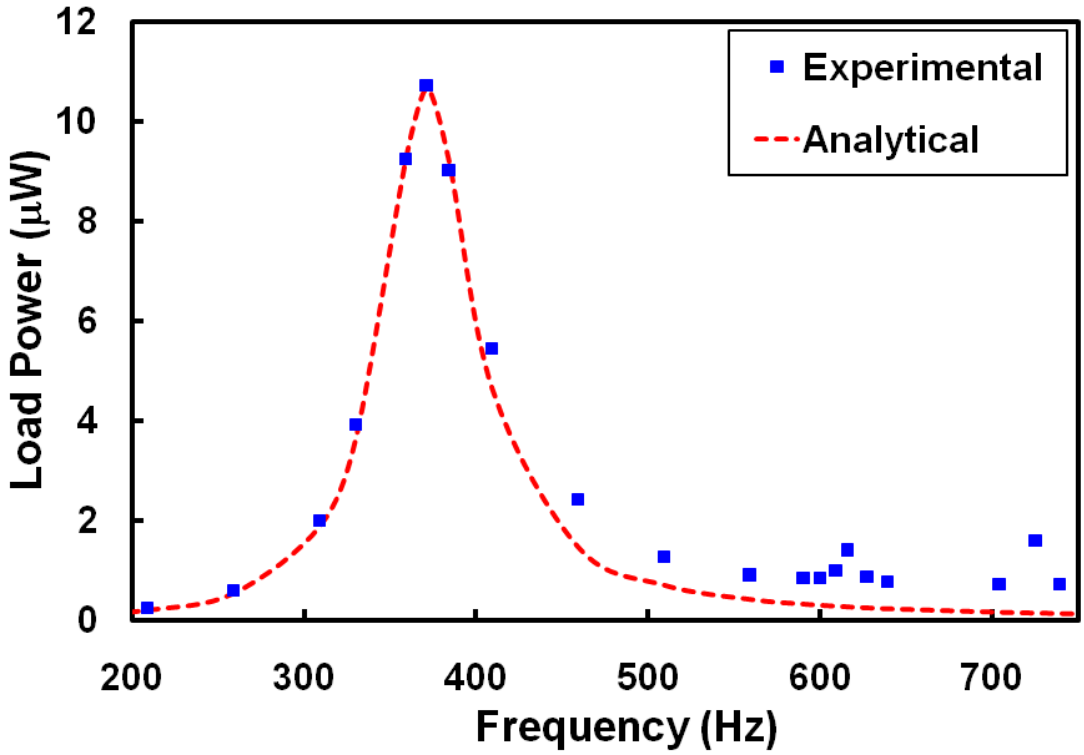

Figure 2.17: Power delivered to the load versus frequency for a 100 Ω load resistance and 13.5 g base excitation.

Figures 2.18 and 2.19 show the load voltage and power versus resistive load. Different load resistances were connected to the EMPG and it was excited at the first mode resonance frequency of 371 Hz at 13.5g acceleration. The simulated load voltage and power are found using equations (2.11) and (2.18), respectively. For simulation purposes the electrical damping ratio ζ_e is calculated using equation (2.17) for different load resistances, this result is shown in Figure 2.20. Knowing the electrical damping ratio at 100 Ω resistance, the mechanical damping ratio ζ_m is extracted from the experimentally computed total damping ratio at 100 Ω resistance. Figures 2.18 and 2.19 indicate that the larger the load resistor, the larger is the measured voltage and the smaller is the through current. The maximum voltage measured was 49.5 mV for the maximum load resistance of 200 Ω in our experiments and the maximum power obtained from the EMPG was about 23.56 μW for a load resistance of about 7.5 Ω that is identical to the resistance of the coils. The term G^2/b_m in the expression for the optimum load (equation 2.20) is only 0.014 Ω for our device, which is small in comparison to the coil resistance of 7.5 Ω and can be ignored as mentioned earlier. Based on the harvester overall volume of 1 cm^3 and operating at the matching impedance the optimum power density of the device is 23.56 $\mu W/cm^3$.

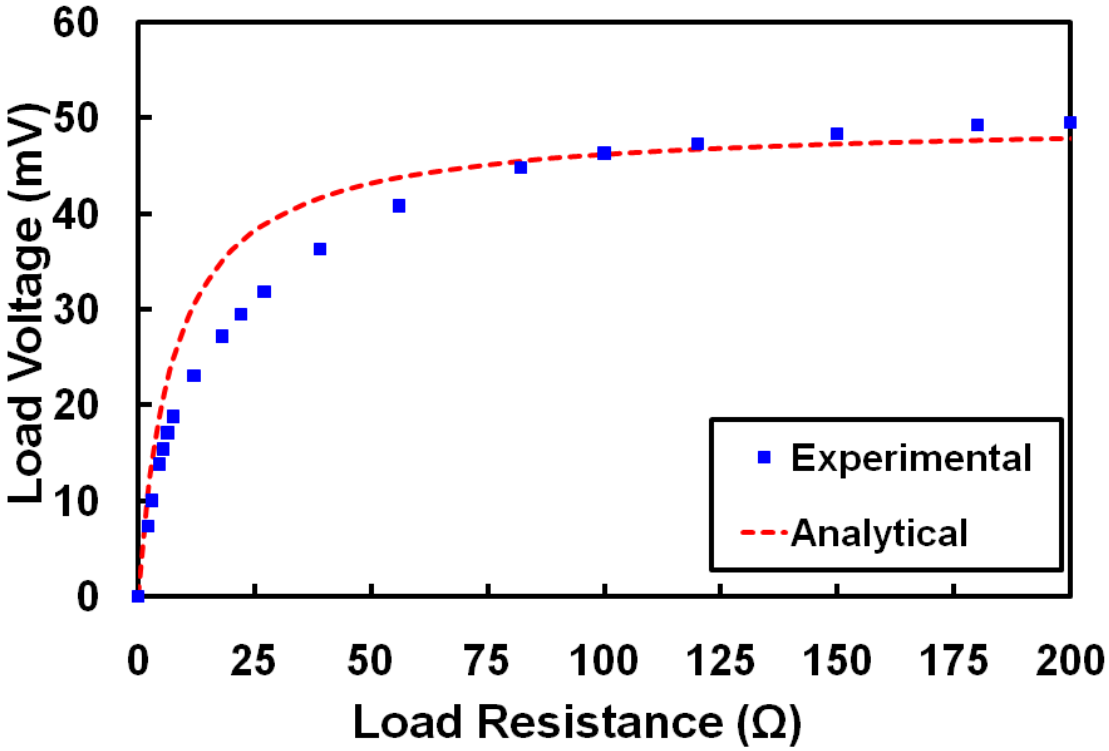

Figure 2.18: Load voltage versus load resistance at 371 Hz and 13.5 g base excitation.

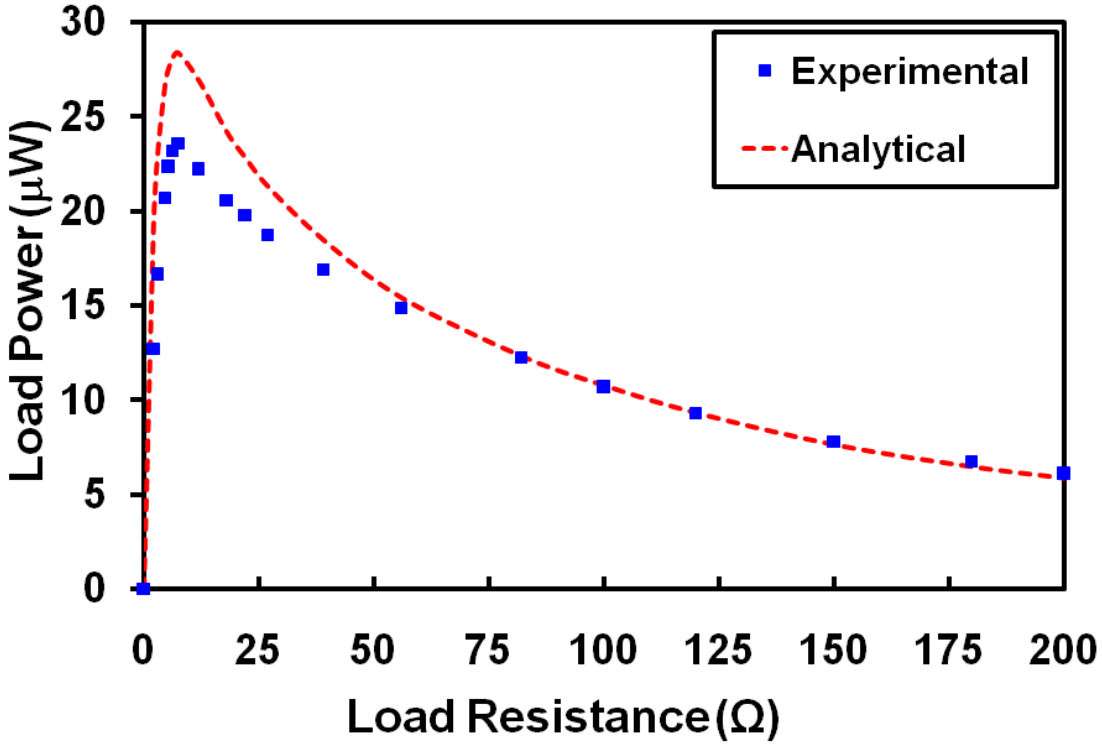

Figure 2.19: Power versus load resistance at 371 Hz and 13.5 g base excitation.

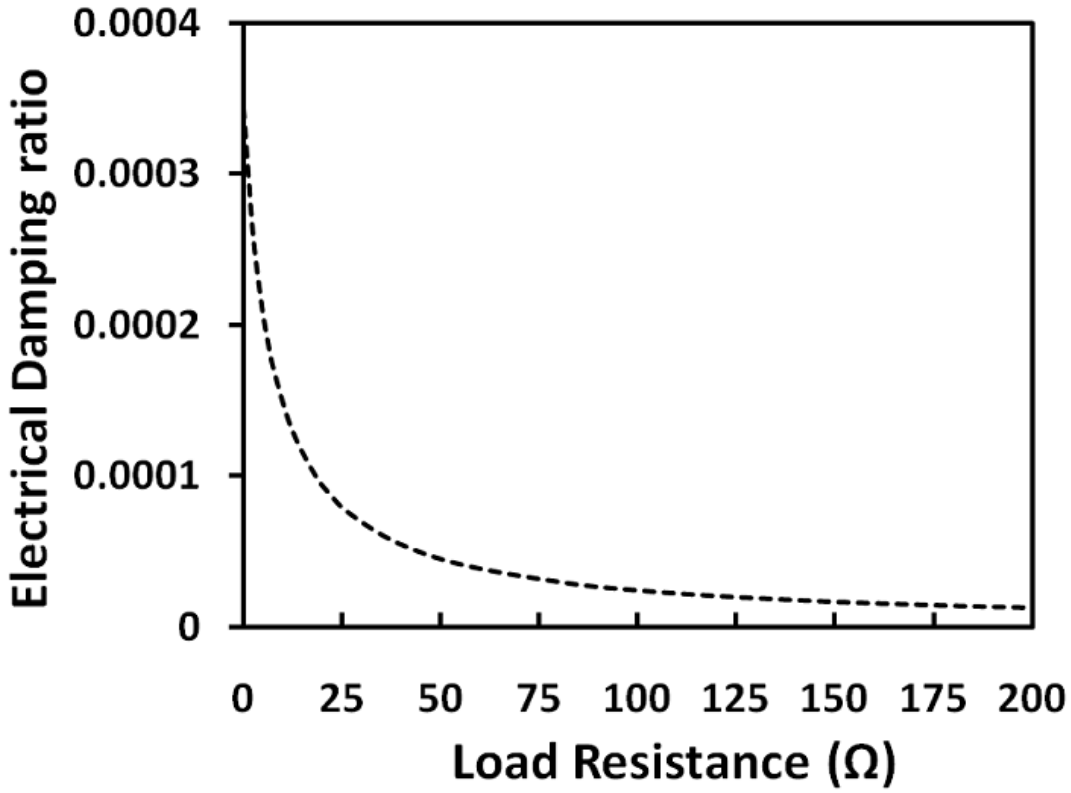

Figure 2.20: Simulated electrical damping ratio against load resistance.

The voltages generated by the developed EMPG are in the mV range (46.3 to 60.1 mV), however, due to the low optimum load impedance of the device, which is only 7.5 Ω, relatively high currents are expected. The EMPG has sufficient power producing capability to operate the majority of the ULP sensors mentioned in section 2.1. However, for the relatively high supply voltage (1.8 to 2.7 V) requirement of these sensors, the low output AC voltage signal of the EMPG must be conditioned with an ultra low voltage (ULV) and ULP rectifier and multiplier circuit. Rectification can be achieved using ultra low forward voltage (ULFV) diodes (for example: PMEG2010AEB, NXP semiconductors, Eindhoven, Netherlands, minimum forward voltage of 30 mV for a forward current of 0.1 mA) and the voltage can be amplified with an ultra low voltage (ULV) DC-DC step-up converter (for example: LTC3108, Linear Technology, Milpitas, CA, USA, operates from an input of 20 mV to provide a selectable step-up voltage outputs of 2.35, 3.3, 4.1 and 5 V).

Vibration-based EMPGs Currently available are summarized in Table 2.4. The comparison of the EMPGs is not straightforward, but power density and normalized power

density [70] of the devices are some criteria for the comparison. Depending on the objective many other criteria can be considered, based on for example, bandwidth, resonant frequency, output impedance, optimum load and fabrication cost. The planar coil type EMPGs, where the number of turns ranges from 10 to 100 are no match to the EMPGs with more than 1000 turns in their wound coils. The wound coil type EMPGs [79, 85, 86] generate relatively high voltages, mostly above 400 mV, however, the resistance of these coils is also high which contributes to greater power loss. Moreover, the wound coil type EMPGs have lesser prospect in being integrated into planar micro fabrication processes. Most planar coil type EMPGs [74, 80, 82, 83, 87, 95, 96, 98] have less coil resistance but produce low output voltages (< 180 mV) and will need a special ULV rectifier and multiplier circuit for practical usage.

Table 2.4: Summary of vibration based electromagnetic power generators.

Type		Materials		V_{load} (mV_{pk})	R_{load} (Ω)	R_{coil} (Ω)	F (Hz)	P_{max} (μW)	Volume (cm^3)	Y (μm)	A (g_{pk})	Power density ($\mu W/cm^3$)	Refs.
		Spring	Coil										
Moving Magnet	Planar coil	Cu	Cu	30	-	-	121.3	-	0.004	-	1.5	-	[80]
		Ni-Fe	Cu	-	-	2	100	1.44	0.036	50	2[a]	40	[81]
		Si	Cu	40	-	-	60	100	0.45		-	222	[82]
		Kapton	Cu	180	100k	100	340	50	1.35	5	2.3[a]	40	[83]
		rubber	Al	-	35	-	-	1.15	-	-	-	-	[84]
		Cu	Cu	9[b]	33	33	55	0.61	0.13	-	1.52	4.7	[98]
		PDMS	Cu	84.3	100	10.1	111	61.5	2.25	-	3	27.33	[74]
		Acrylic	Cu	3.2	0.8	0.8	948	3.2	-	14	50.7[a]	-	[95]
		-	Cu	9	50	50	40-80	0.4	2.27	-	1.9	0.148	[96]
		Cu	Cu	46.3	100	7.5	371	23.56	1	-	13.5	23.56	This work
	Wound coil	BeCu	Cu	931[c]	15k	2.3k	50	58	0.15		0.08	386.7	[85]
		Cu		1440[b]	100k		111	27	1	250	12.4[a]	27	[86]
		Si	Cu	34.5[c]	110		58.5	10.8	0.15	-	0.06	72	[79]
		Steel/ BeCu	Cu	428[c]	4k	1.5k	52	46	0.15	-	0.06	306.7	[79]
		FR4	Cu	-	100	100	24.4	144	4.1	-	0.1	35.1	[97]
Moving Coil	Planar coil	Parylene	Au	10	250	580	4.2-5k	0.4	1.4	1	50	0.286	[87]
		Si	Cu	-	52.7	55	9.84k	0.023	0.106	-	1	0.217	[88]
	Wound coil	Si	Cu	-	100	-	9.5k	0.122	0.1		0.4	1.22	[89]
		steel		-	0.6		322	37	0.84	13	5.4[a]	44	[90]

[a]Calculated using equation $A = Y (2\pi F)^2 / 9.8$.
[b]open circuit voltage.
[c]rms voltage.

The EMPGs [79, 71, 85, 96-98] with a natural frequency below 100 Hz perform well under a base acceleration less than 2g, and are more suitable for low level vibrations that are present in household and office environments. However, these EMPGs are not necessarily suitable for a medium and high g excitation and are prone to catastrophic failure of the spring under such conditions. The EMPGs designed for medium and high g excitations will survive low level of g's but the generated power will be insufficient to provide meaningful amounts of power. The different EMPGs are designed for different applications such as specific vibration frequencies and amplitudes and simply comparing their power densities might therefore not be justified.

3 Modeling of linear electromagnetic energy harvesters with non-uniform magnetic field for sinusoidal vibrations[2]

3.1 Introduction

The ever growing interest for maintenance free embedded [99-102], abandoned [103] and wearable [104-108] devices and sensors has greatly increased the needs for miniature energy harvesting systems [109-111]. With the continuous advancements in the development of ultra low power (ULP) sensors [112] and ULP analog and digital electrical circuitry [113,114], micro scale, autonomous sensors are fast becoming a reality. Like, other energy sources (solar, acoustics, wind or thermal), mechanical energy is abundantly available in the environment in the form of vibration of rotary machines, reciprocating engines or even household appliances. Vibration-based energy harvesters allow converting these mechanical vibrations into electrical energy to power wireless sensors.

Previously, vibration-based energy harvesters based on piezoelectric [115, 116], electrostatic [117] or electromagnetic [118] principles have been demonstrated. Out of those electromagnetic energy harvesters (EMEHs) are experiencing a growing popularity as prospective power sources for self-powered systems due to their ability to generate relatively high current levels. Meso scale as well as micro scale EMEHs [119] have been successfully fabricated and tested.

Based on the input vibration, the optimum parameters of energy harvesters can be predicted with the aid of simulations using mathematical models, in order to design highly efficient energy harvesters for these specific inputs.

---

[2] A version of this chapter has been submitted for publication. Farid Khan, Farrokh Sassani and Boris Stoeber "Modeling of linear electromagnetic energy harvesters with non-uniform magnetic field for Sinusoidal vibrations", Submission date: Feb. 2011.

In EMEH the mechanical vibration energy is converted into the electrical energy due to the change of the magnetic flux that the coil experiences as a result of the relative motion between a permanent magnet and the coil. The coil in EMEHs is either a wound [120-122] or a planar [123-125] type, however, the latter has the advantage of ease of integration with planar micro-fabrication processes.

The reported EMEHs can be classified by different criteria, one possibility is to classify them on the basis of the configuration of the magnetic field between the magnet and the coil, as EMEHs with uniform magnetic field configuration [126] and with non-uniform magnetic field configuration [127-130] behave differently. Mostly Faraday's law is used to describe the electromechanical transduction in EMEHs. The basic forms of Faraday's law for voltage generation in EMEHs with uniform magnetic field configuration as well as for EMEHs with non-uniform field configuration are reported in [131, 93]. An analytical model based on Faraday's law and the simulation of a harvester with a cylindrical magnet and a circular wound coil is reported in [97]. An analytical solution of the normal component of the magnetic flux density (along the line normal to the centre of the magnet) and the magnetostatic simulation of the magnet in Comsol multiphysics® are used to develop expressions for the average normal component of the magnetic flux density and magnetic flux gradient as a function of distance from the magnet. Modeling and simulation for an EMEH with a cylindrical magnet and a square planar coil has been reported in [84]. The model is based on Faraday's law, the simulation of the magnetic flux density of the magnet in electromagnetic modeling software ViziMag is used to compute the rate of change of the average normal flux density for the model.

This chapter reports the analytical modeling and simulation of vibration-based linear electromagnetic EMEHs for harmonic excitations. Analytical models are developed for EMEHs with non-uniform magnetic field over a planar coil. In most of the previously reported work either a uniform magnetic flux density is assumed [87,95] or a uniform gradient of the normal component of the magnetic flux density is used [132] to model the output voltage of EMEHs. These reported models provide good estimations for the EMEHs in which the planar coil is smaller than the size of magnet and/or the gap between the magnet and the coil is relatively small, however, for larger gaps between the magnet and the coil and/or for a coil larger than the magnet, these overestimate the device performance. Models based on both Faraday's law and the

Lorentz force law are developed using analytical solutions for the off-center magnetic flux density to estimate the performance of EMEHs even for larger gaps and larger planar coils with high confidence. Results from simulation based on the developed models are compared with previously reported experimental results for an EMEH made from micromachined parts in Chapter 2. An optimization of the same EMEH is also performed with one of the developed models.

3.2 Modeling of linear EMEHs

Linear EMEHs are seismic or inertial devices, consisting of the inertial mass *m* being the magnet or a proof mass and a suspension with a linear stiffness *k* to support the magnet or the coil. During operation the motion of the inertial mass is damped by the linear damping b_T that comprises mechanical damping b_m (air, material and support damping) and electrical damping b_e induced when a current flows in the coil. The linear EMEH can be modeled as a single degree of freedom, spring-mass-damper system with base excitation as shown in Figure 3.1.

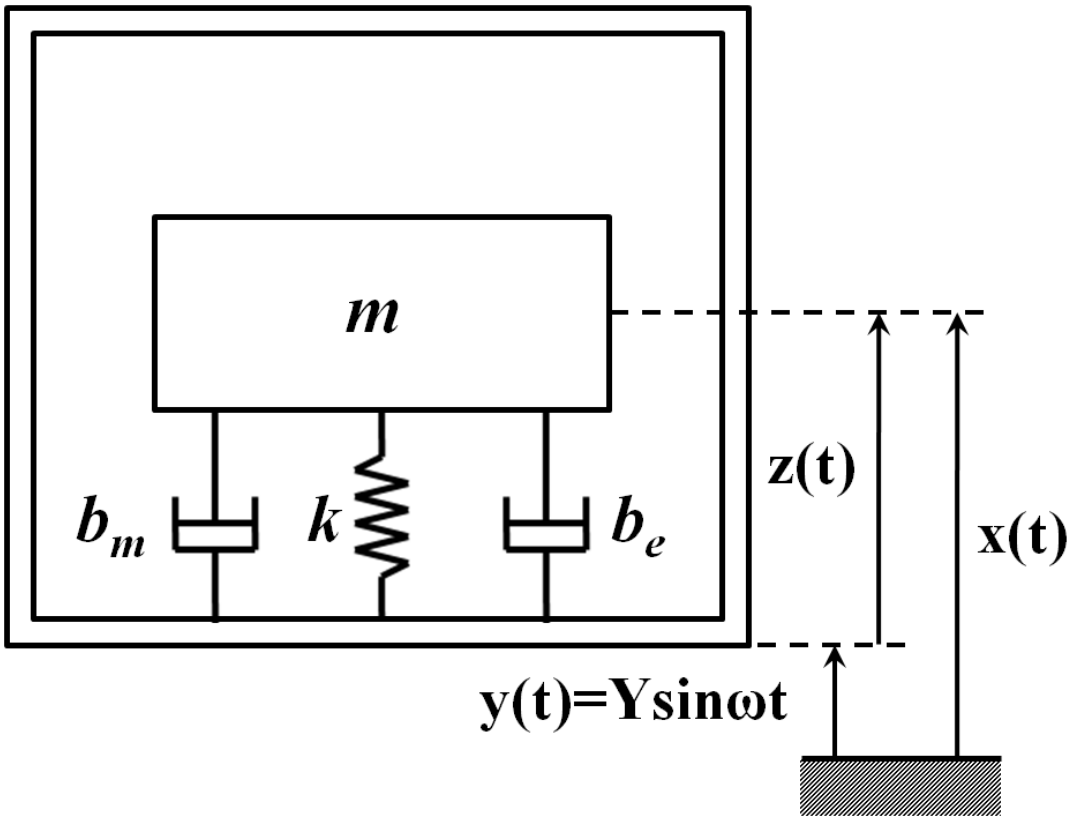

Figure 3.1: Lumped mass model of a linear electromagnetic energy harvester.

For harmonic excitation $y(t) = Y \sin \omega t$, the equation of motion for linear EMEHs

$$m\ddot{z} + b_T \dot{z} + kz = -m\ddot{y} \qquad (3.1)$$

can be solved for the amplitude of the relative displacement

$$Z = \frac{\left(Y\omega^2\right)}{\omega_n^2 \sqrt{\left[1 - \left(\omega / \omega_n\right)^2\right]^2 + \left[2\zeta_T \left(\omega / \omega_n\right)\right]^2}} \qquad (3.2)$$

and for the amplitude of the relative velocity

$$U = \frac{A\omega}{\omega_n^2 \sqrt{\left[1 - \left(\omega / \omega_n\right)^2\right]^2 + \left[2\zeta_T \left(\omega / \omega_n\right)\right]^2}} \qquad (3.3)$$

between the magnets and housing of the device with the frequency of excitation ω, the natural frequency ω_n, the base amplitude of vibration Y, the base acceleration $A = \omega^2 Y$, and the total damping ratio ζ_T.

There are two approaches to model the induced voltage in a coil of the linear EMEH: (1) Faraday's law and (2) the Lorentz force law. The modeling of EMEHs has to account for the configuration of the magnetic field (uniform magnetic field or non-uniform magnet field), shape of the magnet (cylindrical, rectangular or square magnet), size and shape of the planar spiral coil (circular or square spiral planar coil) and the gap between the magnet and the coil at rest.

3.2.1 Analytical model based on Faraday's law

For the architecture of EMEHs in which the magnet is oscillating normal to the plane of the coil [132], the magnetic field over the coil is non-uniform and the voltage induced in the coil by Faraday's law of electromagnetic induction

$$V_G = -\frac{\mathrm{d}\phi_B}{\mathrm{d}t} = -\frac{\mathrm{d}}{\mathrm{d}t}\int \bar{B}\cdot \mathrm{d}\bar{S} = -\int \frac{\mathrm{d}}{\mathrm{d}t} B_z \,\mathrm{d}S = -\int \frac{\mathrm{d}B_z}{\mathrm{d}z}\frac{\mathrm{d}z}{\mathrm{d}t}\mathrm{d}S = -U\int \frac{\mathrm{d}B_z}{\mathrm{d}z}\mathrm{d}S \qquad (3.4)$$

depends on the relative velocity U and the integral of the local gradient $\frac{\mathrm{d}B_z}{\mathrm{d}z}$ of the normal component of the magnetic flux density B_z over the infinitesimal area dS of the coil turn. The solution of the integral in equation (3.4) depends on the shape of the magnet, the shape of the coil, the size of the coil relative to the magnet and the gap between the coil and magnet at rest. The integral needs to be evaluated differently for different cases.

Faraday's law for EMEHs with a small planar coils and a small magnet-coil distance

For the EMEHs where the planar coil is smaller than the size of the magnet and the gap between the magnet and the coil is relatively small, all turns of the coil would experience approximately the same magnetic flux gradient $\frac{\mathrm{d}B_z}{\mathrm{d}z}$ and equation (3.4) reduces to a form [93, 131]

$$V_G = -U\frac{\mathrm{d}B_z}{\mathrm{d}z}S\,, \qquad (3.5)$$

where S is the sum of the areas S_i of the individual coil turns.

The amplitude of the voltage

$$V_L = \left(\frac{R_L}{R_L + R_C}\right)\frac{A\omega}{\omega_n^2\sqrt{\left[1-\left(\omega/\omega_n\right)^2\right]+\left[2\zeta_T\left(\omega/\omega_n\right)\right]^2}}\frac{\mathrm{d}B_z}{\mathrm{d}z}S \qquad (3.6)$$

and the amplitude of the power

$$P_L = \frac{V_L^2}{2R_L} \qquad (3.7)$$

delivered to the load depend on the load resistance R_L and the coil resistance R_C.

The area sum S and the magnetic flux density gradient dB_z/dz in equation (3.6) depend on the shape and size of the coil and the magnet respectively; the expressions for S and $\frac{dB_z}{dz}$ previously developed for EMEHs with square spiral planar coil and square block magnets reported in Chapter 2 are therefore not applicable for EMEHs with cylindrical magnets and circular spiral planar coils.

For a circular spiral planar coil, Figure 3.2, with the starting (initial/inner) radius R_i of the spiral, line width w and spacing b between the adjacent turns, the radius of the turn

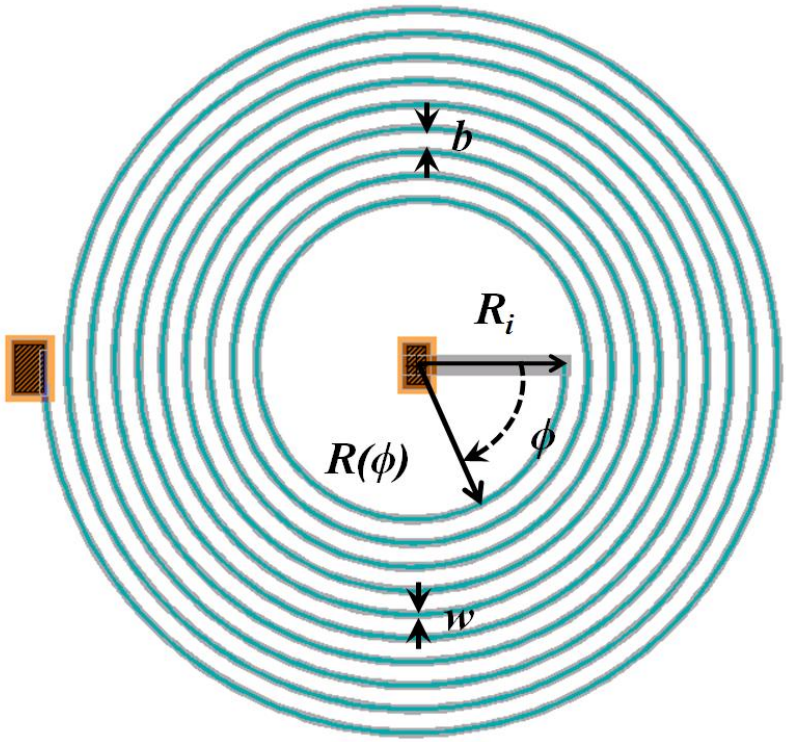

Figure 3.2: Circular spiral planar coil

$$R(\phi) = R_i + (b+w)\frac{\phi}{2\pi} \qquad (3.8)$$

increases with the angle ϕ traced by the coil turns and describes the area sum

$$S = \frac{1}{2}\int_0^{\phi_{max}} \left(R(\phi)\right)^2 d\phi = \frac{R_i^2\phi_{max}}{2} + \frac{R_i(b+w)\phi_{max}^2}{4\pi} + \frac{(b+w)^2\phi_{max}^3}{24\pi^2} \qquad (3.9)$$

of the areas of the individual turns for the total angle $\phi_{\max}$ traced by the whole coil (from the inner electrical pad to the outer electrical pad).

The coil with *N* complete turns, the total angle

$$\phi_{\max} = 2\pi N \qquad (3.10)$$

traced by the coil turns depends only on the number of turns *N*. Substituting $\phi_{\max}$ accordingly in equation (3.9) yields

$$S = \pi N\left(R_i^2 + R_i (b+w)N + \frac{(b+w)^2 N^2}{3} \right). \qquad (3.11)$$

The magnetic flux density for a cylindrical magnet along a line perpendicular to its center [133]

$$B_z = \frac{B_r}{2}\left[\frac{(T+z)}{\sqrt{R^2 + (T+z)^2}} - \frac{z}{\sqrt{R^2 + z^2}} \right] \qquad (3.12)$$

depends on the remanent flux density B_r, the radius of the magnet *R*, the thickness of the magnet *T* and the distance from the magnet *z*. For the analytical computations, $\frac{dB_z}{dz}$ can be obtained by differentiating equation (3.12) with respect to *z* and then setting *z* equal to the gap between the magnet and the coil at rest. By using the value of the magnetic flux gradient and the area sum *S* (equation 3.11) in the analytical model, equation (3.6), the load voltage of an EMEH with a circular spiral planar coil and a cylindrical magnet can be computed.

Faraday's law for EMEHs with a large planar coil and a large gap

The linear EMEHs in which the planar coil is larger than the size of the magnet or the gap between the magnet and the coil is large, the normal component of the magnetic flux density (magnetic flux gradient) is highly non-uniform over the whole area of the coil. The outer edges of the coil face either less magnetic flux density (normal component) or even opposite polarity of the magnetic flux density. In such a situation, the analytical model, equation (3.5), overestimates

the induced voltage. For a better approximation, the gradient of the normal component of the local magnetic flux density should be computed over the entire area of each individual turn and then needs to be averaged for this turn. The integral expression of Faraday's law in equation (3.4) can then be approximated as a sum over the individual turns

$$V_G = -U\sum_{i=1}^{n}\overline{\left(\frac{dB_Z}{dz}\right)}_i S_i \qquad (3.13)$$

where $\overline{\left(\frac{dB_Z}{dz}\right)}_i$ is the average magnetic flux gradient of the normal component over the individual turn area S_i.

Using equation (3.13), for EMEH with a coil resistance R_C, the amplitude of the voltage

$$V_L = \left(\frac{R_L}{R_L + R_C}\right)\frac{A\omega}{\omega_n^2\sqrt{\left[1-\left(\omega/\omega_n\right)^2\right]+\left[2\zeta_T\left(\omega/\omega_n\right)\right]^2}}\sum_{i=1}^{n}\overline{\left(\frac{dB_Z}{dz}\right)}_i S_i \qquad (3.14)$$

delivered to the load resistance R_L can be computed with the device parameters. The computation with equation 3.14 requires the analytical solution for the off-centre normal component, of the magnetic flux density B_z of the permanent magnet. The term in the summation sign depends on the shape and size of the magnet and the planar coil.

For a square block magnet, the off center normal component of the magnetic flux density [134]

$$B_Z(x,y,z)=\frac{B_r}{4\pi}\left\{\begin{array}{l}
\sin^{-1}\left[\dfrac{(x-x_0)(y-y_0)}{\sqrt{\left[(z-l/2)^2+(x-x_0)^2\right]\left[(z-l/2)^2+(y-y_0)^2\right]}}\right]\\
-\sin^{-1}\left[\dfrac{(x-x_0)(y+y_0)}{\sqrt{\left[(z-l/2)^2+(y-y_0)^2\right]\left[(z-l/2)^2+(x-x_0)^2\right]}}\right]\\
-\sin^{-1}\left[\dfrac{(x+x_0)(y-y_0)}{\sqrt{\left[(z-l/2)^2+(x+x_0)^2\right]\left[(z-l/2)^2+(y-y_0)^2\right]}}\right]\\
+\sin^{-1}\left[\dfrac{(x+x_0)(y+y_0)}{\sqrt{\left[(z-l/2)^2+(x+x_0)^2\right]\left[(z-l/2)^2+(y+y_0)^2\right]}}\right]\\
-\sin^{-1}\left[\dfrac{(x-x_0)(y-y_0)}{\sqrt{\left[(z+l/2)^2+(x-x_0)^2\right]\left[(z+l/2)^2+(y-y_0)^2\right]}}\right]\\
+\sin^{-1}\left[\dfrac{(x-x_0)(y+y_0)}{\sqrt{\left[(z+l/2)^2+(x-x_0)^2\right]\left[(z+l/2)^2+(y+y_0)^2\right]}}\right]\\
+\sin^{-1}\left[\dfrac{(x+x_0)(y-y_0)}{\sqrt{\left[(z+l/2)^2+(x+x_0)^2\right]\left[(z+l/2)^2+(y-y_0)^2\right]}}\right]\\
-\sin^{-1}\left[\dfrac{(x+x_0)(y+y_0)}{\sqrt{\left[(z+l/2)^2+(x+x_0)^2\right]\left[(z+l/2)^2+(y+y_0)^2\right]}}\right]
\end{array}\right\} \tag{3.15}$$

over the coil depends on the width x_0, length y_0 and thickness l of the magnet.

The EMEH developed and reported in Chapter 2 has square block magnets and square spiral planar coils. The dimensions and parameters of the EMEH are listed in Table 3.1.

Table 3.1: Dimensions and parameters of the EMEH prototype [132].

Description	**Value**
Device size	12 mm X 12 mm X 7 mm
Magnet (NdFeB)	1.3 T
Mass of each magnet	0.465 g
Coil size	8 mm X 8 mm
No. of turns of coil	21
Resistance of coil	7.5 Ω
Total damping ratio	0.0857
Gap between magnet and coil	500 µm
Resonant frequency f_1	371 Hz

For a remanent magnetic flux density B_r = 1.3 T and a gap of 500 µm between the coil and the magnet, the normal component of the flux density according to equation (3.15), over a coil area of 8 × 8 mm^2 is shown in Figure (3.3). The magnetic flux density is relatively uniform in the middle portion of the coil, whereas closer to the outer edges it sharply varies and changes polarity at the outer turns. The distribution of the flux density depends on the size of the magnet and gap between the coil and the magnet.

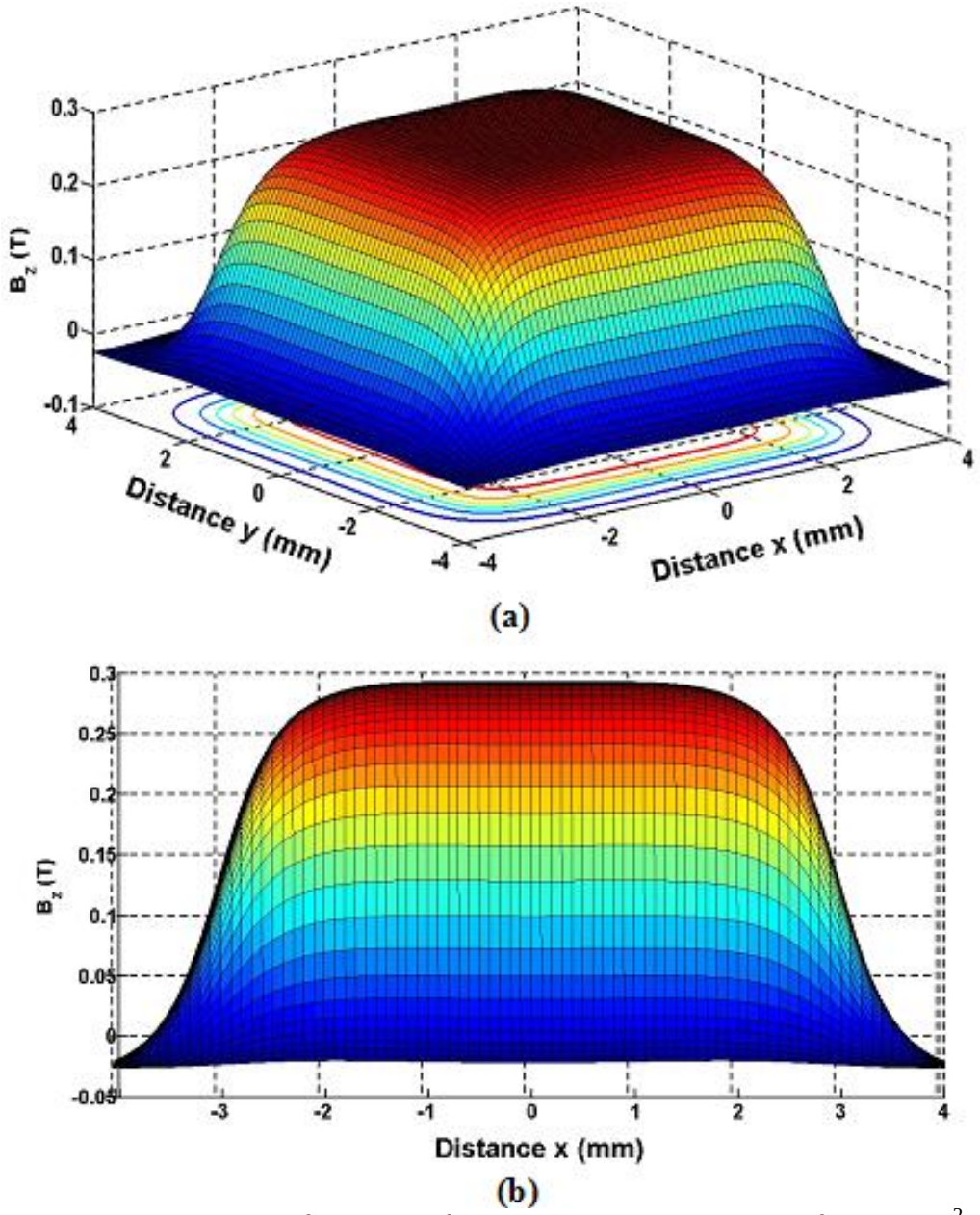

Figure 3.3: Normal component of magnetic flux density over a coil area of 8 × 8 mm^2, for a gap of 500 µm: (a) perspective view of the surface plot, (b) side projection.

Differentiating equation (3.15) with respect to z yields the expression for the magnetic flux density gradient over the coil and then setting z equal to the gap between the coil and the magnet at rest, results in the magnetic flux gradient in the plane of the coil. The corresponding magnetic flux gradient for a gap of 500 µm between the coil and the magnet is shown over a coil area $8 \times 8\ \text{mm}^2$ in Figure (3.4). The central portion of the coil experiences an approximately uniform magnetic flux gradient, however at the outer edges of the coil, the magnetic flux gradient is of opposite polarity, which will result in a decreased net magnetic flux gradient for the outer turns.

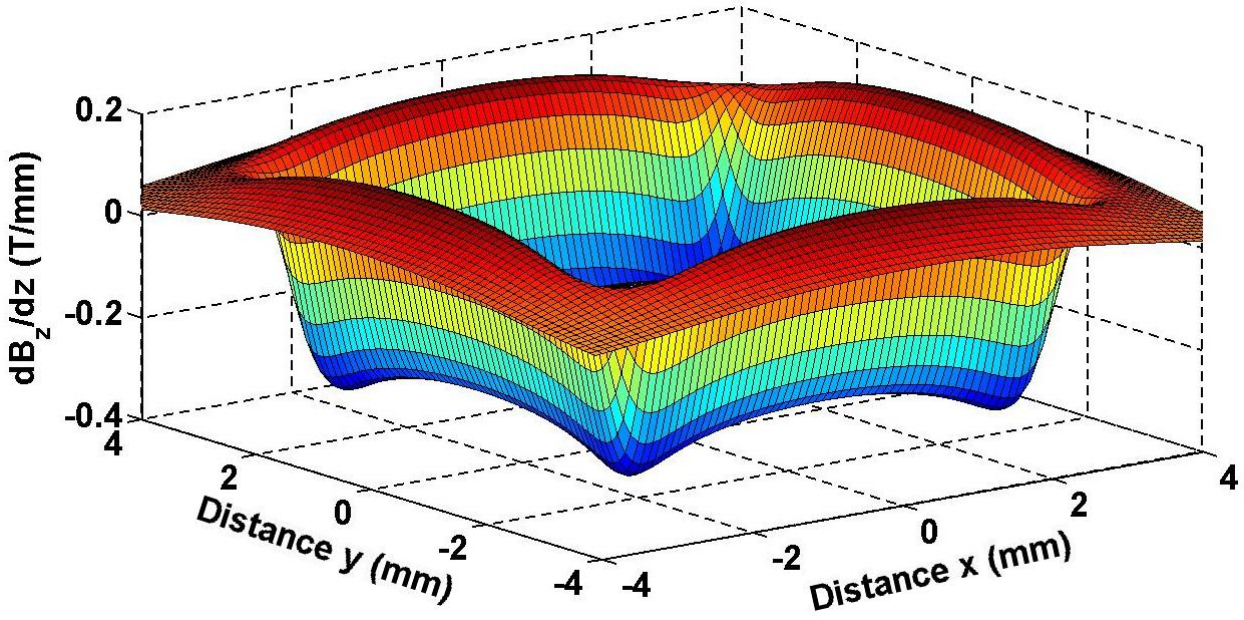

Figure 3.4: Gradient of the normal component of the magnetic flux density over a coil area of $8 \times 8\ \text{mm}^2$.

For the estimation of the output voltage with equation (3.14), the average magnetic flux gradient $\overline{\left(\frac{dB_Z}{dz}\right)_i}$ over a turn area S_i can be obtained by computing and averaging the magnetic flux gradient at several points within the turn.

3.2.2 Analytical model based on the direct method or the Lorentz force law

Figure 3.5 shows a non-uniform magnetic field of a permanent magnet in which a square loop is moving with a relative velocity *U* in the positive z-direction.

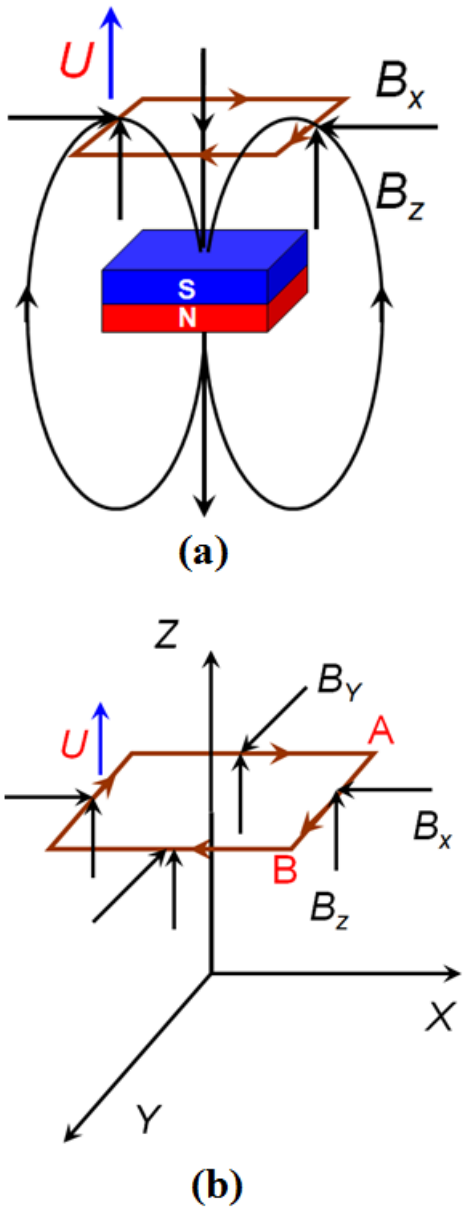

Figure 3.5: Voltage induction in a square loop from a non-uniform field.

According to the Lorentz force law, the line integral of the magnetic force per unit charge, $f_m = F_m / Q = U \times B_x$ over the coil side length AB results in the amplitude of the voltage

$$V_{ab} = \int f_m \cdot dl \qquad (3.16)$$

induced in the side AB and can be expressed in terms of the x-component B_x of the magnetic flux density and the relative velocity U between the magnet and a coil as

$$V_{ab} = \int (U \times B_x) \cdot dl = \int B_x U dl = U \int B_x dl \,. \qquad (3.17)$$

When the center of the magnet is coincident with the centre of the coil, the x-component B_x and y-component B_y of the magnetic flux density B are identical on corresponding sides of the coil (by symmetry), the voltage

$$V_i = 4U \int B_{x_i} dl \qquad (3.18)$$

induced in a whole loop can be approximated for n loops

$$V_G = 4U \sum_{i=1}^{n} \overline{B}_{x_i} L_i \qquad (3.19)$$

in terms of the average of the x-component of the magnetic flux density $\overline{B}_{x_i}$ at the side length L_i of an individual turn. For a square spiral planar coil, Figure 3.6, with the length L_1 of the side of the first turn, line width w and spacing b between the adjacent turns, L_i can be computed as

$$L_i = L_1 + 2(i-1)(w+b) \,. \qquad (3.20)$$

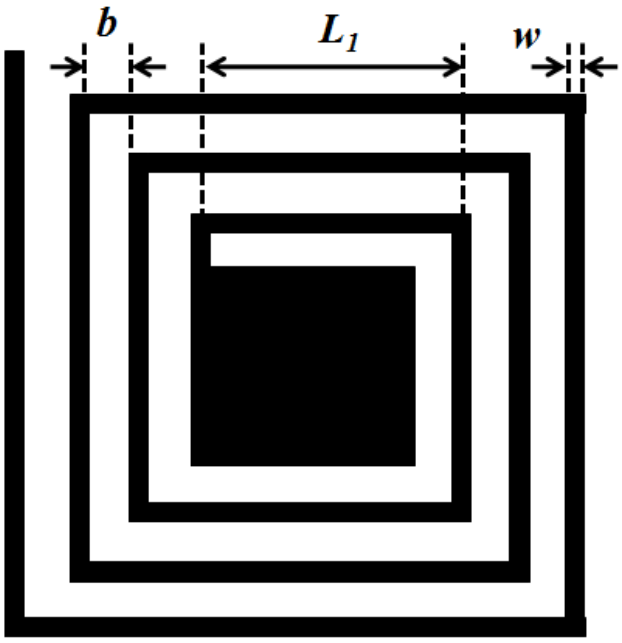

Figure 3.6: Square spiral planar coil.

Using equation (3.19), the amplitude of the voltage delivered to the load R_L becomes

$$V_L = \left(\frac{R_L}{R_L + R_C}\right) \frac{4A\omega \sum_{i=1}^{n} \overline{B}_{x_i} L_i}{\omega_n^2 \sqrt{\left[1 - \left(\omega / \omega_n\right)^2\right] + \left[2\zeta_T \left(\omega / \omega_n\right)\right]^2}} . \qquad (3.21)$$

For computation of the load voltage with equation (3.21), the average x-component $\overline{B}_{x_i}$ of the magnetic flux density at the side of each turn can be obtained with the 2-D magnetostatic analysis in COMSOL multiphysics®. Figure 3.7 shows the magnetic flux density distribution along the magnet's cross-sectional plane, for a remanent magnetic flux density B_r = 1.3 T. In Figure 3.7, the dotted line T at a gap of 500 µm from the magnets, corresponds to the cross-section of half of the coil. The values of the x-component of the magnetic flux density at the points of line T corresponding to the centres of the sides of the individual coil turns and the computation of the side length L_i of individual coil turn with equation (3.20) are sufficient to predict the load voltage of the EMEH.

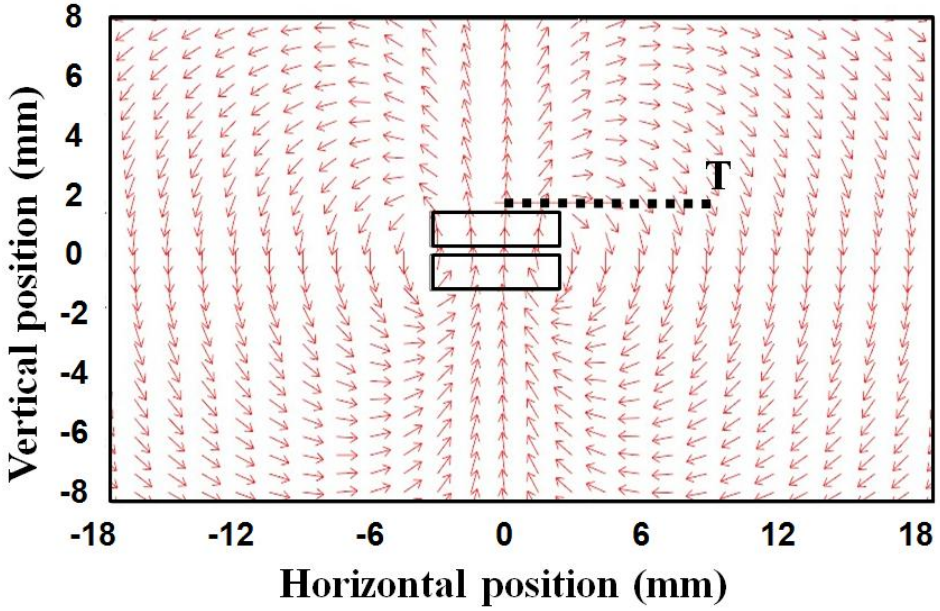

Figure 3.7: Simulated magnetic flux density distribution by COMSOL multiphysics®; the two rectangles indicate the position of the two magnets, line T indicates the location of half of one coil.

The load voltage with equation (3.21) can also be estimated with an analytical solution of the x-component of the magnetic flux density of the rectangular block magnet [134]

$$B_x = \frac{B_r}{4\pi}\ln\left\{\begin{aligned}&\left[\frac{(y-y_0)+\sqrt{(z-l/2)^2+(y-y_0)^2+(x+x_0)^2}}{(y+y_0)+\sqrt{(z-l/2)^2+(y+y_0)^2+(x+x_0)^2}}\right]\times\\&\left[\frac{(y+y_0)+\sqrt{(z-l/2)^2+(y+y_0)^2+(x-x_0)^2}}{(y-y_0)+\sqrt{(z-l/2)^2+(y-y_0)^2+(x-x_0)^2}}\right]\times\\&\left[\frac{(y+y_0)+\sqrt{(z+l/2)^2+(y+y_0)^2+(x+x_0)^2}}{(y-y_0)+\sqrt{(z+l/2)^2+(y-y_0)^2+(x+x_0)^2}}\right]\times\\&\left[\frac{(y-y_0)+\sqrt{(z+l/2)^2+(y-y_0)^2+(x-x_0)^2}}{(y+y_0)+\sqrt{(z+l/2)^2+(y+y_0)^2+(x-x_0)^2}}\right]\end{aligned}\right\}. \quad (3.22)$$

For the computation, the x-component of the magnetic flux density B_{xi} at z equal to the gap between the magnet and the coil at rest needs to be computed at several points over the side length L_i of each individual coil turn in order to obtain an average x-component $\overline{B}_{x_i}$ of the magnetic flux density for the side length of each turn. The x-component of the magnetic flux density (equation 3.22), for a remanent magnetic flux density B_r = 1.3 T and a gap of 500 µm between the coil and the magnet, is shown in Figure 3.8. The surface plot of B_x over a coil area of 8 × 8 mm^2, Figure 3.8(a), is anti-symmetric with respect to the y-axis. The coil turns of side lengths, nearly 6 mm, experience the maximum magnitude of the x-component of the magnetic flux density, as shown in Figure 8(b) and Figure 8(c). The coil turns of side length less than 6 mm, are exposed to an x-component of the flux density between 0 and 0.27 T, while the outer turns at the edges of the coil, experience about 0.15 T flux density.

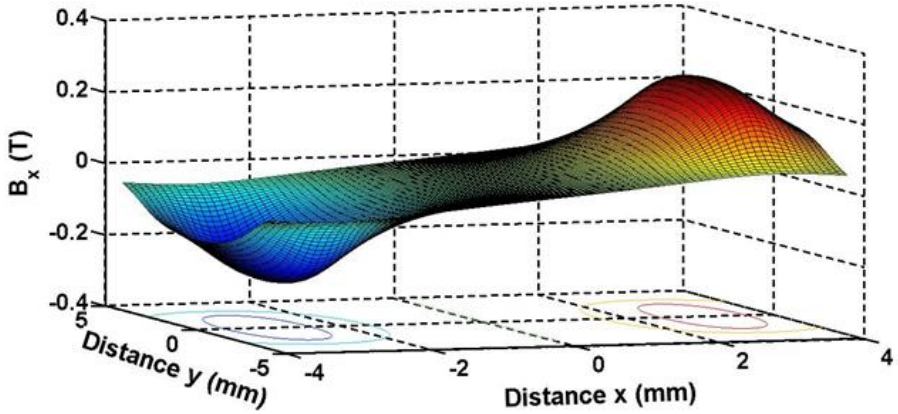

(a)

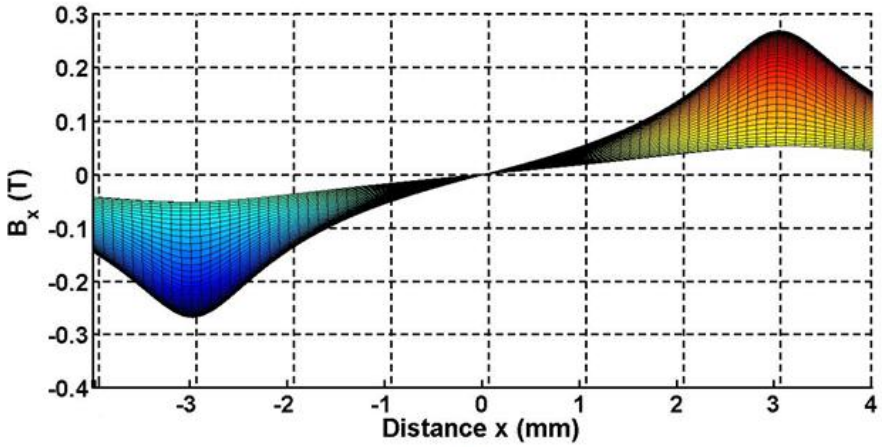

(b)

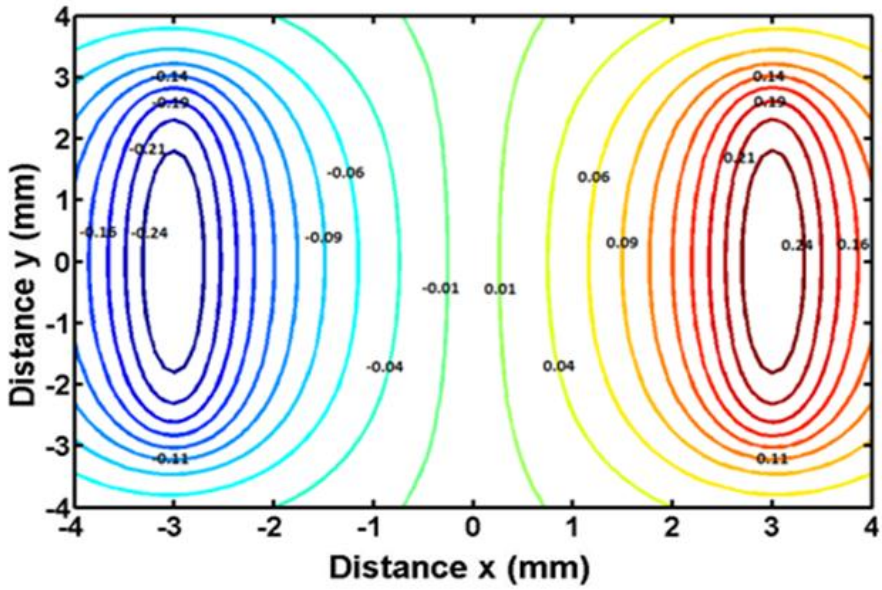

(c)

Figure 3.8: Magnetic flux density, x-component for a gap of 500 µm: (a) perspective view of the surface plot, (b) side view, (c) contour plot.

3.3 Simulation using the analytical models

The analytical models developed in this chapter are simulated for the values and dimensions (Table 3.1) of our EMEH [132], where the non-uniform magnetic field is caused by two permanent magnets that are mounted on a planar spring between two identical planar coils.

Figure 3.9 shows the load voltage amplitude measured experimentally for our EMEH [132]. The device is subjected to a frequency sweep at 13.5 g base acceleration. A 100 Ω resistance is connected to each coil and the voltage signals across the resistors are mathematically summed to obtain the combined load voltage generated by the EMEH. The simulation results in Figure 3.9 are based on the model using Faraday's law, equation (3.14) and equation (3.15), the models using the Lorentz' force law, equation (3.21) with either the analytical expression for the magnetic flux density (3.22) or the comsol simulation. Good agreement is found between the simulation and the experimental results around the fundamental frequency of the EMEH. However, at higher frequencies (beyond 390 Hz) a deviation between the curves appears which is due to the presence of higher resonant modes, and this indicates that the device is no longer following the assumed single degree of freedom analytical models.

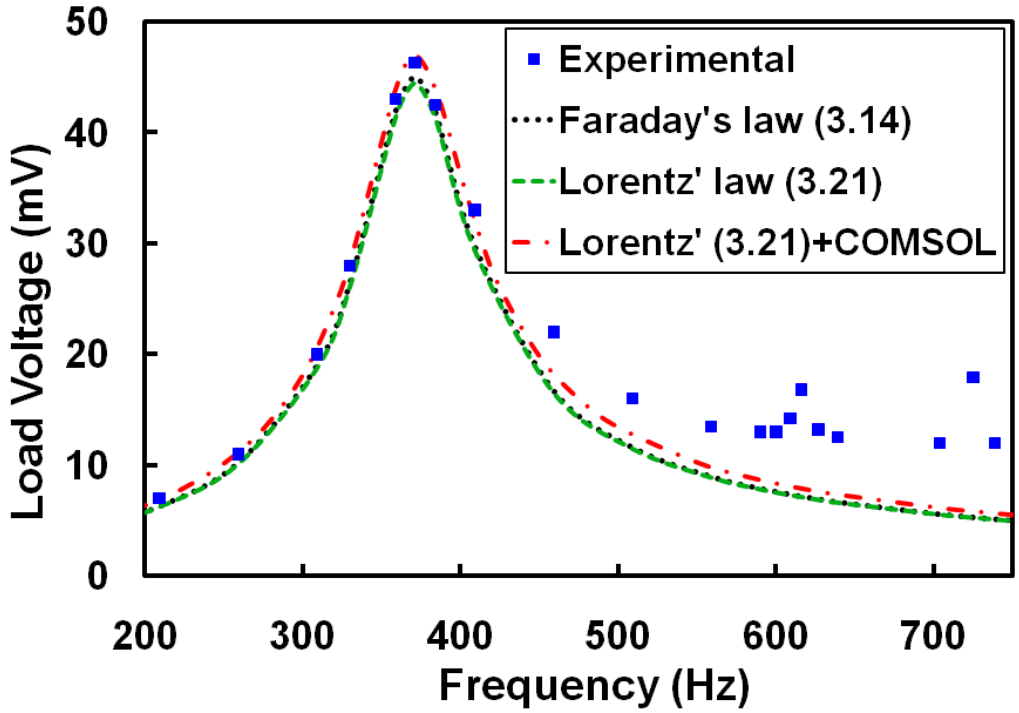

Figure 3.9: Load voltage for a 100 Ω load versus frequency at 13.5 g base excitation.

The load voltage predictions with Faraday's law (3.14) and the Lorentz force law (3.21) are approximately similar since they are equivalent laws and both use the off-centre analytical solutions of the magnetic flux density. However, in comparison to the experimental result these under estimate the output of the EMEH most likely due to the approximation used for the calculation of the area sum or the side length of the each individual turn. The simulation result based on the Lorentz force law and the COMSOL simulation, in comparison to the Lorentz force law (3.21) and analytical solution (3.22) predicts a higher voltage due to the slightly over estimated flux density from the 2D FEM simulation performed using COMSOL.

3.4 Optimization of the EMEH using a device model

The EMEH reported in [132] is optimized for maximum output voltage and power. The optimization is based on practical constraints, for example, the minimum permitted gap between the coil and the magnets and the maximum number of coil turns that can be fabricated in an area of 8 mm X 8 mm.

The experimentally determined absolute displacement between the magnets and a coil for accelerations of 13.5 g at the fundamental frequency is about 166.8 µm. In account for the wire bonded to the central electrical pad, a minimum gap of 250 µm is necessary. The normal component of the magnetic flux density and the magnetic flux gradient over the coil area of 8 mm x 8 mm, according to equation (3.15) are shown in Figure 3.10 and Figure 3.11, respectively both for a gap of 500 µm and 250 µm. The length of the horizontal axis of 8 mm in Figures 3.10 and Figure 3.11 corresponds to the width of the planar coil. With the decrease in magnets-coil distance, the normal component of the magnetic flux density, in Figure 3.10, is more uniform across the coil, also its maximum value increases to 0.32 T. Moreover, the magnetic flux gradient of the normal component of the magnetic flux density, in Figure 3.11, has become more uniform over the central turns of the coil for a reduced magnet-coil distance and the coil experiences an increased magnetic flux gradient that will result in a higher induced voltage.

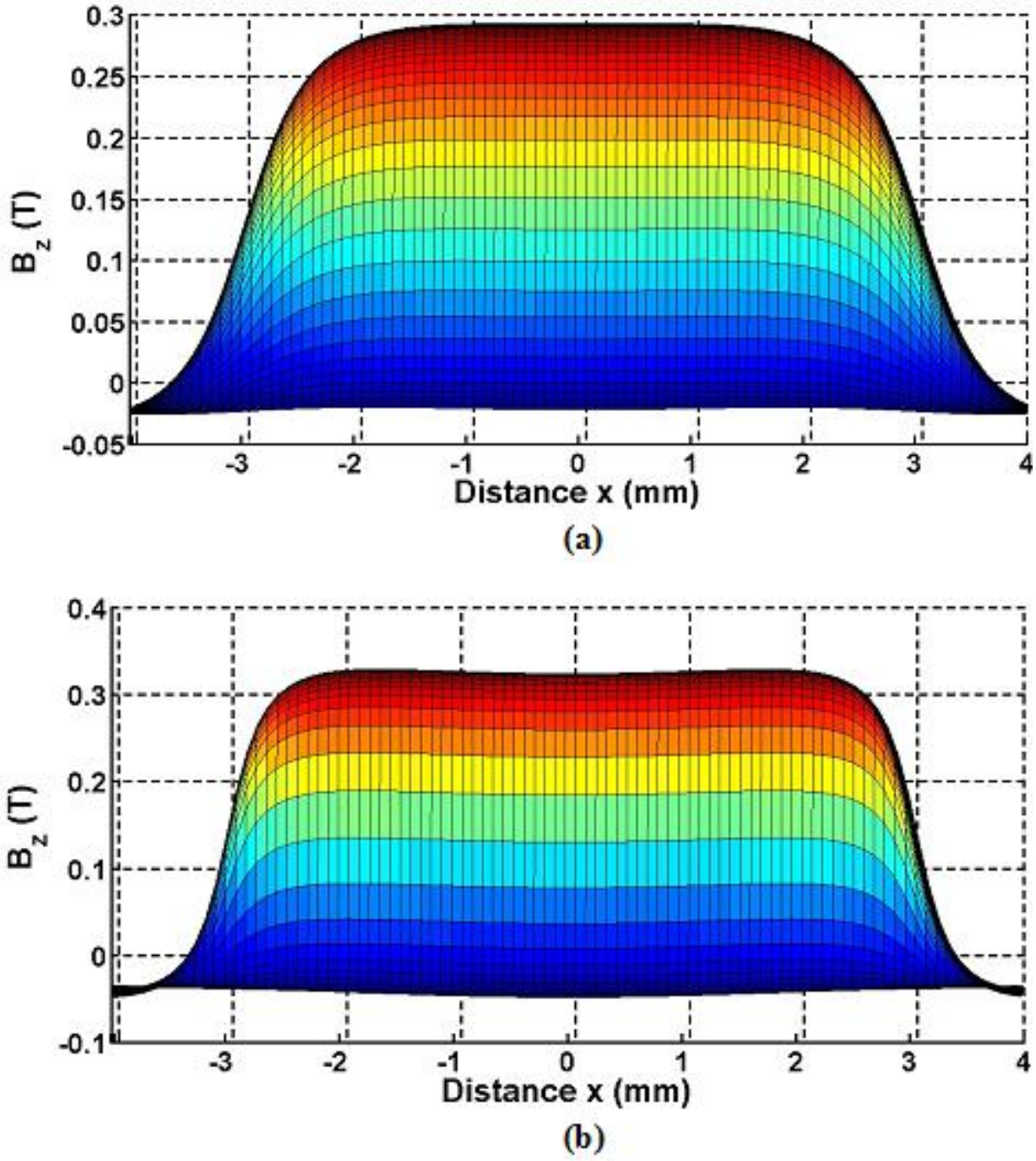

Figure 3.10: Distribution of the normal component of the magnetic flux density: (a) for a gap of 500 µm between the coil and a magnet, (b) for a gap of 250 µm between the coil and a magnet.

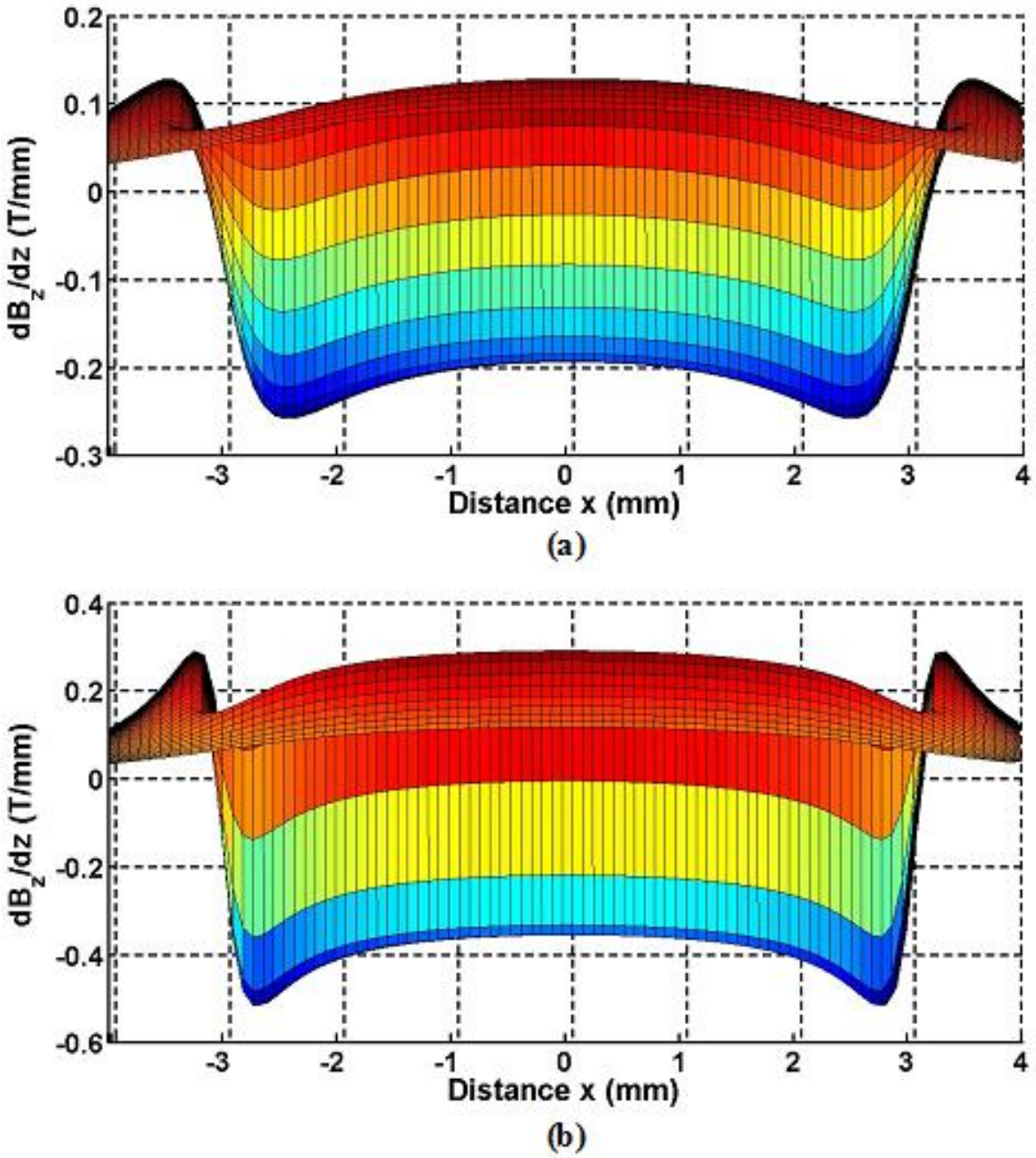

Figure 3.11: Distribution of the gradient of the normal component of the magnetic flux density: (a) for a gap of 500 µm between the coil and a magnet, (b) for a gap of 250 µm between the coil and a magnet.

The coil optimization can be obtained by keeping the overall coil area of 8 mm x 8 mm fixed, the number of turns of the coil can be increased by adjusting the wire width *w* and the gap *b* between the adjacent turns, for example, by decreasing the gap *b* between the adjacent

turns from 100 µm to 50 µm, the number of turns will increase to 35. However, the increase in the number of turns of the coil is accompanied by an increased coil resistance

$$R_C = \frac{\rho_c l_C}{A_C} = \frac{4n\rho_c \left[L_1 + 2(n-1)(w+b)\right]}{wt}, \qquad (3.26)$$

which depends on the resistivity ρ_c of the coil material, the overall coil length l_C and the cross-section area A_C of the coil conductor. The increased coil resistance will lead to increased electrical losses in the EMEH.

The simulation results for the modified EMEH are shown in Figure 3.12 and Figure 3.13. The model based on Faraday's law (equation 3.14) is used for optimization. The parameters and the coil dimensions used in the simulation are given in Table 3.2.

Table 3.2: Parameters and coil dimensions for EMEH optimization.

Description	**Analytical A**	**Analytical B**	**Analytical C**
Gap between magnet and coil	500 µm	250 µm	250 µm
Wire width *w*	50 µm	50 µm	50 µm
Gap between adjacent turns *b*	100 µm	100 µm	50 µm
Thickness of the coil *t*	20 µm	20 µm	20 µm
Resistance of coil R_C	7.5 Ω	7.5 Ω	18.82 Ω

When the gap between the coil and the magnets is reduced to 250 µm (Analytical B) an improvement of 9.5 mV in load voltage and 4.9 µW in load power occur. However, when also the number of coil turns is increased (Analytical C), the load voltage increases to 84.4 mV, which is almost double of the experimental value and the power delivered to the load increases to 35.6 µW that is almost three times the experimental value achieved at resonance for the present device [132].

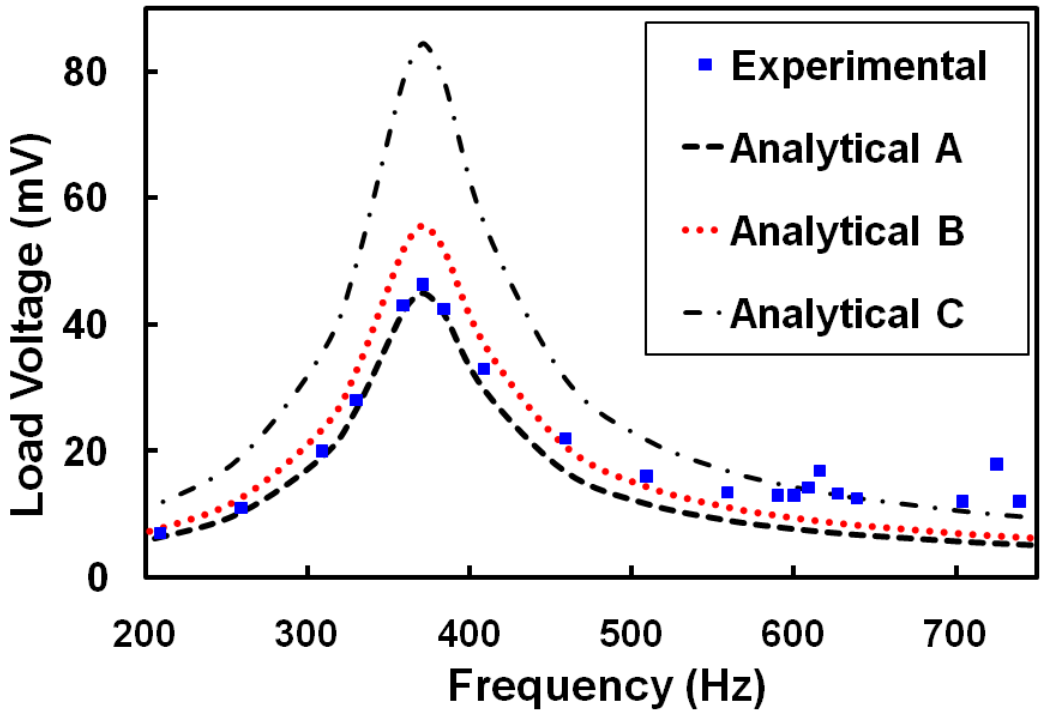

Figure 3.12: Load voltage for a 100 Ω load versus frequency at 13.5 g base excitation.

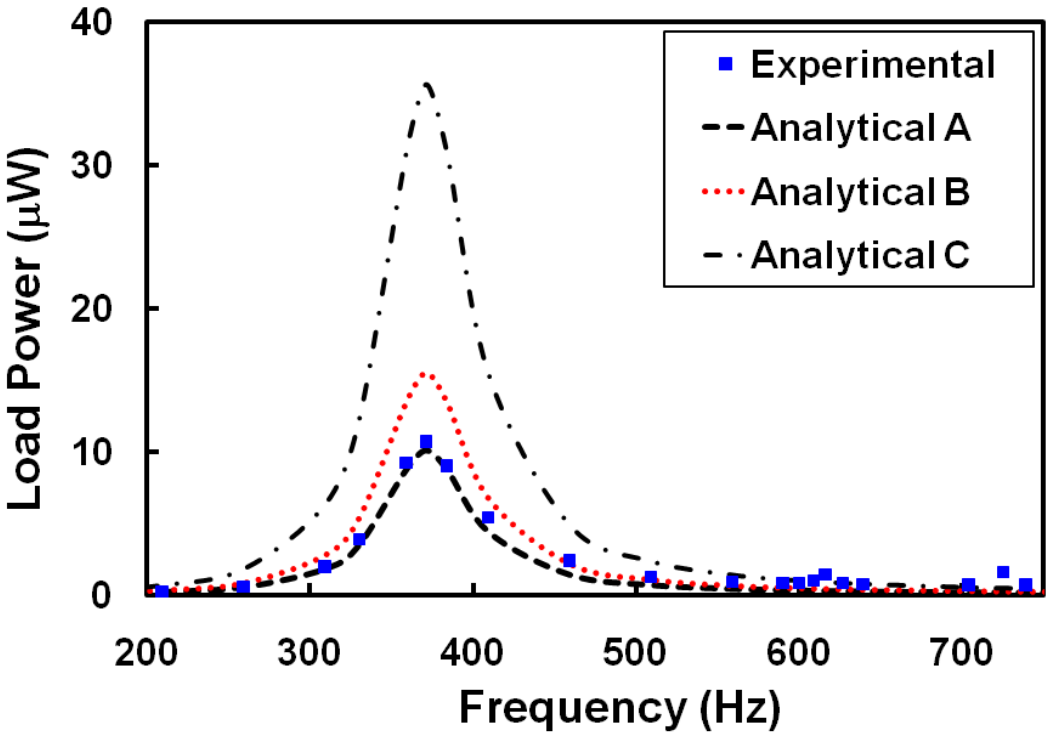

Figure 3.13: Power delivered to the 100 Ω load resistance versus frequency for 13.5 g base excitation.

4 Response of PDMS membrane type electromagnetic energy harvester under narrowband random vibrations[3]

4.1 Introduction

The advancement in low-power microelectronics and MEMS sensors, and the trend toward autonomous and self-powered systems make energy harvesting a viable choice for substituting batteries in sensing systems for environmental or machine-condition monitoring, and other applications. Vibration-based micro power generators (MPGs) are one of the options among the many varieties of MPGs. However, the challenge for vibration-based generators is to harvest energy from low level vibration present in the environments that range from a few Hz to a few kHz at low accelerations (0.25 g to 4 g). Industrial machine vibration levels (electric motors, generators, compressors, reciprocating engines or turbines) range from 0.5 to 15 g peak acceleration, for a frequency range from 0 to 5000 Hz [72], whereas the vibrations of household appliances, such as microwave ovens, kitchen blenders, washing machines, notebook computers or refrigerators typically range from 60 Hz to 385 Hz over a peak acceleration range from 0.01 to 0.65 g [135]. Gao and Cui [73] reported the vibration data for some production machines (lathe, drilling press, etc.) and household appliances from 30 to 200 Hz for a range of peak accelerations from 0.01 to 1.1 g. The general aim of energy harvesting is to develop devices suitable for harvesting energy from these commonly available vibration sources to power wireless sensors and transmitters.

Vibration-based energy harvesters reported in the literature are commonly piezoelectric [136], electrostatic [137] or electromagnetic [138] based. A comparison of these energy harvesters is summarized in Table 4.1. Each MPG has merits and demerits. Piezoelectric and electrostatic MPGs produce high output voltages, however, the output impedance is on the high side, which results in low output currents. The output impedance of electromagnetic MPGs is low,

---

[3] A version of this chapter has been submitted for publication. Farid Khan, Farrokh Sassani and Boris Stoeber "Nonlinear behaviour of membrane type electromagnetic energy harvester under harmonic and random vibrations", Submission date: Feb. 2011.

therefore even with low output voltage levels still comparatively high output current levels can be generated [78], which is the main advantage of electromagnetic MPG over the other two types. The power levels these energy harvesters generate tend to be low, however, with the rapid advancement in ultra low power (ULP) MEMS sensors and microelectronics the power need is on a decline to few μW.

Table 4.1: Comparison of vibration-based micro power generators.

Type	Advantages	Disadvantages
Piezoelectric	• MEMS compatible processes available for the deposition of thin films of piezoelectric materials • A number of piezoelectric materials are available e.g PZT, $BaTiO_3$, PVDF, ZnO, AlN • High output voltage levels • Easy voltage rectification	• Few device architecture options (normally cantilever beam type) • Mechanical properties of piezoelectric films limit the application to low g vibration environment • High resonant frequency • Frequency tuning needs proof mass • High output impedance • Low output electrical current levels
Electrostatic	• Fabrication compatible with standard IC technology • High output voltage • Easy voltage rectification • Easy frequency tuning with beam design • Standard MEMS fabrication process such as MUMPs can be utilized for fabrication • Monolithic fabrication possible	• Mostly silicon based devices • Require switching circuit for operation • Require voltage source for initial charging • High resonant frequency • High output impedance • Low output electrical current levels • Pull-in phenomenon (stiction issue)
Electromagnetic	• A number of options for device architecture, e.g moving mass, moving coil, wound coil, planar coil, metallic or non metallic beam, polymeric membrane etc. • MEMS compatible processes available for fabrication of planar coil and planar spring • A wide range for spring material e.g Si, Cu, steel, parylene, etc available • Standard PCB technology can be utilized for fabrication • Resonant frequency easily adjustable with magnet mass or spring design • Can be tuned to low, medium or high g vibration levels • Relatively low output impedance • Comparatively high output current levels	• Bulk magnets limit the monolithic fabrication • Low output voltage levels • Voltage rectification can be an issue

The power requirement of commercially available ultra low power pressure, temperature and acceleration sensors is given in Table 4.2. The minimum power consumption of ULP sensors depends of the type and model of the sensor but accelerometers need relatively more power to function. For the ULP sensors the overall power consumption range is from 1.8 to 324 µW for supply current levels of 1 to 180 µA. Due to these ultra low power needs, energy harvesting methods have the potential to enable integrated sensing devices with unlimited maintenance-free operation. Wireless sensor power needs are typically a few mW, which is relatively high and most of the power is required for RF transmission. The current MEMS-scale energy harvesting techniques are not developed far enough to completely eliminate the battery from wireless sensor nodes, however, they can still be integrated to supplement the power provided by the battery and increase its life span.

Table 4.2: Power consumption of commercial ultra low-power sensors.

Sensor type	**Company**	**Model type**	**Voltage** (V)	**Current** (µA)	**Standby current** (µA)	**Calculated power** (P=VI) (µW)
Pressure	Measurement Specialties	MS5607-B	1.8	1	0.15	1.8
	BOSCH	BMPO85	1.8	3	n.r.	5.4
	VIT Technologies	SCP1000	2.4	3.5	0.2	8.4
	Sensonor	SP300 (Pressure mode)	2.1	4	n.r.	8.4
Temperature	Sensonor	SP300 (Temperature mode)	2.1	0.9	n.r.	1.89
	STMicroelectronics	STLM20	2.4	4.8	0.02	11.52
	Fairchild Semiconductor	FM20	2.4	9	n.r.	21.6
	Andigilog sensors Inc.	TS10	2.4	12	n.r.	28.8
	Andigilog sensors Inc.	aSM121 (SiMISTOR ™)	2.7	14	n.r.	37.8
Acceleration (3-Axis)	STMicroelectronics	LIS331DLH	2.16	10	1	21.6
	Analog Devices Inc.	ADXL346	1.7	23	0.2	39.1
	VTI Technologies	CMA3000-D01	1.7	70	4	119
	Kionix Inc.	KXSD9-1026	1.8	120	0.3	216
	VTI Technologies	SCA3000-E05	2.5	120	n.r.	300
	Analog Devices Inc.	ADXL330	1.8	180	n.r.	324

n.r. : not reported in the data sheet provided by the manufacturer

Electromagnetic energy harvesters (EMEHs) in which the relative motion of a magnet and a coil is used to harvest energy, normally include a magnet that is bonded to a multi-mask fabricated micro beam structure [80]. The micro-structured nature of the beam not only contributes to the fabrication complexity and cost of the device but also exhibits low vibration amplification or displacement magnification, which in turn limits the power generation. Replacement of micro-fabricated beam structures by a thin polymer membrane is a cost effective alternative. However, this replacement comes with increased air damping and associated decreased output power. One solution to this problem is to package the device in vacuum [139], or to design the device in such a way to allow the air on either side of the membrane to flow in and out of the device during the vibration of the magnet. A relatively soft membrane and low levels of air damping would help in increasing the amplitude of the relative displacement of the mass at low vibration levels and would therefore enable energy harvesting from low vibration levels.

Besides harvesting the energy from low level vibrations, there is an increasing interest in expanding the frequency bandwidth of such harvesters, since environmental vibrations are random and their frequency content can be quite broad. The spectral density (SD) of acceleration along the tangential direction of a car tire at a speed of 50 km/h, for example, has a rich energy content in a broad band from 5 Hz to 1 kHz [140]. The vibration of a car driven on a highway at 65 mph is within a broad band that ranges from 1 Hz to 500 Hz [141]. The vibration levels of household appliances reported in [142] also cover a broad band from 1 Hz to 500 Hz. The use of arrays of multi-frequency cantilever beams [143-146] is one of the approaches adopted to harvest energy from a relatively broad band of excitation. Recently, the exploitation of mechanical nonlinearities to broaden the harvester bandwidth has been also gaining increased interest [147, 148]. These nonlinearities can be created with beam deflection stoppers, beam preloading or with intrinsic characteristics of the flexible structure such as internal stresses in the membrane, for example due to stretching. The nonlinearities of the beams suspending the proof mass in an electrostatic energy harvester have been used to harvest under wide and narrow band excitations [149]. Magnetically coupled piezoelectric cantilevers [150, 151, 152] have been used to create bistable oscillators bouncing between the two stable energy states to harvest over a wider band of excitations. Prestressed beams have been utilized to tune piezoelectric energy harvesters to operate over a broader range of excitation frequencies [153, 154, 155]. Stoppers

have been used to restrict the motion of a beam to transform the EMEH from a linear oscillator to a piecewise-linear oscillator. It has been shown that with this method a broad bandwidth is obtained in the vicinity of the natural frequency of the unrestricted beam [156].

Other nonlinear EMEHs reported in the literature use membranes as the restoring spring element. The polyimide membrane type EMEH reported in [139] consists of two silicon wafers, one contains the polyimide membrane and a samarium-cobalt magnet, and a planar gold coil is fabricated on the other. Both wafers are bonded together by silver epoxy. The response of the device is nonlinear beyond 5 nm base amplitudes. The device was tested in air as well as in vacuum (10^{-5} Torr) and under vacuum it produced a maximum power of 0.3 μW at an excitation frequency of 4.14 kHz. A Kapton membrane type harvester having a single coil micro-fabricated on a silicon wafer and a NdFeB magnet bonded to the Kapton membrane is reported in [157]. The magnet is allowed to move in the etched recess in the middle coil wafer. The EMEH generated 0.2 μW peak power at 360 Hz and 6.8 μm base amplitude. Serre *et al.* [83] developed an EMEH using a single copper coil, electroplated on a SiO_2 coated silicon wafer, a Kapton membrane bonded between two PCB frames and two magnets. The upper magnet moving in the recess was held on the membrane with the help of a smaller magnet located on the opposite side of the membrane. The device response was nonlinear and it produced 50 μW for an impedance-matched load. They reported a power density of 40 μW/cm^3.

At high excitation levels, the nonlinear response of the polymeric membrane type EMEHs is attributed to the nonlinear elasticity of the membrane. For such nonlinear harvesters the lumped parameter model (Figure 3.1, in Chapter 3) comprises of linear damping and nonlinear stiffness. The nonlinear response of harvesters can be described by the duffing oscillator. When the harvester with nonlinear stiffness is subjected to the base excitation $\ddot{y} = A\sin\omega t$, the equation of motion

$$\ddot{z} + 2\zeta_T \omega_n \dot{z} + \omega_n^2 z + \beta z^3 = -\ddot{y} \qquad (4.1)$$

depends on the linear natural frequency ω_n, the total damping ratio ζ_T and the nonlinearity coefficient β.

From equation (4.1), the frequency response equation [158]

$$\left[(2\zeta_T \omega_n^2)^2 + (2\omega\omega_n - 2\omega_n^2 - \frac{3}{4}\beta Z^2)^2 \right] Z^2 = A^2 \qquad (4.2)$$

for the harvester can be obtained by using the method of multiple scales.

For the frequency response, equation (4.2), a third order polynomial in Z^2, can be solved for the three roots of relative displacement Z in terms of excitation frequency ω. However, an alternative approach adopted in [158] considers ω as the dependent variable instead of Z that results equation (4.2) in the form

$$\frac{\omega}{\omega_n} = 1 + \frac{3\beta}{8\omega_n} Z^2 \pm \sqrt{\left(\frac{-A}{2\omega_n^2 Z}\right)^2 - \zeta_T^2}$$

$$= \frac{f}{f_n} = 1 + \frac{3\beta}{16\pi f_n} Z^2 \pm \sqrt{\left(\frac{-A}{8\pi^2 f_n^2 Z}\right)^2 - \zeta_T^2} \qquad (4.3)$$

that computes the data for the frequency curve in the form of $\omega(Z)$.

The values of the relative displacement Z from the frequency response curve of the harvester obtained by equation (4.3) can be used to compute the amplitude of the relative velocity $U = Z\omega$ for the load voltage

$$V_L = \frac{R_L}{R_L + R_C} GU \qquad (4.4)$$

that depends on load resistance R_L, and harvester transformation factor G and coil resistance R_C.

Figure 4.1 shows the frequency response simulation for EMEH with f_n = 50 Hz, $\beta = 10^{11}$ N/kgm^3, G = 0.1 Tm and ζ_T = 0.05, when it is subjected to a base acceleration amplitude of A = 1 g. The distortion of the peak of the response curve towards higher frequencies is attributed to the spring hardening ($\beta > 0$) that results in the increase of resonant frequency of the harvester.

The relative velocity obtained from the data of the frequency curve in Figure 4.1 is plotted as a function of frequency in Figures 4.2.

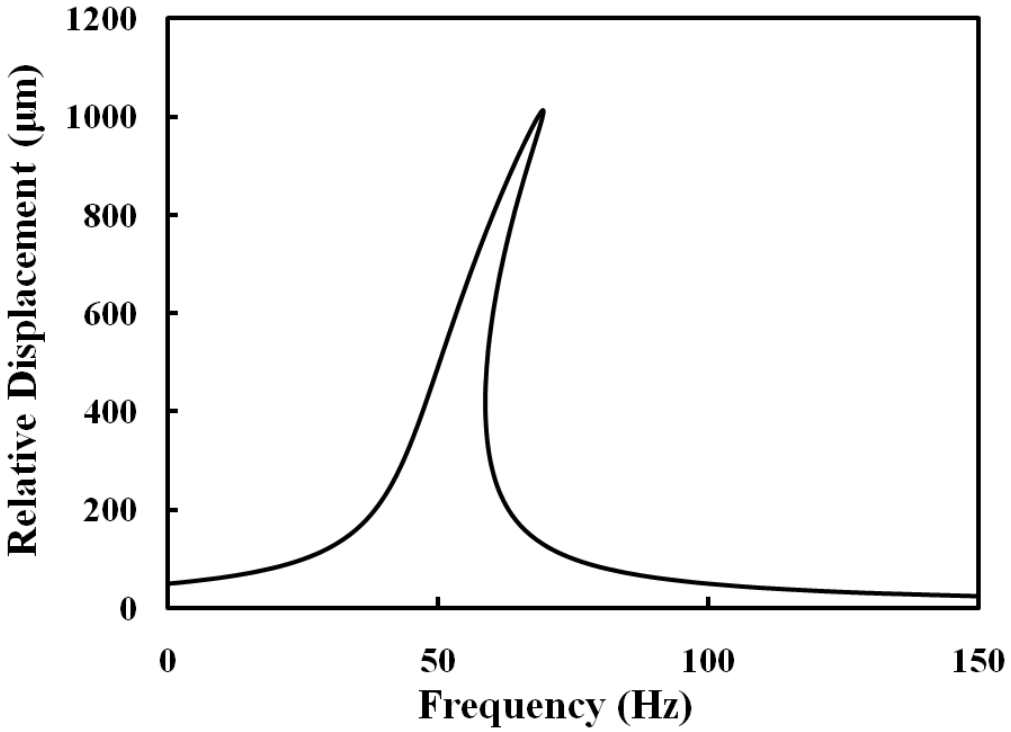

Figure 4.1: Relative displacement as a function of frequency for f_n = 50 Hz, $\beta = 10^{11}$ N/kgm^3, G = 0.1 Tm and ζ_T = 0.05 for a base acceleration of A = 1 g.

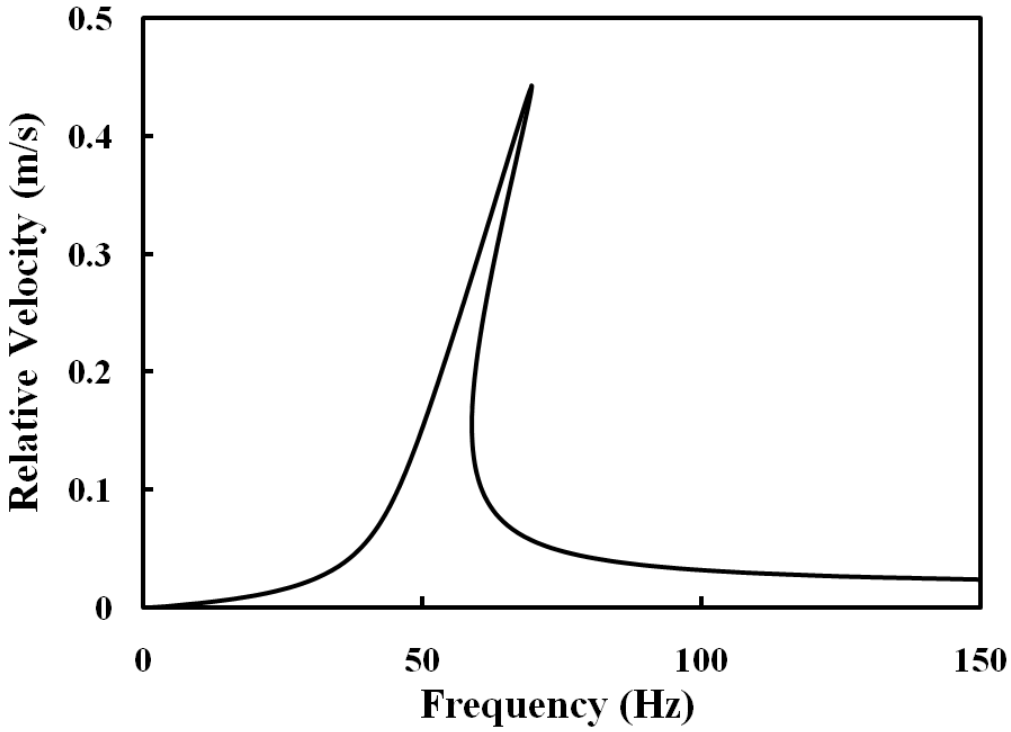

Figure 4.2: Relative velocity as a function of frequency for f_n = 50 Hz, $\beta = 10^{11}$ N/kgm^3, G = 0.1 Tm and ζ_T = 0.05 for a base acceleration of A = 1 g.

The load voltage computed with equation 4.4 is shown in Figure 4.3. At base acceleration amplitude of 1 g the simulation result predicts a load voltage of about 80 mV. The response of the nonlinear harvester comprises of an unstable path, line CD, in Figure 4.3. During frequency sweeps the unstable path CD is not followed and the harvester response exhibits the sudden drop (line CE) in forward frequency sweep and a sudden jump (line DB) during the backward frequency sweep. The region BCEDB is the hysteresis loop of the response attributed to the unstable path CD, which is the result of the nonlinearity of the device.

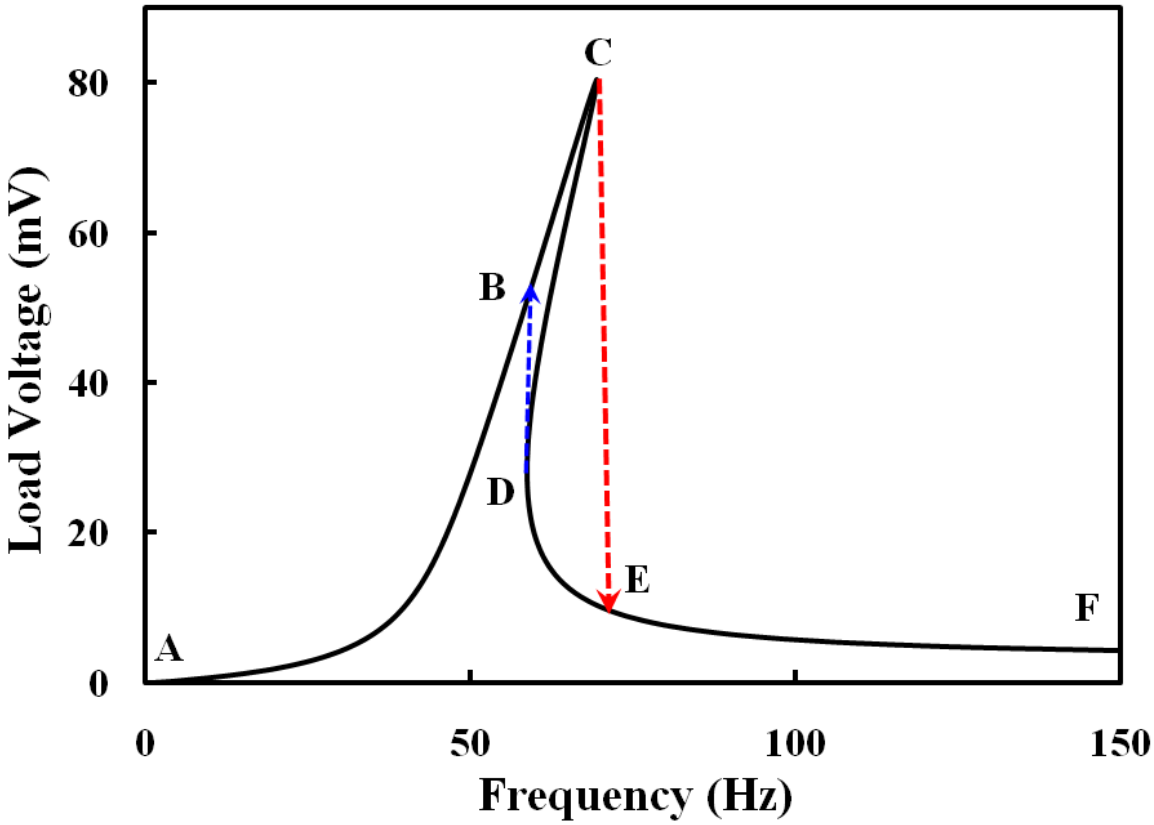

Figure 4.3: Load voltage for 100 Ω load verses frequency for f_n = 50 Hz, $\beta = 10^{11}$ N/kgm^3, G = 0.1 Tm and ζ_T = 0.05 for a base acceleration of A = 1 g.

Although a nonlinear behaviour for polymeric membrane type EMEHs has been reported, to our knowledge no previous study has exploited this nonlinearity to harvest energy from random vibrations. There exists no report yet on the relation between the nonlinear behaviour of the membrane type EMEH and the harvester bandwidth.

This chapter reports on fabrication, characterization, and analysis of a polydimethylsiloxane (PDMS) membrane type EMEH suitable for harvesting energy from low

level sinusoidal and narrow band random vibration environments. Our novel, low cost, one-mask micro-fabrication technique reported in Chapter 2 is used to fabricate the planar coils from commercially available copper foil. A 200 µm thick and 11 mm by 11 mm square PDMS membrane supports the magnets and allows large amplitudes of vibration from low acceleration level excitation. Slotted polycarbonate plastic spacers permit flow of air between the coil substrate and the membrane, which results in reduced air damping and enhanced power generation. Planar copper coils on glass substrates are placed on opposite sides of the magnets to provide enhanced double-acting power generation capability.

4.2 Prototype architecture and working principle

The cross-sectional and exploded views of the EMEH reported in this chapter are shown in Figure 4.4 and Figure 4.5, respectively. Two NdFeB magnets (K & J Magnetics Inc., Jamison, PA, USA) mounted on a PDMS membrane and two planar copper coils fabricated on glass substrates are separated by 4 mm thick slotted polycarbonate plastic spacers (Sheffield Plastics Inc., Sheffield, MA, USA).

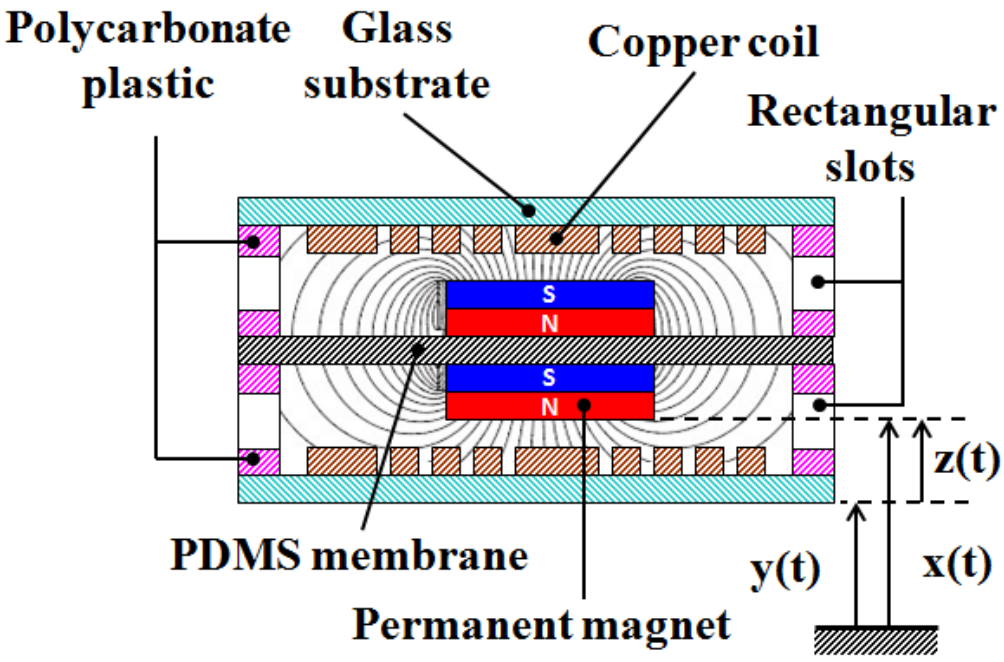

Figure 4.4: Cross-sectional view of the developed EMEH.

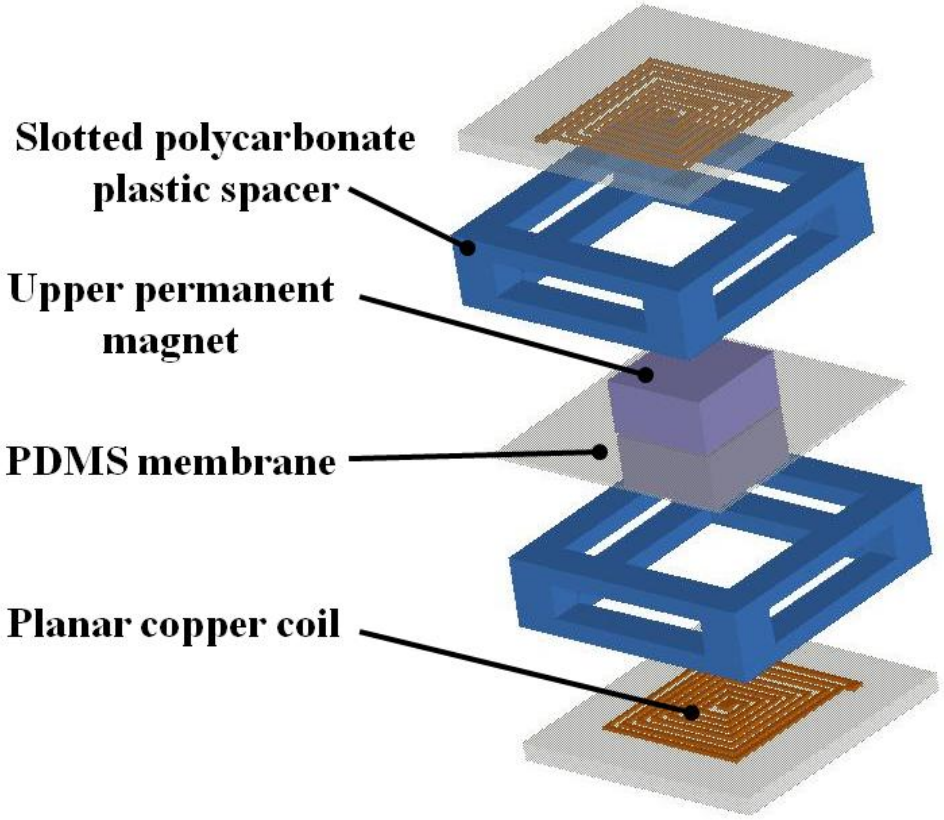

Figure 4.5: Exploded view of the EMEH.

The induced open-circuit voltage in a single coil of the device, according to Faraday's law of electromagnetic induction

$$V_G(t) = -NA\frac{\mathrm{d}B_z}{\mathrm{d}z}\dot{z}(t) \qquad (4.5)$$

depends on the relative velocity $\dot{z}(t)$ between the magnets and the coil, the magnetic flux density gradient $\frac{\mathrm{d}B_z}{\mathrm{d}z}$ of the normal component of the magnetic flux density B_z, and the number of turns of the coil N or area sum NA of the individual turns. To understand how the number of turns or the overall area of the coil is affected by the magnetic flux density distribution, a 2-D magnetostatic analysis is performed in COMSOL multiphysics®.

According to the manufacturer of the magnets the remanent magnetic flux density of the NdFeB magnets can range from 1.0-1.4 T. Two NdFeB magnets of size 6 mm x 6 mm x 3 mm are stacked together and the normal component of the magnetic flux density is measured experimentally using a teslameter (Sypris Test & Measurement, Orlando, FL, USA) and a measuring stage (Thorlabs, Newton, NJ, USA). The normal component of the magnetic flux

density, along the axis passing through the center of the magnets is measured and compared with the COMSOL simulation results obtained for different remanent flux densities in order to identify the correct value. Figure 4.6 shows the experimental and the simulation results obtained along the line J in Figure 4.7. The simulation of the magnetic flux density along this line for 1.32 T remanent magnetic flux density agrees well with the experimental result and therefore 1.32 T remanent magnet flux density is used to model the magnets in COMSOL.

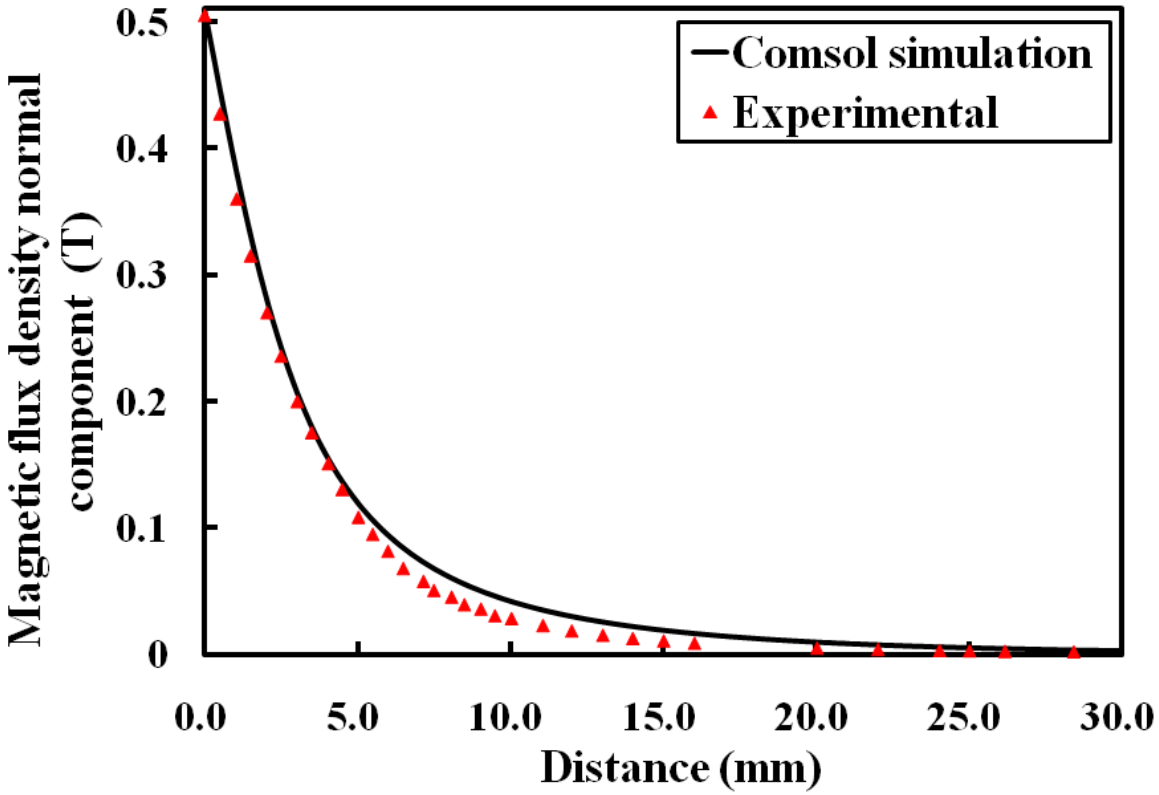

Figure 4.6: Magnetic flux density, normal component along the axis passing through the center of the magnets (line J in Figure 4.7).

Figure 4.7 shows the magnetic flux density distribution along the magnets' cross-sectional plane. The simulation shows that the magnetic flux density is mostly concentrated in an area 8 mm x 8 mm, near the surface of the magnets. Away from the magnets the flux density decreases drastically.

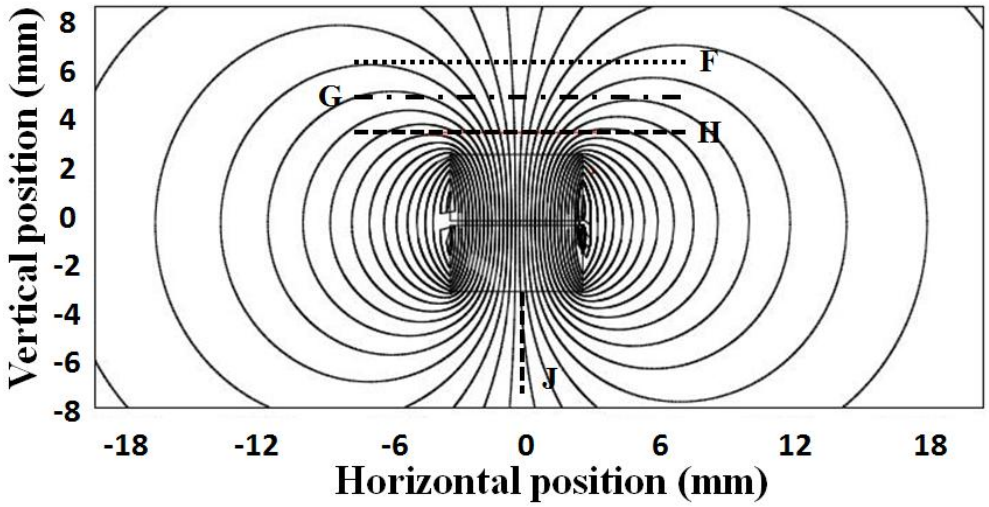

Figure 4.7: Simulated magnetic flux lines by COMSOL.

Since the magnetic flux density gradient is high near the surface of the magnets, the gap between the coil and magnets should be kept as small as possible in order to maximize the voltage generated according to equation (4.5), however, to accommodate the movement of the magnets the gap should be adjusted according to the amplitude of the displacement of the magnets at resonance. Figure 4.8 shows the distribution of the normal component of the magnetic flux density for gaps of 1250, 1000 and 750 μm (lines F, G, H respectively in Figure 4.7). A horizontal distance of 8 mm in Figure 4.8 corresponds to the width of the planar coil. The simulation result shows distribution of the same polarity of the flux density over the coil at gaps of 1000 and 1250 μm whereas for a gap of 750 μm, near the edges of the coil the polarity of the flux density changes. The opposite polarity of magnetic flux density within the area of the coil will decrease the net magnetic flux or the magnetic flux density gradient during operation of the device and will lead to reduced voltage generation in the outer turns of the coil. By accounting for the flexibility of the PDMS membrane and the desire for the same polarity of the magnetic flux density over the coil, the initial gap between each magnet and coil is kept at 1000 μm. The effective normal component of the magnetic flux density, acting on the 8 mm x 8 mm planar coil at various gaps is estimated by averaging the values of the magnetic flux density in Figure 4.8, for each gap. The computed average normal component of the magnetic flux density at the gaps of 750, 1000 and 1250 μm is 0.325, 0.264 and 0.188 T respectively, thus giving an approximate magnetic flux density gradient of 2.74×10^{-4} T/μm for a gap of 1000 μm.

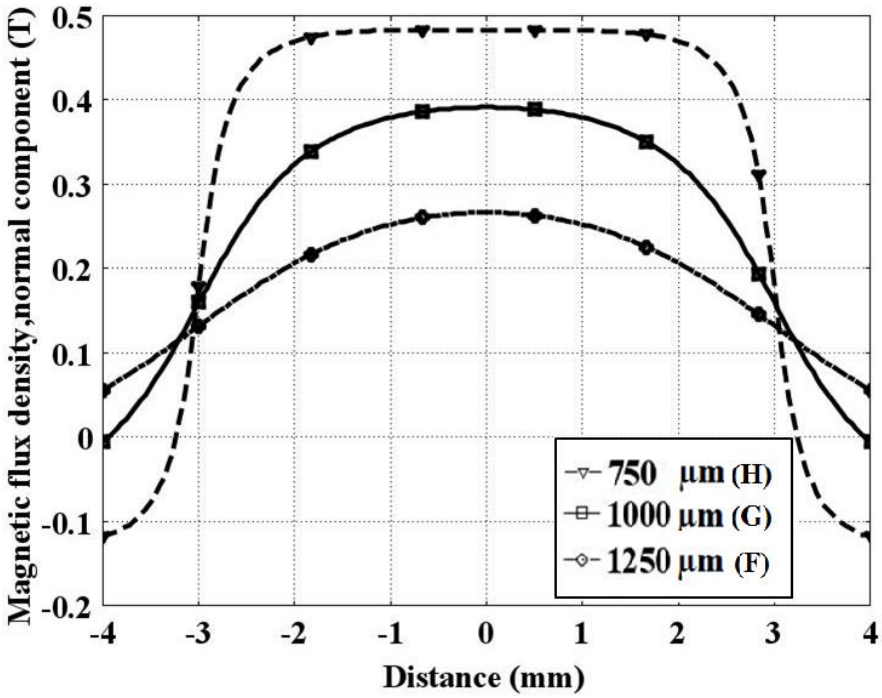

Figure 4.8: Normal component of the magnetic flux density for various gaps (lines F, G and H in Figure 4.7).

4.3 Fabrication of the prototype

The planar copper coils for the EMEH are fabricated from a commercially available copper foil using our low cost, one mask fabrication technique detailed in [132]. A 200 µm thick PDMS membrane is made by spinning Sylgard® 184 PDMS (mixture of 10 parts elastomer base and 1 part elastomer curing agent) on a glass substrate. The spinning is performed in two steps. In the first the sample is spun for 10 seconds at 500 rpm followed by 1200 rpm for 20 seconds. After curing the PDMS in an oven at 80^{o}C for 2 hours, a second coat of PDMS is applied on top of the first one by the same two spin steps. The cured 200 µm thick PDMS membrane is then peeled off the glass substrate.

The assembly steps of the energy harvester are shown in Figure 4.9. During the first step the two permanent magnets are mounted on the opposite sides of the PDMS membrane. A glass jig is used for mounting the two permanent magnets and bonding the two plastic spacers to the PDMS membrane. After placing one magnet in the recess provided in the glass jig, the membrane is laid down and the second magnet is then mounted on the reverse side (Figure 4.9(a)). The force of attraction between the magnets keeps the membrane firmly squeezed between them as shown in Figure 4.9(b). The slotted plastic spacer, shown in Figure 4.10, is then carefully bonded to the

sub-assembly by epoxy (UHU plus sofortfest, UHU GmbH & Co. KG, Bühl, Germany) (which sets in 2 minutes) (Figure 4.9(c)). The sub-assembly is then removed from the glass fixture, turned upside down and the second plastic spacer is carefully bonded as shown in Figure 4.9(d), (e). The excessive membrane material is then removed with a surgical knife, Figure 4.9(f). Finally, the two glass substrates containing the micro-fabricated coils are bonded to the top sides of the plastic spacers (Figure 4.10) under a stereo microscope (Olympus SZ61, Olympus Imaging America Inc., Center Valley, PA, USA) using the same epoxy. The assembled EMEH is shown in Figure 4.11 and the dimensions and parameters of the device and its components are given in Table 4.3.

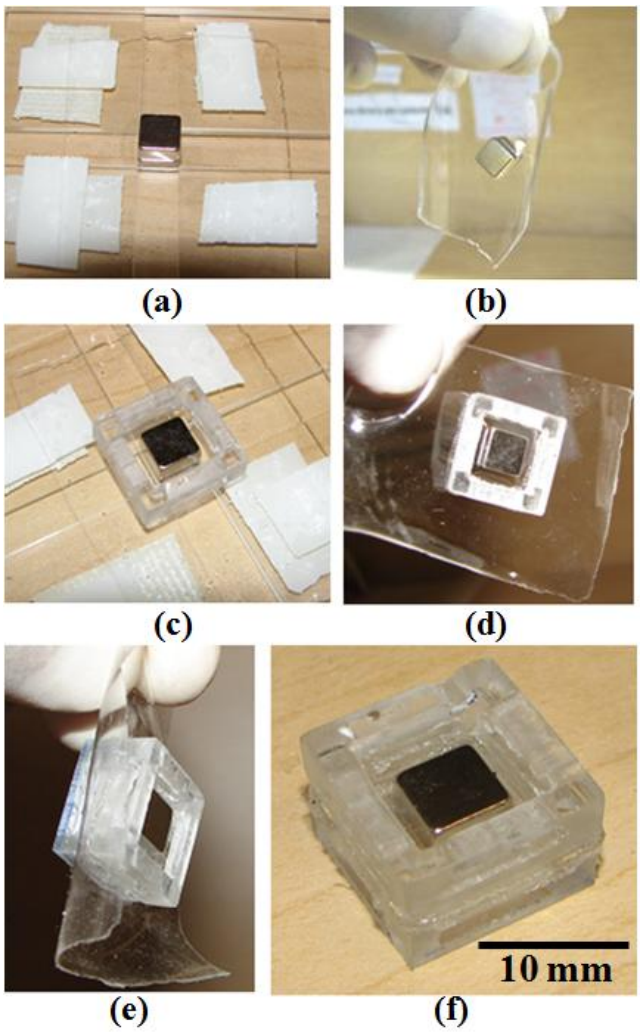

Figure 4.9: Photographic images of the prototype during assembly: (a) magnets and PDMS membrane on glass jig, (b) PDMS membrane squeezed between magnets, (c) first plastic spacer bonded to PDMS membrane, (d) sub-assembly removed from glass jig, (e) second plastic spacer bonded to PDMS membrane, (f) assembly after trimming excessive membrane material.

Figure 4.10: Slotted polycarbonate plastic spacer.

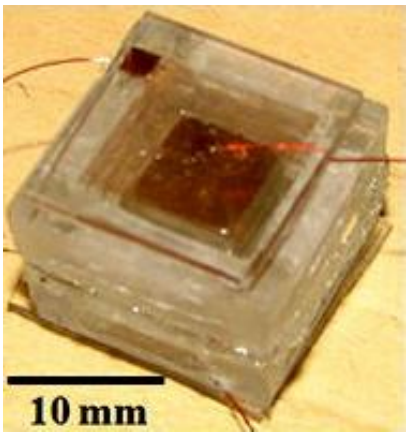

Figure 4.11: Assembled electromagnetic energy harvester.

Table 4.3: Dimensions and parameters of the EMEH prototype.

Description	Value
Device dimensions	15 mm X 15 mm X 10 mm
Magnet (NdFeB)	1.32 T
Magnet dimensions	6 mm X 6 mm X 3 mm
Membrane size	11 mm X 11 mm
Membrane thickness	200 µm
Coil size	8 mm X 8 mm
Gap between magnet and coil	1000 µm
No. of turns of coil	25
Resistance of coil	10.1 Ohms

4.4 Experimentation and discussion

Figure 4.12 shows the block diagram of the experimental setup. A Bruel and Kjaer 4809 vibration shaker is used to produce the mechanical vibrations. A National Instruments™ data acquisition (DAQ) card (NI USB-6212) and a Bruel and Kjaer 2718 amplifier regulate the frequency and vibration levels of the shaker. A 7 cm thick Teflon spacer block is mounted onto the shaker table to safeguard the device from the ferromagnetic parts of the shaker. The EMEH and an accelerometer (MMA1220, Freescale Semiconductor) are bonded to the Teflon block by a double-sided adhesive tape. A Polytech Inc. laser Doppler vibrometer is used for the measurement of the amplitude and frequency of the base vibration. The signals from EMEH, accelerometer and vibrometer are fed into the DAQ card, which in turn is connected to a computer by a USB cable. LabView software (National Instruments™) is used for the simultaneous measurement of the signals from the EMEH, the accelerometer and the vibrometer.

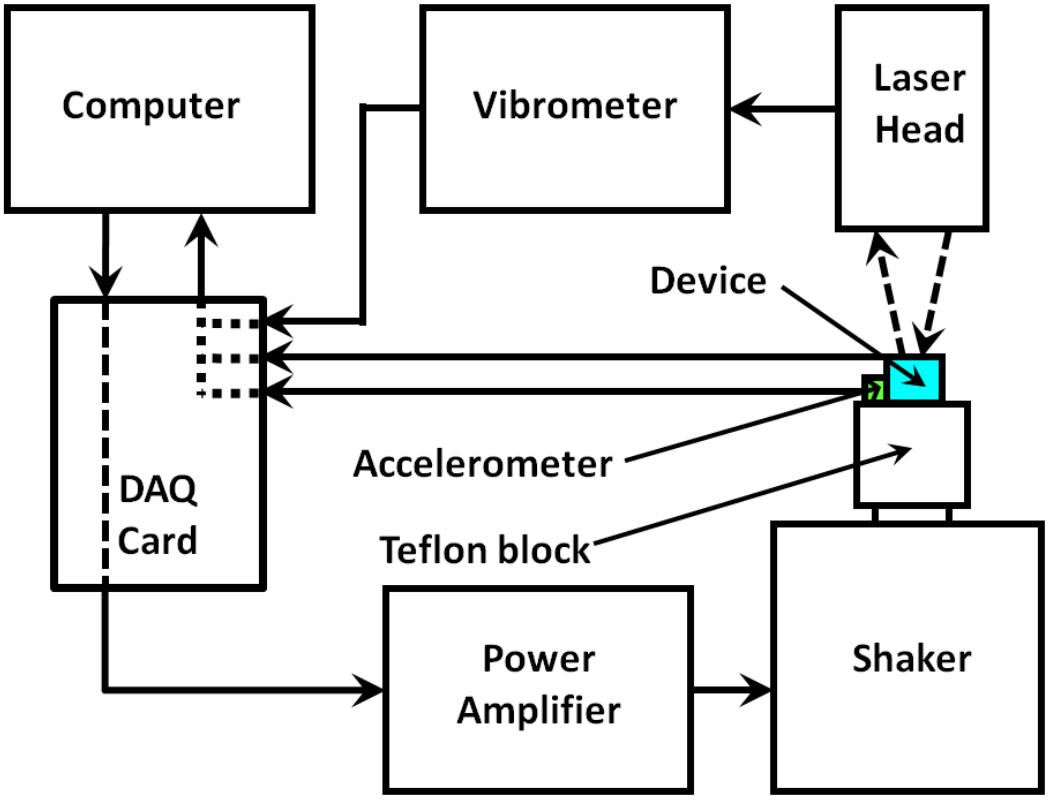

Figure 4.12: Block diagram of the experimental setup.

4.4.1 Characterization of the prototype under sinusoidal excitation

For characterization of the device under sinusoidal excitation, each coil is connected to a 100 Ω resistance and both signals are combined in LabVIEW. The device is first subjected to low levels of base excitations. Figure 4.13 shows the combined load voltage amplitude from both coils as a function of frequency for base accelerations of 0.1, 0.2 and 0.3 g. For acceleration level of 0.1 g the response curve is approximately symmetrical, indicating the linear behavior of the EMEH at this base acceleration. The response spectrum is distorted to the right as the amplitude of the base acceleration is increased. This is attributed to the nonlinear behaviour of the device due to spring hardening of the PDMS membrane at larger deflections. Higher base amplitude results in increasing membrane stiffness and thus increases the resonant speed that causes the response spectrum to distort to the right side for 0.2 and 0.3 g acceleration amplitudes. For 0.1 g and lower levels of base excitations the device will behave as a linear system. Maximum load voltages of 8.4, 12.7, 17 mV are produced when the EMEH is subjected to a frequency sweep from 10 to 90 Hz at acceleration levels of 0.1, 0.2 and 0.3 g, respectively.

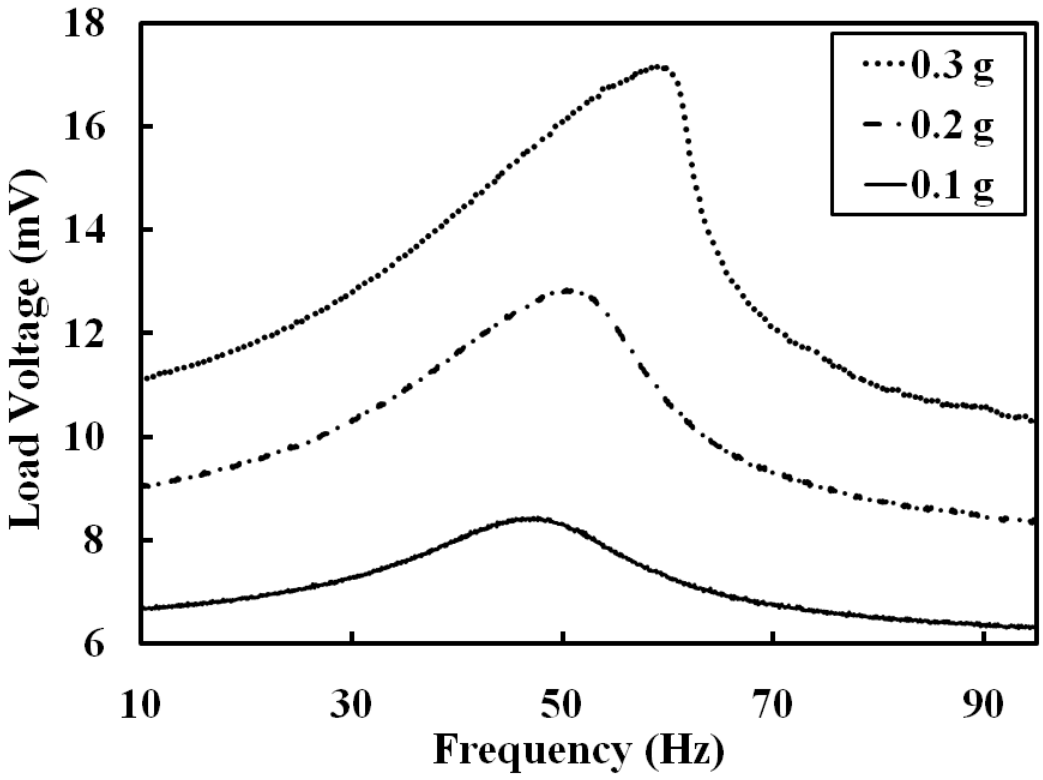

Figure 4.13: Load voltage for a 100 Ω load versus frequency at low levels of base accelerations.

Figure 4.14 shows the combined load voltage amplitude as a function of frequency when the EMEH is subjected to relatively high base accelerations. The EMEH is subjected to both increasing as well as decreasing frequency sweeps. Maximum load voltages of 48.5, 62.6, 79.4 and 88.8 mV are produced when the EMEH is subjected to increasing frequency sweep from 60 to 140 Hz at acceleration levels of 1 g, 1.5 g, 2 g and 3 g, respectively. The frequency response curves of the harvester in Figure 4.14, for the increasing (downward arrow) and decreasing (upward arrow) sweeps exhibit the phenomena of sharp drops and jumps [159] that are normally observed in nonlinear oscillators. Due to the non-monotonic response there are two possible amplitudes for the mass near the resonant frequency. During the decreasing sweeps an overshoot is also recorded which is consistent with that observed in a nonlinear electrostatic energy harvester reported in [149]. The resonant frequency of the EMEH increases as the acceleration of the applied vibration is increased as shown in Figures 4.13 and 4.14. Resonant frequencies of 89.0, 96.8, 104.5 and 108.4 Hz are recorded when the device is subjected to acceleration levels of 1, 1.5, 2, 3 g respectively, as shown in Figure 4.15. This increase in resonant frequency is a result of the nonlinear behaviour related to spring stiffening of the PDMS membrane. In addition, such a nonlinear behavior of the EMEH is consistent with that observed in polymeric membrane type EMEHs reported in [139] and [83]. When the EMEH is subjected to higher acceleration or higher base amplitude levels the membrane stretches more and that results in increased tensile stresses in the membrane which in turn increases the stiffness of the membrane [139]. In addition, since PDMS is an elastomer, the nonlinear elasticity of the PDMS membrane results in an increasing effective Young's modulus when the membrane is subjected to larger deflections (strains) [160]. At low levels of excitation the developed EMEH therefore shows a linear response similar to that reported in [139] and [157], while at large base excitation it exhibits the common jump phenomenon of nonlinear oscillators.

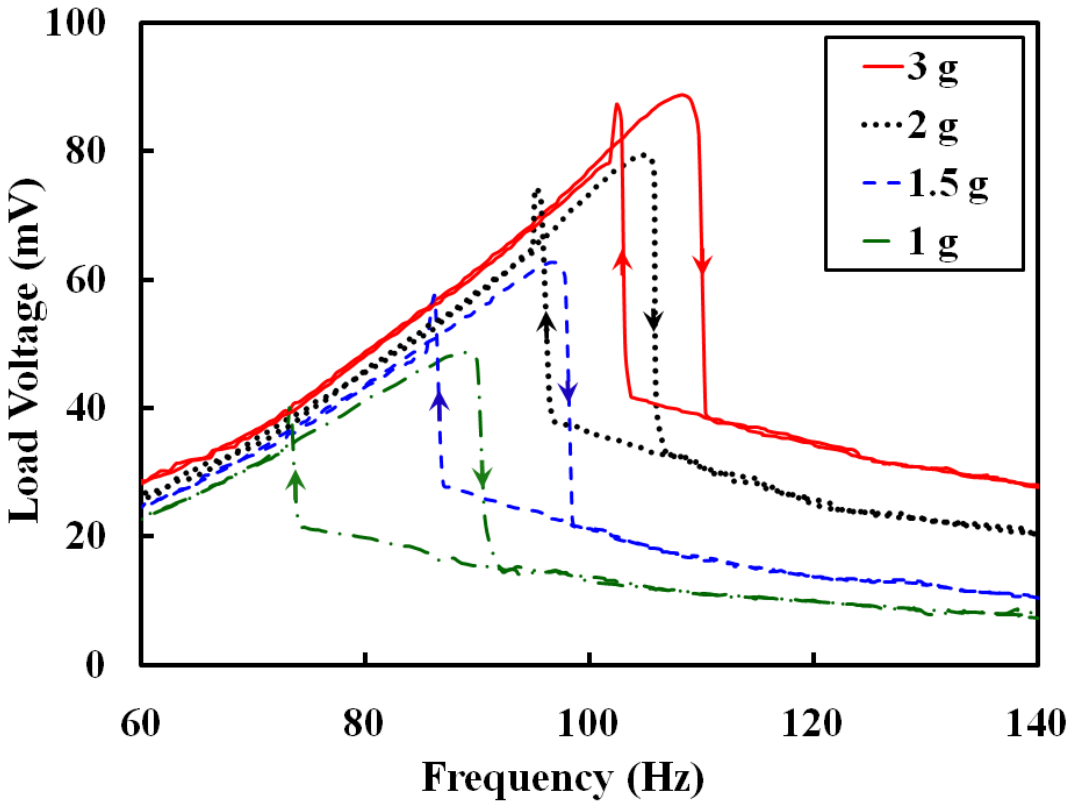

Figure 4.14: Load voltage for a 100 Ω load versus frequency at various base accelerations (forward and backward sweeps).

Figure 4.15 indicates the dependence of the resonant frequency of the device on the amplitude of the base acceleration during an increasing frequency sweep. This nonlinear characteristic of the device can be exploited to harvest energy from narrow band random vibrations, for example, if the device is subjected to random excitation with acceleration amplitude changes between 0.2 and 3 g in a narrow band of frequencies from 50 to 115 Hz. Within the range, there exists a higher probability for the harvester to resonate and harvest the energy over the narrow band, unlike the linear harvesters, where the resonant frequency is independent of the strength of the base acceleration. The increase in resonant frequency is not unbounded but in reality it is constrained by the maximum stress (ultimate tensile strength) of the membrane. The ultimate strength of the PDMS membrane depends on thickness and increases as the thickness of the membrane is decreased [160]; the membrane can therefore be tuned to cover frequencies present in the random excitation.

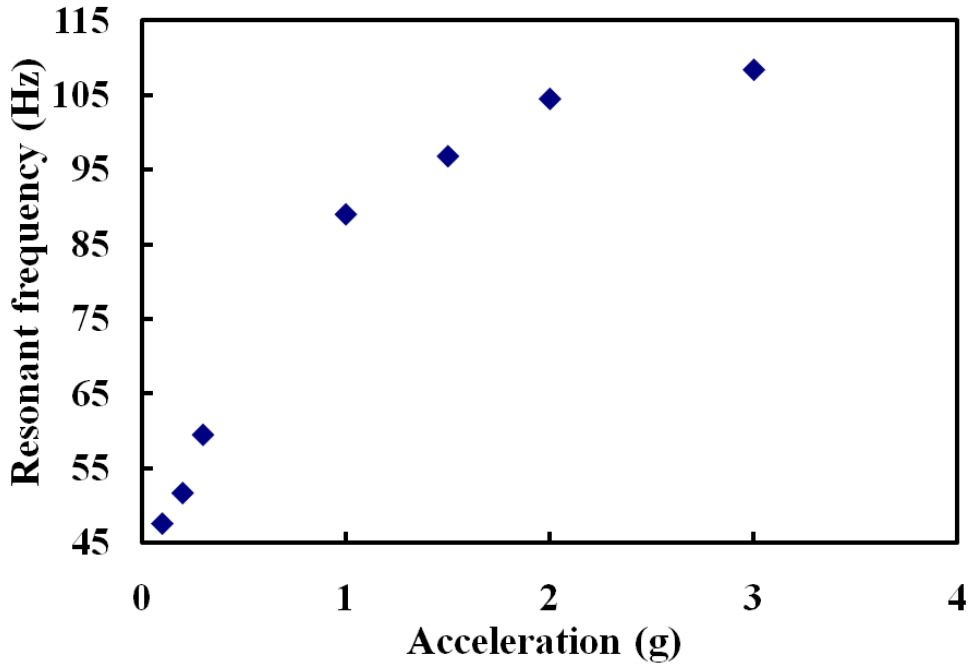

Figure 4.15: Resonant frequency of the EMEH at different base accelerations.

The power delivered by both coils to the 100 Ω load as a function of frequency during increasing frequency sweep is plotted in Figure 4.16. At resonance 11.8, 19.6, 31.5 and 39.4 μW power is delivered at the different base accelerations.

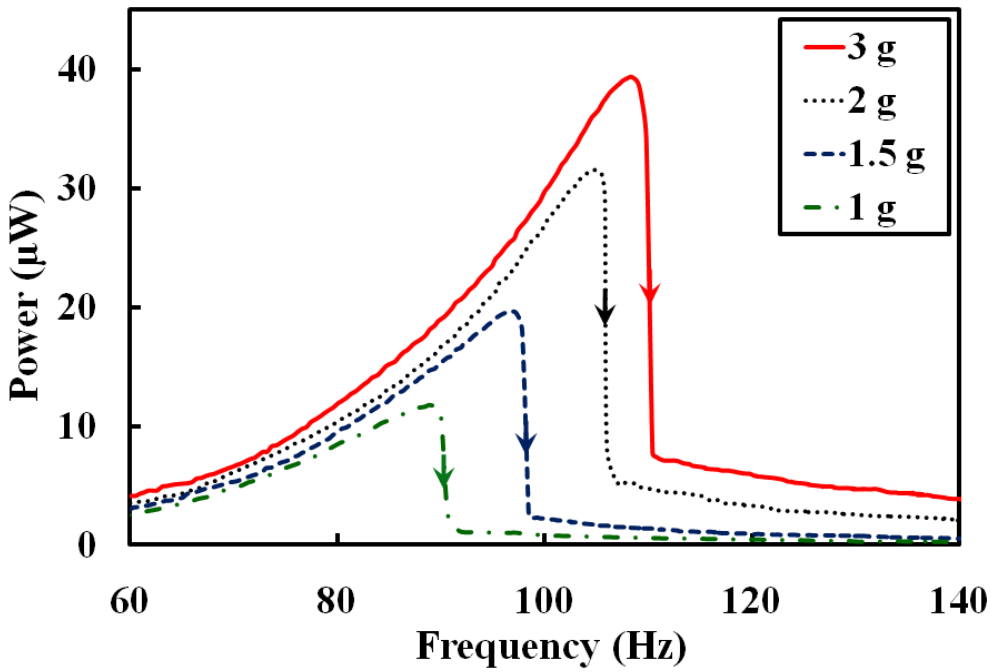

Figure 4.16: Power dissipated in a 100 Ω load versus frequency at various base accelerations (increasing frequency sweep).

In Figure 4.17, the measured load voltage and power at resonance are plotted against the base acceleration. The output of the device is not linear with respect to acceleration and this is most likely due to the nonlinear increase of the membrane stiffness and the increased damping at higher acceleration levels.

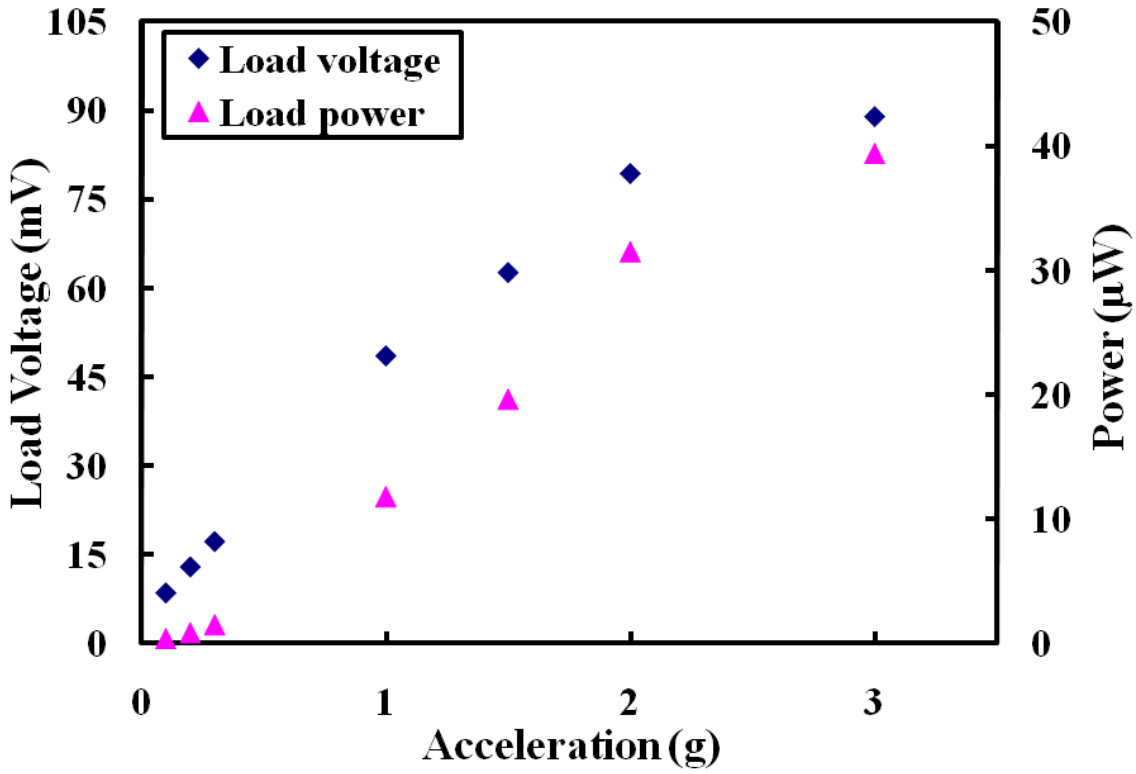

Figure 4.17: Load voltage and power delivered to a 100 Ω load at resonance versus base acceleration.

Figures 4.18 and 4.19 show the dependence of the output voltage and power on the load resistance. Different load resistances are connected to the coil and the EMEH is vibrated at resonant frequency (increasing sweep), at a constant base acceleration. These plots indicate that the larger the external resistor is, the larger is the measured voltage and the smaller is the load current. According to the experimental results in Figure 4.19, at matching impedance of 10.1 Ω the EMEH is capable of delivering a maximum power of 68.0 μW, when excited at 108.4 Hz and 3 g acceleration.

Based on the overall volume of the device, 2.25 cm^3, and the experimental data for optimum loading conditions, the EMEH is capable of generating power densities of 12.9, 18.1, 25.2, 30.2 $\mu W/cm^3$ at the four base accelerations investigated.

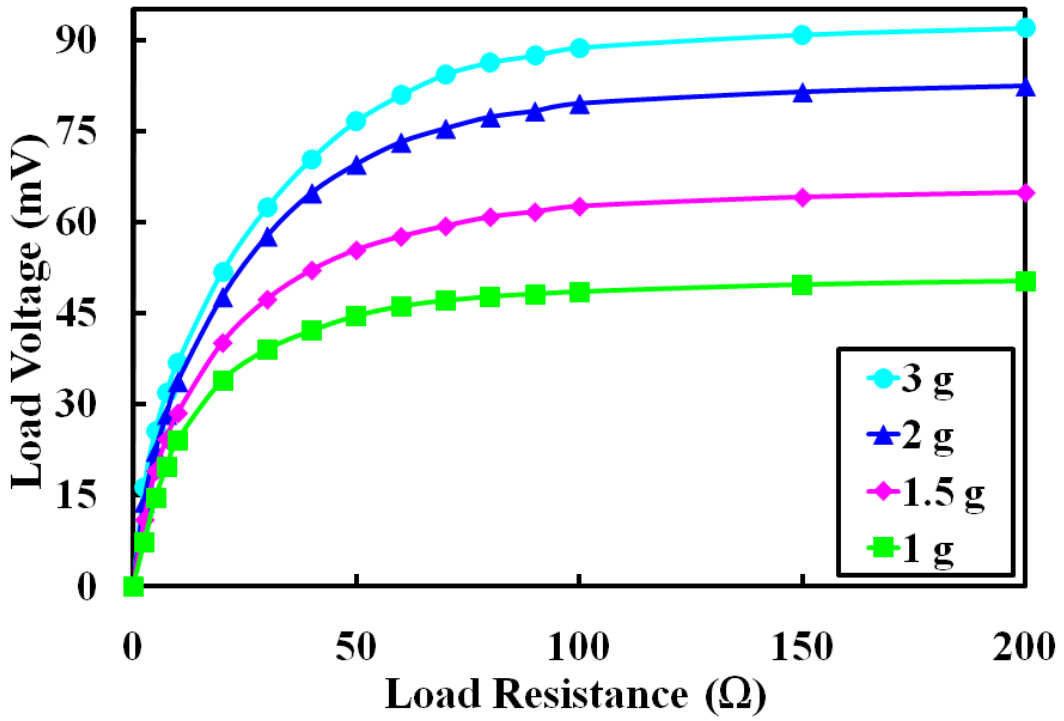

Figure 4.18: Load voltage at resonance versus load resistance.

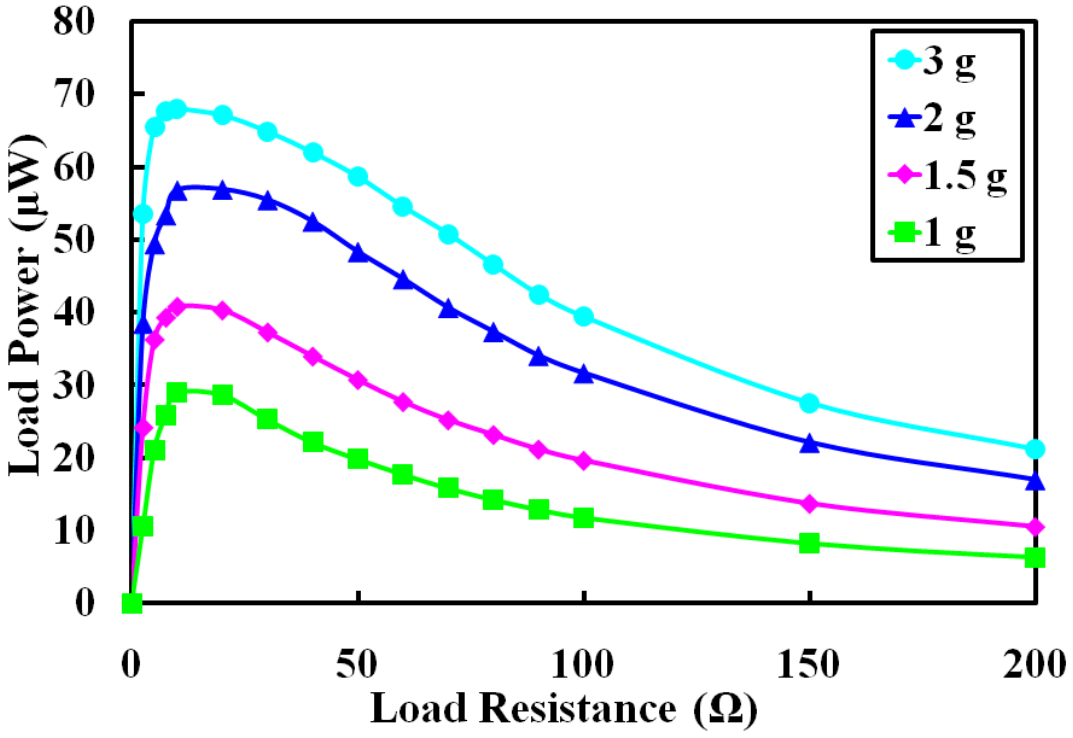

Figure 4.19: Load power at resonance versus load resistance.

4.4.2 Characterization of the prototype under narrow band random excitation

Nonlinear EMEHs exhibit variable resonant frequencies depending on the amplitude of the base excitation. The nonlinear EMEHs are thus more suitable to harvest mechanical energy from narrow band random vibrations where the amplitude and frequency of the excitation varies randomly. A linear EMEH when subjected to random vibration will act like a filter and will resonate at its natural frequency. However a nonlinear EMEH will be able to harvest the energy over a wider frequency range depending on the characteristics of the nonlinear spring and the randomness of the amplitude of the random base excitation.

For characterization of the device under narrow band random vibration, an NI DAQ card (NI USB-6212) and LabVIEW Signal Express (Sound and Vibration assistance) is used to generate a narrow band random signal for the vibration shaker. The program steps used in LabVIEW Signal Express are shown in Figure 4.20. A Gaussian white noise signal is passed through a bandpass filter to obtain the narrow band signal, which with the DAQ card and the amplifier is fed to the vibration shaker. Figure 4.21 shows the schematic of the program steps in LabVIEW Signal Express used for the SD analysis of the signals from the accelerometer and the EMEH. The DAQmx module represents the DAQ card and acquires the analog input signals from the accelerometer and from the EMEH; these signals are further processed including spectral density analysis and statistical steps using Signal Express. The scaling and conversion tool converts the analog voltage signal of the accelerometer into the corresponding acceleration. In Signal Express, the analog signal generation tool uses a sampling rate of 10 kS/s and a block size (samples) of 10 k, and in the bandpass filter tool a Butterworth filter is used to produce a band limited random signal. In the SD step, a Hanning window and RMS averaging are used to compute the SDs of the load voltage and of the acceleration.

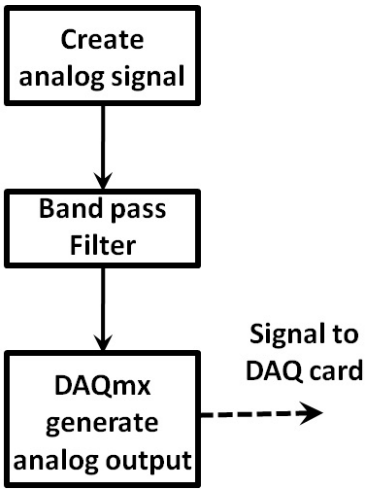

Figure 4.20: Schematic of narrow band random signal generation in LabVIEW Signal Express.

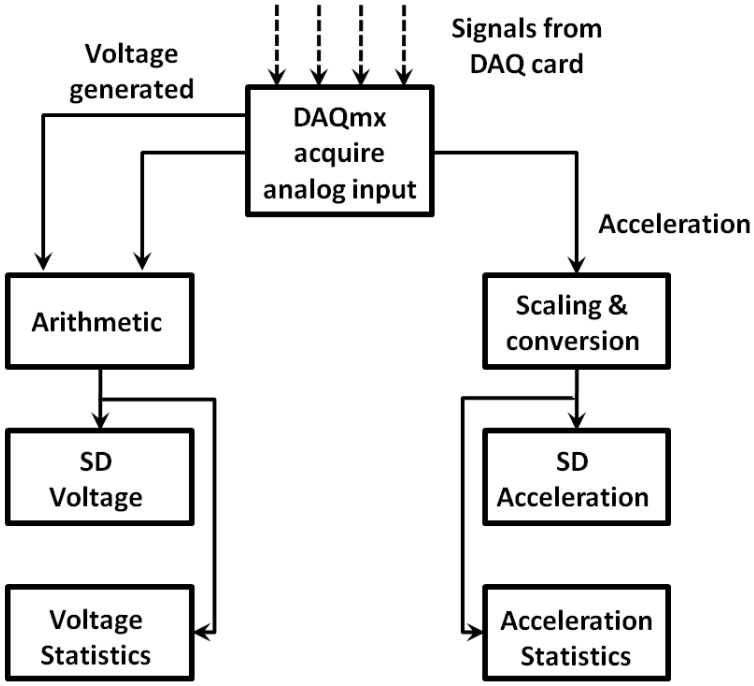

Figure 4.21: Schematic of spectral density analysis in LabVIEW Signal Express.

The device is subjected to low levels (0.05 to 0.1 g) of narrow band (5 to 150 Hz) random excitation; the acceleration measurements are shown in Figure 4.22. The SD values of 1.48×10^{-5}, 2.67×10^{-5} and 4.23×10^{-5} g^2/Hz correspond to the average of the individual acceleration SD over a band from 5 to 150 Hz. The excitation levels are not strong enough to invoke the nonlinear effects of the PDMS membrane as indicated from the response (SD of the load voltage) in

Figure 4.23. The resonant frequency is stable (not changing with increased base excitation), showing the linear response of the device under these low base acceleration levels.

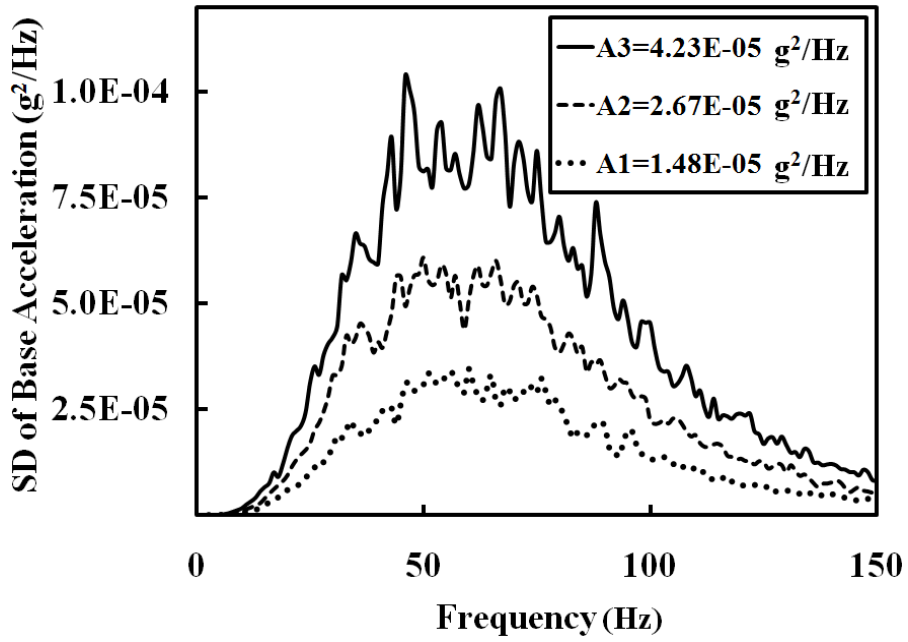

Figure 4.22: SD of low base acceleration for a narrowband random vibration from 5 to 150 Hz.

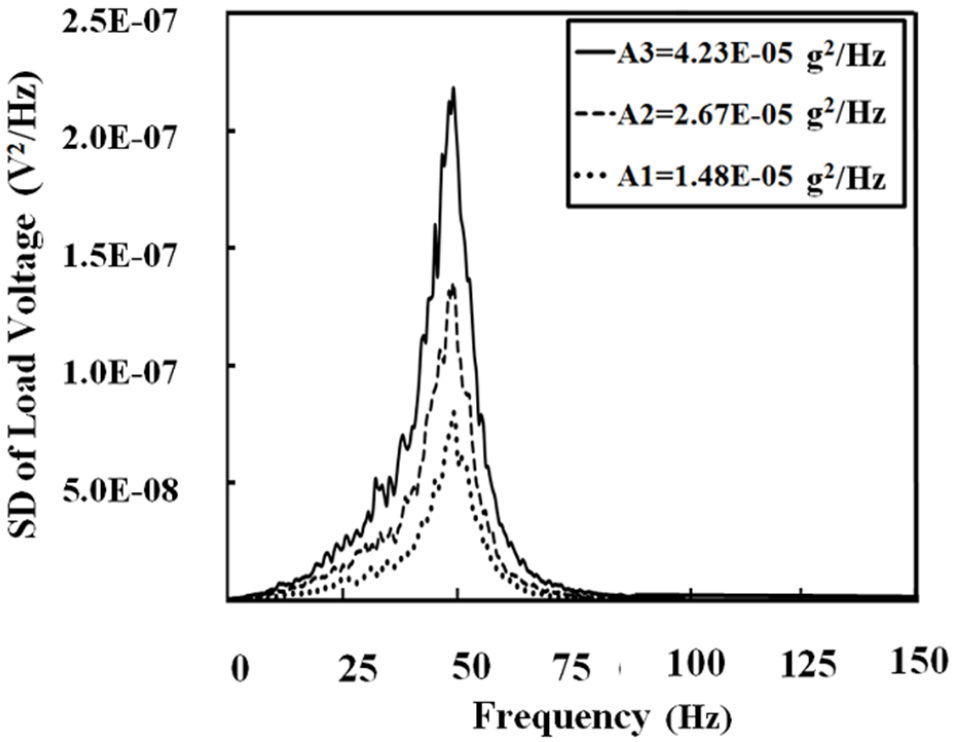

Figure 4.23: SD of the load voltage for a 100 Ω load at low levels of narrowband (5 to 150 Hz) random excitation.

The SD of different levels of narrow band (50 to 150 Hz) random acceleration, under which the device is further tested, is shown in Figure 4.24. The SD values of 0.00265, 0.00544 and 0.0128 g^2/Hz correspond to the average of the individual acceleration SD over a band from 50 to 150 Hz; here, the excitation levels (0.8 to 2.0 g) are high enough to invoke the nonlinear effects of the PDMS membrane.

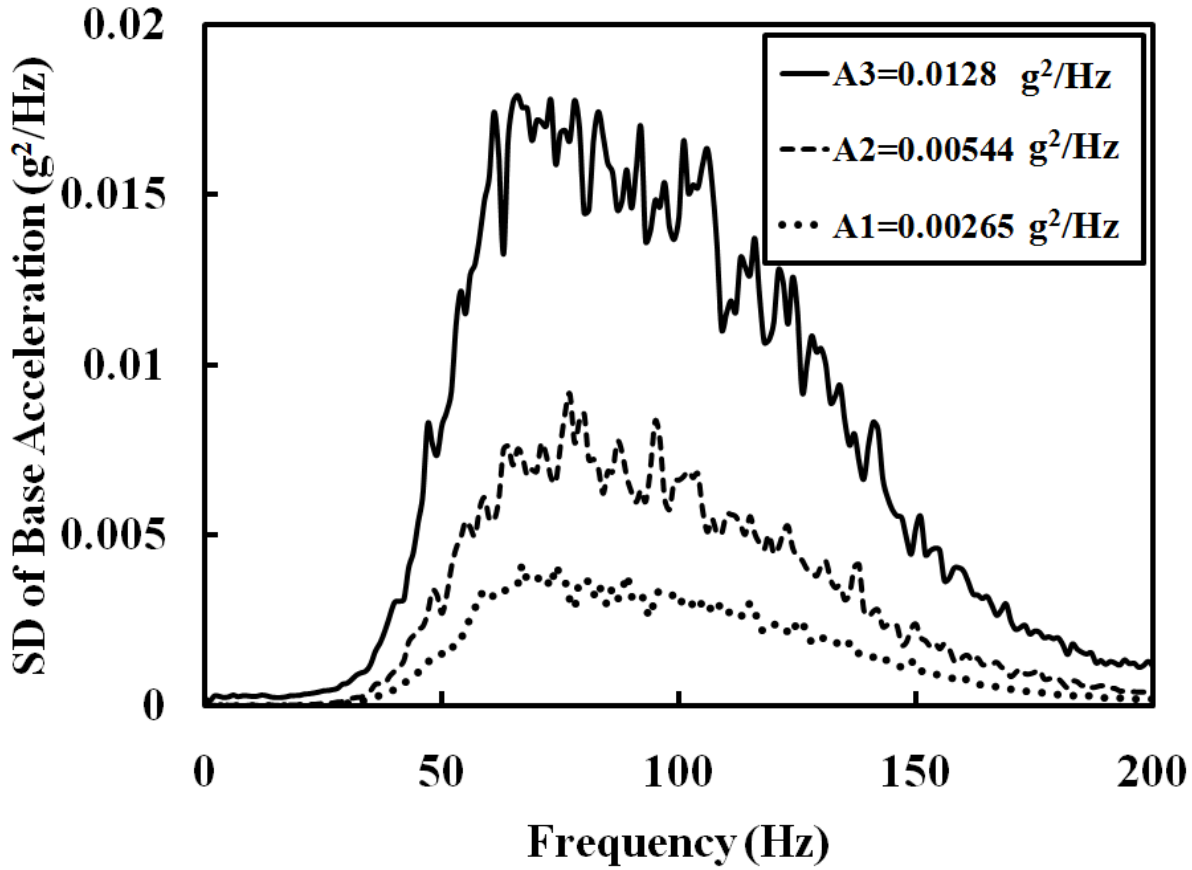

Figure 4.24: SD of base acceleration for a narrowband from 50 to 150 Hz.

Figure 4.25 shows the SD of the voltage delivered to a 100 Ω load resistance at average acceleration SD levels of 0.00265, 0.00544 and 0.0128 g^2/Hz respectively. The maximum value of the load voltage spectrum increases with increasing strength of the acceleration SD, moreover, the central frequency of the load voltage SD is shifting towards higher frequencies and this is consistent with an increase in membrane stiffness (resonant frequency) of the device when it is subjected to stronger excitation levels. At relatively stronger base acceleration levels the large

relative displacement of the mass invokes the nonlinear spring stiffening, the EMEH operates in the nonlinear regime where the resonant frequency increases with increasing base acceleration. Moreover in comparison to the load voltage SD under low levels of acceleration (Figure 4.23), at high levels of base acceleration, the SD of the load voltage is broader, showing an increase in the bandwidth of the device.

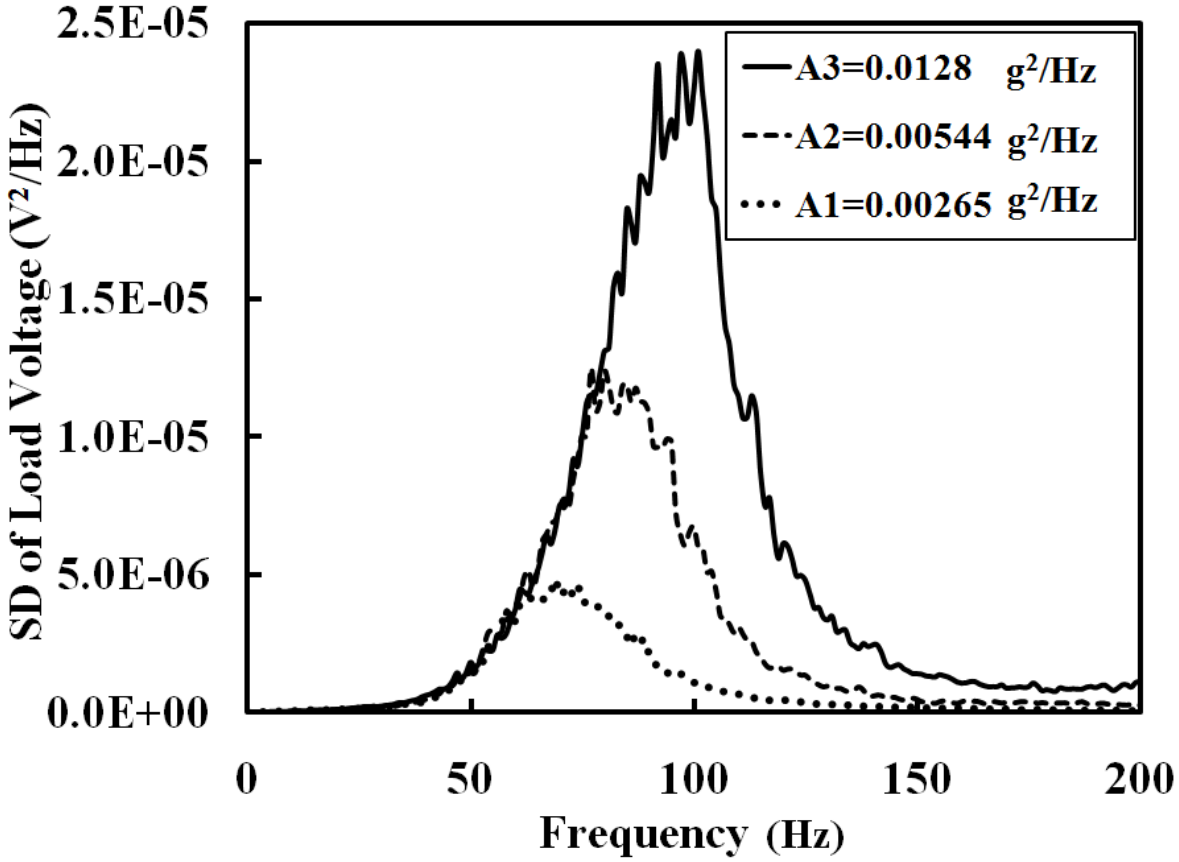

Figure 4.25: SD of the load voltage for a 100 Ω load at different narrowband (50 to 150 Hz) random excitation levels.

The SD of the load voltage at different SD levels of acceleration, over a frequency range of 50 to 400 Hz is shown in Figure 4.26. The acceleration levels of narrow band (50 to 400 Hz) random excitation to which the harvester is subjected (Figure 4.27) are kept high enough (0.8 to 1.5 g) to drive the device in the nonlinear regime. The response of the device is approximately the same as for base excitations over a frequency range of 50 to 150 Hz (Figure 4.25).

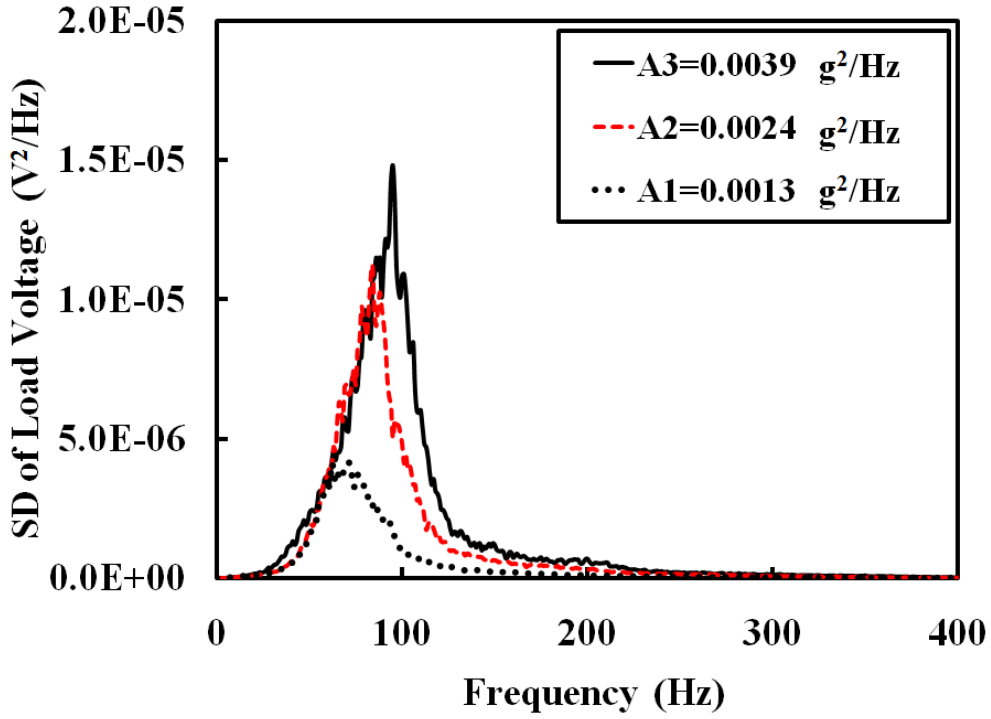

Figure 4.26: SD of the load voltage for a 100 Ω load at different narrowband (50 to 400 Hz) random excitation levels.

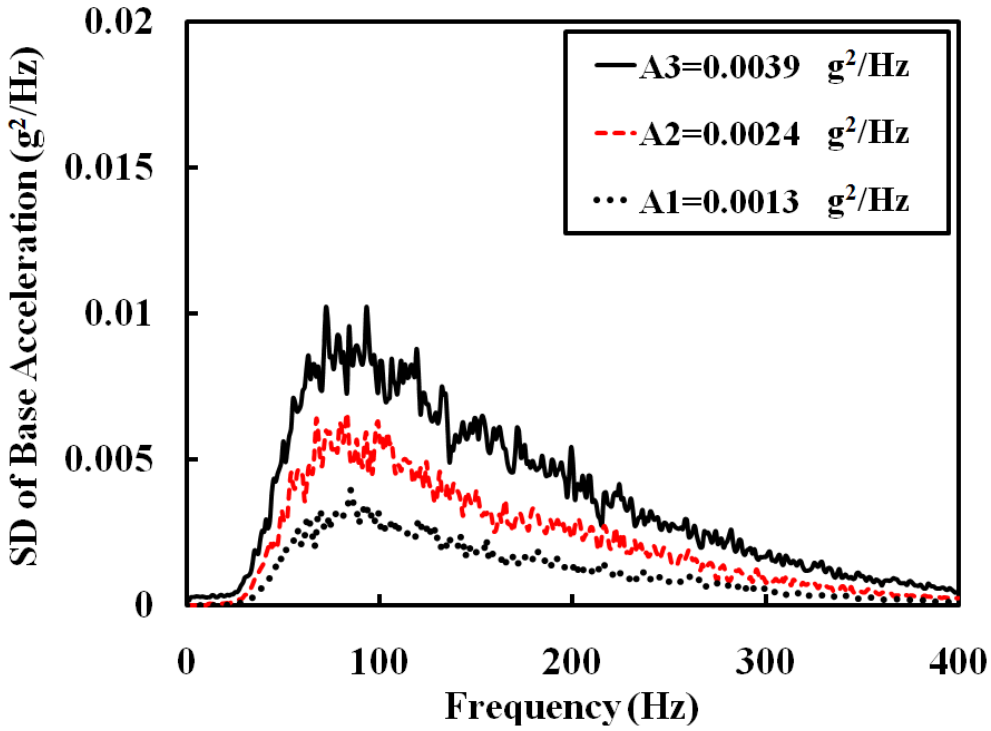

Figure 4.27: SD of base acceleration for a narrowband from 50 to 400 Hz.

The central (resonant) frequency of the SD of the load voltage which depends on the tensile stresses in the PDMS membrane is bounded by the ultimate tensile strength (maximum permissible tensile stress) of the membrane. The resonant frequency of the harvester will not further increase when the membrane is stretched or stressed to its maximum, as already observed in Figure 4.15, where the achieved resonant frequencies seemed to saturate near 110 Hz at high acceleration levels. However, the maximum stress (ultimate tensile strength) of the PDMS membrane depends on the thickness of the membrane [160]. Table 4.4 shows the ultimate tensile strength values for various membrane thicknesses. Thinner membranes can be stressed over a broader range and thus a relatively wider band of resonant frequencies can be obtained in the nonlinear regime. For example, decreasing the thickness of the PDMS membrane in the investigated EMEH from 200 μm to 30 μm, is expected to increase the range of the resonant frequencies in the nonlinear regime by approximately fourfold.

Table 4.4: Ultimate tensile strength of PDMS membrane [160].

PDMS membrane thickness (μm)	**Ultimate tensile strength** (MPa)
250	25
130	75
50	85
30	100

5 Modeling and simulation of linear and nonlinear MEMS scale electromagnetic energy harvesters for random vibration environments[4]

5.1 Introduction

The growing demand for autonomous and self powered sensors [161] has resulted in immense interest in harvesting energy from the environment. Like other energy harvesting techniques [161,162] harvesting energy from ambient mechanical vibrations [163] with piezoelectric [164], electrostatic [165] and electromagnetic [166] energy harvesters has gained increasing interest in the last few years. Mechanical vibrations are abundant in the environment in the form of machine vibration [72] and the vibration of household and office appliances [73]. These sources have sufficient vibration levels to generate power to run ultra low power (ULP) sensors [74] and ULP electronic circuitry; however, the frequency content of these vibrations is spread over a wide frequency range.

Most of the developed linear and nonlinear resonant energy harvesters have been tested and characterized under a harmonic excitation, however, real environmental vibrations do not lead to single frequency excitation but the vibrational energy content is rather distributed over a broad band of frequencies and is random in nature. The power spectral density (PSD) of acceleration along the tangential direction of a car tire at a speed of 50 km/h, for example, has a rich energy content in a broad band from 5 Hz to 1 kHz [140]. The vibration of a car driven on a highway at 65 mph is in a broadband that ranges from 1 Hz to 500 Hz [141]. The vibration levels of household appliances reported in [142] also cover a broad band from 1 Hz to 500 Hz.

The models developed to predict the performance of linear resonant energy harvesters under harmonic excitation [92, 93, 97, 98, 132, 167, 168] are not suitable to estimate the performance of the same energy harvesters when subjected to the narrow or broad band of

[4] A version of this chapter has been submitted for publication. Farid Khan, Farrokh Sassani and Boris Stoeber "Modeling and simulation of linear and nonlinear MEMS scale electromagnetic energy harvesters for random vibration environments", Submission date: Feb. 2011.

random excitation. A model for piezoelectric energy harvesters under broadband random vibration has been developed by [169]; where they assume the ambient base excitation as a stationary Gaussian white noise with constant spectral density (SD) over the considered frequency range. The circuit simulator, a simulation program with integrated circuit emphasis (SPICE) is used in [170, 171] to study an energy harvester under broadband random vibrations. With the same SPICE technique an electrostatic energy harvester has been simulated for input acceleration spectral densities of $5x10^{-5}$ and $5x10^{-4}$ g^2/Hz [170]. A two-port transducer model developed for performance tracking of linear electromechanical energy harvesters under random broadband excitation [172] has been extended for the application of linear and non-linear piezoelectric and electrostatic harvesters excited by broadband and narrow band random vibrations [173]. The simulation of the harvester output power, proof mass displacement, and optimum load has been performed under broadband Gaussian white noise and band limited noise excitation. The author has suggested a mapping method to extend the model application to electromagnetic energy harvesters.

This chapter presents the analytical modeling and simulation results for linear and nonlinear resonant electromagnetic energy harvesters (EMEHs) under broadband and narrow band excitations. The models are parameterized such that they are applicable to all types of linear and nonlinear resonant EMEHs. Resonant EMEHs with moving magnet or moving coil architecture, with wound coil or planar coil, and with uniform magnetic field or non-uniform magnetic field configuration, all can be investigated for narrow and broadband random vibrations using these models. The results of this work can be utilized for designing and performance estimation of MEMS scale, linear and nonlinear EMEHs under random vibrations. For broadband and narrow band random excitations, spectral densities (SDs) of load voltage and load power, mean square load voltage and mean power delivered to the load can be predicted for the harvester design parameters, such as, mechanical quality factor, transformation factor and natural frequency. Nonlinear harvesters with only spring nonlinearity and with both spring and damping nonlinearity have been modeled using the method of statistical linearization. These nonlinear models are useful in investigating the effects of mechanical nonlinearity on the performance and bandwidth of the harvesters, when they are subjected to random vibrations.

5.2 Modeling

The EMEHs are seismic or inertial devices consisting of the inertial mass *m* being a magnet or a proof mass and a suspension with the restoring spring force $s(z)$ to support the magnet or the coil. During operation the motion of the inertial mass is damped by a damping force $d(\dot{z})$ that arises due to mechanical damping (air, material and support damping) and electrical damping induced when current flows in the coil. The linear and nonlinear EMEHs can be modeled as single degree of freedom, spring-mass-damper systems with base excitation as shown in Figure 5.1.

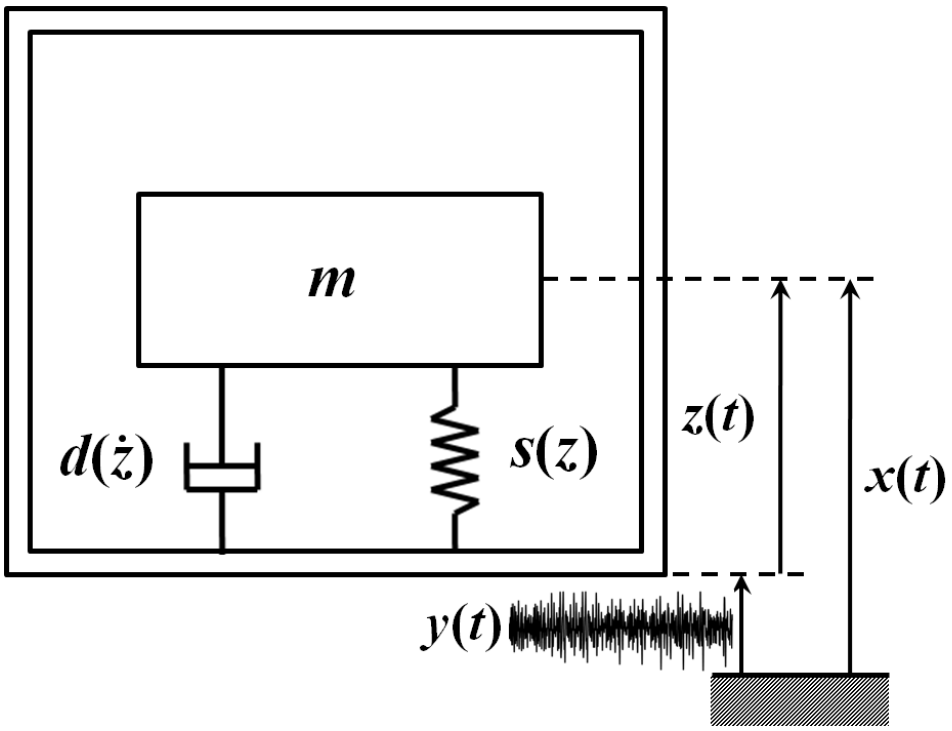

Figure 5.1: Lumped parameter model of an inertial electromagnetic energy harvester.

For an excitation $\ddot{y}(t)$, the general form of the equation of motion for an inertial EMEH

$$m\ddot{z} + d(\dot{z}) + s(z) = -m\ddot{y}, \qquad (5.1)$$

depends on the relative acceleration $\ddot{z}(t)$, relative velocity $\dot{z}(t)$ and relative displacement $z(t)$ between the permanent magnet and the coil. The expressions for the damping force $d(\dot{z})$ and the

spring force $s(z)$ are modeled according to the physical nature of the damping and stiffness present in the harvester, that is, whether these are linear or nonlinear for the operational excitation conditions. Depending upon the architecture and design of the EMEH, and the excitation conditions, both damping force and spring force can be linear or one of these or both can be nonlinear. The behaviour of a linear EMEH (both $d(\dot{z})$ and $s(z)$ are linear) and a nonlinear EMEH (one or both $d(\dot{z})$ and $s(z)$ are nonlinear) is different and requires separate models to investigate the performance under broadband or narrow band excitations.

5.2.1 Harvester with linear stiffness and linear damping

In linear EMEHs the damping force $d(\dot{z}) = b_T \dot{z}$ and the spring force $s(z) = kz$ are represented using the linear total damping coefficient $b_T = b_m + b_e$ and the linear spring stiffness k, respectively. The mechanical damping coefficient b_m and the electrical damping coefficient b_e contribute to the total damping of the harvester. The equation of motion (5.1), for linear EMEHs reduces to

$$m\ddot{z} + b_T \dot{z} + kz = -m\ddot{y}, \qquad (5.2)$$

or

$$\ddot{z} + 2\zeta_T \omega_n \dot{z} + \omega_n^2 z = -\ddot{y}, \qquad (5.3)$$

which can be written in the form

$$\frac{\mathrm{d}}{\mathrm{dt}} \dot{z} + 2\zeta_T \omega_n \dot{z} + \omega_n^2 \int \dot{z}\, \mathrm{dt} = -\ddot{y} \qquad (5.4)$$

expressed in terms of the relative velocity $\dot{z}(t)$, the natural frequency ω_n and the total damping ratio ζ_T of the system, the complex frequency response of the system

$$H(i\omega) = \frac{U}{A} = \frac{-1}{i\omega + 2\zeta_T \omega_n + \omega_n^2 / i\omega} = \frac{-i\omega}{-\omega^2 + 2\zeta_T \omega_n \omega i + \omega_n^2} = \frac{\omega}{(\omega_n^2 - \omega^2)i - 2\zeta_T \omega_n \omega} \qquad (5.5)$$

is obtained using Fourier analysis by letting $\ddot{y}(t) = Ae^{i\omega t}$ and $\dot{z}(t) = Ue^{i\omega t}$ in equation (5.4).

The magnitude of the complex frequency response

$$\left|H(i\omega)\right| = \frac{\left(\omega/\omega_n\right)}{\omega_n\sqrt{\left[1-\left(\omega/\omega_n\right)^2\right]^2+\left[2\zeta_T\left(\omega/\omega_n\right)\right]^2}} \qquad (5.6)$$

and the spectral density (SD) of the base acceleration $S_A(\omega)$ yield the SD of the relative velocity

$$S_U(\omega) = \left|H(i\omega)\right|^2 S_A(\omega). \qquad (5.7)$$

The open-circuit voltage induced in EMEHs [132]

$$V_G(t) = G\dot{z}(t) \qquad (5.8)$$

across the coil is directly proportional to the transformation factor *G*. The transformation factor *G* describes the coupling between the mechanical and electrical energy domains of the EMEH and greatly influences the energy conversion between these two domains. For EMEHs that have a uniform magnetic field perpendicular to the coil displacement [92], the transformation factor

$$G = BL \qquad (5.9)$$

results from the uniform magnetic flux density *B* and the effective length of the coil *L*.

In EMEHs with non-uniform magnetic field configuration [132], where the coil moves in the magnetic field direction, the transformation factor

$$G = S\frac{\mathrm{d}\,B_z}{\mathrm{d}\,z} \qquad (5.10)$$

depends on the magnetic flux gradient $\frac{\mathrm{d}\,B_z}{\mathrm{d}\,z}$ of the normal component of the magnetic flux density B_z and the area sum *S* of the coil turns.

An EMEH with the coil resistance R_C delivers a voltage of

$$V_L(t) = \left(\frac{R_L}{R_L + R_C} \right) G\dot{z}(t) \qquad (5.11)$$

to the load resistance R_L connected to the device. Using Fourier analysis, the load voltage in the frequency domain

$$V_L(\omega) = \left(\frac{R_L}{R_L + R_C} \right) G\left|H(i\omega)\right| A(\omega) \qquad (5.12)$$

contains the complex frequency response

$$\left|H_V(i\omega)\right| = \left(\frac{R_L}{R_L + R_C} \right) G\left|H(i\omega)\right|. \qquad (5.13)$$

When the EMEH is subjected to a broadband random vibration with the SD S_A of the base acceleration, the SD of the load voltage

$$S_{V_L}(\omega) = \left|H_V(i\omega)\right|^2 S_A(\omega) \qquad (5.14)$$

can be expressed in the parameters of the system as

$$S_{V_L}(\omega) = \left(\frac{R_L}{R_L + R_C} \right)^2 G^2 \frac{\left(\omega / \omega_n^2 \right)^2}{\left[1 - \left(\omega / \omega_n \right)^2 \right]^2 + \left[2\zeta_T \left(\omega / \omega_n \right) \right]^2} S_A(\omega). \qquad (5.15)$$

If the excitation is a stationary Gaussian random process with zero mean, the response of the system will also be stationary Gaussian with a zero mean [174]. The mean square value of the load voltage

$$\overline{V_L^2} = \int_{-\infty}^{\infty} S_{V_L}(\omega) d\omega = \int_{-\infty}^{\infty} \left|H_V(i\omega)\right|^2 S_A(\omega) d\omega = \left(\frac{R_L}{R_L + R_C} \right)^2 G^2 \int_{-\infty}^{\infty} \left|H(i\omega)\right|^2 S_A(\omega) d\omega \qquad (5.16)$$

yields the average power delivered into the load resistance [173]

$$P_L = \frac{\overline{V_L^2}}{R_L} = \frac{1}{R_L}\int_{-\infty}^{\infty} S_{V_L}(\omega)d\omega = \int_{-\infty}^{\infty} S_{P_L}(\omega)d\omega = \frac{1}{R_L}\left(\frac{R_L}{R_L+R_C}\right)^2 G^2 \int_{-\infty}^{\infty} |H(i\omega)|^2 S_A(\omega)d\omega .$$

(5.17)

Equation (5.17) yields the SD of the power delivered to the load

$$S_{P_L}(\omega) = \frac{1}{R_L} S_{V_L}(\omega) = \frac{1}{R_L}\left(\frac{R_L}{R_L+R_C}\right)^2 G^2 \frac{\left(\omega/\omega_n^2\right)^2}{\left[1-\left(\omega/\omega_n\right)^2\right]^2 + \left[2\zeta_T\left(\omega/\omega_n\right)\right]^2} S_A(\omega). \quad (5.18)$$

Broadband white noise excitation

When the excitation is a stationary Gaussian white noise process, the SD of the acceleration $S_A(\omega)$ is flat and independent of frequency. Substituting the constant $S_A(\omega) = S_0$ in equations (5.16) and (5.17) yields the mean square load voltage

$$\overline{V_L^2} = S_0\left(\frac{R_L}{R_L+R_C}\right)^2 G^2 \int_{-\infty}^{\infty} |H(i\omega)|^2 d\omega \quad (5.19)$$

and the mean power delivered to the load

$$P_L = \frac{S_0}{R_L}\left(\frac{R_L}{R_L+R_C}\right)^2 G^2 \int_{-\infty}^{\infty} |H(i\omega)|^2 d\omega . \quad (5.20)$$

The integral in equations (5.19) and (5.20) is obtained by the method [175] described in Appendix A, that results in

$$\overline{V_L^2} = S_0\left(\frac{R_L}{R_L+R_C}\right)^2 G^2 \frac{\pi}{2\zeta_T\omega_n}, \quad (5.21)$$

and

$$P_L = \frac{S_0}{R_L}\left(\frac{R_L}{R_L + R_C}\right)^2 G^2 \frac{\pi}{2\zeta_T \omega_n}. \qquad (5.22)$$

The total damping ratio $\zeta_T = \zeta_m + \zeta_e$ consists of the mechanical damping ratio

$$\zeta_m = \frac{1}{2Q_m} \qquad (5.23)$$

that is expressed in terms of the mechanical quality factor Q_m of the EMEH, and the electrical damping ratio

$$\zeta_e = \frac{G^2}{2m\omega_n(R_L + R_C)} \qquad (5.24)$$

that can be obtained from the equivalent electrical circuit for the EMEH as described in [132].

By substituting for the total damping ratio ζ_T, using (5.23) and (5.24), equation (5.22) becomes

$$P_L = m\pi S_0 \frac{R_L}{R_L + R_C} \frac{G^2 Q_m}{m\omega_n(R_L + R_C) + G^2 Q_m}, \qquad (5.25)$$

which is more suitable to derive the optimum power condition for impedance matching. Optimizing equation (5.25) with respect to R_L yields the condition for optimum power transfer to the load as

$$R_{L,opt} = \sqrt{R_C^2 + \frac{G^2 Q_m R_C}{m\omega_n}} = \sqrt{R_C^2 + \frac{G^2 R_C}{b_m}}. \qquad (5.26)$$

Equation (5.26) reveals that the optimum load, when an EMEH is subjected to random vibration is different from the optimum load $R_{L,opt} = R_C + \frac{G^2}{b_m}$ when it is subjected to sinusoidal vibration [132].

The product $G^2 Q_m$ in equation (5.25) is known as the figure of merit for energy harvesters driven by random vibrations [173]. Increasing the product $G^2 Q_m$ for an EMEH will increase the mean power delivered to the load. The mechanical quality factor Q_m can be increased by packaging the device in vacuum [139] or by incorporating air passages in the device design that allow flow paths for the trapped air during operation to reduce damping [112]. For EMEHs with uniform magnetic field configuration the transformation factor G can be increased by increasing the magnetic flux density B and/or by increasing the effective length L of the coil within the constrained footprint of the device. For EMEHs with non-uniform magnetic field configuration, the increase in the transformation factor G requires increasing the magnetic flux gradient $\frac{\mathrm{d}B_z}{\mathrm{d}z}$ of the normal component of the magnetic flux density B_z and/or by increasing the area sum S of the turns of the coil within the constrained footprint of the device. However, the increase in the number of coil turns also increases the coil resistance leading to increased electrical losses. Therefore, increasing the magnetic flux density B in uniform magnetic field configuration devices, and the magnetic flux gradient in non-uniform magnetic field devices is a preferred method for increasing the transformation factor.

Values of the mechanical quality factor Q_m and of the transformation factor G for various devices reported in literature are summarized in Table 5.1. The mechanical quality factor for EMEHs ranges from 5.8 to 258.7. Due to their larger number of coil turns, wound coil type EMEHs exhibit higher values for the transformation factor that contribute to the higher values of the product of merit $G^2 Q_m$ in comparison to planar coil type EMEHs.

Table 5.1: Parameters of electromagnetic energy harvesters.

Coil type	***m*** (kg)	$F_{resonant}$ (Hz)	R_C (Ω)	R_L (Ω)	**Mech. quality factor** Q_m	**Elect. quality factor** Q_e	**Total quality factor** Q_T	***G*** (Tm)	G^2Q_m (T^2m^2)	**Ref.**
Wound	42.8 x10^{-3}	13.11	18		117.52	6.53[a]		3.118[b]	1142.52	[177]
	25 x10^{-3}	84	3.65			329.88[a]		0.3821[b]		[177]
	3.8 x10^{-3}	94.8	1.2	2.7	258.7[c]	24.61[a]		0.3322[b]	28.55	[91]
	0.44 x10^{-3}	350	93	100	216	1120	181	0.41[b]	36.31	[119]
	0.028 x10^{-3}	9.5k		100			164			[119]
		52.1	100	200	232	243	119			[79]
	1.02 x10^{-3}	50	2323			210-60		6.04		[85]
			1530					4.43		[85]
	0.028x10^{-3}	8.08k	112		26					[88]
		208			121.8					[90]
		106			141.3					[90]
Planar	4.036 x10^{-3}	24.8	100	100	23.36					[97]
	0.0304 x10^{-3}	100	2	4	16.2[c]	403.23[a]	7.94[c]	0.017[b]	0.005	[81]
	0.014x10^{-3}	9.837k	55		164					[88]
	0.54x10^{-3}	60	110	110	48.5[c]	2345.33[a]		0.0691[b]	0.232	[88]
			31	39	136		120	1.5x10^{-3}	0.0003	[128]
					221[d]		207[d]			[128]
	0.93x10^{-3}	371	7.5	100	5.835		5.83[c]	0.075	0.033	[132]

[a]Calculated using equation $Q_e = \frac{1}{2\zeta_e}$

[b]Calculated using equation $G = \sqrt{(R_L + R_C)\frac{2\pi mF}{Q_e}}$

[c]Calculated using equation $Q_m = \frac{1}{2\zeta_m} = \frac{2\pi mF}{b_m}$

[d]Determined from testing in vacuum

For simulation we used the dimensions and parameters (Table 5.2) of our EMEH [132] described in Chapter 2, where the non-uniform magnetic field is caused by two permanent magnets with remanent flux density B_r that are suspended by a planar spring between two identical coils.

Table 5.2: Dimensions and parameters of an EMEH prototype [132].

Description	**Value**
Device size	12 mm X 12 mm X 7 mm
Magnet (NdFeB)	1.2-1.32 T
Mass of each magnet	0.465 g
Coil size	8 mm X 8 mm
Resistance of coil R_C	7.5 Ω
Mechanical quality factor Q_m	5.7
Resonant frequency $F_{resonant}$	371 Hz
Transformation factor G	0.075 Tm

The mean power as a function of load resistance for various values of G^2Q_m is shown in Figure 5.2. The computation was performed for the acceleration SD of $S_A(\omega) = S_0 = 0.01$ g^2/rad/s. The simulation results verify that there is an optimum value for the load resistance for each product of merit (POM) G^2Q_m, moreover, the optimum load resistance increases as the POM is increased. As the POM is increased the curves become increasingly flat beyond the optimum load resistance, which shows that an EMEH with a high POM value is less dependent on the optimum load resistance beyond the optimum operating condition and will perform well even at the load resistance greater than the optimum load resistance. Figure 5.3 shows the dependence of the mean power on the transformation factor as a function of the load resistance. This corresponds to the situation where the mechanical quality factor Q_m for the EMEH remains constant while the transformation factor is varied. The curves in Figure 5.3 are more spiked in comparison to Figure 5.2, where the product G^2Q_m is varied. This indicates that an EMEH becomes more sensitive to load resistance variations when its Q_m is low and only the transformation factor is changed. Further, the optimum load resistance is quite different than the case where the POM is increased.

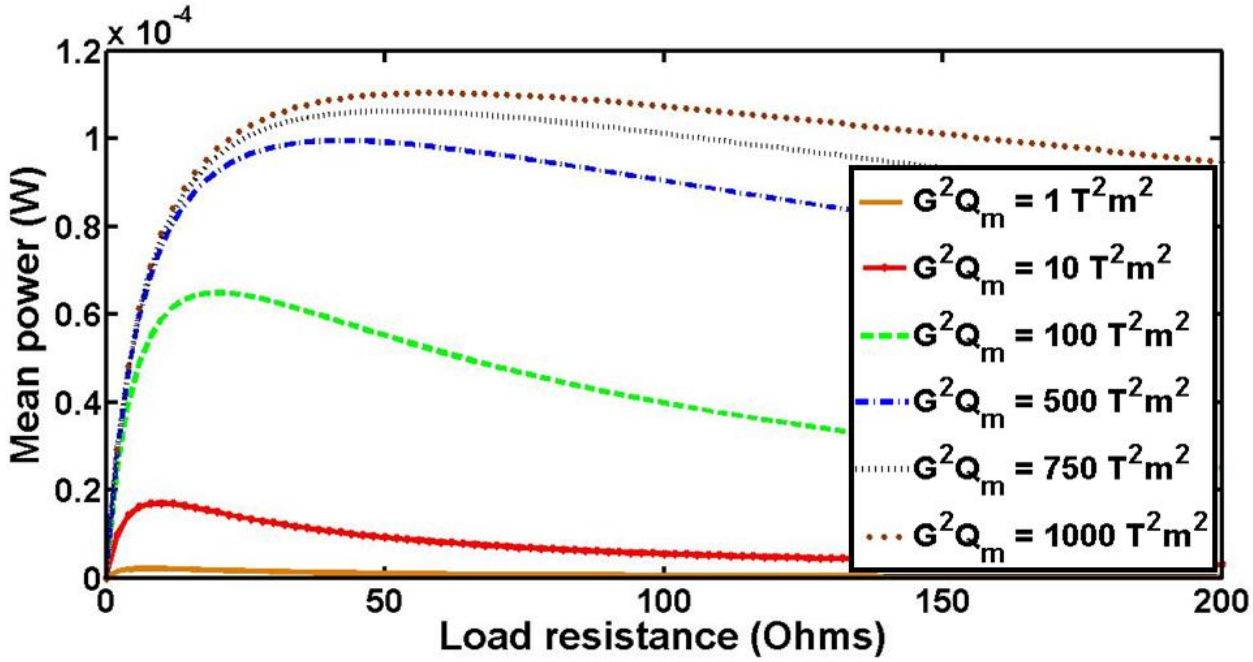

Figure 5.2: Mean power as a function of load resistance for different values of G^2Q_m.

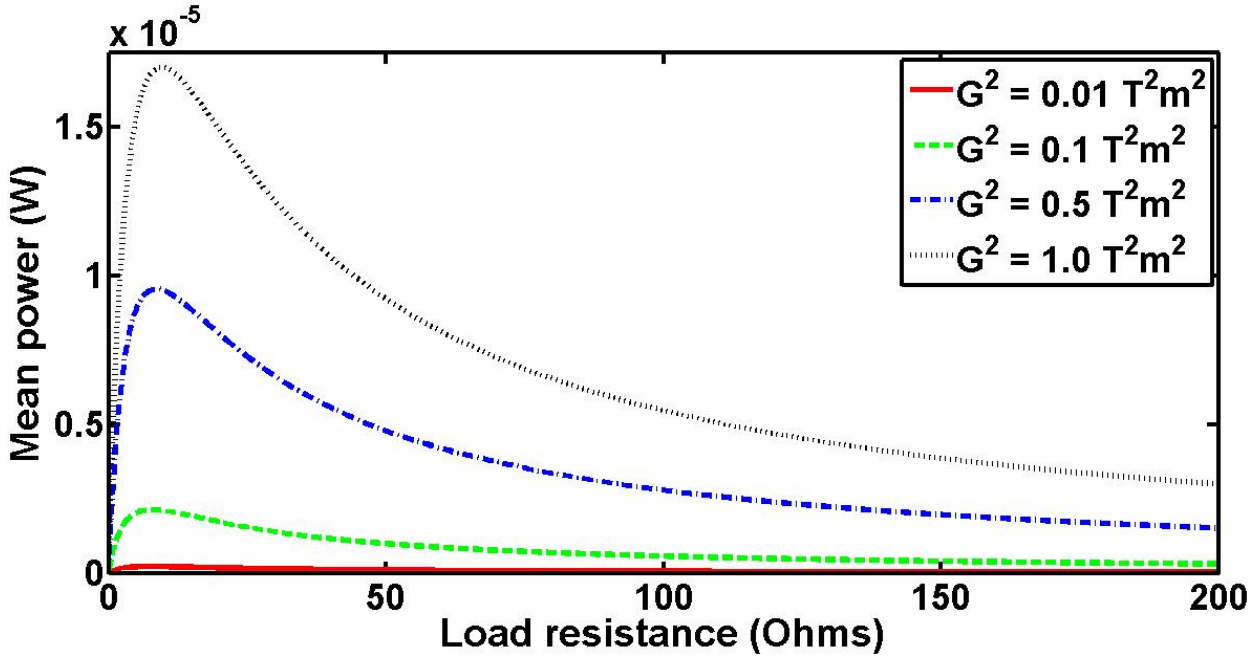

Figure 5.3: Mean power as a function of load resistance for different values of G^2 for Q_m = 5.7.

From equations (5.15), (5.23) and (5.24) the SD of the load voltage and the power for white noise base excitation becomes

$$S_{V_L}(\omega) = \left(\frac{R_L}{R_L + R_C}\right)^2 G^2 S_0 \frac{\left(\omega/\omega_n^2\right)^2}{\left[1-\left(\omega/\omega_n\right)^2\right]^2 + \left[2\zeta_T\left(\omega/\omega_n\right)\right]^2}$$

$$= \left(\frac{R_L}{R_L + R_C}\right)^2 G^2 S_0 \frac{\left(\omega/\omega_n^2\right)^2}{\left[1-\left(\omega/\omega_n\right)^2\right]^2 + \left[\left(\frac{1}{Q_m} + \frac{G^2}{m\omega_n(R_L + R_C)}\right)\left(\omega/\omega_n\right)\right]^2} \qquad (5.27)$$

and

$$S_{P_L}(\omega) = \frac{R_L}{(R_L + R_C)^2} G^2 S_0 \frac{\left(\omega/\omega_n^2\right)^2}{\left[1-\left(\omega/\omega_n\right)^2\right]^2 + \left[\left(\frac{1}{Q_m} + \frac{G^2}{m\omega_n(R_L + R_C)}\right)\left(\omega/\omega_n\right)\right]^2}. \qquad (5.28)$$

The SD of the load voltage as a function of frequency is shown in Figure 5.4 for different values of G^2. The SD of the load voltage shows a significant peak in the vicinity of the natural frequency of the linear EMEH. The EMEH is acting as a mechanical filter, generating power in a limited band that depends on the bandwidth

$$\Delta\omega = 2\zeta_T\omega_n = 2(\zeta_m + \zeta_e)\omega_n = \left(\frac{1}{Q_m} + \frac{G^2}{m\omega_n(R_L + R_C)}\right)\omega_n \qquad (5.29)$$

of the EMEH. A broader bandwidth of the EMEH is preferred in order to convert the vibration energy from a wider band of random excitation. The increase in the transformation factor

contributes to increase the EMEH bandwidth. However, increasing the transformation factor by increasing the number of coil turns within a constrained area is undesirable, as this increases coil resistance which leads to power loss and negatively affects the bandwidth. As seen in Figure 5.2, it is more significant for the EMEH subjected to broadband vibration, to optimize both Q_m and G^2, however, the increase in the mechanical quality factor Q_m adversely affect the bandwidth of the device. This can be compensated by the significant increase in a transformation factor of the harvester.

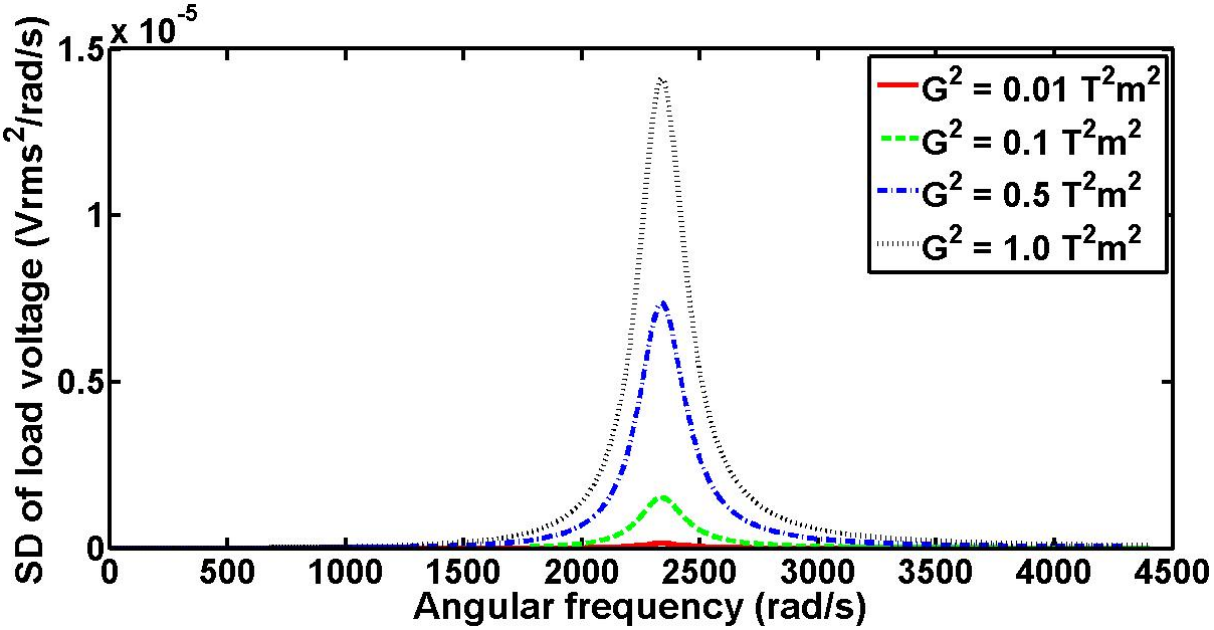

Figure 5.4: SD of the load voltage as a function of frequency for various values of G^2, Q_m = 5.7.

Figure 5.5 shows the bandwidth of a linear EMEH as a function of the load resistance for several values of G^2 and Q_m = 5.7. Energy harvesters with large transformation factor exhibit relatively broader bandwidths that drop sharply as the load resistance is increased. At higher load resistances the contribution due to the transformation factor term in equation (5.29) is minimal and the device bandwidth is controlled by the dominant mechanical quality factor term. However, for EMEHs with small transformation factor, the contribution due to the transformation factor term in equation (5.29) is negligible and the bandwidth becomes independent of the load resistance as evident in Figure 5.5.

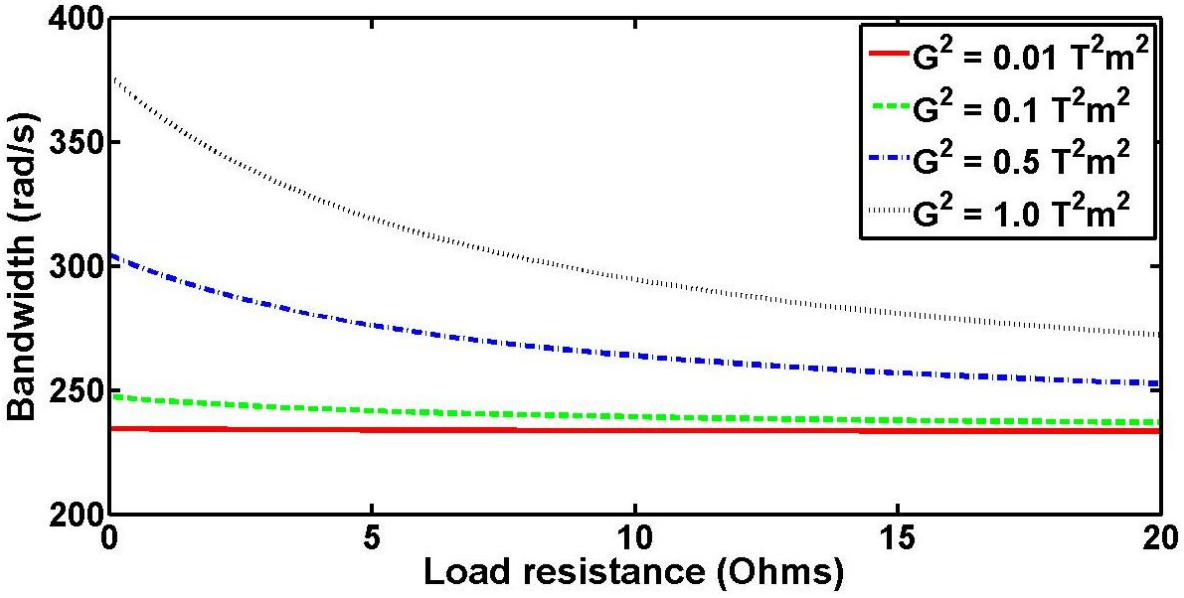

Figure 5.5: Linear EMEH bandwidth as a function of the load resistance for different G^2 and Q_m = 5.7.

The maximum value of the SD of the load voltage

$$S_{V_{L1}}(\omega) = S_{V_L}(\omega = \omega_n) = \frac{R_L^2}{R_L + R_C} \frac{mS_0 G^2 Q_m}{\omega_n (m\omega_n (R_L + R_C) + G^2 Q_m)} \qquad (5.30)$$

occurs at resonance and likewise, the mean power, also depends on the POM. Increasing the POM for the EMEH will lead to an increase in the peak value of the SD of the load voltage.

The SD of the power as a function of frequency and load resistance is shown in Figure 5.6. Similar to the SD of the load voltage it shows a narrow peak in the vicinity of the natural frequency and at the optimum load resistance.

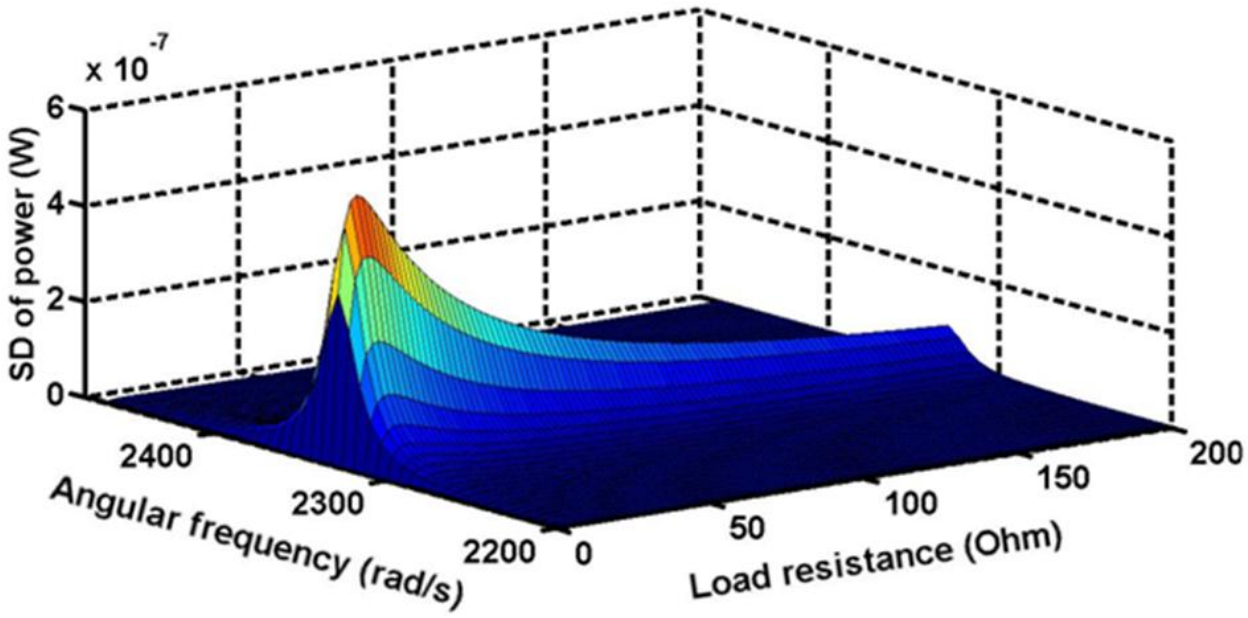

Figure 5.6: SD of the power as a function of frequency and load resistance for Q_m = 5.7 and G^2 = 0.01 T^2m^2.

Band-limited white noise excitation

When the linear EMEH is excited by a stationary band-limited Gaussian white noise $S_A(\omega) = S_0$ between the angular frequency limits ω_1 and ω_2 the power spectral density of the load voltage becomes

$$S_{V_L}(\omega) = \begin{cases} \left(\frac{R_L}{R_L + R_C}\right)^2 G^2 S_0 \frac{\left(\omega/\omega_n^2\right)^2}{\left[1-\left(\omega/\omega_n\right)^2\right]^2 + \left[\left(\frac{1}{Q_m} + \frac{G^2}{m\omega_n(R_L+R_C)}\right)\left(\omega/\omega_n\right)\right]^2} & \omega_1 \le |\omega| \le \omega_2 \\ 0 & \text{elsewhere} \end{cases}. \quad (5.31)$$

The SD of the load voltage for various values of G^2 for an EMEH excited by a band-limited random vibration from ω_1 = 1640 rad/s to ω_2 = 3022 rad/s is shown in Figure 5.7. The SD of the load voltage under band-limited excitation peaks in the vicinity of the natural frequency similar to that of a broadband excitation, except, it is only non-zero over the frequency band of the input excitation.

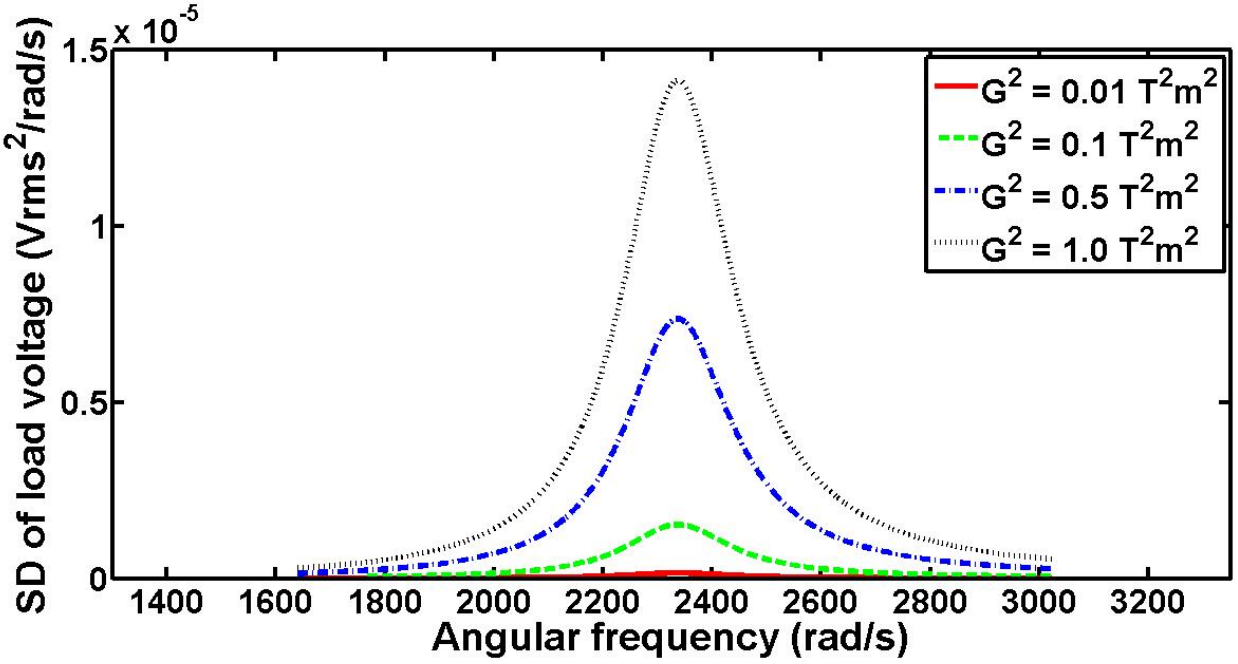

Figure 5.7: SD of the load voltage as a function of frequency for various values of G^2 at band-limited random excitation.

Under band-limited Gaussian white noise random excitation, the mean square value of the load voltage

$$\overline{V_L^2} = \int_{-\omega_2}^{-\omega_1} |H_V(i\omega)|^2 S_A(\omega) d\omega + \int_{\omega_1}^{\omega_2} |H_V(i\omega)|^2 S_A(\omega) d\omega$$

$$= S_o \left[\int_{-\omega_2}^{-\omega_1} |H_V(i\omega)|^2 d\omega + \int_{\omega_1}^{\omega_2} |H_V(i\omega)|^2 d\omega \right] \qquad (5.32)$$

when expressed in terms of the total damping ratio and the frequency ratio

$$\overline{V_L^2} = \left(\frac{R_L}{R_L + R_C} \right)^2 G^2 S_0 \left[\int_{-\omega_2}^{-\omega_1} \frac{\left(\omega / \omega_n^2 \right)^2}{\left[1 - \left(\omega / \omega_n \right)^2 \right]^2 + \left[2\zeta_T \left(\omega / \omega_n \right) \right]^2} d\omega + \int_{\omega_1}^{\omega_2} \frac{\left(\omega / \omega_n^2 \right)^2}{\left[1 - \left(\omega / \omega_n \right)^2 \right]^2 + \left[2\zeta_T \left(\omega / \omega_n \right) \right]^2} d\omega \right] \qquad (5.33)$$

contains incomplete integrals that can be obtained by using the method of partial fraction expansion [175] or can be found with indefinite integral tables (for example by G. Petit Bois, 1961) [176]. Equation (5.33) can be written in a more compact form

$$\overline{V_L^2} = \left(\frac{R_L}{R_L + R_C} \right)^2 \frac{\pi G^2 S_0}{2\zeta_T \omega_n} \left[\Gamma\left(\omega_2 / \omega_n , \zeta_T \right) - \Gamma\left(\omega_1 / \omega_n , \zeta_T \right) \right] \qquad (5.34)$$

where the integral factor Γ [176] can be expressed in terms of the frequency ratio and the total damping ratio as

$$\Gamma\left(\omega / \omega_n , \zeta_T \right) = \frac{1}{\pi} \arctan \frac{2\zeta_T \left(\omega / \omega_n \right)}{1 - \left(\omega / \omega_n \right)^2} - \frac{\zeta_T}{2\pi\sqrt{1-\zeta_T^2}} \ln \frac{1 + \left(\omega / \omega_n \right)^2 + 2\sqrt{1-\zeta_T^2}\left(\omega / \omega_n \right)}{1 + \left(\omega / \omega_n \right)^2 - 2\sqrt{1-\zeta_T^2}\left(\omega / \omega_n \right)} . \qquad (5.35)$$

In equation (5.34) the terms in front of the brackets describe the mean square load voltage (variance) of the harvester due to broadband Gaussian white noise excitation. The integral factor Γ in the brackets is the correction factor when the excitation is band-limited. For broadband Gaussian white noise excitation the value of the integral factor Γ (∞, ζ_T) – Γ (0, ζ_T) is 1, whereas for band-limited excitation it is always less than 1.

For three values of the total damping ratio $\zeta_T = \zeta_m + \zeta_e$, the integral factor Γ is shown in Figure 5.8. The factor Γ increases monotonically as a function of the frequency ratio ω/ω_n with values residing between 0 and 1. Higher values of the mean square load voltage (or correction factor in the brackets) in equation (5.34) require lower values of the total damping factor. The electrical damping ratio ζ_e (or proportionally G^2) needs to be as high as possible for high power generation, therefore for smaller values of the total damping ratio the mechanical quality factor should be increased and the associated reduction in the bandwidth of the device should be compensated by increasing the transformation factor.

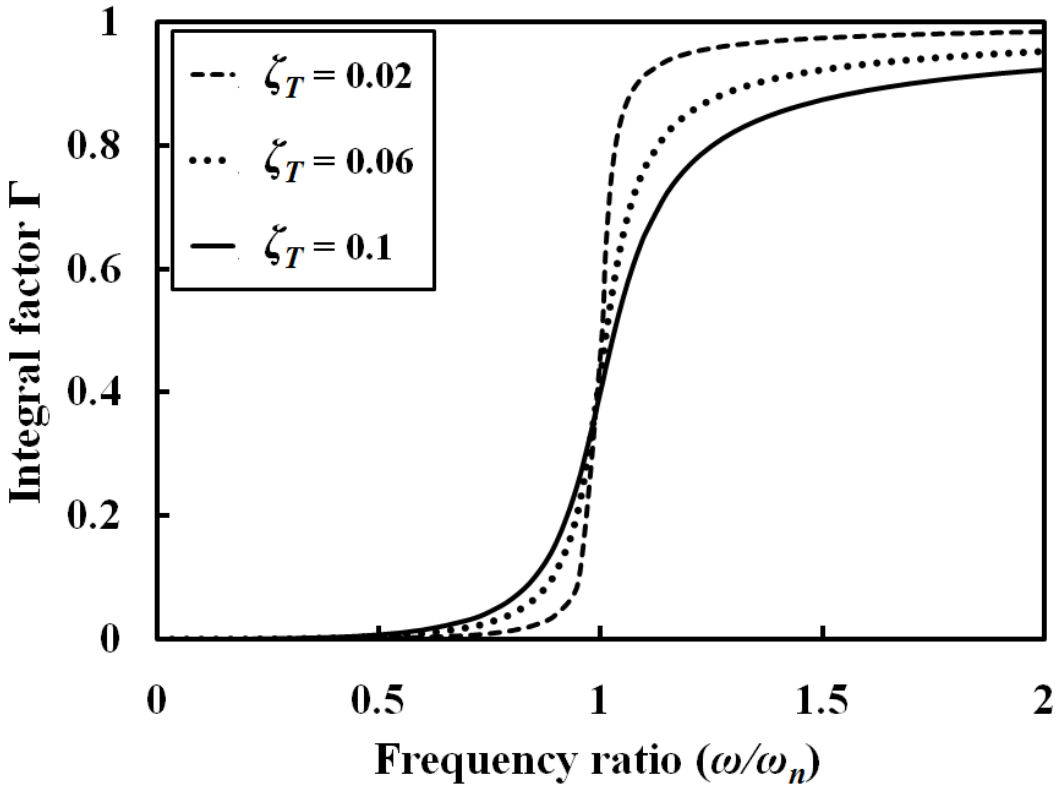

Figure 5.8: Integral factor for mean square load voltage of an EMEH subjected to band-limited Gaussian white noise.

5.2.2 Harvesters with nonlinear stiffness

For a nonlinear EMEH with linear damping force $d(\dot{z}) = b_T \dot{z}$ and nonlinear spring force $s(z) = kz + \eta k N(z)$, the general equation of motion (5.1) of the harvester reduces to

$$m\ddot{z} + b_T \dot{z} + [kz + \eta k N(z)] = -m\ddot{y}, \qquad (5.36)$$

in which, the nonlinear spring force $s(z) = kz + k\eta N(z)$ comprises of a linear stiffness component kz, and the nonlinear stiffness component $k\eta N(z)$. The scaling factor η and the nonlinear function $N(z)$ represent the nonlinearity of the stiffness of the harvester. For an EMEH with a symmetric suspension spring, the potential energy is a symmetric (even) function of *z* and that requires the spring force to be an anti-symmetric polynomial (odd function) of *z*. The nonlinear function $N(z)$ is therefore a polynomial with only odd terms. The scaling factor

η represents the magnitude of the nonlinearity of the spring, for small nonlinearity, η is small, however, for severe nonlinearity, η can be significant.

A nonlinear spring force, that is common in EMEHs with a polymeric membrane as the spring restoring member [112] can be modeled to good approximation by a duffing spring with the nonlinear spring force $s(z) = kz + k\eta z^3$. By substituting for $s(z)$ and expressing in terms of the linear natural frequency ω_n and the total damping ratio ζ_T, equation (5.36), results in

$$\ddot{z} + 2\zeta_T \omega_n \dot{z} + \omega_n^2 (z + \eta z^3) = -\ddot{y}. \qquad (5.37)$$

For a stationary Gaussian random excitation with zero mean, the response of the harvester will also be stationary Gaussian with zero mean. The solution of (5.37) can be obtained by the method of statistical linearization [178-181]. The replacement of the nonlinear component $\omega_n^2 (z + \eta z^3)$ by an equivalent linear component $\omega_{eq}^2 z$ yields the equation of motion of an equivalent linear energy harvester

$$\ddot{z} + 2\zeta_{eq_T} \omega_{eq} \dot{z} + \omega_{eq}^2 z = -\ddot{y}, \qquad (5.38)$$

that depends on the equivalent damping ratio $\zeta_{eq_T} = \frac{\omega_n}{\omega_{eq}} \zeta_T$ and equivalent frequency ω_{eq} of the equivalent linear EMEH. To obtain an approximate solution for the response of the nonlinear harvester, the mean square value, $E[e^2]$ of the error

$$e = \omega_n^2 (z + \eta z^3) - \omega_{eq}^2 z \qquad (5.39)$$

which would be produced by representing the nonlinear harvester by an equivalent linear harvester, must be minimized for the value of the equivalent frequency ω_{eq}, that is, the equation

$$\frac{\mathrm{d}}{\mathrm{d}\,\omega_{eq}^2} E[e^2] = 0 \qquad (5.40)$$

must be satisfied.

By substituting equation (5.39) into (5.40) and then performing differentiation yields the expression for the equivalent frequency

$$\omega_{eq}^2 = \omega_n^2 \frac{E[z.z(1+\eta z^2)]}{E[z^2]} = \omega_n^2 \frac{E[z.z(1+\eta z^2)]}{\sigma_z^2} \qquad (5.41)$$

in terms of the standard deviation σ_z of the relative displacement $z(t)$. Using the method [178], describe in Appendix B reduces equation (5.41) to a much simpler form

$$\omega_{eq}^2 = \omega_n^2 (1 + 3\eta\sigma_z^2) . \qquad (5.42)$$

For a Gaussian white noise random excitation, the variance of the relative displacement

$$\sigma_z^2 = \int_{-\infty}^{\infty} S_z(\omega) d\omega = S_o \int_{-\infty}^{\infty} |H(i\omega)|^2 d\omega \qquad (5.43)$$

can be solved for the complex frequency response

$$H(i\omega) = \frac{-1}{-\omega^2 + i2\zeta_{eq_T}\omega_{eq}\omega + \omega_{eq}^2} \qquad (5.44)$$

with the method [175, 178] described in Appendix A that results in

$$\sigma_z^2 = \frac{\pi S_o}{2\zeta_{eq_T}\omega_{eq}^3} = \frac{\pi S_o}{2\zeta_T \omega_n \omega_{eq}^2} . \qquad (5.45)$$

With equation (5.42), the elimination of the equivalent frequency ω_{eq} from equation (5.45), yields a quadratic equation in σ_z^2

$$3\eta\sigma_z^4 + \sigma_z^2 = \sigma_{z_{Lin}}^2 = \frac{\pi S_o}{2\zeta_T \omega_n^3} \qquad (5.46)$$

where $\sigma_{z_{Lin}}$ is the standard deviation of the relative displacement for the linear case where $\eta = 0$.

By substituting the positive root

$$\sigma_z^2 = \frac{\sqrt{1 + 12\eta\sigma_{z_{Lin}}^2} - 1}{6\eta} \qquad (5.47)$$

of equation (5.46) in equation (5.42) we obtain the equivalent frequency ω_{eq}

$$\omega_{eq}^2 = \omega_n^2 \left[1 + \frac{\sqrt{1 + 12\eta\sigma_{z_{Lin}}^2} - 1}{2} \right] \qquad (5.48)$$

that minimizes the error *e*.

Equations (5.11) and (5.38) yield the equation

$$\frac{1}{G} \frac{R_L + R_C}{R_L} \left[\frac{\mathrm{d}}{\mathrm{dt}} V_L(t) + 2\zeta_{eq_T} \omega_{eq} V_L(t) + \omega_{eq}^2 \int V_L(t)\,\mathrm{dt} \right] = -\ddot{y}(t) \qquad (5.49)$$

which by Fourier analysis results in the frequency response of the harvester

$$H_V(i\omega) = \frac{R_L}{R_L + R_C} G \frac{-i\omega}{-\omega^2 + i2\zeta_{eq_T}\omega_{eq}\omega + \omega_{eq}^2} = \frac{R_L}{R_L + R_C} G \frac{\omega}{(\omega_{eq}^2 - \omega^2)i - 2\zeta_{eq_T}\omega_{eq}\omega}. \qquad (5.50)$$

For a Gaussian white noise base excitation $S_A(\omega) = S_0$, the SD of the load voltage

$$S_{V_L}(\omega) = \left(\frac{R_L}{R_L + R_C} \right)^2 G^2 S_0 \frac{\left(\omega / \omega_{eq}^2 \right)^2}{\left[1 - \left(\omega / \omega_{eq} \right)^2 \right]^2 + \left[2\zeta_{eq_T} \left(\omega / \omega_{eq} \right) \right]^2}$$

$$= \left(\frac{R_L}{R_L + R_C} \right)^2 G^2 S_0 \frac{\left(\omega / \omega_{eq}^2 \right)^2}{\left[1 - \left(\omega / \omega_{eq} \right)^2 \right]^2 + \left[\left(\frac{\omega_n}{\omega_{eq}} \right) \left(\frac{1}{Q_m} + \frac{G^2}{m\omega_n (R_L + R_C)} \right) \left(\omega / \omega_{eq} \right) \right]^2} \qquad (5.51)$$

results in the SD of the power delivered to the load

$$S_{P_L}(\omega) = \frac{R_L}{(R_L + R_C)^2} G^2 S_0 \frac{\left(\omega / \omega_{eq}^2\right)^2}{\left[1 - \left(\omega / \omega_{eq}\right)^2\right]^2 + \left[2\zeta_{eq_T}\left(\omega / \omega_{eq}\right)\right]^2}$$

$$= \frac{R_L}{(R_L + R_C)^2} G^2 S_0 \frac{\left(\omega / \omega_{eq}^2\right)^2}{\left[1 - \left(\omega / \omega_{eq}\right)^2\right]^2 + \left[\left(\frac{\omega_n}{\omega_{eq}}\right)\left(\frac{1}{Q_m} + \frac{G^2}{m\omega_n (R_L + R_C)}\right)\left(\omega / \omega_{eq}\right)\right]^2}. \quad (5.52)$$

For the harvester, the mean square load voltage

$$\overline{V_L^2} = S_0 \int_{-\infty}^{\infty} |H_V(i\omega)|^2 \, d\omega = S_0 \left(\frac{R_L}{R_L + R_C}\right)^2 G^2 \frac{\pi}{2\zeta_{eq_T}\omega_{eq}} \quad (5.53)$$

and the mean power delivered to the load

$$P_L = \frac{S_0}{R_L} \int_{-\infty}^{\infty} |H_V(i\omega)|^2 \, d\omega = \frac{S_0}{R_L} \left(\frac{R_L}{R_L + R_C}\right)^2 G^2 \frac{\pi}{2\zeta_{eq_T}\omega_{eq}} \quad (5.54)$$

can be expressed as functions of the equivalent total damping ratio and the equivalent frequency.

For simulating a nonlinear EMEHs, the dimensions and parameters (Table 5.3) of our nonlinear membrane type EMEH [112] are used. The EMEH has a non-uniform magnetic field configuration caused by two permanent magnets with remanent flux density B_r that are suspended by a polydimethylsiloxane (PDMS) membrane between two identical coils.

Table 5.3: Dimensions and parameters of the nonlinear EMEH prototype.

Description	**Value**
Device size	15 mm X 15 mm X 10 mm
Magnet (NdFeB)	1.2-1.32 T
Mass of each magnet	0.93 g
Coil size	8 mm X 8 mm
Resistance of coil	10.1 Ω
Linear resonant frequency	50 Hz

The SD of load voltage for a 100 Ω load at low levels of broadband Gaussian white noise random vibration is shown in Figure 5.9. The simulation is the result of equations (5.48) and (5.51) for a scaling factor $\eta = 5\ m^{-2}$ and a mechanical quality factor $Q_m = 300$. Under low levels of random vibrations the contribution of the second term in equation (5.48) is negligible. As a result, the resonant frequency is stable (not changing with increased base excitation), showing the linear response of the device. Therefore, the nonlinear EMEH operates in the linear regime under low levels of broadband random vibrations, where the relative displacement of the magnets is too small to cause a significant contribution from the nonlinear spring stiffness term.

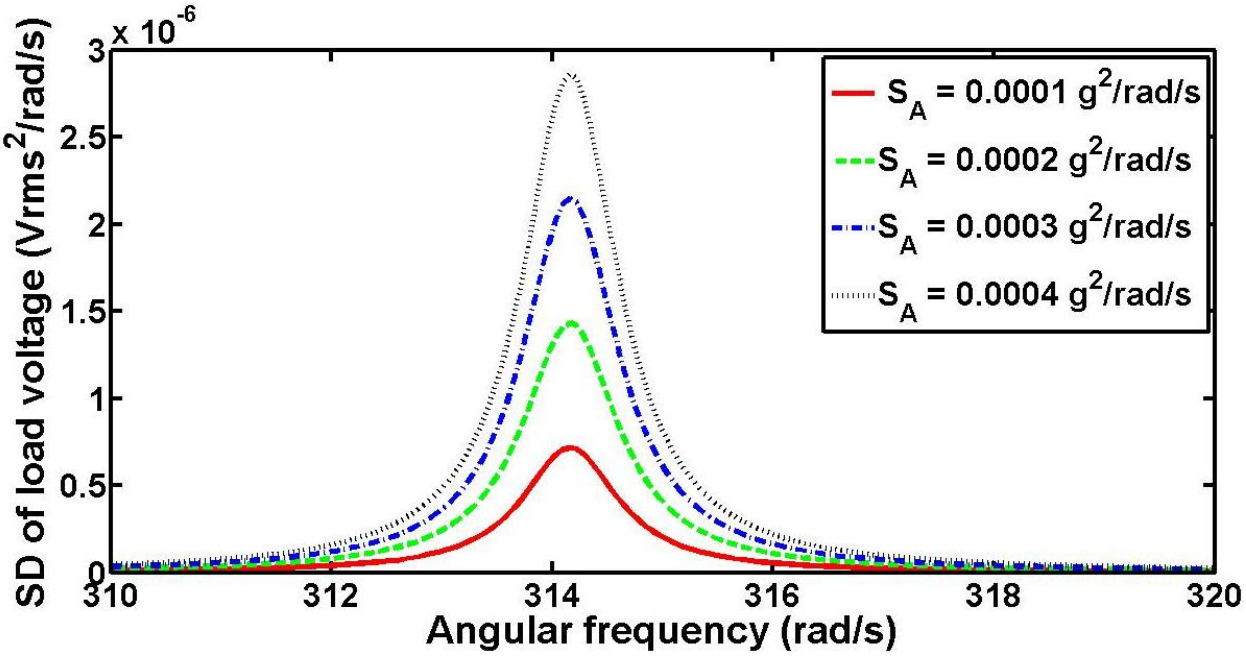

Figure 5.9: SD of the load voltage as a function of frequency for low levels of broadband Gaussian white noise random excitation, (scaling factor $\eta = 5\ m^{-2}$).

The simulation results of the SD of the load voltage for relatively high levels of broad band Gaussian white noise random vibrations is shown in Figure 5.10. The maximum value of the load voltage spectrum increases with increasing base acceleration, moreover, the central frequency of the load voltage SD shifts towards higher frequencies and this is attributed to the increase in spring stiffness (resonant frequency) of the device when it is subjected to stronger levels of random excitation. At relatively large base acceleration the large relative displacement of the mass invokes the nonlinear spring stiffening term, and the EMEH then operates in the nonlinear regime where the resonant frequency ω_{eq} given by equation (5.48) increases with increasing base acceleration. Moreover, in comparison to the load voltage SD under low levels of acceleration (Figure 5.9) at high levels of base acceleration the SD of the load voltage slightly broadens, showing an increase in the bandwidth of the device.

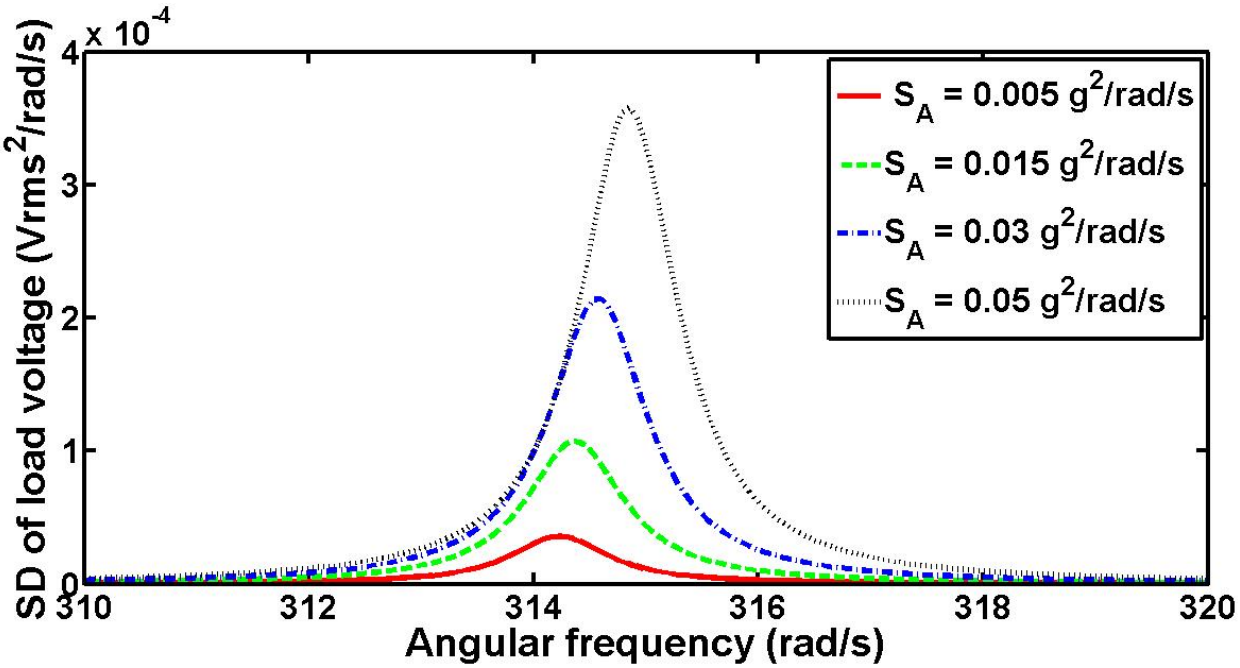

Figure 5.10: SD of the load voltage as a function of frequency for high levels of broadband Gaussian white noise random excitation, (scaling factor η = 5 m^{-2}).

5.2.3 Harvester with nonlinear stiffness and nonlinear damping

For EMEH with nonlinear damping $d(\dot{z}) = b_T \dot{z} + b_T \alpha D(\dot{z})$ and nonlinear stiffness $s(z) = kz + k\eta N(z)$, the general form of the equation of motion (5.1) of the harvester becomes

$$m\ddot{z} + [b_T \dot{z} + b_T \alpha D(\dot{z})] + [kz + k\eta N(z)] = -m\ddot{y}, \qquad (5.55)$$

A good approximation is obtained by assuming the nonlinear EMEH as a duffing oscillator, with linear-plus-cubic damping. The equation of motion for such a nonlinear EMEH

$$\ddot{z} + 2\zeta_T \omega_n (\dot{z} + \alpha \dot{z}^3) + \omega_n^2 (z + \eta z^3) = -\ddot{y}\,, \qquad (5.56)$$

contains the nonlinear damping force $d(\dot{z}) = b_T \dot{z} + b_T \alpha \dot{z}^3$ that consists of a linear damping component $b_T \dot{z}$ and the nonlinear damping component $b_T \alpha \dot{z}^3$, with α as the scaling factor.

When the excitation and response of the harvester are both stationary Gaussian with zero mean, the solution of (5.56) can also be obtained by the method of statistical linearization [178-181]. The replacement of the nonlinear damping force $2\zeta_T \omega_n (\dot{z} + \alpha \dot{z}^3)$ and the nonlinear spring force $\omega_n^2 (z + \eta z^3)$ by an equivalent linear damping force $\mu_{eq} \dot{z} = 2\zeta_{eq_T} \omega_{eq} \dot{z}$ and equivalent linear spring force $\omega_{eq}^2 z$ respectively, yields the equation of motion of an equivalent linear energy harvester

$$\ddot{z} + \mu_{eq} \dot{z} + \omega_{eq}^2 z = -\ddot{y}\,. \qquad (5.57)$$

To obtain an approximate solution for the response of the nonlinear harvester, the error

$$e = 2\zeta_T \omega_n (\dot{z} + \alpha \dot{z}^3) + \omega_n^2 (z + \eta z^3) - \mu_{eq} \dot{z} - \omega_{eq}^2 z \qquad (5.58)$$

resulting from this assumption, must be minimized. The mean square of the error $E[e^2]$ is to be minimized with respect to equivalent damping coefficient term μ_{eq} and equivalent frequency ω_{eq}, that is equations

$$\frac{\partial}{\partial \omega_{eq}^2} E[e^2] = 0 \qquad (5.59)$$

and

$$\frac{\partial}{\partial \mu_{eq}} E[e^2] = 0 \qquad (5.60)$$

must be satisfied. By substituting (5.58) into equations (5.59) and (5.60), two simultaneous equations

$$E[\dot{z}2\zeta_T\omega_n(\dot{z}+\alpha\dot{z}^3)+\omega_n^2(z+\eta z^3)]-\mu_{eq}E[\dot{z}^2]-\omega_{eq}^2E[z\dot{z}]=0 \tag{5.61}$$

$$E[z2\zeta_T\omega_n(\dot{z}+\alpha\dot{z}^3)+\omega_n^2(z+\eta z^3)]-\mu_{eq}E[z\dot{z}]-\omega_{eq}^2E[z^2]=0 \tag{5.62}$$

are obtained for the equivalent damping term μ_{eq} and the equivalent frequency ω_{eq}.

For the relative displacement $z(t)$ being a stationary Gaussian random process, with zero mean, the substitutions $E[z\dot{z}]=0$, $E[z^2]=\sigma_z^2$ and $E[\dot{z}^2]=\sigma_{\dot{z}}^2$ [178-180] in equations (5.61) and (5.62), yields the relation for the equivalent damping term

$$\mu_{eq}=\frac{E[\dot{z}2\zeta_T\omega_n(\dot{z}+\alpha\dot{z}^3)+\omega_n^2(z+\eta z^3)]}{\sigma_{\dot{z}}^2} \tag{5.63}$$

as a function of the standard deviation $\sigma_{\dot{z}}$ of the relative velocity $\dot{z}(t)$ as well as the relation for the equivalent frequency

$$\omega_{eq}^2=\frac{E[z2\zeta_T\omega_n(\dot{z}+\alpha\dot{z}^3)+\omega_n^2(z+\eta z^3)]}{\sigma_z^2} \tag{5.64}$$

as a function of the standard deviation σ_z of the relative displacement *z*(*t*). The assumption of $z(t)$ and $\dot{z}(t)$ being both Gaussian yields the much simpler equations

$$\mu_{eq}=E\left[\frac{\partial}{\partial\dot{z}}[2\zeta_T\omega_n(\dot{z}+\alpha\dot{z}^3)+\omega_n^2(z+\eta z^3)]\right] \tag{5.65}$$

$$\omega_{eq}^2=E\left[\frac{\partial}{\partial z}[2\zeta_T\omega_n(\dot{z}+\alpha\dot{z}^3)+\omega_n^2(z+\eta z^3)]\right] \tag{5.66}$$

which after differentiation, result in the equivalent damping term

$$\mu_{eq}=E[2\zeta_T\omega_n(1+3\alpha\dot{z}^2)]=\mu_T(1+3\alpha\sigma_{\dot{z}}^2) \tag{5.67}$$

as a function of linear damping term $\mu_T=2\zeta_T\omega_n$ of the linear EMEH where α = 0, and the equivalent frequency

$$\omega_{eq}^2=E[\omega_n^2(1+3\eta z^2)]=\omega_n^2(1+3\eta\sigma_z^2) \tag{5.68}$$

in terms of the natural frequency ω_n of the linear case where $\eta = 0$.

For a Gaussian white noise random excitation, the variance of the relative displacement

$$\sigma_z^2 = \int_{-\infty}^{\infty} S_z(\omega) d\omega = S_o \int_{-\infty}^{\infty} \left| H(i\omega) \right|^2 d\omega \qquad (5.69)$$

can be solved for the complex frequency response

$$H(i\omega) = \frac{-1}{-\omega^2 + i2\zeta_{eq_T} \omega_{eq} \omega + \omega_{eq}^2} \qquad (5.70)$$

of the equivalent linear EMEH with the method described in [175, 178]:

$$\sigma_z^2 = \frac{\pi S_o}{2\zeta_{eq_T} \omega_{eq}^3} = \frac{\pi S_o}{\mu_{eq} \omega_{eq}^2} \qquad (5.71)$$

and the variance of the relative velocity

$$\sigma_{\dot{z}}^2 = \frac{\pi S_o}{2\zeta_{eq_T} \omega_{eq}} = \frac{\pi S_o}{\mu_{eq}} . \qquad (5.72)$$

With the variance of the relative velocity of the linear EMEH

$$\sigma_{\dot{z}_L}^2 = \frac{\pi S_o}{2\zeta_T \omega_n} = \frac{\pi S_o}{\mu_T} \qquad (5.73)$$

and equation (5.72), elimination of μ_{eq} and μ_T from equation (5.67), yields a quadratic equation for the variance of the relative velocity $\sigma_{\dot{z}}^2$

$$\sigma_{\dot{z}}^2 (1 + 3\alpha \sigma_{\dot{z}}^2) = \sigma_{\dot{z}_L}^2 . \qquad (5.74)$$

Substitution of the positive root

$$\frac{\sigma_{\dot{z}}^2}{\sigma_{\dot{z}_L}^2} = \frac{\mu_T}{\mu_{eq}} = \frac{\sqrt{1 + 12\alpha \sigma_{\dot{z}_L}^2} - 1}{6\alpha \sigma_{\dot{z}_L}^2} \qquad (5.75)$$

of equation (5.74) into equation (5.67) yields the relation for the equivalent damping term

$$\mu_{eq} = \mu_T \left[1 + \frac{\sqrt{1+12\alpha\sigma_{\dot{z}_L}^2} - 1}{2} \right]. \qquad (5.76)$$

With the variance of the relative displacement of the linear EMEH

$$\sigma_{z_L}^2 = \frac{\pi S_o}{2\zeta_T \omega_n^3} = \frac{\pi S_o}{\mu_T \omega_n^2} \qquad (5.77)$$

and equation (5.71), elimination of ω_{eq} and ω_n from equation (5.68), yields a quadratic equation for the variance of the relative displacement σ_z^2

$$\sigma_z^2 (1 + 3\eta\sigma_z^2) \frac{\mu_{eq}}{\mu_T} = \sigma_{z_L}^2 . \qquad (5.78)$$

Substitution of the positive root

$$\frac{\sigma_z^2}{\sigma_{z_L}^2} = \left(\frac{\sqrt{1+12L} - 1}{6L} \right) \frac{\mu_T}{\mu_{eq}} \qquad (5.79)$$

of equation (5.78) into equation (5.68) yields the relation for the equivalent natural frequency

$$\omega_{eq}^2 = \omega_n^2 \left[1 + \frac{\sqrt{1+12L} - 1}{2} \right] \qquad (5.80)$$

where

$$L = \eta\sigma_{z_L}^2 \frac{\mu_T}{\mu_{eq}} = \eta\sigma_{z_L}^2 \left[1 + \frac{\sqrt{1+12\alpha\sigma_{\dot{z}_L}^2} - 1}{2} \right]^{-1} . \qquad (5.81)$$

Equations (5.11) and (5.57) yield

$$\frac{1}{G} \frac{R_L + R_C}{R_L} \left[\frac{\mathrm{d}}{\mathrm{d}t} V_L(t) + 2\zeta_{eq_T} \omega_{eq} V_L(t) + \omega_{eq}^2 \int V_L(t)\,\mathrm{d}t \right] = -\ddot{y}(t), \qquad (5.82)$$

which by Fourier analysis results in the frequency response of the harvester

$$H_V(i\omega) = \frac{R_L}{R_L + R_C} G \frac{-i\omega}{-\omega^2 + i2\zeta_{eq_T}\omega_{eq}\omega + \omega_{eq}^2} = \frac{R_L}{R_L + R_C} G \frac{\omega}{(\omega_{eq}^2 - \omega^2)i - 2\zeta_{eq_T}\omega_{eq}\omega} \quad (5.83)$$

in terms of transformation factor G , coil resistance R_C and load resistance R_L.

For a Gaussian white noise base excitation $S_A(\omega) = S_0$, the SD of the load voltage

$$S_{V_L}(\omega) = \left(\frac{R_L}{R_L + R_C}\right)^2 G^2 S_0 \frac{\left(\omega / \omega_{eq}^2\right)^2}{\left[1 - \left(\omega / \omega_{eq}\right)^2\right]^2 + \left[2\zeta_{eq_T}\left(\omega / \omega_{eq}\right)\right]^2} \quad (5.84)$$

and the SD of the load power

$$S_{P_L}(\omega) = \frac{R_L}{(R_L + R_C)^2} G^2 S_0 \frac{\left(\omega / \omega_{eq}^2\right)^2}{\left[1 - \left(\omega / \omega_{eq}\right)^2\right]^2 + \left[2\zeta_{eq_T}\left(\omega / \omega_{eq}\right)\right]^2} \quad (5.85)$$

can be expressed in EMEH parameters.

Substitution of $\mu_{eq} = 2\zeta_{eq_T}\omega_{eq}$ and $\mu_T = 2\zeta_T\omega_n$ in (5.76) yields the equivalent total damping ratio

$$\zeta_{eq_T} = \frac{\omega_n \zeta_T}{\omega_{eq}} \left[1 + \frac{\sqrt{1 + 12\alpha\sigma_{\dot{z}_L}^2} - 1}{2}\right] \quad (5.86)$$

in terms of the total damping ratio ζ_T of the linear harvester.

With equations (5.23), (5.24) and (5.86) the equivalent total damping ratio becomes

$$\zeta_{eq_T} = \frac{\omega_n \zeta_T}{\omega_{eq}} \left[1 + \frac{\sqrt{1+12\alpha\sigma_{\dot{z}_L}^2} - 1}{2} \right]$$
$$= \frac{\omega_n}{\omega_{eq}} \left[\frac{1}{Q_m} + \frac{G^2}{m\omega_n (R_L + R_C)} \right] \left[1 + \frac{1}{2} \left(\sqrt{1+12\alpha\sigma_{\dot{z}_L}^2} - 1 \right) \right] \quad . \quad (5.87)$$
$$= \frac{\omega_n}{2\omega_{eq}} \left[\frac{1}{Q_m} + \frac{G^2}{m\omega_n (R_L + R_C)} \right] \left[1 + \frac{1}{2} \left(\sqrt{1 + \frac{12\pi\alpha m S_0 Q_m (R_L + R_C)}{m\omega_n (R_L + R_C) + G^2 Q_m}} - 1 \right) \right]$$

Likewise, equation (5.81) becomes

$$L = \eta\sigma_{z_L}^2 \frac{\mu_T}{\mu_{eq}} = \eta \frac{\pi S_0}{2\zeta_T \omega_n^3} \left[1 + \frac{\sqrt{1+12\alpha\sigma_{\dot{z}_L}^2} - 1}{2} \right]^{-1}$$
$$= \eta \frac{\pi m S_0 Q_m (R_L + R_C)}{\omega_n^2 \left[m\omega_n (R_L + R_C) + G^2 Q_m \right]} \left[1 + \frac{1}{2} \left(\sqrt{1 + \frac{12\pi\alpha m S_0 Q_m (R_L + R_C)}{m\omega_n (R_L + R_C) + G^2 Q_m}} - 1 \right) \right]^{-1} \quad (5.88)$$

as functions of transformation factor G and mechanical quality factor Q_m, and the mean square load voltage

$$\overline{V_L^2} = S_0 \left(\frac{R_L}{R_L + R_C} \right)^2 G^2 \frac{\pi}{2\zeta_{eq}\omega_{eq}}, \quad (5.89)$$

and mean power delivered to the load

$$P_L = \frac{S_0}{R_L} \left(\frac{R_L}{R_L + R_C} \right)^2 G^2 \frac{\pi}{2\zeta_{eq}\omega_{eq}}. \quad (5.90)$$

can be computed in terms of the EMEH parameters.

Figure 5.11 shows the SD of the load voltage of an EMEH with nonlinear damping and nonlinear stiffness, for a 100 Ω load, at low levels of broadband Gaussian white random vibration. The simulation results are based on equations (5.80), (5.84) and (5.87) with a spring scaling factor η = 5 m^{-2} and a damping scaling factor α = 0.05 s^2m^{-2}. In comparison to the load voltage SD of an EMEH with linear damping and nonlinear stiffness in Figure 5.9, almost the

same response is obtained. Under such low levels of base acceleration the linear damping and linear stiffness terms are dominant, whereas the nonlinear damping and nonlinear stiffness terms have negligible contributions due to the small values of the standard deviation of the relative velocity and the relative displacement, respectively. At low base accelerations the second term in equations (5.80) and (5.87) is negligible, so that the nonlinear EMEH operates in the linear regime with a stable central frequency (resonant frequency) of the load voltage SD.

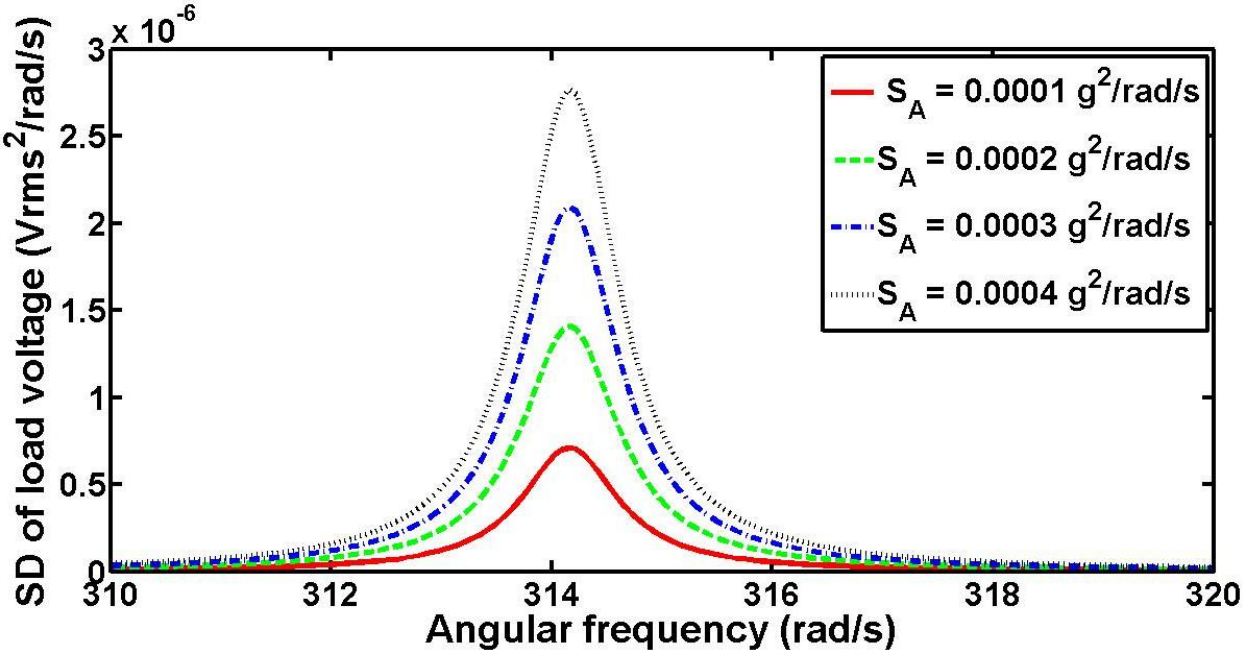

Figure 5.11: SD of the load voltage as a function of frequency for low levels of broad band Gaussian white random excitation, (spring scaling factor η = 5 m^{-2} and damping scaling factor α = 0.05 s^2m^{-2}).

The simulation results of an EMEH with nonlinear damping and stiffness at relatively high levels of broadband Gaussian white random vibrations is shown in Figure 5.12. With increased base acceleration level, the shift of the central frequency of the load voltage SD towards higher frequencies indicates the operation of the device in the nonlinear regime. Under these conditions, the higher values of the standard deviations of the relative velocity and the relative displacement of the mass invoke the nonlinear effects of the system. In other words, the contribution of the second terms in equations (5.80) and (5.87) becomes significant.

In comparison to the response of an EMEH with nonlinear stiffness only as in Figure 5.10, the same shift in the SD maximum value and central frequency is evident in the case of the

fully nonlinear harvester. However, in Figure 5.12, these shifts are smaller due to the existence of the nonlinear damping. The nonlinear damping of the EMEH, which increases as the standard deviation of the relative velocity is increased, is not allowing the same increase in the maximum value for the load voltage SD and the central frequency as in case of the EMEH with linear damping. Moreover, the increased damping leads to broader bandwidths in comparison to the EMEH with nonlinear stiffness only in Figure 5.10.

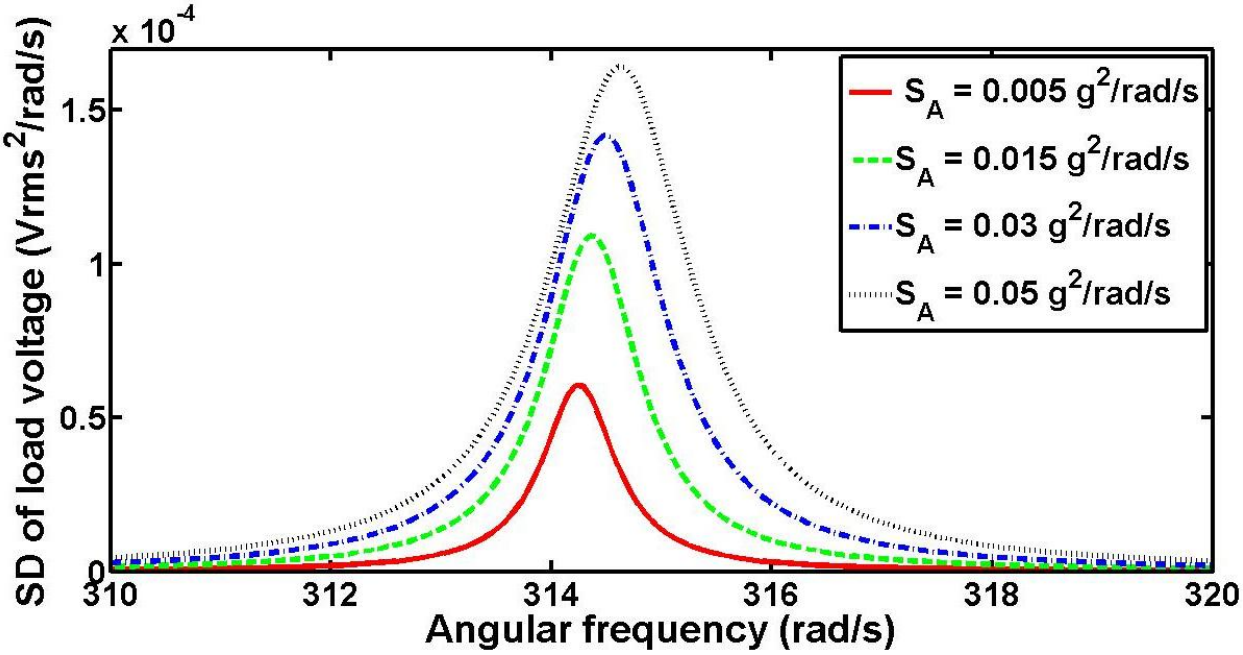

Figure 5.12: SD of the load voltage as a function of frequency for high levels of broadband Gaussian white noise random excitation, (spring scaling factor η = 5 m^{-2} and damping scaling factor α = 0.05 s^2m^{-2}).

The response of the nonlinear EMEH with a larger value for the damping scaling factor α = 5 s^2m^{-2}, is shown in Figure 5.13. In this case a much smaller increase in the maximum value of the load SD is seen; moreover the central frequency is almost constant and does not change with increasing base acceleration. Broader bandwidths are obtained in comparison to a nonlinear EMEH with smaller damping scaling factor α = 0.05 s^2m^{-2}. The larger values of the nonlinear damping term diminish the effects of the nonlinear stiffness term, until and unless the spring scaling factor is very large.

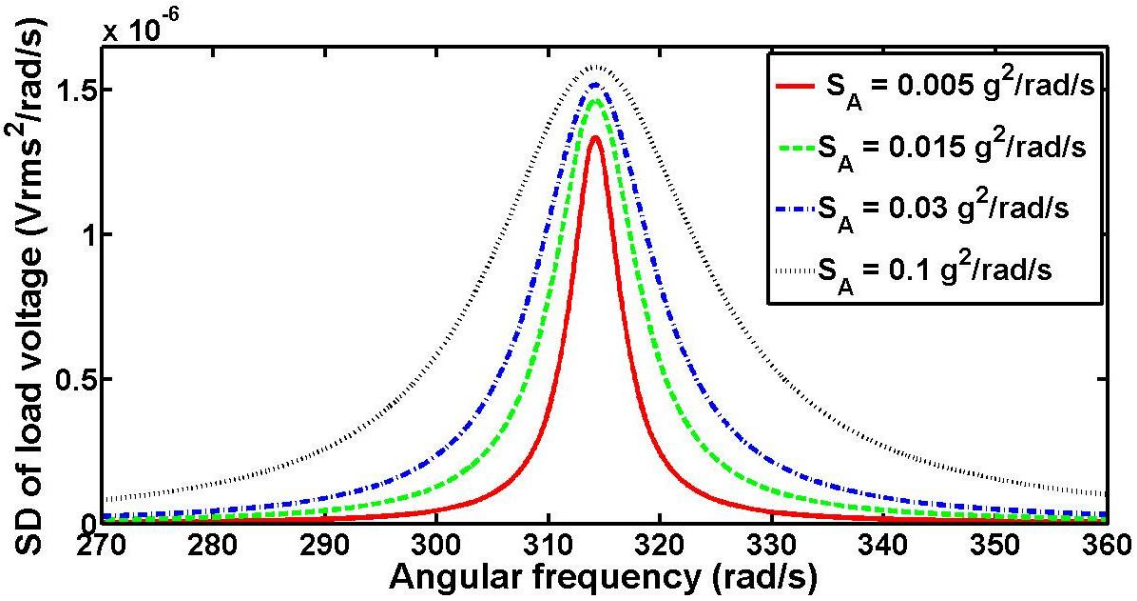

Figure 5.13: SD of the load voltage as a function of frequency for high levels of broadband Gaussian white random excitation, (spring scaling factor η = 5 m^{-2} and damping scaling factor α = 5 s^2m^{-2}).

For a nonlinear EMEH with combined nonlinear stiffness and damping, the equivalent resonant frequency for stiffness damping factor of η = 5 m^{-2} and several values of damping scaling factor α is plotted in Figure 5.14. When the EMEH is subjected to increasing SD levels of the acceleration, for smaller values of α, the shift in the equivalent frequency of the response is significant, however this shift decreases as α is increased. For, α = 5 s^2m^{-2} or larger values, the change in the equivalent frequency is negligible. Moreover it can be seen from the plot that at lower SD levels of the acceleration the shift in resonant frequency is minimal even if the difference in α is large. This indicates that at the excitation level equal to or less than 0.0001 g^2/rad/s, contribution from the nonlinear effects are negligible. The EMEH will be operating in the linear regime with approximately constant resonant (central) frequency of the SD of the response.

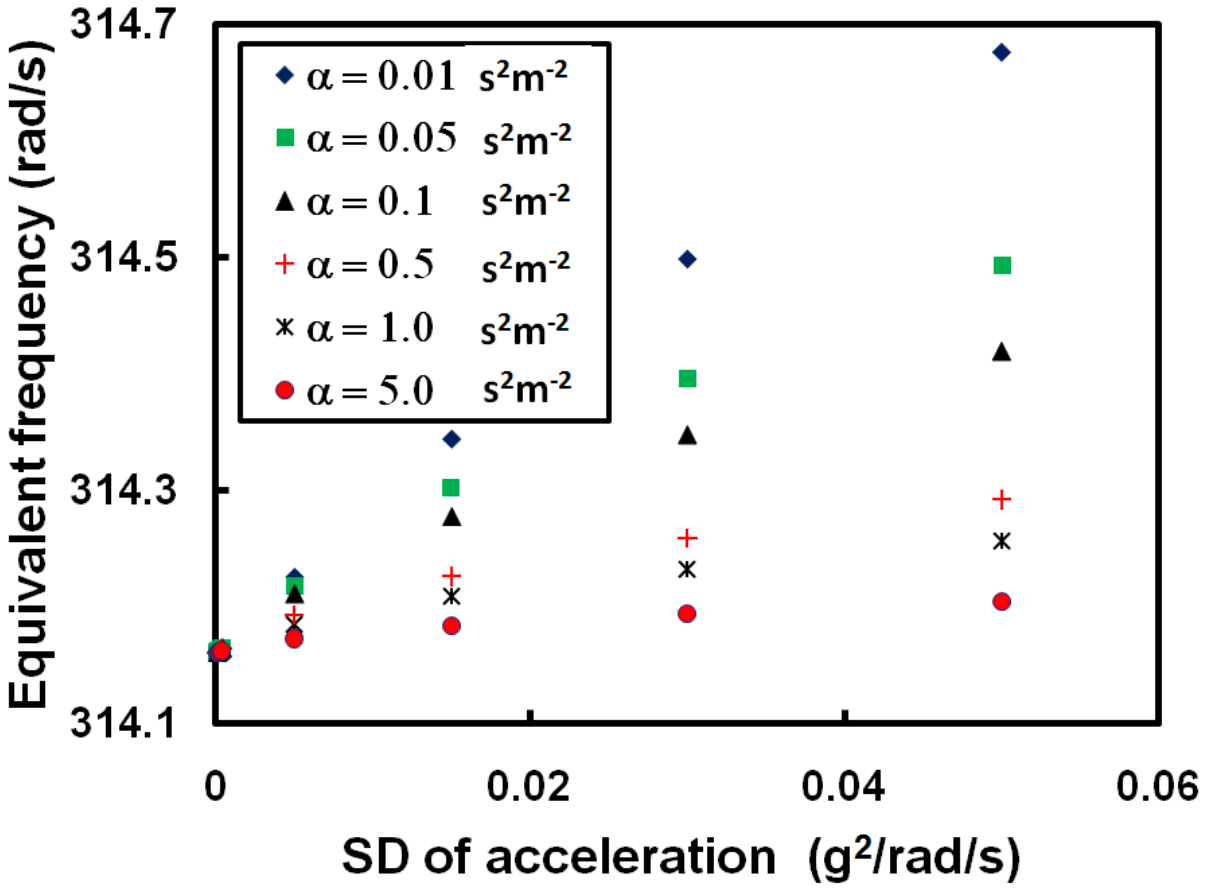

Figure 5.14: Equivalent frequency as a function of SD of acceleration for several values of the damping scaling factor α (η = 5 m^{-2}).

The mean power as a function of load resistance for several values of the transformation factor is shown in Figure 5.15. The plots are obtained by using equations (5.80) and (5.87) in (5.90). The computation is performed for the acceleration SD of 0.01 g^2/rad/s. With increase in the transformation factor, the peak value of the mean power increases as well as the optimum load resistor.

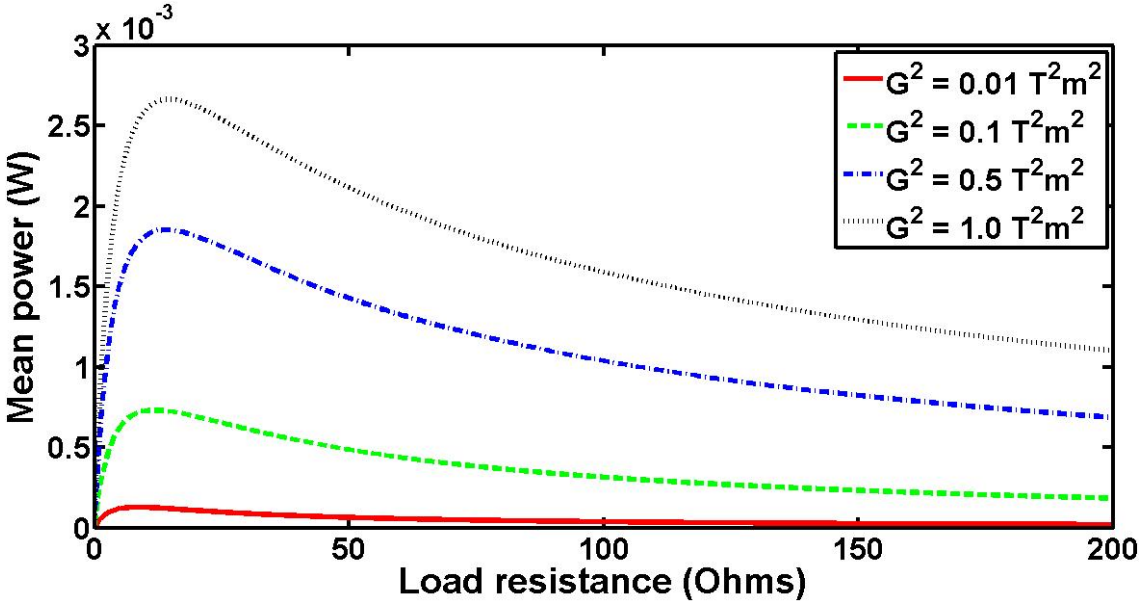

Figure 5.15: Mean power as a function of load resistance for different values of G^2 at the acceleration SD of 0.01 g^2/rad/s (spring scaling factor η = 5 m^{-2} and damping scaling factor α = 5 s^2m^{-2}).

6 Conclusions and recommendations

6.1 Summary

Vibration-based electromagnetic energy harvesters are alternative power sources for ultra low power micro sensors and can have a major impact on how wireless sensor nodes are converted into completely autonomous systems in the future.

In this thesis, a low cost fabrication technique for the components of EMEHs, analytical models of linear EMEHs with uniform magnetic field configuration for harmonic vibrations, analytical models of linear and nonlinear EMEHs for random vibrations and characterization of the developed EMEHs under harmonic and random vibration were reported.

6.2 Conclusions

We have developed a low cost, one-mask technology to fabricate the components for a non-silicon-based EMEH. With the devised technology a copper foil type EMEH has been developed and characterized under harmonic vibrations in Chapter 2, and a PDMS membrane type EMEH has been developed and characterized under harmonic as well as random vibrations in Chapter 4. The voltage and power generated by these harvesters are comparable to other developed EMEHs which use more involved fabrication processes. In the former harvester the spring stiffness of the planar copper spring can be readily customized through mask design to achieve other resonant frequencies for a broader range of applications. Likewise with the spring design EMEH can easily be tuned to low, medium and high acceleration vibration environments. In the second EMEH the incorporation of a more flexible polymeric membrane helped in reduction of the harvester's resonant frequency and made it suitable for extracting energy from low level vibration environments. Moreover, unlike the planar spring, the fabrication of the PDMS membrane does not require expensive photolithography and etching steps in the clean room. In the PDMS membrane type EMEH the nonlinear behaviour was attributed to the nonlinear elasticity of the PDMS membrane, which led to the commonly observed drop, jump and hysteresis phenomena, and the resonant frequency changing with the level of base acceleration. The nonlinear response of the harvester was exploited to harvest energy from narrow band

random vibrations. Similar to sinusoidal excitations, the device displayed linear behaviour under low levels of narrow band (5 to 150 Hz) random vibrations, with a stable central (resonant) frequency of the spectral density (SD) of the load voltage. However, when subjected to stronger narrow band (50 to 150 Hz) random vibration levels to invoke the nonlinear effects of the PDMS membrane, a shift in the central (resonant) frequency of the SD of the output voltage was observed. In comparison to the load voltage SDs under low levels of random excitation, at high levels of random excitation the SDs of the load voltage are relatively broader, showing an increase in the bandwidth of the device.

The analytical study conducted in Chapter 3 for linear EMEHs with a non-uniform magnetic field under harmonic vibrations, comprised of a simple model based on Faraday's law and a uniform gradient of the normal component of the magnetic flux density that is more suitable for EMEHs where the entire coil experiences approximately the same magnetic flux density or the same gradient of the normal component of the magnetic flux density. The limitations of the former model were resolved by the development of more robust analytical models based on Faraday's law and the Lorentz force law, and analytical solution of the off-center magnetic flux density. We averaged the gradient of the normal component of the magnetic flux density for each coil turn for the model based on Faraday's law, and we averaged the x-component of the magnetic flux density at the side length of each turn for the formulation based on the Lorentz force law. The resulting models can accurately predict the EMEHs performance where the entire coil does not experience the same gradient of the normal component of the flux density. We showed based on the practical constraints of the copper foil type EMEH that the models can be very effectively used to optimize the output voltage and power of the harvester.

In Chapter 5, analytical models for linear and nonlinear EMEHs under random vibration were used to investigate the behaviour of the harvesters under broadband and narrow band random vibrations. We showed the significance of the harvester design parameters, such as the mechanical quality factor and the transformation factor, on the device mean power, the mean square load voltage and the spectral density of the load voltage. We found that under broadband vibration, linear EMEHs with higher values of the product-of-merit the mean power is less sensitive to the load, and moreover, the optimum load condition for linear EMEHs under random vibration differs from that under harmonic vibrations. The simulation results for the nonlinear

EMEHs showed that the response of the harvester not only depends on the spectral density of the base acceleration but also on the standard deviations of the relative velocity and the relative displacement. We noted that under low levels of random excitation, the contribution from the nonlinear terms was negligible, the linear stiffness and linear damping were dominant, and the harvesters operated in the linear regime, where and the response of a nonlinear device is similar to a linear one. However, when subjected to higher levels of random excitations to invoke the contribution of the nonlinear effects, the simulation results showed that not only the maximum value of the load voltage increases but also the central (resonant) frequency of the spectral density shifts towards higher frequencies. The shift in the central frequency is attributed to the increased stiffness. This shift, however, became less significant in the case of an EMEH with nonlinear damping, since the nonlinear damping term contributes inversely to the resonance frequency. Moreover, slightly broader bandwidths are obtained in the nonlinear regime in comparison to operation in the linear regime. The presence of large nonlinear damping not only increases the bandwidth of the harvester at the expense of a decreased peak value of the load voltage spectral density but also a stable resonant frequency is obtained even at relatively high levels of random excitation.

6.3 Recommendations for future research

This research has revealed a number of potential venues for further research and investigation in the field of electromagnetic energy harvesting. These are briefly discussed below:

The low cost, one mask fabrication technology developed in this thesis can easily be extended to the fabrication of suspended and embedded parts for other MEMS devices. The technology is not limited only to the use of copper foil, depending on the type of the fabricated device, aluminum, nickel or gold foils can be utilized. The developed fabrication technique can readily be implemented to fabricate the following devices:

- Energy harvesters
    - Acoustic energy harvesters
    - Electrostatic energy harvesters
    - Energy harvesters for pressure- changing environments

    - RF energy harvesters
- Micro sensors
    - Acoustic sensors
    - Pressure sensors
    - Flow sensors
- Micro actuators
    - Micro pumps
    - Electromagnetic actuators
    - Electrostatic actuators
    - Externally controlled micro valves
- Other applications
    - Micro heaters
    - Variable gap capacitors
    - Micro robots

The incorporation of PDMS in the developed technology makes it suitable for integration with lab-on-a-chip technology, where the PDMS is one of the main fabrication materials.

For the architecture proposed in this thesis for the EMEHs, vacuum can be produced in the cavity in which the magnets are oscillating. The vacuum will results in reduced air damping and more power generation. The power enhancement can also be obtained by fabricating coils on both sides of the glass substrate, this can almost double the output voltage and increase the generated power. In the developed devices coils were fabricated on 1 mm thick glass substrate, however, they can be easily fabricated on thinner glass substrate (for example, 170 µm thick Fisherfinest® micro slides), this will result in smaller and lighter devices and increase the power density of the harvester.

The EMEHs developed in this study are lightweight and suitable for small as well as large area applications. To harvest energy from ambient vibrations over a fairly broad frequency bandwidth, array of EMEHs with different resonant frequencies can be used. The output voltage signals from each harvester can then be rectified before being combined for use.

The analytical models developed in Chapters 2 and 3 for linear electromagnetic energy harvesters with non-uniform field configuration under harmonic vibrations, can be extended for nonlinear EMEHs. With proper modeling of the nonlinear stiffness, which is the main cause of the mechanical nonlinearity in the harvesters, the drop, jump and hysteresis phenomena in nonlinear harvesters can be explained more explicitly.

Realistic environmental vibration is random in nature, As a result, recent research has started to investigate the behaviour of energy harvesters subjected to broadband or random vibrations. Very little research has been reported with regard to the response of harvesters under random vibrations, moreover the research which has been conducted, as in this work, is for uni-axial random vibration. However, real vibrations are more of tri-axial nature and relevant research can be conducted in modeling, fabrication and characterization of suitable devices.

The analytical models developed, in Chapter 5, for linear and nonlinear EMEHs under broadband random vibrations, must be validated. This requires the identification of realistic model parameters for the harvesters and verification of the models by comparing modeling results to experimental results.

Bibliography

[1] Kadirvel S, Liu F, Horowitz S, Nishida T, Ngo K, Cattafesta L and Sheplak M 2006 A self-powered wireless active acoustic liner *12th AIAA/CEAS Aeroacoustics Conf.* (*Cambridge, MA,USA, 08-10 May*)

[2] Phipps A, Liu F, Cattafesta L, Sheplak M and Nishida T 2009 Demonstration of a wireless, self-powered, electroacoustic liner system *J. Acoust. Soc. Am.* **125** 873–81

[3] Horowitz S B, Sheplak M, Cattafesta III L N and Nishida T 2006 A MEMS acoustic energy harvester *J. Micromech. Microeng.* **16** 174–81

[4] Lai T, Huang C, and Tsou C 2008 Design and Fabrication of Acoustic Wave Actuated Microgenerator for Portable Electronic Devices *Symposium on Design, Test, Integration and Packaging of MEMS/MOEMS* (*Nice, France, 09-11 April*) 28–33

[5] Horowitz S 2005 Development of a MEMS-based acoustic energy harvester *PhD Dissertation* University of Florida, Gainesville, FL, USA

[6] Liu F, Phipps A, Horowitz S, Ngo K, Cattafesta L, Nishida T and Sheplak M 2008 Acoustic energy harvesting using an electromechanical Helmholtz resonator *J. Acoust. Soc. Am.* **123** 1983-90

[7] Shih P J, Shih W P 2010 Design, fabrication and application of bio-implantable acoustic power transmission *J. Microelectromech. Syst.***19** 494-502

[8] Pajewski W 1972 Ultrasonic transducers with vibrating piezoelectric plates *J. Physique* **33** 258–62

[9] Leonov V, Fiorini P, Sedky S, Torfs T and van Hoof C 2005 Thermoelectric MEMS generators as a power supply for a body area network *Proc. 13th Int. Conf. Solid-State Sensors, Actuators and Microsystems, Transducers'05* (*Seoul, Korea, 5-9 June*) **1** 291-4

[10] Schaevitz S B, Franz A J, Jensen K F and Schmidt M A 2001 A combustion-based MEMS thermoelectric power generator *Proc. 11th Int. Conf. Solid-State Sensors and Actuators and Microsystems, Transducers'01* (*Munich, Germany, 10-14 June*)

[11] Snyder G J, Lim J R, Huang C-K and Fleurial J P 2003 Thermoelectric microdevice fabricated by a MEMS-like electrochemical process *Nature Mater. Lett.* **2** 528-31

[12] Venkatasubramanian R, Siivola E, Colpitts T and O'Quinn B 2001 Thin-film thermoelectric devices with high room-temperature figures of merit *Nature* **413** 597-602

[13] Wang W, Jia F, Huang Q and Zhang J 2005 A new type of low power thermoelectric micro-generator fabricated by nanowire array thermoelectric material *Microelectron. Eng.* **77** 223-9

[14] Bottner H *et al* 2004 New thermoelectric components using microsystem technologies *J. Microelectromech. Syst.* **13** 414-20

[15] Strasser M, Aigner R, Franosch M and Wachutka G 2002 Miniaturized thermoelectric generators based on poly-Si and poly-SiGe surface micromachining *Sensors Actuators* A **97-8** 535-42

[16] Strasser M, Aigner R, Lauterbach C, Sturm T F, Franosch M and Wachutka G 2004 Micromachined CMOS thermoelectric generators as on-chip power supply *Sensors Actuators* A **114** 362-70

[17] Leonov V, Torfs T, Fiorini P and Van Hoof C 2007 Thermoelectric converters of human warmth for self-powered wireless sensor nodes *IEEE Sensors J.* **7** 650-7

[18] Paing T, Shin J, Zane R and Popovic Z 2008 Resistor emulation approach to low-power RF energy harvesting *IEEE Trans. Power Electron.* **23** 1494-1501

[19] Mi M, Mickle M H, Capelli C and Swift H 2005 RF energy harvesting with multiple antennas in the same space IEEE *Antennas Propag. Mag.* **47** 100-6

[20] Salter T, Choi K, Peckerar M, Metze G and Goldsman N 2009 RF energy scavenging system utilizing switched capacitor DC-DC converter *Electronics Letters* **45** 374-6

[21] Harrist D W 2004 Wireless Battery Charging System Using Radio Frequency Energy Harvesting *Master's Thesis*, University of Pittsburgh, USA

[22] Mickle M H, Lovell M, Mats L, Neureuter L and Gorodetsky D 2001 Energy harvesting, profiles and potential sources *International Journal of Parallel and Distributed Systems and Networks*, **4** 150-60

[23] Dondi D, Bertacchini A, Brunelli D, Larcher L and Benini L 2008 Modeling and optimization of a solar energy harvester system for self-powered wireless sensor networks *IEEE Trans. Ind. Electron.* **55** 2759-66

[24] Kimball J W, Kuhn B T and Balog R S 2009 A system design approach for unattended solar energy harvesting supply *IEEE Trans. Power Electron.* **24** 952-62

[25] Lin K *et al.* 2005 Heliomote: enabling long-lived sensor networks through solar energy harvesting *Proc. ACM SenSys*. (*San Diego, CA, USA, 2-4 Nov*) 309

[26] Gratzel M 2005 Solar Energy conversion by dye-sensitized photovoltaic cells *Inorg. Chem.* **44** 6841–51

[27] Li J S, Yu H Y, Wong S M, Zhang G, Sun X W, Lo G Q and Kwong D L 2009 Si nanopillar array optimization on Si thin films for solar energy harvesting *Appl. Phys. Lett.* **95** 033102

[28] Kim S H, Ji C H, Galle P, Herrault F, Wu X, Lee J H, Choi C A and Allen M G 2009 An electromagnetic energy scavenger from direct airflow *J. Micromech. Microeng.* **19** 094010

[29] Federspiel C C and Chen J 2003 Air-powered sensor *Proc. IEEE Sensors* (*Toronto, Canada, 22-24 Oct*) **1** 22-5

[30] Holmes A S, Hong G, Pullen K R and Buffard K R 2004 Axial-flow microturbine with electromagnetic generator: design, CFD simulation, and prototype demonstration *Proc. MEMS 2004* (*Maastricht, Netherlands, 25-29 Jan*) 568-71

[31] Shiming Y, Jianbin T, Hong Q and Chengrong C 2007 Wireless communication based tire pressure monitoring system *IEEE int. conf. Wireless Communications, Networking and Mobile Computing, WiCom* (*Shanghai, China 21-25 Sept*) 2511–14

[32] Leng Y, Li Q, Hou B, Liu S and Dong T 2007 Wheel antenna of wireless sensors in automotive tire pressure monitoring system *IEEE int. conf. Wireless Communications, Networking and Mobile Computing, WiCom* (*Shanghai, China 21-25 Sept*) 2755–58

[33] Dixon B, Kalinin V, Beckley J and Lohr R 2006 A second generation in-car tire pressure monitoring system based on wireless passive SAW sensors *IEEE International Frequency Control Symposium and Exposition (Miami, Florida, USA Jun 5-7)* 374–80

[34] Ho I H, Chung J M, Chen H C and Chiu H W 2009 A Battery-Less Tire Pressure Monitoring System *69th IEEE Vehicular Technology Conference VTC 2009* (*Barcelona, Spain 26-29 April*) 1-5

[35] Matsuzaki R and Todoroki A 2008 Wireless Monitoring of Automobile Tires for Intelligent Tires *Sensors* **8** 8123-38

[36] Sodano H A, Inman D J and Park G 2005 Comparison of piezoelectric energy harvesting devices for recharging batteries *J. Intell. Mater. Syst. Struct.* **16** 799-807

[37] Ramsay M J and Clark W W 2001 Piezoelectric energy harvesting for bio MEMS applications *Proc. SPIE* **4332** 429-38

[38] White N M, Glynne-Jones P and Beeby S P 2001 A novel thick-film piezoelectric micro-generator *Smart Mater. Struct.* **10** 850-2

[39] Roundy S and Wright P K 2004 A piezoelectric vibration based generator for wireless electronics *Smart Mater. Struct.* **13** 1131-42

[40] Mitcheson P D, Sterken T, He C, Kiziroglou M, Yeatman E M and Puerso R 2008 Electrostatic microgenerators *Meas. Control* **41** 114-9

[41] Sterken T, Altena G, Fiorini P and Puers R 2007 Characterisation of an electrostatic vibration harvester *DTIP of MEMS & MOEMS* (*Stresa, Italy, 25-27 April*) 297-300

[42] Naruse Y, Matsubara N, Mabuchi K, and Suzuki S 2009 Electrostatic micro power generation from low-frequency vibration such as human motion *J. Micromech. Microeng.* **19** 094002

[43] Basset P, Galayko D, Mahmood P A, Marty F, Dudka A and Bourouina T 2009 A batch-fabricated and electret-free silicon electrostatic vibration energy harvester *J. Micromech. Microeng.* **19** 115025

[44] Saha C R, O'Donnell T, Wang N and McCloskey P 2008 Electromagnetic generator for harvesting energy from human motion *Sensors Actuators* A **147** 248-53

[45] Duffy M and Carroll D 2004 Electromagnetic generators for power harvesting *35th IEEE Conf. Power Electronics Specialists, PESC 04* (*Aachen, Germany, 20-25 June*) **3** 2075-81

[46] Zorlu O, Topal E T and Kulah H 2011 A vibration-based electromagnetic energy harvester using mechanical frequency up-conversion method *IEEE Sensors J.* **11** 481-488

[47] Polla D L and Francis L F 1998 Processing and characterization of piezoelectric materials and integration into microelectromechanical systems *Annu. Rev. Mater. Sci.* **28** 563-597

[48] Khaligh A, Zeng P and Zheng C 2010 Kinetic energy harvesting using piezoelectric and electromagnetic technologies-state of the art *IEEE Trans. Ind. Electron.* **57** 850–60

[49] Erturk A and Inman D J 2008 On mechanical modeling of cantilevered piezoelectric vibration energy harvesters *J. Intell. Mater. Syst. Struct.* 1**9** 1311-25

[50] Yoon H S, Washington G and Danak A 2005 Modelling, optimisation, and design of efficient initially curved piezoceramic unimorphs for energy harvesting applications *J. Intell. Mater. Syst. Struct.* **16** 877-88

[51] Roundy S, Wright P K and Rabaye J 2003 A study of low level vibrtions as a power source for wireless sensor nodes *Comput. Commun.* **26** 1131-44

[52] Jiang S, Li X, Guo S, Hu Y, Yang J and Jiang Q 2005 Performance of a piezoelectric bimorph for scavenging vibration energy *Smart Mater. Struct.* **14** 769-74

[53] Ajitsaria J, Choe S Y, Shen D and Kim D J 2007 Modeling and analysis of a bimorph piezoelectric cantilever beam for voltage generation *Smart Mater. Struct.* **16** 447-54

[54] Ferrari M, Ferrari V, Guizzetti M, Marioli D and Taroni A 2008 Piezoelectric multifrequency energy converter for power harvesting in autonomous microsystems *Sensors Actuators* A **142** 329-35

[55] Meninger S, Mur-Miranda J O, Amirtharajah R, Chandrakasan A P and Lang J H 2001 Vibration-to-electric energy conversion *IEEE Trans. Very Large Scale Integr. (VLSI) Syst.* **9** 64–76

[56] Lee C, Lim Y M, Yang B, Kotlanka R K, Heng C H, He H, Tang M, Xie J and Feng H H 2009 Theoretical comparison of the energy harvesting capability among various electrostatic mechanisms from structure aspect *Sensors Actuators* A **156** 208-16

[57] Tashiro R, Kabei N, Katayama K, Tsuboi F, Tsuchiya K, 2002 Development of an electrostatic generator for a cardiac pacemaker that harnesses the ventricular wall motion, *J. Artif. Organs.* 239-45

[58] Yang B, Lee C, Kotlanka R K, Xie J and Lim S P 2010 A MEMS rotary comb mechanism for harvesting the kinetic energy of planar vibrations *J. Micromech. Microeng.* **20** 065017

[59] Roundy S, Wright P K and Pister K S J 2002 Micro-electrostatic vibration-to-electricity converters *Proc. ASME IMECE 2002* (*New Orleans, LA, USA, 17-22 Nov*) 1-10

[60] Beeby S P, Torah R N and Tudor M J 2008 Kinetic energy harvesting *ACT workshop on Innovation Concepts ESA-ESTEC* (*Noordwijk, Netherlands, 28-29 Jan*)

[61] Serre C, Perez-Rodriguez A, Fondevilla N, Morante J R, Montserrat J and Esteve J 2007 Vibrational energy scavenging with Si technology electromagnetic inertial microgenerators *Microsyst. Technol.* **13** 1655-61

[62] Perez-Rodrigues A, Serre C, Fondevilla N, Morante J R, Montserrat J and Esteve J 2005 Electromagnetic inertial generator for vibrational energy scavenging compatible with Si technology *PowerMEMS'05* (*Tokyo, Japan, 28-30 Nov*) 57-60

[63] Sari I, Balkan T and Kulah H 2008 A electromagnetic micro power generator for wideband environmental vibrations *Sensors Actuators* A **145** 405-13

[64] Jong Cheol Park, Dong Hyun Bang, and Jae Yeong Park 2010 Micro-fabricated electromagnetic power generator to scavenge low ambient vibration *IEEE Trans. Magnetics* **46** 1937-41

[65] Kim S, Dong H L, Lee Y P, Chang Y S and Park M C 2008 Low frequency properties of micro power generator using a gold electroplated coil and magnet *Current Appl. Phys. J.* **8** 138-41

[66] Torah R N, Beeby S P, Tudor M J, O'Donnell T and Roy S 2006 Development of a cantilever beam generator employing vibration energy harvesting *PowerMEMS'06* (*Berkeley, USA, 29 Nov –1 Dec*) 181-4

[67] Ching N N H, Wong H Y, Li W J, Leong P H W and Wen Z 2002 A laser-micromachined vibrational to electrical power transducer for wireless sensing systems *Sensors Actuators* A **97-98** 685-90

[68] Torah R N, Glynne-Jones P, Tudor M J and Beeby S P 2007 Energy aware wireless microsystem powered by vibration energy harvesting *Proc. PowerMEMS'07* (*Freiburg, Germany, 28-29 Nov*)

[69] Naigang Wang and David P. Arnold 2009 Fully batch-fabricated MEMS magnetic vibrational energy harvesters *PowerMEMS'09* (*Washington, USA, 1-4 Dec*) 348-51

[70] Roundy S, Wright P K and Rabaey J M 2004 *Energy scavenging for wireless sensor networks with special focus on vibrations* (Norwell, MA, USA: Kluwer-Academic) pp 3–24

[71] Gilbert J M and Balouchi F 2008 Comparison of energy harvesting systems for wireless sensor networks *Int. J. Autom. Comput.* **05** 334–47

[72] Wowk V 2005. Machine Dynamics, Inc. a professional machine vibration services and training firm, Article by a principal training instructor [online]. Available from http://www.machinedyn.com/revised/tutorial.pdf [cited 12 July 2010].

[73] Gao R X and Cui Y 2005 Vibration-based energy extraction for sensor powering: design, analysis, and experimental evaluation *Proc. SPIE* (*San Diego, CA, USA, Mar 7*) **5765** 794–801

[74] Khan F, Sassani F and Stoeber B 2010 Vibration-based PDMS membrane type electromagnetic power generator for low vibration environments *Proc. CSME FORUM 2010 (Victoria, Canada, June 7-9)*

[75] Anton S R and Sodano H A 2008 A review of power harvesting using piezoelectric materials (2003–2006) *Smart, Mater. Struct.* **16** 1–21

[76] Hoffmann D, Folkmer B and Manoli Y 2009 Fabrication, characterization and modelling of electrostatic micro-generators *J. Micromech. Microeng.* **19** 094001

[77] Arnold D P 2007 Review of microscale magnetic power generation *IEEE Trans. Magn.* **43** 3940–50

[78] Beeby S P, Tudor M J and White N M 2006 Energy harvesting vibration sources for microsystems applications *Meas. Sci. Technol.* **17** 175–95

[79] Beeby S P, Torah R N, Tudor M J, Glynne-Jones P, O'Donnell T, Saha C R, and Roy S 2007 A micro electromagnetic generator for vibration energy harvesting *J. Micromech. Microeng.* **17** 1257–65

[80] Wang P H, Dai X H, Fang D M and Zhao X L 2007 Design, fabrication and performance of a new vibration-based electromagnetic micro power generator *Microelectron. J.* **38** 1175–80

[81] Huang W S, Tzeng K E, Cheng M C, and Huang R S 2007 A silicon mems micro power generator for wearable micro devices *J. Chinese Inst. Engrs.* **30** 133–40

[82] Pan C T, Hwang Y M, Hu H L and Liu H C 2006 Fabrication and analysis of a magnetic self-power microgenerator *J. Magn. Magn. Mater.* **304** 394–6

[83] Serre C, Pe´rez-Rodrıguez A, Fondevilla N, Martincic E, Morante J R, Montserrat J and Esteve J 2009 Linear and non-linear behavior of mechanical resonators for optimized inertial electromagnetic microgenerators *Microsyst. Technol.* **15** 1217–23

[84] Wacharasindhu T and Kwon J W 2008 A micromachined energy harvester from a keyboard using combined electromagnetic and piezoelectric conversion *J. Micromech. Microeng.* **18** 104016

[85] Torah R, Glynne-Jones P, Tudor M, O'Donnell T, Roy S and Beeby S 2008 Self-powered autonomous wireless sensor node using vibration energy harvesting *Meas. Sci. Technol.* **19** 125202

[86] Yuen S C L, Lee J M H, Luk M H M, Chan G M H, Lei K F, Leong P H W, Li W J and Yam Y 2004 AA size micro power conversion cell for wireless applications *Proc. 5th World Congress on Intelligent Control and Automation, (Hangzhou, China, 15-19 June)* **6** 5629–34

[87] Sari I, Balkan T and Kulah H 2008 An electromagnetic micro power generator for wideband environmental vibrations *Sensors Actuators* A **145–146** 405–13

[88] Kulkarni S, Koukharenko E, Torah R, Tudor J, Beeby S, O'Donnell T and Roy S 2008 Design, fabrication and testing of integrated micro-scale vibration-based electromagnetic generator *Sensors Actuators* A **145–146** 336–42

[89] Koukharenko E, Beeby S P, Tudor M J, White N M, O'Donnell T, Saha C, Kulkarni S and Roy S 2006 Microelectromechanical systems vibration powered electromagnetic generator for wireless sensor applications *Microsyst. Technol.* **12** 1071–7

[90] Glynne-Jones P, Tudor M J, Beeby S P and White N M 2004 An electromagnetic vibration-powered generator for intelligent sensor systems *Sensors Actuators* A **110** 344–9

[91] Soliman M S M, Abdel-Rahman E M, El-Saadany E F and Mansour R R 2008 A wideband vibration-based energy harvester *J. Micromech. Microeng*. **18** 115021

[92] Sterken T, Baert K, Van Hoof C, Puers R, Borghs G and Fiorini P 2004 Comparative modeling for vibration scavengers *Proc. IEEE Sensors Conf.* (*Vienna, Austria 24-27 Oct*) **3** 1249-52

[93] Mitcheson P D, Green T C, Yeatman E M and Holmes A S 2004 Architectures for vibration-driven micropower generators *J. Microelectromech. Syst.* **13** 429–40

[94] Svoboda J 2004 *Magnetic techniques for the treatment of materials* (Dordrecht, Netherland: Kluwer-Academic) pp 260–263

[95] Yang B, Lee C, Xiang W, Xie J, He J H, Kotlanka R K, Low S P and Feng H 2010 Electromagnetic energy harvester from vibrations of multiple frequencies *J. Micromech. Microeng*. **19** 035001

[96] Yang B and Lee C 2010 Non-resonant electromagnetic wideband energy harvesting mechanism for low frequency vibrations *Microsyst. Technol.* **16** 961–66

[97] Hatipoglu G and Urey H 2009 FR4-based electromagnetic energy harvester for wireless sensor nodes *Smart, Mater. Struct.* **19** 015022

[98] Wang P, Tanaka K, Sugiyama S, Dai X, Zhao X and Liu J 2009 A micro electromagnetic low level vibration energy harvester based on MEMS technology *Microsyst. Technol.* **15** 941–51

[99] Krantz D, Belk J, Biermann P, Dubow J, Gause L, Harjani R, Mantell S, Polla D, and Troyk P 1999 Project update: Applied research on remotely-queried embedded microsensors *Proc. of SPIE* **3673** 157-64

[100] Hautamaki C, Zurn S, Mantell S, and Polla D 2000 Embedded microelectromechanical systems (MEMS) for measuring strain in composites *Journal of Reinforced Plastics and Composites* **19** 268-77

[101] Lee C Y, Hsieh W J and Wu G W 2008 Embedded flexible micro-sensors in MEA for measuring temperature and humidity in a micro-fuel cell *J. Power Sources* **181** 237-43

[102] Srovnal V 2005 Using of Embedded Systems in Biomedical Applications *Proc. 3rd Conf. European Medical and Biological Engineering EMBEC'05* (*Prague, Czech Republic, 20-25 Nov*) **11**

[103] Val C, Couderc P and Lartigues P 2009 Stacking of full rebuilt wafers for sip and abandoned sensors/applications *Conf. European Microelectronics and Packaging EMPC2009* (*Rimini, Italy, 15-18 June*) 1-9

[104] Zhang Z 2009 Ubiquitous human motion capture using wearable micro-sensors *Proc. IEEE Int. Conf. Pervasive Computing and Communications PerCom2009* (*Galveston, TX, USA 9-13 Mar*) 1–2

[105] Zhang Z, Wong L W C and J K Wu 2010 3D Upper Limb Motion Modeling and Estimation Using Wearable Micro-sensors *Int. Conf. Body Sensor Networks BSN2010* (*Singapore 7-9 June*) 117-23

[106] Lukowicz P, Kirstein T and Tröster G 2004 Wearable systems for health care applications *Methods Inf. Med.* **43** 232–9.

[107] Scheffler M and Hirt E 2004 Wearable devices for the emerging healthcare applications *Proc. 26th Int. Conf. IEEE IEMBS 2004* (*San Francisco, CA, USA, 1-5 Sept*) 3301-04

[108] Pantelopoulos A and Bourbakis N G 2010 A Survey on Wearable Sensor-Based Systems for Health Monitoring and Prognosis *IEEE Tran. Syst. Man. Cybern. Part C: Appl. Rev.* **40** 1-12

[109] Vullers R J M, Schaijk R V, Doms I, Hoof C V and Mertens R 2009 Micropower energy harvesting *Solid-State Electronics* **53** 684–93

[110] Priya S and Inman D J 2009 *Energy Harvesting Technologies* (New York: Springer)

[111] Cook-Chennault K A, Thambi N and Sastry A M 2008 Powering MEMS portable devices-a review of non-regenerative and regenerative power supply systems with special emphasis on piezoelectric energy harvesting systems *Smart Mater. Struct.* **17** 043001

[112] Khan F, Sassani F and Stoeber B 2010 Vibration-based PDMS membrane type electromagnetic power generator for low vibration environments *Proc. CSME FORUM 2010 (Victoria, Canada, June 7-9)*

[113] Berg Y, Wisland D T and Lande T S 1999 Ultra low-voltage/low-power digital floating-gate circuits *IEEE Trans. Circuits Syst. II* **46** 930-6

[114] Makihara K, Onoda J and Miyakawa T 2006 Low energy dissipation electric circuit for energy harvesting *Smart Mater. Struct.* **14** 717-21

[115] Shen D N, Park J H, Ajitsaria J, Choe S Y, Wikle III H C and Kim D J 2008 The design, fabrication and evaluation of a MEMS PZT cantilever with integrated Si proof mass for vibration energy harvesting *J. Micromech. Microeng.* **18** 055017

[116] Sodano H A, Inman D J and Park G 2004 A review of power harvesting from vibration using piezoelectric materials *Shock Vibration Dig.* **36** 197-206

[117] Torres E O and Rincón-Mora G A 2009 Electrostatic energy-harvesting and battery-charging CMOS system prototype *IEEE Trans. Circuits Syst. I* **56** 1938–48.

[118] Kulah H and Najafi K 2008 Energy scavenging from low frequency vibrations by using frequency up-conversion for wireless sensor applications *IEEE Sensors Journal* **3** 261-8

[119] Beeby S P, Tudor M J, Torah R N, Koukharenko E, Roberts S, O'Donnell T and Roy S 2006 Macro and micro scale electromagnetic kinetic energy harvesting generators *Proc. DTIP Conf. (Stresa, Italy, 26-28 April)*

[120] Saha C R, O'Donnell T, Wang N and McCloskey P 2008 Electromagnetic generator for harvesting energy from human motion *Sensors Actuators* A **147** 248-53

[121] James E P, Tudor M J, Beeby S P, Harris N R, Glynne-Jones P, Ross J N and White N M 2004 An investigation of self-powered systems for condition monitoring applications *Sensors Actuators* A **110** 171-6

[122] Spreemann D, Manoli Y, Folkmer B and Mintenbeck D 2006 Non-resonant vibration conversion *J. Micromech. Microeng.* **16** 169–73

[123] Kulkarni S, Koukharenko E, Tudor J, Beeby S, O'Donnell T, Roy S 2007 Fabrication and Test of Integrated Micro-Scale Vibration Based Electromagnetic Generator *Proc. 14th conf. Solid-State Sensors, Actuators and Microsystems, Transducers & Eurosensors'07* (*Lyon, France, 10-14 June*) 879–82

[124] Sari I, Balkan T and Kulah H 2007 A wideband electromagnetic micropower generator for wireless microsystems *14th conf. Solid-State Sensors, Actuators and Microsystems, Transducers & Eurosensors'07 (Lyon, France, 10-14 June)* 275-8

[125] Kulah H and Najafi K 2004 An electromagnetic micro power generator for low-frequency environmental vibrations *17th IEEE Int. Conf. Micro Electro Mechanical Systems MEMS 2004* (*Maastricht, Netherlands, 25-29 Jan*) 237-40

[126] Torah R N, Tudor M J, Patel K, Garcia I N and Beeby S P 2007 Autonomous low power microsystem powered by vibration energy harvesting *Proc. IEEE Sensors'07* (*Atlanta, GA, USA, 28-31 Oct*) 141-2

[127] Khan F, Sassani F, Stoeber B 2010 Vibration-based electromagnetic energy harvester *Proc. ASME IMECE2010 (Vancouver, Canada, Nov 12-18)*

[128] Williams C B, Shearwood C, Harradine M A, Mellor P H, Birch T S and Yates R B 2001 Development of an electromagnetic micro-generator *IEEE Proc. Circuits Devices Syst.* **148** 337–42

[129] Sari I, Balkan T, Kulah H 2009 An Electromagnetic Micro Power Generator for Low Frequency Environmental Vibrations based on the Frequency Up-Conversion Technique *IEEE Conf. MEMS 2009* (*Sorrento, Italy, 25-29 Jan*) 1075 – 1078

[130] To T K H, Sun W, Hui A P, Li W J 2001 A wireless self-powered rotation sensing system using a vibration-based micro power transducer. *IEEE/ASME M2VIP* (*Hong Kong, 27–28 Aug*)

[131] Kazmierski T J and Beeby S 2010 *Energy harvesting systems: principles, modeling and applications* (New York, USA: Springer) pp 8–11

[132] Khan F, Sassani F, Stoeber B 2010 Copper foil-type vibration-based electromagnetic energy harvester *J. Micromech. Microeng*. **20** 125006

[133] Spreemann D, Hoffmann D, Folkmer B and Manoli Y 2008 Numerical optimization approach for resonant electromagnetic vibration transducer designed for random vibration *J. Micromech. Microeng.* **18** 104001

[134] Selvaggi J A and Selvaggi J P 1987 External and internal magnetic field equations for domain oriented permanent magnets *Proc. Magnet Technology Conf. MT-10* (*Boston, USA*)

[135] Roundy S J 2003 Energy Scavenging for wireless sensor nodes with a focus on vibration to electricity conversion *Ph.D. dissertation*, Dept. Mech. Eng., Univ. of California, USA

[136] Renaud M, Karakaya K, Sterken T, Fiorini P, Van Hoof C and Puers R 2008 Fabrication, modelling and characterization of MEMS piezoelectric vibration harvesters *Sensors Actuators* A **145-146** 380-6

[137] Naruse Y, Matsubara N, Mabuchi K, Izumi M and Suzuki S 2009 Electrostatic micro power generation from low-frequency vibration such as human motion *J. Micromech. Microeng* **19** 094002

[138] Bouendeu E, Greiner A, Smith P J, Korvink J G 2010 A low cost electromagnetic generator for vibration energy harvesting A low cost electromagnetic generator for vibration energy harvesting **11** 107-113

[139] Williams C B, Shearwood C, Harradine M A, Mellor P H, Birch T S and Yates R B 2001 Development of an electromagnetic micro-generator *Proc. IEEE Circuits Device Syst.* **148** 337–42

[140] Lohndorf M, Kvisteroy T, Westby E and Halvorsen E 2007 Evaluation of energy harvesting concepts for a tire pressure monitoring systems *Proc. PowerMEMS* (*Freiburg Germany 28-29 Nov*) 331-4

[141] Priya S 2007 Advances in energy harvesting using low profile piezoelectric transducers *J Electroceram* **19** 165–82

[142] Roundy S, Wright P K and Rabaey J 2003 A study of low level vibrations as a power source for wireless sensor nodes *Comput. Commun.* **26** 1131–44

[143] Sari I, Balkan T and Kulah H 2009 An electromagnetic micro energy harvester based on an array of parylene cantilevers *J. Micromech. Microeng.* **19** 105023

[144] Ferrari M , Ferrari V, Guizzetti M, Marioli D and Taroni A 2008 Piezoelectric multifrequency energy converter for power harvesting in autonomous microsystems *Sensors Actuators* A **142** 329–35

[145] Liua J Q, Fanga H B, Xub Z Y, Maob X H, Shena X C, Chena D, Liaob H and Caia B C 2008 A MEMS-based piezoelectric power generator array for vibration energy harvesting *Microelectron. J.* **39** 802–6

[146] Lin S C, Lee B S, Wu W J and Lee C K 2009 Multi-cantilever piezoelectric MEMS generator in energy harvesting *Proc. IEEE Ultrasonics Symposium (Roma, Italy, 20-23 Sep)* 755–8

[147] Moehlis J, DeMartini B E, Rogers J L and Turner K L 2009 Exploiting nonlinearity to provide broadband energy harvesting *Proc. ASME 2009 DSCC (Hollywood, California, USA, 12-14 Oct)*

[148] Cottone F, Vocca H and Gammaitoni L 2009 Nonlinear energy harvesting *Phys. rev. lett.* **102** 1–4

[149] Tvedt L G W, Nguyen D S and Halvorsen E 2010 Nonlinear behaviour of an electrostatic energy harvester under wide- and narrowband excitation *J. Microelectromech. Syst.* **19** 305–16

[150] Ferrari M, Ferrari V, Guizzetti M, Ando B, Baglio S and Trigona C 2010 Improved energy harvesting from wideband vibrations by nonlinear piezoelectric converters *Sensors Actuators* A 162 425–31

[151] Stanton S C, McGehee C C and Mann B P 2010 Nonlinear dynamics for broadband energy harvesting: Investigation of a bistable piezoelectric inertial generator *Physica* D **239** 640–53

[152] Lin J T, Lee B and Alphenaar B 2010 The magnetic coupling of a piezoelectric cantilever for enhanced energy harvesting efficiency *Smart Mater. Struct.* **19** 045012

[153] Elvin N G and Elvin A A 2010 Effects of axial forces on cantilever piezoelectric resonators for structural energy harvesting *Strain* doi: 10.1111/j.1475-1305.2010.00751.x

[154] Lesieutre G A and Davis C L 1997 Can a coupling coefficient of a piezoelectric device be higher than those of its active materials? *Syst. Struct.* **8** 859–67

[155] Leland E S and Wright P K 2006 Resonance tuning of piezoelectric vibration energy scavenging generators using compressive axial preload *Smart Mater. Struct.* **15** 1413–20

[156] Soliman M S M, Abdel-Rahman E M, El-Saadany E F, and Mansour R R 2009 A design procedure for wideband micropower generators Journal of microelectromechanical systems **18** 1288–99

[157] Serre C, Perez-Rodrıguez A, Fondevilla N, Morante J R, Montserrat J , Esteve J 2007 Vibrational energy scavenging with Si technology electromagnetic inertial microgenerators *Microsyst. Technol.* **13** 1655–61

[158] Thomsen J J 2003 *Vibrations and Stability; Advanced Theory, Analysis and Tools* (Berlin, Germany:Springer-Verlag) pp 116–119

[159] Dimarogonas A 1996 *Vibration for Engineers* (New Jersey, USA: Prentice-Hall) pp 607–8

[160] Liu M, Sun J, Sun Y, Bock C, and Chen Q 2009 Thickness-dependent mechanical properties of polydimethylsiloxane membranes *J. Micromech. Microeng.* **19** 035028

[161] Sardini E and Serpelloni M 2009 Passive and self-powered autonomous sensors for remote measurements *Sensors* **9** 943–60

[162] Vullers R J M, Schaijk R V, Doms I, Hoof C V, Mertens R 2009 Micropower energy harvesting Solid-State Electronics **53** 684–93

[163] S Chalasani and Conrad J M 2008 A Survey of Energy Harvesting Sources for Embedded Systems *IEEE SoutheastCon* (*Huntsville, AL, USA, 3-6 April*) 442-7

[164] Platt S R, Farritor S and Haider H 2005 On low-frequency electric power generation with PZT ceramics *IEEE/ASME Trans. Mech.* **10** 240-52

[165] Chiu Y, Kuo C T and Chu Y S 2007 MEMS design and fabrication of an electrostatic vibration-to-electricity energy converter *Microsyst. Technol.* **13** 1663-9

[166] Koukharenko E, Beeby S, Tudor J, White N, O'Donnell T, Saha C, Kulakrni S and Roy S, 2006, MEMS vibration powered electromagnetic generator for wireless sensor applications, *Microsyst. Technol.* **12** 1071–77

[167] Stephen N G 2006 On energy harvesting from ambient vibration *J. Sound Vib.* **293** 409–25

[168] Williams C B and Yates R B 1996 Analysis of a micro-electric generator for Microsystems *Sensors Actuators* A **52** 8–11

[169] Adhikari S, Friswell M I and Inman D J 2009 Piezoelectric energy harvesting from broadband random vibrations *Smart Mater. Struct.* **18** 115005

[170] Halvorsen E, Blystad L C J, Husa S and Westby E 2007 Simulation of electromechanical systems driven by large random vibrations *MEMSTECH'2007* (*Lviv-Polyana, Ukraine, 23-26 May*) 117–22

[171] Tvedt L G W, Blystad L C J and Halvorsen E 2008 Simulation of an electrostatic energy harvester at large amplitude narrow and wide band vibrations *DTIP MEMS & MOEMS* (*Nice, France, 9-11 April*) 296-301

[172] Halvorsen E 2007 Broadband excitation of resonant energy harvesters Proc. PowerMEMS (*Freiburg, Germany, 28-29 Nov*) 319–322

[173] Halvorsen E 2008 Energy harvesters driven by broadband random vibrations *J. Microelectromech. Syst.* **17** 1061–71

[174] Dimarogonas A 1996 *Vibration for engineers* (New Jersey, USA: Prentice-Hall Inc.)

[175] Crandall S H and Mark W D 1963 *Random vibration in mechanical systems* (New York, USA: Academic Press Inc.)

[176] Preumont A 1994 *Random vibration and spectral analysis* (Dordrecht, Netherlands: Kluwer-Academic)

[177] Saha C R, O'Donnell T, Loder H, Beeby S and Tudor J 2006 Optimization of an electromagnetic energy harvesting device *IEEE Trans. Magn.* **42** 3509–11

[178] Roberts J B and Spanos P D 1990 *Random vibration and statistical linearization* (Sussex, England: John Wiley & Sons Ltd.) pp 122–73

[179] Nigam 1983 *Introduction to random vibrations* (London, England: The MIT Press) pp 267–78

[180] Dinca F and Teodosiu C 1973 *Nonlinear and random vibrations* (New York, USA: Academic Press Inc.) pp 336–8

[181] Bulsara A R, Lindenberg K and Shuler 1982 Spectral analysis of a nonlinear oscillator driven by random and periodic forces. I. Linear theory *J. Stat. Phys.* **27** 787–808

[182] Bois G P 1961 *Tables of indefinite integrals* (New York, USA: Dover Publications)

Appendix A

Evaluation of the integral of the square of the absolute value of complex frequency response

For a system if the complex frequency response function is of the form

$$H(i\omega) = \frac{i\omega B_1 + B_0}{-\omega^2 A_2 + i\omega A_1 + A_0}, \qquad \text{(A.1)}$$

the integral of the square of the absolute value of complex frequency response can be computed as

$$\int_{-\infty}^{\infty} \left|H(i\omega)\right|^2 d\omega = \pi \frac{\left(B_0^2 \diagup A_0\right) A_2 + B_1^2}{A_1 A_2} \qquad \text{(A.2)}$$

For other forms of complex frequency response functions, the evaluation of the integral of the square of the absolute value of complex frequency response can be obtained from [175] or integral tables, for example by G. Petit Bois, 1961 [182].

Appendix B

Calculation of the equivalent frequency for statistical linearization of the nonlinear system with nonlinear stiffness

For x being a random process, the average of the ensemble of x

$$E[x] = \int_{-\infty}^{\infty} xp(x)dx \qquad \text{(B.1)}$$

depends on the probability density function $p(x)$ of x, it is also the mean or the expected value of x. The mean square value of x is expressed as

$$E[x^2] = \int_{-\infty}^{\infty} x^2 p(x)dx\,. \qquad \text{(B.2)}$$

In statistical linearization, the replacement of the nonlinear component $\omega_n^2(z+\eta z^3)$ by an equivalent linear component $\omega_{eq}^2 z$ to obtain the equation of motion of an equivalent linear energy harvester produces an error

$$e = \omega_n^2(z+\eta z^3) - \omega_{eq}^2 z\,. \qquad \text{(B.3)}$$

The mean square value of the error e according to equation (B.1) can be written

$$E[e^2] = \int_{-\infty}^{\infty} e^2 p(z)dz \qquad \text{(B.4)}$$

in terms of the error e and the probability density function $p(z)$ of the relative displacement z between the magnets and a coil.

Substituting (B.2) into (B.3) yields the following equation

$$E[e^2] = \int_{-\infty}^{\infty} [\omega_n^2 (z + \eta z^3) - \omega_{eq}^2 z]^2 \, p(z) dz$$

$$= \int_{-\infty}^{\infty} [\omega_n^4 (z + \eta z^3)^2 + \omega_{eq}^4 z^2 - 2\omega_n^2 (z + \eta z^3) \omega_{eq}^2 z] p(z) dz \, . \qquad \text{(B.5)}$$

Differentiating (B.5) with respect to ω_{eq}^2 and setting it equal to zero

$$\frac{dE[e^2]}{d\omega_{eq}^2} = \int_{-\infty}^{\infty} [2\omega_{eq}^2 z^2 - 2\omega_n^2 (z + \eta z^3) z] p(z) dz = 0 \qquad \text{(B.6)}$$

$$2\omega_{eq}^2 \int_{-\infty}^{\infty} z^2 p(z) dz - 2\omega_n^2 \int_{-\infty}^{\infty} z(z + \eta z^3) p(z) dz = 0 \qquad \text{(B.7)}$$

$$\omega_{eq}^2 E[z^2] - \omega_n^2 E[z.z(1 + \eta z^2)] = 0 \qquad \text{(B.8)}$$

yields the equation for the equivalent frequency

$$\omega_{eq}^2 = \omega_n^2 \frac{E[z.z(1 + \eta z^2)]}{E[z^2]} = \omega_n^2 \frac{E[z.z(1 + \eta z^2)]}{\sigma_z^2} \qquad \text{(B.9)}$$

that minimize the error *e*.

The expected value of the product $[z.z(1 + \eta z^2)]$ can be obtained by the expansion method of [174] as

$$E[z.z(1 + \eta z^2)] = E[z.z] E\left[\frac{d}{dz} z(1 + \eta z^2) \right] = E[z^2] E\left[1 + 3\eta z^2\right]$$

$$= E[z^2] \left\{ \int_{-\infty}^{\infty} (1 + 3\eta z^2) \, p(z) dz \right\}$$

$$= E[z^2] \left\{ \int_{-\infty}^{\infty} p(z) dz + 3\eta \int_{-\infty}^{\infty} z^2 p(z) dz \right\} = E[z^2] \left\{1 + 3\eta E[z^2]\right\} = \sigma_z^2 (1 + 3\eta \sigma_z^2) \, . \qquad \text{(B.10)}$$

Form (B.10) by substituting the value of $E[z.z(1+\eta z^2)]$ into (B.9), results in the equivalent frequency

$$\omega_{eq}^2 = \omega_n^2(1+3\eta\sigma_z^2) \qquad \text{(B.11)}$$

of the equivalent linear harvester in terms of the linear natural frequency ω_{eq}, scaling factor η of the nonlinear stiffness, and the standard deviation σ_z of the relative velocity z.

Appendix C

Experimental procedure

C.1 Measurement of the relative displacement

The measurement of the relative displacement

$$z(t) = x(t) - y(t) \qquad \text{(C.1)}$$

between the coil and magnet at various frequencies require a measurement of the displacement signal $x(t)$ at the magnet and the base oscillation signal $y(t)$ at the frame of the device. An optical reflective adhesive tape is bonded at proper spots to acquire a better reflection of the optical signal for the vibrometer. While recording these signals separately, a signal from the voltage amplifier is used as the reference.

For a noise free signal the following settings were used for the displacement sensor on the vibrometer:

- Decoder: DD-200
- Range: 80 µm/V (selectable: 2, 4, 8, 16, 32, 80, 160, 320, 640, 1280, 2560, 5120, 10240 µm/V)
- Resolution: 80 nm (Auto-selected with range)
- Maximum velocity: 2.5 m/s (Auto-selected with range)
- Tracking filter: Slow

The velocity sensor can also be used to measure the velocity of the magnet or frame and then the respective displacement can be calculated with the measurement. With the velocity sensor there is low pass filter option that helps in obtaining a better signal compared to the displacement sensor. The displacement

$$x = \frac{\dot{x}}{2\pi f} \qquad \text{(C.2)}$$

can be obtained from the velocity $\dot{x}$ reading at frequency f.

The following settings for the velocity sensor can be used during velocity measurement

- Decoder: VD-02
- Range: 5 mm/s/V (selectable: 5, 25, 125, 1000 mm/s/V)
- Maximum frequency: 250 kHz (Auto-selected with range)
- Tracking filter: Slow
- Low pass filter: 5 kHz (Selectable: 5 kHz, 205 kHz, 1005 kHz, 1.5 MHz)
- High pass filter: 100 Hz

Following are the steps involved in obtaining the amplitude of the relative displacement between the magnets and the coil of Figure 2.15 in Chapter 2:

1. Turn on laser, allow 15 minutes for system warm-up
2. Set the displacement or velocity sensor parameters
3. Focus laser spot on the magnet or device frame by using the x-y-z motion knobs of the microscope (probe station). Check the reflection indicator on vibrometer for precise focusing and good signal.
4. Set frequency of excitation with signal generator
5. Turn on power amplifier (keep current knob on maximum)
6. On voltage amplifier display, rotate the variable gain knob clockwise to start the vibration of the shaker
7. On the oscilloscope check the signals from vibrometer, accelerometer and the voltage amplifier
8. Adjust acceleration level with the variable gain knob on voltage amplifier display
9. On the oscilloscope adjust the displayed signals with horizontal and vertical positioning knobs and press “Trig” to trigger the signals
10. Press “Save/Recall” button in oscilloscope to record the signals as data files.
11. Repeat the measurement on the device frame
12. In Excel, along the reference signal $r(t)$ plot the signals $x(t)$, $y(t)$ and $z(t)$
13. Read the amplitude Z of $z(t)$
14. Repeat the same procedure (steps 1-13) for different frequencies to obtain several points for relative displacement verses frequency

With the outlined procedure, the relative displacement obtained at resonance is shown in Figure C.1.

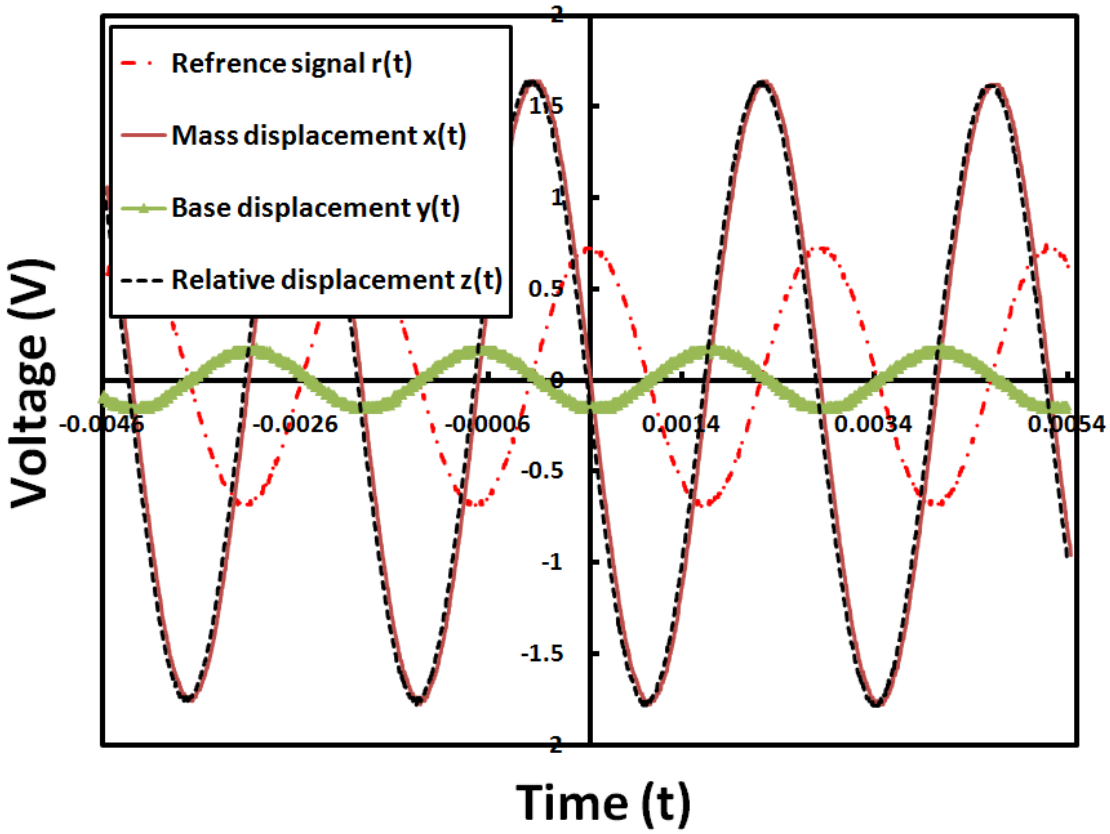

Figure C.1: Signals recorded at the resonance frequency of 371 Hz.

C.2 Noise reduction during frequency sweeps

In order to obtained frequency response of the PDMS membrane type EMEH (Chapter 4, Figures 4.10 and 4.11) with minimal noise or disturbance due to the sudden jump phenomena, the frequency sweeps are performed at low speeds, moreover, a band-pass filter is used in a LabView program to reduce the high frequency noise in the acquired signals. The response of the device recorded at fast forward sweep and without a band-pass filter shown in Figure C.2, contains noise. However, the noise in the measurement decreased considerablely when the device was subjected to slow frequency sweep and with the band-pass filter in the LabView program, Figure C.3.

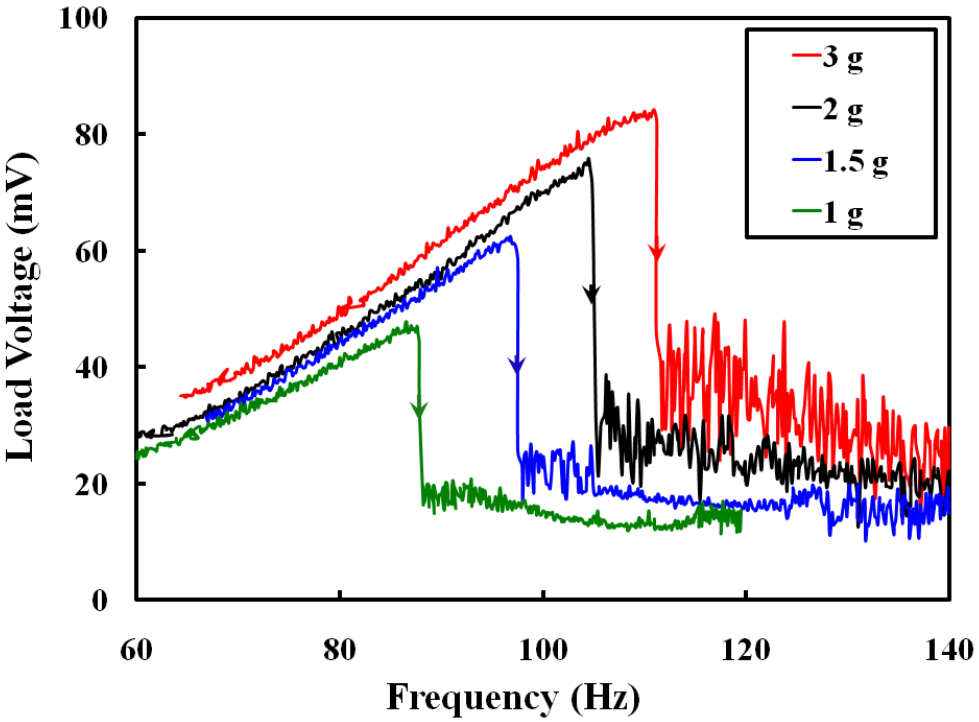

Figure C.2: Frequency response of the harvester during fast forward sweeps and without band-pass filter in LabView program.

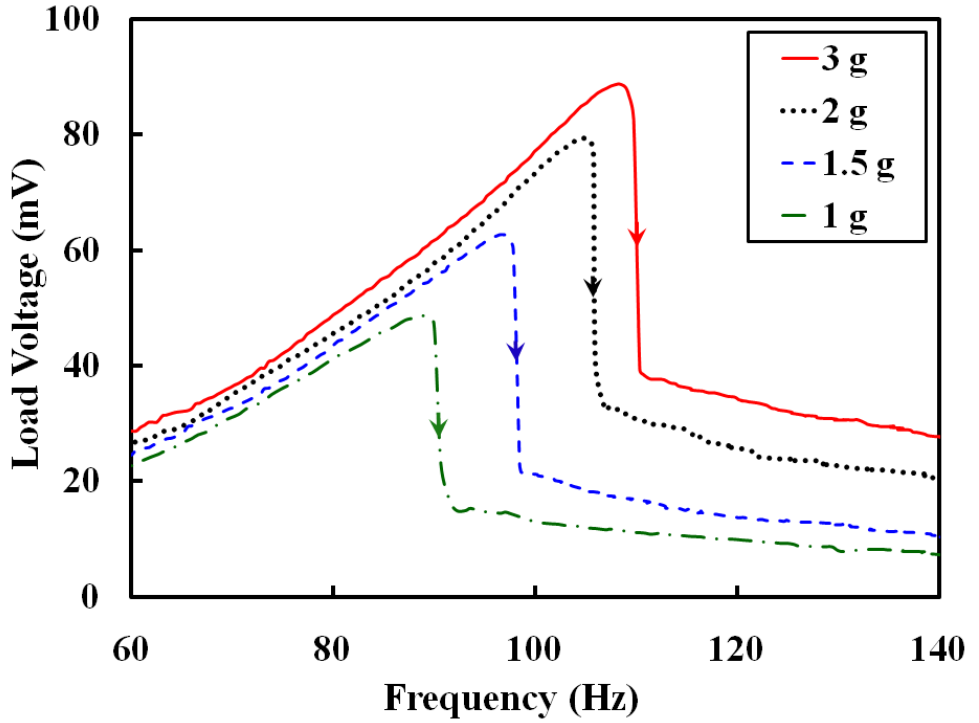

Figure C.3: Frequency response of the harvester during slow forward sweeps and with band-pass filter in LabView program.